X–ray Evolution and Variability of Active Galactic Nuclei

Mathew James Page

A thesis submitted to the University of London for the
degree of Doctor of Philosophy

Mullard Space Science Laboratory
Department of Space and Climate Physics
University College London

May 1997

Abstract

The Luminosity function and cosmic evolution of active galactic nuclei (AGN) selected in the 0.5 - 2 keV X–ray band is studied using the sample of AGN from the RIXOS survey. It is found that pure luminosity evolution models represent the data well, provided rapid evolution stops at redshift ~ 2.

The evolution of narrow emission line galaxies (NELGs), which may be important contributors to the cosmic X–ray background, is examined using the sample of NELGs obtained from the *ROSAT* UK Deep Survey and RIXOS. I detect evolution at high significance but find that this evolution is probably slower than the evolution of broad line AGN, and/or ceases at a lower redshift.

Data from deeper *ROSAT* surveys are used to extend the AGN luminosity function to lower luminosities and higher redshifts, and biases caused by the dispersion of AGN spectral slopes are incorporated in the analysis. Some deviations from pure luminosity evolution are seen for a critical ($q_0 = 0.5$) universe, and the previous conclusions regarding the lack of evolution at high redshift are strengthened.

The possibility of improved surveys of AGN with the next generation of X–ray satellites is investigated. An efficient survey for the study of the high redshift ($z > 2$) AGN luminosity function is described.

The X–ray variability of the narrow line Seyfert 1 galaxy Markarian 766 is studied using *ROSAT* data. The spectrum is well described by a power law and a blackbody soft excess. The power law component varies continuously but variability of the soft excess is not detected within the observations. The power law component is always steeper when it is brighter. This variability can be explained if the power law is produced by thermal or non-thermal Comptonisation of soft photons. The behaviour of Markarian 766 is analogous to that of Galactic black hole candidates in the low state.

Finally, the results of this thesis are related to the evolution and history of individual active galaxies.

Contents

List of Tables

List of Figures

Chapter 1

Introduction

1.1 Active Galactic Nuclei

Active galactic nuclei (AGN) are very luminous, very energetic, and very compact sources of radiation found at the centres of some galaxies. Galaxies which contain AGN are known as 'active galaxies'. In the nearby universe, most active galaxies are Seyfert galaxies which have bright, point like nuclei and strong emission lines in their optical spectra. In the far distant universe, most of the active galaxies that we are aware of are the very luminous quasi stellar objects (QSOs); they are point sources presumably because the galaxies which contain them are so distant as to be beyond detection. The extreme luminosity of AGN allow them to be detected at greater distances than any other class of astronomical objects; AGN thus provide an unique opportunity to study the universe when it was only a fraction of its present age.

1.1.1 What Powers an Active Galactic Nucleus?

It has long been known that AGN show large amplitude rapid variability, particularly in X–rays (e.g. Marshall *et al.* 1981). This variability provides limits on the size of the emitting region, because signals cannot propagate across a source faster than the light travel time. It is found that the central engines of AGN must be extremely compact, less than a light day across. It is thought that the only means of producing such a high luminosity in such a small volume is **accretion onto a massive black hole** (Rees 1984).

Dense star clusters with high rates of supernovae could reproduce many properties of at least low luminosity AGN (Terlevich *et al.* 1992, Terlevich *et al.* 1995) but would have difficulty reproducing the rapid X–ray variability seen in AGN, and would probably evolve into massive black holes on a cosmologically short time scale of $\sim 10^7$ years (Frank, King and Raine 1992).

1.1.2 Types of AGN

It is common to categorise AGN on the basis of their observed (mostly spectral) properties. I give a brief description of all types, concentrating on those which are relevant to this thesis.

QSOs are high luminosity AGN that show strong, broad (> 1000km s^{-1}) permitted emission lines, narrow forbidden emission lines, and non-stellar continua in their optical spectra. Originally, only unresolved sources were classified as QSOs, but now host galaxies of nearby QSOs can be seen in deep images, and the luminosity limit $M_b < -23$ (Schmidt & Green 1983) is used to (arbitrarily) separate QSOs and Seyfert galaxies. Those QSOs which emit a significant fraction of their luminosity at radio frequencies are called **quasars** or 'radio loud' QSOs; they are about 20 times less numerous than ordinary QSOs (Ciliegi *et al.* 1995).

Seyfert 1 galaxies are normally spirals, and have bright point like nuclei which are less luminous than QSOs (i.e. have $M_b > -23$). The nuclear optical spectrum of a Seyfert 1 is similar to that of a QSO with broad permitted, and narrow forbidden, emission lines and a non-stellar power law continuum. It is often considered that Seyfert 1 nuclei are low luminosity QSOs because of the apparent continuity between the two classes. Some Seyfert galaxies have properties intermediate between Seyfert 1 and Seyfert 2 galaxies (see below), showing both broad and narrow components in their permitted emission lines; they are commonly classified as Seyfert 1.5, 1.8 or 1.9 galaxies. The widespread classification scheme used for Seyfert galaxies can be found in Osterbrock 1993.

Seyfert 2 galaxies, like Seyfert 1s, have bright point like nuclei and are normally spiral galaxies. Both permitted and forbidden emission lines of Seyfert 2 nuclei are narrow, and the ratio of the permitted line luminosities to the forbidden line luminosities is generally smaller than for Seyfert 1 nuclei. Seyfert 2 nuclei are normally of lower luminosity than Seyfert type 1 nuclei, and their optical spectra have a much stronger contribution from the host galaxy.

Narrow line Seyfert 1 galaxies have permitted lines which are only slightly broader than the forbidden lines, but have a ratio of permitted to forbidden emission line flux which is more typical of Seyfert 1 galaxies than Seyfert 2 galaxies (Osterbrock & Pogge 1985). Many narrow line Seyfert 1 galaxies (unlike Seyfert 2s) are particularly soft X–ray sources (Boller Brandt and Fink 1996, Puchnarewicz *et al.* 1992). Narrow line Seyfert 1 galaxies often show strong blends of Fe II lines in their optical spectra; these features are rarely seen in Seyfert 2 spectra (Goodrich 1989). In chapter 5 the X–ray emission from one such object, Markarian 766, is examined in detail.

Radio galaxies have a somewhat analogous relationship with Seyfert galaxies to that of quasars with QSOs, and similarly are about 20 times less numerous.

Radio galaxies have point like optical nuclei and emit a significant fraction of their luminosity at radio frequencies. This radio emission is frequently arranged as jets or lobes emanating from the optical nucleus. Nearby radio galaxies and quasars are frequently found to be giant elliptical galaxies at the centres of galaxy clusters, and in many cases may be fueled by cooling flows from the cluster gas (Burns, White & Hough 1981, Jones & Forman 1984).

Narrow emission line galaxies or **NELGs** are those galaxies with only narrow ($< 1000\mathrm{kms}^{-1}$) emission lines in their optical spectra. This is a broad classification, that includes Seyfert 2 galaxies as well as low ionisation nuclear emission region (LINER) galaxies, starburst and HII region-like galaxies. In starburst and HII region-like galaxies the emission lines are believed to come from gas photo-ionised by hot massive stars. LINERs are more ambiguous, and it is not clear whether the emission line gas is illuminated by hot stars or non thermal emission from accretion onto a massive black hole, or whether shocked gas, perhaps from supernovae, is responsible for the emission lines. In many cases there is evidence that both a massive black hole and star formation contribute to the emission (e.g. Gonzalez-Delgado 1995); the relation between 'real' activity (i.e. accretion onto a massive black hole) and star formation in NELGs is currently the subject of much debate.

Blazars are highly variable and highly polarised AGN. Optically violent variables (OVVs) show emission lines in their spectra, particularly when faint, while BL Lacertae type objects (BL Lacs) have no emission lines. Both have strongly enhanced continuum emission. These properties are thought to be the result of relativistic beaming of synchrotron radiation. All blazars are radio loud.

1.1.3 The Basic Design of AGN

It is thought that AGN form a single family, and that all types of AGN have a similar physical nature (Osterbrock 1993, Mushotzky, Done and Pounds 1993). It is possible to explain most of the observed properties of AGN using only a single 'unified' model, in which the different types of AGN are explained by orientation and luminosity effects. Fig. 1.1.3 illustrates the different components of an AGN in the unified scheme. The essential features of the current AGN unified model are as follows:

At the centre of an AGN a black hole accretes material, probably through an accretion disk. Surrounding this, within a few light months of the central source, are the high velocity broad line clouds, from which the permitted lines are emitted. Of the order of a few parsecs from the central region, a massive, dusty, optically thick molecular torus obscures the central regions from about half of the sky. In two ionisation cones, hundreds of parsecs in extent, around the axis of symmetry of the torus, lies the low density forbidden line emitting region (the narrow line region). When viewed end on (along the axis of symmetry of the torus) both the broad and narrow line regions are seen (i.e. a Seyfert 1 type of spectrum is observed) but when viewed edge on the broad line region is obscured by the molecular torus and only the narrow lines are visible (i.e. a Seyfert 2 type of spectrum). A similar description can explain the difference between broad line and narrow line radio galaxies. When a radio galaxy is viewed straight down a radio jet, the relativistically beamed continuum emission dominates the spectrum; this is a blazar.

1.1.4 Multiwavelength Spectra of AGN

To within an order of magnitude, the spectrum of a typical QSO from the far infrared right up to hard X–ray frequencies is a power law of the form $f_\nu \propto \nu^{-\alpha}$ where $\alpha \sim 1$ (Weedman 1986). This means that approximately the same amount of energy is emitted in each decade in frequency. Radio loud objects have a power law spectrum that extends far into the radio, while the emission of radio quiet objects dies at greater than a few mm wavelength. The multiwavelength spectrum becomes progressively less smooth as luminosity decreases from the QSOs through Seyfert

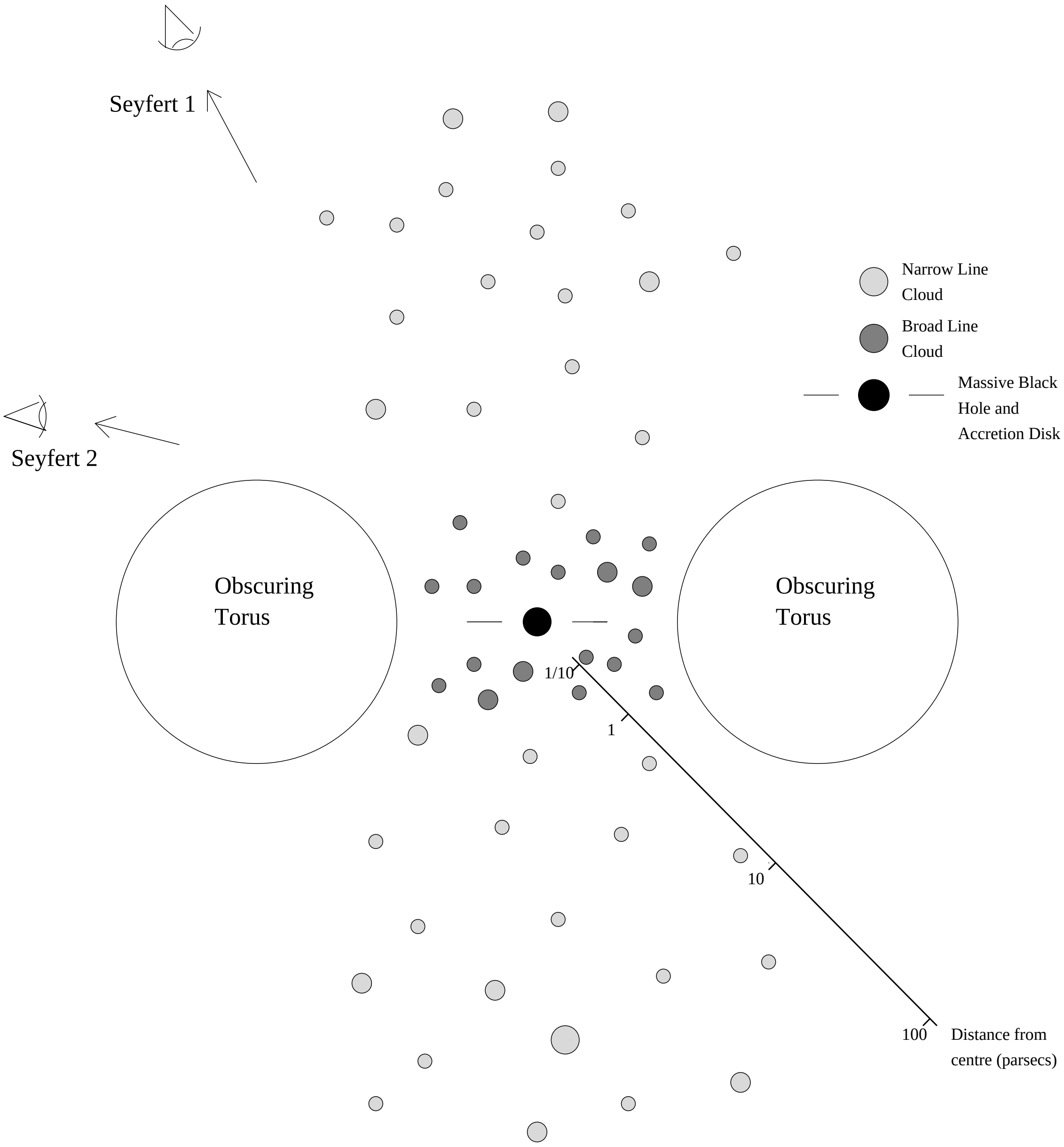

Figure 1.1: The unified model for a radio quiet AGN.

1s to Seyfert 2s. Seyfert 2 nuclei show strong absorption of blue, ultraviolet and soft X–ray radiation by dust and gas; this is subsequently reemitted as the infrared bump which is seen in both Seyfert type 1s and type 2s. Seyfert 1 nuclei frequently have a strong excess of emission from ultraviolet to soft X–ray frequencies, called the big blue bump. This is generally thought to be thermal in origin, from optically thin gas near the central engine, or, more likely, from optically thick gas in an accretion disk. A combination of blended FeII and Balmer lines produces another spectral bump, called the small blue bump, around 4000 $\AA$. Radio emission (in those objects which show it) is almost certainly synchrotron emission from relativistic electrons, and has a power law form.

1.1.5 X–rays from AGN

In the 1970s it was established that X–ray emission was a common property of AGN from the number of Seyfert 1 galaxies in the *Ariel* 5 sky survey catalogue. It is now believed that there may *no* X–ray quiet Seyfert galaxies or QSOs. From 1 to 10 keV, QSOs and Seyfert 1s have a powerlaw spectrum, $F_\nu = \nu^{-\alpha}$ where $\alpha \sim 1$; this spectrum appears to be modified by reflection from cold material in Seyfert 1 galaxies, giving them have an effective observed spectral index of $\alpha \sim 0.7$ and an Fe fluorescence line at 6.4 keV. Emission lines and absorption features from highly ionised material, particularly OVII and OVIII, further modify the spectrum. An additional soft excess component seems to be common in Seyfert 1 galaxies, with 30% of all hard X–ray selected AGN showing some excess below 1 keV (Turner & Pounds 1989). It is thought that this soft excess may be the high energy tail of the big blue bump seen from optical to ultraviolet wavelengths, although line emission could equally account for it.

Seyfert 2 nuclei, which probably have obscured central regions, are photo-electrically absorbed and are therefore harder sources, although their intrinsic unabsorbed spectra may be the same as those of Seyfert 1s. They are probably an important source population in hard X–rays, where absorption by neutral material has a smaller effect.

Narrow emission line galaxies appear to have, on average, harder spectra than QSOs (see Romero Colmenero *et al.* 1996 and Almaini *et al.* 1996 for observational evidence of this), but the heterogeneity of NELGs as a class, means that they probably have a wide mix of X–ray spectra.

1.2 K Correction

The redshift of extragalactic objects, such as AGN, makes it necessary to correct luminosities, so that all luminosities are over the same emitted band (without this correction all luminosities are over the same observed bands and hence different emitted bands for different redshifts). This emitted band is usually chosen to be the detection band, hence at $z = 0$ no K correction is applied.

$$L = L_{obs} \times K_{corr}(z)$$

where L_{obs} is the luminosity in the observers' bandpass and L is the luminosity over the same bandpass in the emitting object's frame of reference. For an object with a power law spectrum $F_\nu = k\nu^{-\alpha_0}$

$$K_{corr}(z) = (1+z)^{\alpha_0 - 1}$$

This is the form of typical K corrections used in the X–ray regime.

The K correction is unity (and hence can be neglected) for $\alpha_0 = 1$. If $\alpha_0 \neq 1$ then neglecting the K-correction will result in spurious pure luminosity evolution with redshift.

In practice, not all AGN have the same spectral index, and the K corrections for individual AGN are not known. An average K correction is applied, equivalent to the assumption that all AGN have the same spectral index. In the appendix I discuss the more realistic assumption that AGN have a distribution of spectral slopes, and how this affects the AGN luminosity function and evolution.

1.3 Detection and Identification of AGN

To study the AGN population, we have to detect AGN, and distinguish them from stars and ordinary galaxies. The selection of AGN is crucial to most of the work in this thesis, so I review the various methods of obtaining AGN samples, and their relative merits.

Optical spectroscopy is the only accurate way to classify and determine the redshifts of AGN. It is not efficient to search for AGN by taking slit spectra of all objects over a region of sky, because the sky density of AGN is less than that of normal galaxies at faint magnitudes and less than that of galactic stars at bright magnitudes. The advantage of optical spectroscopic surveys is that they are very thorough; if good spectra are taken of every object down to some limiting magnitude, it is unlikely that many AGN will be missed. With multi object spectrographs it is possible to observe enough sources that a reasonable number of AGN are identified. Faint galaxy redshift surveys, which use this technique, inevitably produce useful samples of AGN as a by product.

Objective prism surveys have been successfully used to search for AGN; each object within the field of view has a low resolution optical spectrum projected across the detector. This is the method used by Markarian who looked for galaxy nuclei with unusually strong ultraviolet emission. The technique is useful for finding bright, nearby AGN. More recently the Palomar **grism survey** was successful in detecting objects with strong emission lines down to $M_v \sim 18$. A major advantage of prism and grism surveys is that redshifts for most of the identified AGN are obtained from the prism or grism spectra, leaving a relatively small number which require slit spectroscopy.

Optical colour selection is one of the most successful methods for identification of QSOs. The broadband spectra, and hence optical colours, of QSOs are very different to those of galactic stars. The small proportion of objects which fulfil the colour selection criteria are then identified spectroscopically. The optical colours of QSOs change with redshift because different parts of the intrinsic QSO spectrum are seen at different redshifts through fixed observation passbands. It is important that the redshift dependence of colour selection is taken into account when calculating the space density of colour selected QSOs. The most widely used QSO colour selection is ultraviolet excess, known commonly as 'UVX', selection based on $U-B$ colour. It is only suitable for selection of QSOs with $0.3 < z < 2.2$.

Variability can also be used to select QSOs: Hawkins & Veron (1995) successfully selected a sample of QSOs on the basis of long term optical variability. The lack of colour dependence in this selection technique means that that there are no obvious redshift dependent selection effects. Variability amplitude and time scale do change with luminosity (Veron & Hawkins 1994) hence variability based selection will have some luminosity dependent selection effects.

Radio selection is an effective method of selecting radio loud objects because the sky density of other radio bright objects is low; at high galactic latitudes almost all radio sources in flux limited samples are extragalactic (Peacock 1985). However, most AGN are radio quiet, hence cannot be selected by radio emission.

Far infrared selection is efficient at selecting AGN, which have different *IRAS* colours to most stars and star forming galaxies (Keel *et al.* 1988). This technique is particularly effective for finding Seyfert 2 galaxies (see de Grijp *et al.* 1992), which are difficult to select at other wavelengths due to their obscured nature.

X–ray emission is perhaps the most efficient method of selecting AGN. The *ROSAT* UK Deep Survey finds AGN with a greater sky density than any other detection method (Jones *et al.* 1995). Objects are spectroscopically observed on the basis of X–ray emission, not X–ray colours, which minimises redshift dependent selection effects. To date, large surveys have only been possible at soft X–ray energies, because of the lack of high spatial resolution instruments at hard X–ray energies. Obscured sources (i.e. Seyfert 2s) are selected against at soft X–ray energies, because of their intrinsic photoelectric absorption. With the next generation of X-ray observatories, hard X–ray surveys will make X–ray selection viable for these sources.

1.4 The X–ray Background

The diffuse X–ray background was discovered by Giacconi (*et al.* 1962) using a rocket borne instrument. Since then, the spectrum and isotropy of the background have been measured from 0.1 keV to gamma ray (MeV) energies. Below 1 keV most of the X–ray background originates within our own galaxy and is probably due to a local bubble of hot gas (McCammon & Saunders 1990), but above 1 keV almost all of the X–ray background is thought to be the integrated emission of unresolved X–ray sources. The observed isotropy of the X–ray background at >3 keV and the presence of a weak dipole anisotropy which is probably caused by the motion of the Galaxy (Fabian & Barcons 1992) strongly suggests that it has an extragalactic origin. A truly diffuse (intergalactic) origin for the extragalactic X–ray background has been ruled out by the lack of Compton distortion in the shape of the cosmic microwave background, which was measured by the *COBE* satellite (Mather *et al.* 1990).

From 3 to 45 keV the spectrum of the X–ray background can be well fitted by a ~ 40 keV thermal bremsstrahlung model (Marshall *et al.* 1980). This is equivalent to a power law with energy index $\alpha \sim 0.4$ in the 1 - 7 keV band, which is the observed spectrum from joint *ROSAT* and *ASCA* fitting (Chen *et al.* 1996). Between 0.5 and 1 keV the X–ray background is brighter and softer than an extrapolation of the >1 keV background; this may be due to the contribution of Seyfert galaxies and quasars which have softer spectra ($\alpha \sim 1$) than that of the background (Fabian & Barcons 1992). The X–ray background may harbour information about large scale structure in the universe, and galaxy formation at early epochs. Determining how much of the X–ray background is produced by AGN, NELGs, absorption line galaxies, clusters, stars, etc., and at what energies the different classes of objects dominate, is clearly of considerable importance.

1.5 The Space Distribution of AGN

As AGN can be detected to a greater distance than any other class of object (up to $z \sim 5$ to date), they are of great interest for what they can tell us about the universe at earlier epochs. In this section I present a concise description of the mathematical tools which are used for examining the AGN population and its change with cosmological epoch. A Friedman model universe has been assumed (i.e. the universe is sufficiently rarefied that there is no pressure, and the cosmological constant Λ is assumed to be zero.) Where possible, I have given equations which are applicable for any value of the cosmological deceleration parameter q_0. In this thesis I have used $q_0 = 0$ and $q_0 = 0.5$ which is common in the literature; equations relevant to both these specific cases are given here.

All observations have a limiting flux for detection, such that an object with a flux less than this limit cannot be distinguished from the background or noise of the detector. The flux over a band is related to the luminosity of a source by

$$S = \frac{L}{(4\pi D_l^2) K_{corr}}$$

where S is flux, L is intrinsic luminosity, and K_{corr} is the K correction term. D_l is the luminosity distance and is:

$$D_l = \frac{c(1 - q_0 + q_0 z + (q_0 - 1)(2q_0 z + 1)^{1/2})}{H_0 q_0^2} \quad q_0 > 0$$

$$D_l = \frac{c(z + z^2/2)}{H_0} \quad q_0 = 0$$

$$D_l = \frac{2c((1+z) - (1+z)^{1/2})}{H_0} \quad q_0 = 0.5$$

where c is the speed of light, H_0 is the Hubble constant, and z is the redshift.

The limiting luminosity for detection varies with distance and so we are seeing different populations of AGN at different redshifts. To enable us to show what is observed in terms of numbers of objects at different distances and luminosities we use the luminosity function, ϕ. This is defined as the number of objects detected per unit volume per unit luminosity interval, i.e.

$$\phi = \frac{d^2N}{dVdL} \tag{1.1}$$

In general ϕ is a function of luminosity and redshift. For all calculations in this thesis, the comoving volume has been used rather than the observed volume. The comoving volume is the volume that a region of space would have if it was seen at the present cosmological epoch. This comoving volume is obtained by integrating the differential comoving volume, which is equal to $(1+z)^3$ times the observed differential volume.

The differential observed volume is

$$dV_o = -cdtD_a^2 d\Omega$$

where V_o is the observed volume, D_a is the angular distance, t is light travel time and Ω is solid angle.

$$D_a = D_l/(1+z)^2$$

and

$$dt = \frac{-dz}{H_0(1+z)^2} \quad q_0 = 0 \tag{1.2}$$

$$dt = \frac{-dz}{H_0(1+z)^2(1+2q_0z)^{1/2}} \quad q_0 > 0 \tag{1.3}$$

Hence the comoving volume, V_c between here and redshift z_1 is:

$$V_c = \Omega \int_0^{z_1} \frac{c^3(z+z^2/2)^2 dz}{H_0^3(1+z)^3} \quad q_0 = 0$$

$$V_c = \Omega \int_0^{z_1} \frac{c^3(q_0z + (q_0-1)((1+2q_0z)^{1/2}-1))^2 dz}{H_0^3(1+z)^3 q_0^4 (1+2q_0z)^{1/2}} \quad q_0 > 0$$

There are analytical expressions for the volume in the special cases $q_0 = 0$ and $q_0 = 0.5$:

$$V_c = \frac{\Omega c^3}{8H_0^3}((1+z)^2 - (1+z)^{-2} - 4ln(1+z)) \quad q_0 = 0$$

$$V_c = \frac{8\Omega c^3}{H_0^3}((1+z)^{-1} - (1+z)^{-1/2} - 1/3(1+z)^{-3/2} + 1/3) \quad q_0 = 0.5$$

The comoving volume is independent of the expansion of the Universe, and hence there is no density evolution of objects caused by this cosmological expansion.

Evolution in the comoving space density or luminosity of AGN, with redshift, is seen as a change in ϕ.

The two simplest forms of evolution are pure density and pure luminosity evolution (PLE). In pure density evolution, the number of AGN per unit comoving volume is assumed to evolve while the distribution of luminosities remains constant. In PLE, the number of AGN per unit comoving volume remains constant, while the luminosity of each AGN evolves.

1.5.1 Pure Luminosity Evolution

PLE has been a successful model for the evolution of AGN at X–ray, optical, and radio wavelengths, although deviations from this model are seen at high redshift. Most evolutionary models found in the literature for the last ten years have been based on PLE.

In PLE, only the luminosities of AGN evolve, at a rate which is the same for AGN of all luminosities. The space number density of objects remains constant, which is equivalent to:

$$\phi(L,z)dL = \phi_0(Lo)dLo \tag{1.4}$$

or in integral form

$$\int_{L_1}^{L_2} \phi(L,z)dL = \int_{Lo_1}^{Lo_2} \phi_0(Lo)dLo$$

where Lo is the de-evolved (i.e. $z = 0$) luminosity and ϕ_0 is the de-evolved (i.e. $z = 0$) luminosity function. This relation is used to determine the luminosity function at any redshift if the de-evolved ($z = 0$) luminosity function is known. The evolution is independent of luminosity, hence depends only on redshift:

$$L(z) = f(z) \times Lo$$

Changing the variable in the right hand side of equation 1.4 to L, we obtain

$$\phi(L,z) = \frac{\phi_0(L/f(z))}{f(z)} \tag{1.5}$$

In the framework of a PLE model the XLF retains its shape at all redshifts, hence the XLF at any redshift depends on only the evolution law and the XLF at zero redshift (hereafter $z = 0$ XLF).

1.5.2 Pure Density Evolution

Although PDE does not fit the current observations very well, it is important to define it, since it may describe behaviour at high redshift where the luminosity function is less well understood, and good models of the luminosity function may be a combination of density evolution and luminosity evolution. For PDE:

$$L(z) = Lo$$

$$\phi(z,L) = g(z)\phi_0(L) \tag{1.6}$$

where Lo and ϕ_0 are the luminosity and luminosity function respectively at $z = 0$. Due to the luminosity independence of $g(z)$, the XLF retains its shape at all redshifts in PDE,.

1.5.3 Other Observable Quantities Related to the Luminosity Function

It requires a large amount of observing time to obtain optical spectra of sufficient quality to give reliable redshifts, and hence distances, for faint samples of AGN. The number flux relation (number of sources N brighter than a flux S as a function of S, often expressed as the log N - log S) is used as a tool for studying evolution of faint samples without redshift information. The observed log N - log S at faint fluxes can be compared to the predictions of evolution models, if the luminosity function is known from brighter samples. The number of objects per unit volume brighter than a given luminosity L is simply the integral of the differential luminosity function from L to infinity, and so the luminosity function is related to the number flux relation by:

$$N(>S) = \int_0^\infty dz \int_{(4\pi D_l^2 S)K_{corr}}^\infty \phi(L,z)\frac{dV}{dz}dL$$

The luminosity function can also be used to predict the number of AGN seen as a function of redshift to a given limiting flux by:

$$N(>S, z_1 < z < z_2) = \int_{z_1}^{z_2} dz \int_{(4\pi D_l^2 S)K_{corr}}^\infty \phi(L,z)\frac{dV}{dz}dL$$

The luminosity function is also an essential tool for calculating the fraction of the X–ray background due to the combined luminosity of AGN. This amounts to finding the X–ray flux per square degree. The flux of each object with (L, z) multiplied by $\phi(L, z)$ gives the flux per unit luminosity interval per unit volume. To obtain the total X–ray background we must integrate over volume and luminosity, but this time there is no limiting flux for detection, we simply integrate over given Luminosity (or de-evolved Luminosity) and redshift ranges.

$$I_{XRB} = \int_0^{z_{max}} dz \int_{L_{min}}^{L_{max}} \phi(L,z) \times \frac{L}{(4\pi D_l^2)K_{corr}}\frac{dV}{dz}dL$$

1.6 Evolution of the AGN Luminosity Function at Non X–ray Wavelengths

Much of this thesis is concerned with the X–ray luminosity function of AGN, which is discussed in detail in the next chapter. To put this work in context, I briefly describe our current knowledge of the AGN luminosity function in other wavebands.

1.6.1 The Radio Luminosity Function

It has long been known (since Schmidt 1968), that the number of radio quasars increases very rapidly with redshift such that the number of quasars per unit volume in the distant past is much greater than that observed locally, even after correcting for cosmological expansion of the universe. Initially, the evolution was parameterised as PDE, but this model was found to be a poor fit when quasar samples increased in size. Dunlop and Peacock (1990) demonstrated that PLE could describe the evolution of both quasars and radio galaxies, and that the strong evolution at low redshift could not continue beyond $z \sim 2$. The different environment of radio loud objects to that of radio quiet objects may lead to different evolutionary properties between the two classes.

1.6.2 The Optical Luminosity Function

Soon after the evolution of radio quasars had been established, evolution was also discovered in the Braccesi *et al.* (1970) optically selected sample of QSOs. Boyle *et al.* (1988) showed that PLE is a good model for the evolution of QSOs using a substantial UVX sample ($>$ 400 QSOs) observed spectroscopically at the Anglo Australian Telescope (AAT). For $0.3 < z < 2.2$ the evolution can be modelled as $L \propto (1+z)^{3.2\pm0.1}$. Subsequent samples of higher redshift QSOs have constrained the luminosity function at $z > 2.2$. Hawkins & Veron 1995, using a variability selected sample, proposed that the evolution slows from $z \sim 1.5$ to $z \sim 2$ and the luminosity function is roughly constant for $2 < z < 3.2$. However, in an analysis of the Large Bright Quasar Survey (LBQS), which was conducted using several complementary selection criteria, Hewett *et al.* (1993) propose that the luminosity function continues to increase in the interval $2 < z < 3$, although at a much reduced rate compared to the evolution seen at $z < 2$. At $z > 3$ a decline in the luminosity function with redshift is found by Hawkins & Veron (1996) using variability selection, and by Schmidt *et al.* (1995) using the Palomar Transit Grism Survey.

1.7 Evolution of NELGs

Redshift surveys conducted in the B and I bands (Ellis *et al.* 1996 and Lilly *et al.* 1995 respectively) show that blue galaxies, the majority of which are NELGs, are evolving with cosmological epoch out to $z \sim 1$. It has not yet been determined whether all blue galaxies, NELGs, or only some subclasses, are evolving. At faint optical magnitudes, blue galaxies are very numerous; at $B_j = 25$, blue galaxies are overabundent by a factor of 5 - 15 compared with the expected numbers if the population were not evolving with redshift (Tyson 1988). This evolution is not seen in the red galaxy population.

Rowan-Robinson *et al.* (1993) find that faint radio sources, which are largely spiral galaxies including many starbursts and some Seyferts, are evolving with PLE at a similar rate to quasars. The low redshift of the sample, up to $z \sim 0.5$, means that evolution at higher redshift has not been determined.

Surveys of Infrared Astronomy Satellite (IRAS) sources show that galaxies selected by 60-micron emission are evolving strongly with cosmological epoch (Saunders *et al.* 1990), although with IRAS samples PLE and PDE can not be distinguished. The limited sensitivity of IRAS means that IRAS galaxy samples are dominated by objects with $z < 0.1$, and hence it has not been possible to study evolution at $z > 0.5$. Most of the IRAS selected galaxies are NELGs, many of which are starbursts and some of which are Seyferts. Much of the activity in IRAS galaxies is believed to be related to galaxy mergers (Clements *et al.* 1996).

Chapter 2

Evolution of the RIXOS AGN Luminosity Function

2.1 The X–ray Luminosity Function Before RIXOS

The first X–ray luminosity functions were constructed for AGN using data from *Uhuru* (Pye and Warwick 1979) and *HEAO 1* A-2 (Piccinotti *et al.* 1982), however the sample sizes were so small that it was not possible to investigate evolution. A major improvement in the sample sizes of AGN came with the *Einstein* satellite. Using the 31 AGN found in the completely identified *Einstein* Medium Sensitivity Survey, Maccacaro *et al.* (1983) proved that the X–ray luminosity function of AGN was evolving.

The *Einstein* Extended Medium Sensitivity Survey (hereafter EMSS Gioia *et al.* 1990, Stocke *et al.* 1991) contains 421 AGN from a surveyed sky area of 778 deg^2. It is still the largest single sample of X–ray selected AGN published, and is almost complete in that 96% of the EMSS sources have been optically identified. Maccacaro *et al.* (1991) constructed the X–ray luminosity function of the EMSS AGN in several redshift shells, showing the evolution with redshift visually, in a non parametric way. The X–ray luminosity function of the EMSS AGN is clearly steeper at high luminosities than at low luminosities; Maccacaro *et al.* (1991) used a two power law form to model the luminosity function:

$$\phi = K_1 L^{-\gamma_1} \quad L < L_{break}$$

$$\phi = K_2 L^{-\gamma_2} \quad L > L_{break}$$

where L_{break} is the luminosity at which the two power laws meet, and K_1 *and* K_2 are normalisations of the two power laws. Since we require the luminosity function to be continuous, the two normalisations are not independent. A single normalisation K_1 is adequate, since

$$K_2 = K_1 / L_{break}^{(\gamma_1 - \gamma_2)}$$

The evolution of the EMSS AGN was successfully modelled by pure luminosity evolution, and Della Ceca *et al.* (1992) showed that the evolution of the EMSS AGN is better modelled as power law PLE,

$$L(z) = L(0)(1+z)^C \tag{2.1}$$

than as PLE which is exponential with look back time.

$$L(z) = L(0)e^{C\tau} \tag{2.2}$$

where τ is look back time,

$$\tau = z/(1+z) \quad q_0 = 0$$

$$\tau = 1 - 1/(1+z)^{3/2} \quad q_0 = 0.5$$

In both cases, C is the parameter which defines the speed of evolution. Maccacaro found bestfit values of $C = 2.56 \pm 0.17$ for the power law evolution model, and $C = 4.18 \pm 0.35$ for the exponential model, where errors are 1σ. The relatively high flux limit of the EMSS (typically $> 10^{-13}$erg s^{-1} cm^{-2} in the energy range 0.3 to 3.5

keV) means that it is dominated by low redshift objects (median $z \sim 0.2$). Evolution and the luminosity function at high redshift could not be constrained using only the 13 EMSS AGN with $z > 1.5$; fainter samples were required to examine evolution over a greater area of (L,z) parameter space. Deeper *Einstein* surveys (Primini *et al.* 1991) identified only 11 AGN, and less than 70% of the sources were optically identified.

Only *ROSAT* , with its high sensitivity, low instrumental background and good spatial resolution, has made large deep surveys possible. The survey of Boyle *et al.* (1994) included 107 broad line AGN discovered in 5 deep *ROSAT* pointings. This survey covers about 1.5 deg^2 and probes to flux levels lower than 4×10^{-15}erg s^{-1} cm^{-2} (0.5 to 2.0 keV), but is only 70% complete at this flux limit. In Boyle *et al.* (1994), and Boyle *et al.* (1993), it was proposed that evolution may stop at high redshifts $z > 2$ and that evolution was occurring at a faster rate than found by Maccacaro *et al.* (1991) and Della Ceca *et al.* (1992). This conclusion was based on results obtained by adding the faint *ROSAT* AGN sample to the EMSS AGN sample, and is very sensitive to the conversion of *Einstein* to *ROSAT* fluxes. The *ROSAT* survey of Boyle *et al.* (1994) has very little overlap in source fluxes with the EMSS, so a comparison of the log N - log S relations to check for consistency is not practical.

A number of other *ROSAT* surveys have been used to construct samples of AGN suitable for investigation of the X–ray luminosity function and were contemporary with this work. They will be discussed in detail in Chapters 3 and 4.

2.2 The *ROSAT* International X–ray Optical Survey

The *ROSAT* International X–ray Optical Survey (hereafter RIXOS, see Mason *et al.* in preparation) was a program to optically identify serendipitously discovered

ROSAT X–ray sources. Deep ($exposure > 8000s$) *ROSAT* pointings were searched for X–ray sources, which were subsequently identified using optical spectroscopy. The RIXOS project was awarded international time on four optical telescopes at La Palma by the Comite Cientifico International. The large scale of the project meant that the observations and reduction of both X–ray and optical data were undertaken by a considerable number of people at a number of institutions. I went to three spectroscopic observing runs, and most of my share of the workload was reducing a significant proportion of the RIXOS optical spectra.

2.2.1 X–ray Observations

I will describe only briefly the points relevant to the work in this thesis, because I was not involved directly with either obtaining or reducing the X–ray observations which were used for RIXOS.

The majority of X–ray data reduction took place at MPE in Germany. Initially, 40 *ROSAT* fields were searched. More were added to suit optical telescope scheduling as required; ultimately 98 *ROSAT* pointings were searched for sources. All the fields were in regions of high galactic latitude ($|b| > 28^{\circ}$) to ensure a high proportion of extragalactic objects, and most fields have a low galactic column ($N_{\rm H} < 3 \times 10^{20} cm^{-2}$) according to the survey of Stark *et al.* (1992). All fields were reasonably long exposures (>8,000 s), some longer than 30,000 s. A sliding cell source detection algorithm was used to detect sources in the 0.4 to 2.4 keV band, the poorer point spread function, interstellar absorption, diffuse Galactic X–ray emission, and the increased contribution of Galactic stars complicate the detection of extragalactic sources in the 0.1 to 0.4 keV band. The positions of the X–ray sources were then cross correlated with positions of optical objects in the field of view to correct for small pointing inaccuracies of *ROSAT* . The flux of each detected source was calculated from the count rate assuming an intrinsic spectral slope $\alpha_X = 1$, which is approximately the slope found for AGN in this energy range, and all sources were corrected for absorption by Galactic $N_{\rm H}$. Sources more than 17 arc minutes off axis have been excluded due to their larger positional uncertainty (the point spread function of *ROSAT* deteriorates as off axis angle increases) and possible masking by the detector window support structure. The target of each observation and sources very close by (< 3 arc minutes) have also been excluded, so that RIXOS consists of only serendipitous sources.

Only sources with fluxes of greater than 3.0×10^{-14}erg s^{-1} cm^{-2} (0.5 to 2.0 keV) have been used. At this flux limit, all the X–ray sources are substantially above the 5σ detection threshold and source confusion is not a significant problem; the RIXOS X–ray source lists can therefore be considered statistically complete. RIXOS source positions are well determined, with 1σ error circles typically of 10 arc seconds diameter for point sources. This level of positional accuracy is essential for effective optical identification.

2.2.2 Optical Observations

The X–ray source positions were cross correlated with large astronomical databases including NED, SIMBAD and LEDA. X–ray sources coincident with likely catalogued counterparts (e.g. catalogued QSOs) were considered identified and were not observed spectroscopically; in cases where catalogue identification was ambiguous (for example catalogue objects without accurate positions) the X–ray source was included in the optical observing program.

The automatic plate measuring (APM) facility at the Royal Greenwich Observatory, Cambridge, and the Palomar Sky Survey E and O plates were used to make finding charts for each X–ray source. Error circles of the X–ray position were then superimposed. Where the APM finding charts were not sufficient (for example if no optical counterparts appeared near the X–ray source position) CCD images were obtained using the 2m Nordic Optical Telescope (NOT), the 2.5m Isaac Newton Telescope (INT), the 1m Jacobus Kapteyn Telescope (JKT), and if the source position was still blank, the 4.5m William Herschel Telescope.

Optical spectra were taken of optical counterparts within the 1σ error circle of each X–ray source. If no likely counterpart was found, the optical counterparts in the larger 2σ and 3σ error circles were investigated. The majority of the optical identification was performed using the intermediate dispersion imaging spectrograph (ISIS) on the WHT and the faint object spectrograph (FOS) on the INT. ISIS is a two arm spectrograph with CCD detectors; it was used with the 5,400Å dichroic and the R300B (blue arm) and R158 (red arm) gratings, resulting in wavelength ranges of approximately 3,900Å – 5,400 Å for the blue arm and 5,200Å – 8,300Å for the red arm. Most observations were taken through a 1 arc second slit, giving a resolution of $\sim$ 6Å for the red arm and $\sim$ 3Å for the blue arm. FOS is a fixed format spectrograph with a cross disperser and covers the wavelength range 5,200Å – 10,000Å (first order) and 3600Å – 5500Å (second order). It was used with a 1 arc second slit to give a resolution of about 15Å (first order) and 8Å (second order). The intermediate dispersion spectrograph (IDS) on the INT was used for high resolution spectroscopy of bright star optical counterparts, and was used for low resolution spectroscopy ($\sim$ 20 Å) with a wavelength range of 3,000 – 10,000 Å, when FOS was unavailable in 1995. Observations were made at the paralactic angle, except for some cluster candidates, when the slit was positioned to observe two or more galaxies simultaneously.

Optical counterparts were reobserved if the spectra were not of sufficient quality. As well as improving the overall completeness, reobserving objects that could not be identified on the basis of their original spectrum was essential to prevent selection effects within the AGN sample, such as the loss of AGN with $z \sim 0.7$, whose only strong emission line in the ISIS wavelength range, MgII 2798Å, occurs in the noisy region where the red and blue spectra are merged.

2.2.3 Construction of the RIXOS AGN Sample

Owing to the limited amount of optical telescope time available, some X–ray sources remain unobserved and/or unidentified. To obtain the optimum sample for study of the AGN population, we have not used all the RIXOS fields to the intended 3×10^{-14}erg s^{-1} cm^{-2} flux limit. Of the 98 fields that were originally searched for sources, I have excluded 17 fields, of which, 15 have had no optical identification, 1 is a repeat exposure of another field, and 1 has an error in the pointing position which has made optical identification impossible.

This leaves 81 fields in which some or all of the X–ray sources have been observed. In 62 fields, all objects have been identified or observed spectroscopically to the intended flux limit of 3.0×10^{-14}erg s^{-1} cm^{-2} (0.5 to 2.0 keV), while in each of the other 19 fields some, but not all, of the X–ray sources have been observed to this limit; these 19 fields are, however, fully observed to a flux of 8.4×10^{-14}erg s^{-1} cm^{-2} (0.5 to 2.0 keV) and are included in the RIXOS AGN sample with this flux limit. It would be possible to include some of these 19 fields at a lower flux limit than 8.4×10^{-14}erg s^{-1} cm^{-2}. However, the limited observation time devoted to these fields means that the identification rate below 8.4×10^{-14}erg s^{-1} cm^{-2} is lower than for the 62 completely observed fields. Incompleteness and spectroscopic selection effects would therefore be increased in the sample as a whole if more flux limits were used.

It is important to stress that these limits are based on whether the X–ray sources in a field have been observed, not on whether they are identified. As a result, the completeness of the sample is representative of the spectroscopic success rate. If completeness limits were assigned to each field on the basis of identification, systematic biases will be present in the sample. For example, fields with fewer sources would be more likely to be included to the lowest flux limit, while fields with a large number of sources would be those most likely to contain unidentified sources, and hence have higher completeness limits imposed. Allocating completeness limits on the basis of identification would result in a sample that was 100% complete in that all the X–ray sources above the flux limits of their parent fields would be identified; however this completeness level would not be representative of the actual spectroscopic success rate.

Spectroscopic completeness of the fields used in the RIXOS AGN sample, as a function of limiting flux, is shown in Figure 2.1.

At the lowest flux limit, 3.0×10^{-14}erg s^{-1} cm^{-2}, the sample is 93% complete; the remaining 7% of sources which are unidentified are those for which the optical counterpart(s) were too faint for us to obtain reliable optical spectra. I have made the assumption that the fraction of unidentified sources which are AGN is the same as that for the identified sources. Accordingly, the sky area used for this analysis has been corrected by multiplying the area by the fraction of sources identified; as the unidentified fraction is small, this has only a small effect on the results. Since optical completeness is a function of flux limit we have calculated the effective sky area at 3.0×10^{-14}erg s^{-1} cm^{-2}, 8.4×10^{-14}erg s^{-1} cm^{-2}, and three intermediate fluxes corresponding to significant changes in spectroscopic completeness. Again, the high level of completeness in RIXOS makes this a small correction, which has only a small effect on the results. The number of *ROSAT* fields, corrected sky coverage and identified fractions at their respective limiting fluxes are listed in Table 2.1.

2.2.4 Combination of the RIXOS and EMSS AGN Samples

The redshift distribution, $N(z)$, of the 198 AGN in the RIXOS sample is shown in Figure 2.2. The sample has a significantly higher median redshift, 0.6, than the EMSS (0.2).

To obtain the largest possible working sample of AGN, the RIXOS and EMSS surveys have been combined coherently (Avni & Bahcall 1980). This means that the source lists have been merged, and are treated as though each AGN could have been detected in any of the EMSS or RIXOS fields which have a flux limit lower than the

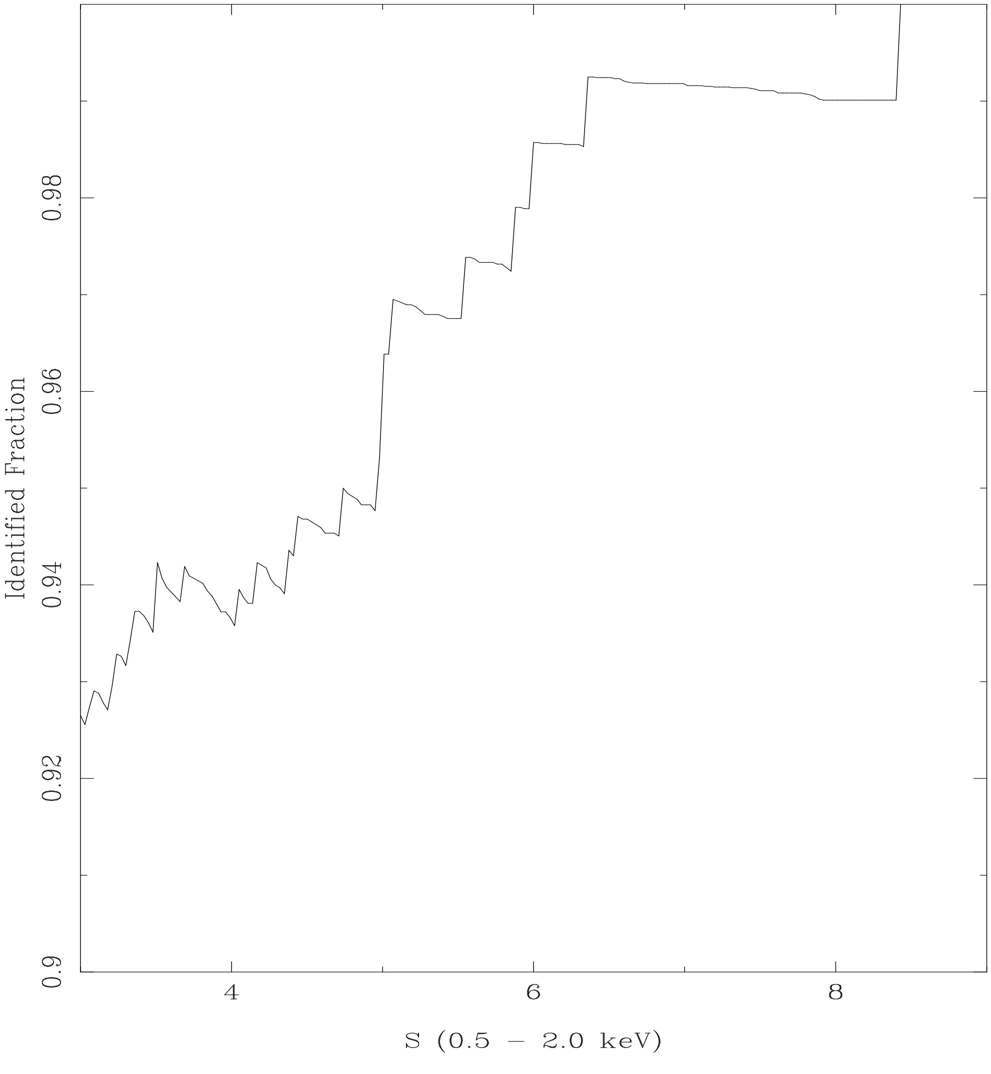

Figure 2.1: The identified fraction of sources, with flux greater than S. The calculation includes all sources from the 62 fields which are fully observed, and sources with flux greater than 8.4×10^{-14}erg s^{-1} cm^{-2} from the 19 fields used with this flux limit.

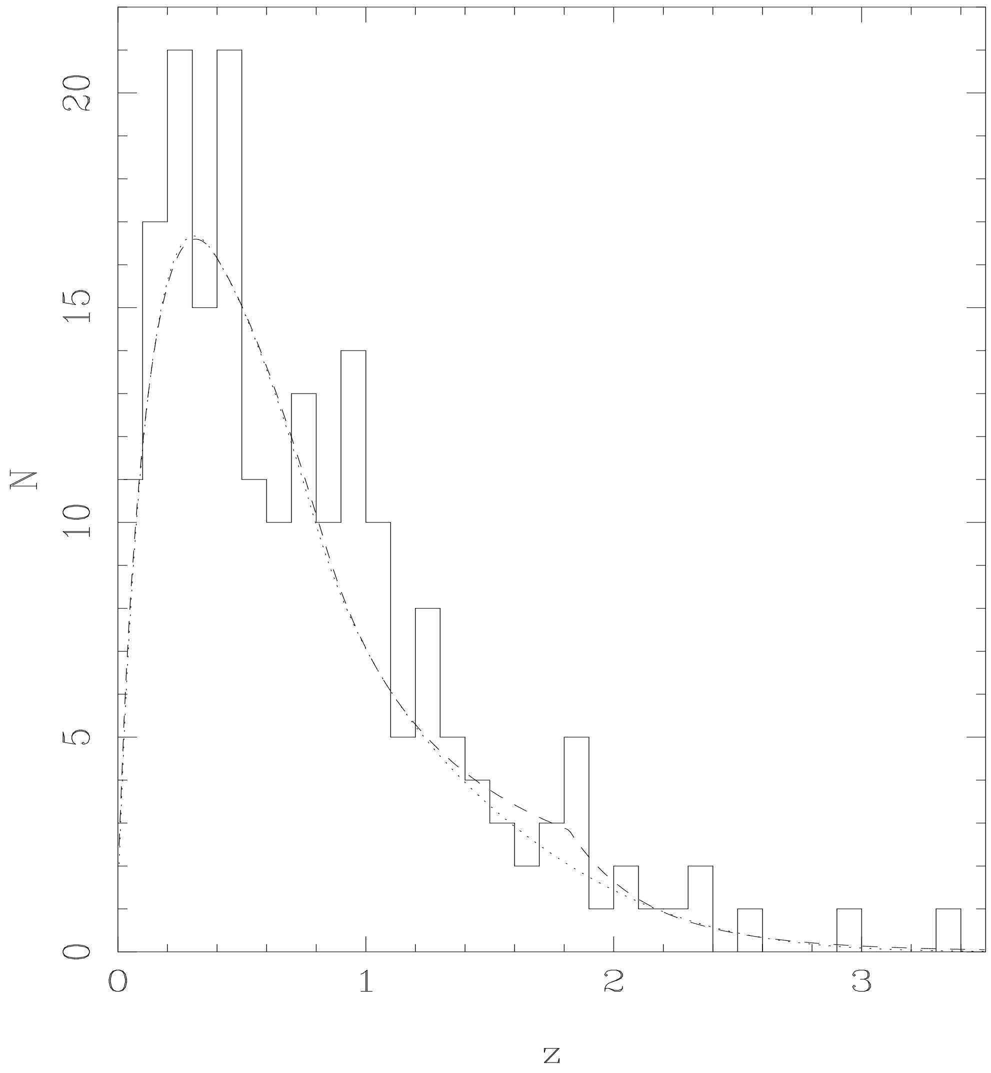

Figure 2.2: Redshift Distribution, $N(z)$, of RIXOS. The solid histogram is the actual distribution while the dashed and dotted lines are the $N(z)$ relations predicted by the power law with redshift cutoff and polynomial models respectively, for $q_0 = 0$.

Table 2.1: RIXOS cumulative sky coverage corrected for incompleteness

Flux Limit ($\mathrm{erg\ s^{-1}\ cm^{-2}}$) 0.5 – 2 keV	Corrected Area ($\mathrm{deg^2}$)	Optically Identified Fraction	Number of Fields
3.0×10^{-14}	14.16	93%	62
3.5×10^{-14}	14.36	95%	62
5.0×10^{-14}	14.73	97%	62
6.0×10^{-14}	15.09	99%	62
8.4×10^{-14}	20.04	99%	81

flux of the AGN. The few sources common to both samples are only included once, and the overall sky area is corrected for overlapping fields. This combined sample contains over 600 AGN and will be referred to as 'RIXOS + EMSS' hereafter.

I use the same AGN classification criteria in RIXOS as Stocke *et al.* (1991) use for the EMSS, which means that any object with at least one broad (FWHM > 1000km/s) emission line and/or [OIII]5007 > [OII]3727 has been included in the AGN sample. This classification scheme has been followed to avoid any significant difference between the RIXOS and EMSS optical selection. The RIXOS AGN sample (like the EMSS AGN sample) does include some objects for which only narrow lines (FWHM < 1000km/s) are visible; the effect of excluding these narrow line objects is discussed in Section 2.6.2.

To correct the EMSS sample for incompleteness, the EMSS 'expected' AGN (see Maccacaro *et al.* 1991) have been included in the EMSS and EMSS + RIXOS samples. An AGN power law X–ray spectral index, $\alpha_X = 1$, has been assumed. This is appropriate for both the EMSS AGN which have a median X–ray slope of $\alpha_X = 1.03 \pm 0.05$ (Maccacaro *et al.* 1988) and the RIXOS AGN which have a median X–ray slope of $\alpha_X = 1.05 \pm 0.05$, (see Mittaz *et al.* 1997). Boyle *et al.* (1994) and Maccacaro *et al.* (1991), also assumed an X–ray spectral slope of

$\alpha_X = 1$, hence the results of these authors can be directly compared to the results obtained here. The X–ray luminosity - redshift (L_X, z) distribution for the RIXOS and EMSS AGN are compared in Figure 2.3. As expected from a deeper survey, the RIXOS AGN typically have lower luminosity and/or higher redshift than the EMSS AGN. The combined RIXOS + EMSS sample clearly has greatly improved coverage of parameter space than either RIXOS or the EMSS alone, and therefore provides a more stringent test of evolution models.

2.3 Log N – Log S

The survey of Boyle *et al.* (1994) contains a larger number of AGN than would be predicted by extrapolating the EMSS log N – log S to lower fluxes; these authors suggested that this may be partly due to an error in their conversion from *ROSAT* to *Einstein* fluxes. In practice there are a number of factors which might affect the relative source counts and/or fluxes of the two samples, including differences in the source detection and parameterisation algorithms, uncertainties in the detector response matrices used to transform count rates to fluxes, uncertainties in the spectral form used to convert from fluxes in the *Einstein* 0.3 to 3.5 keV band to the *ROSAT* 0.5 to 2.0 keV band and the effects of incompleteness or other biases.

To assess these effects Figure 2.4 compares the integral log N – log S for the RIXOS and EMSS AGN. This plot is derived using a conversion factor (CF) of 1.8 between the fluxes in the two bands which is appropriate for a powerlaw spectrum of $\alpha_X = 1$ if we use the standard published response matrices for *ROSAT* and *Einstein* . It is clear that RIXOS has a larger number of sources than the EMSS by about 30% at almost all fluxes when using this conversion. Although RIXOS samples a larger area than the EMSS at low fluxes, there is significant overlap in the fluxes of objects found in the two samples, and there is thus no physical reason why the log N – log S relations of the two surveys should be different.

Further investigation of the reasons for this discrepancy is beyond the scope of

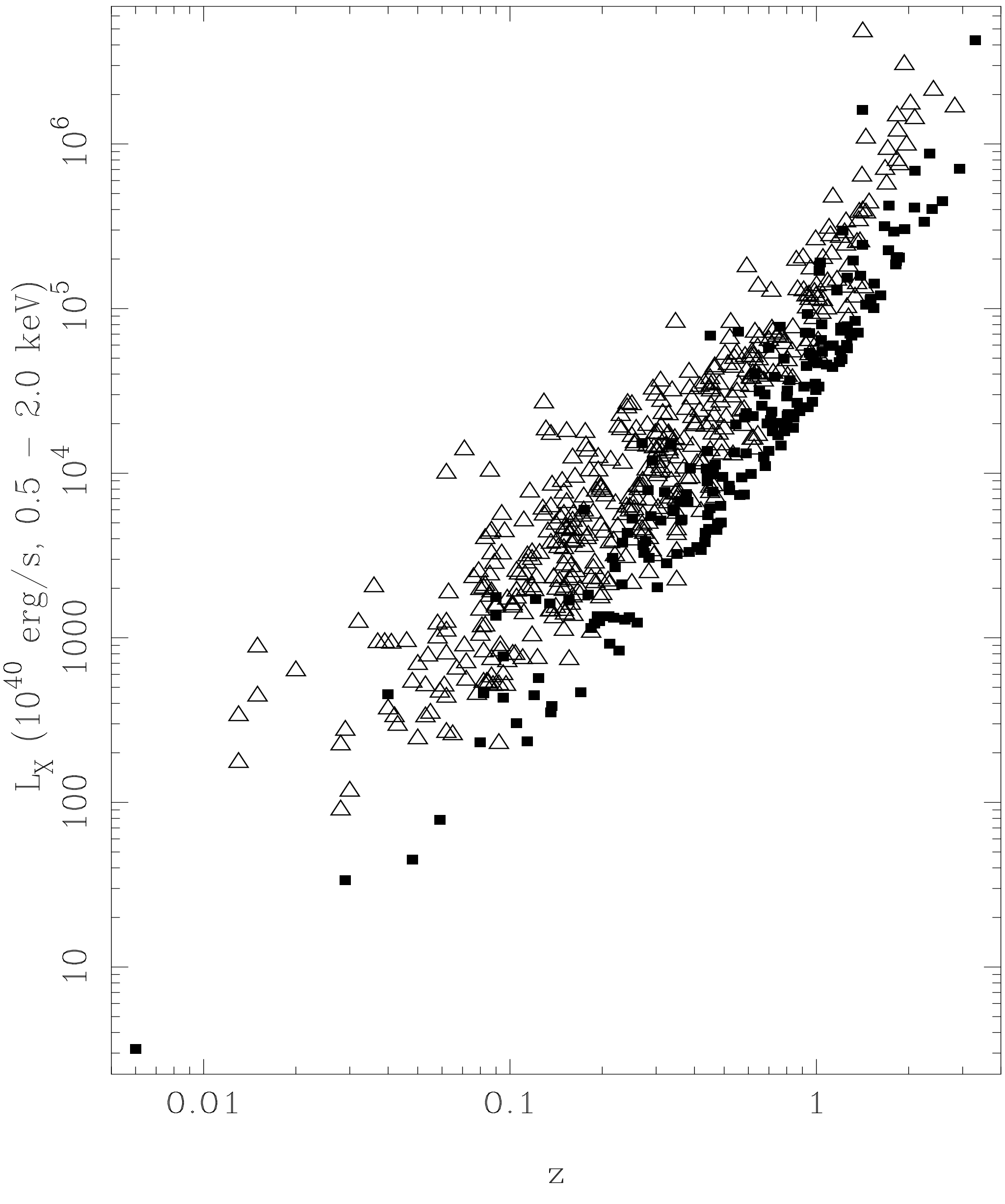

Figure 2.3: X–ray luminosity and redshift of RIXOS AGN (closed squares) and EMSS AGN (open triangles). Luminosities have been calculated using $q_0 = 0$.

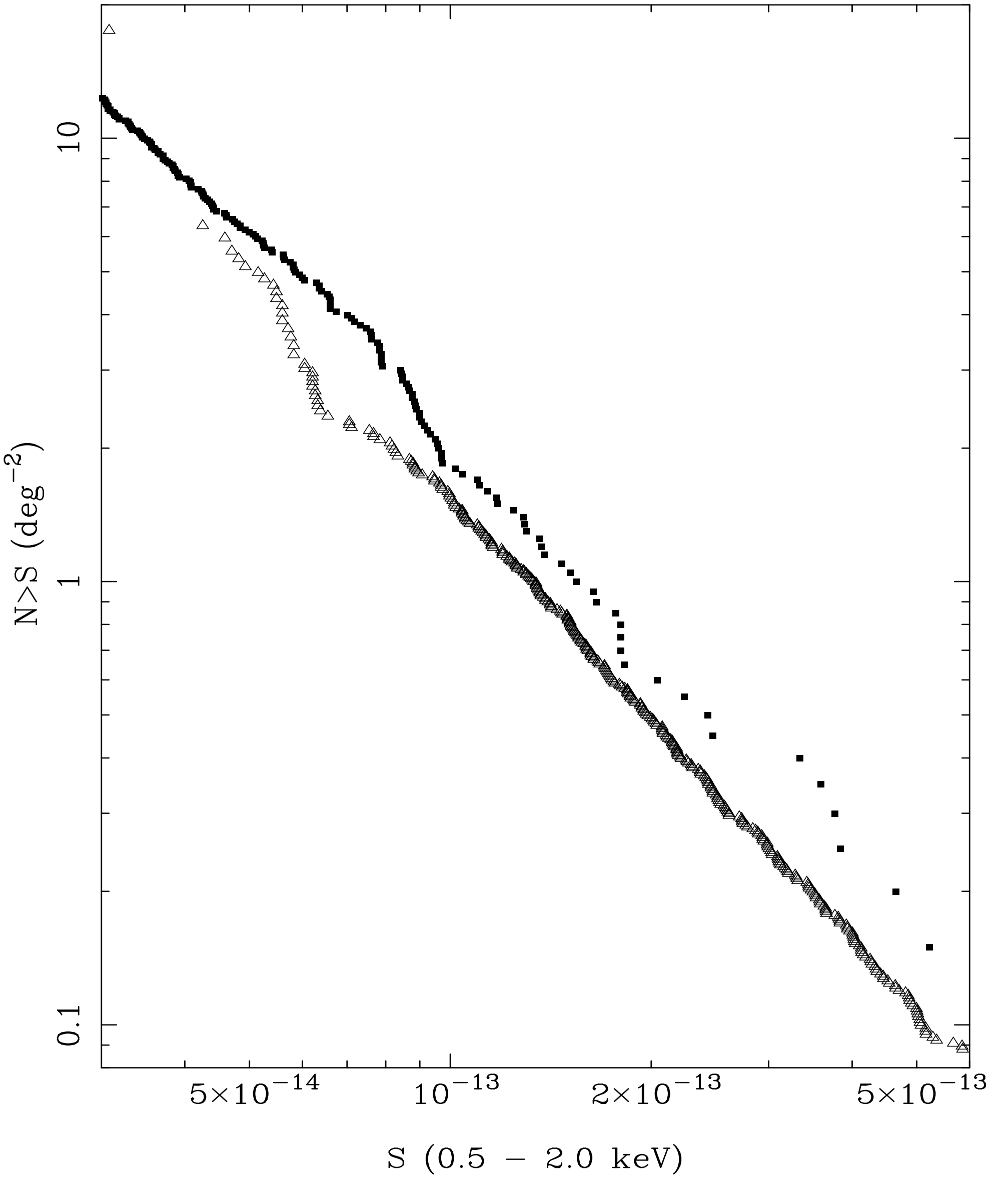

Figure 2.4: Integral log N – log S of RIXOS AGN (closed squares) and EMSS AGN (open triangles).

this thesis. Instead, I parameterise the discrepancy empirically, and investigate to what extent the uncertainty in this number affects the results on AGN evolution when I combine the RIXOS and EMSS samples. The device used for this empirical parameterisation is to find the CF for which the two log N – log S relations are consistent. At the flux limits of the EMSS and RIXOS the *N(S)* relation is well fit by a power law. Using maximum likelihood, the two samples have been fitted simultaneously with a single power law slope but different normalisations.

$$\frac{dN}{dS} = k_E S^{-\gamma} \quad \text{EMSS objects, S(0.3} - \text{3.5keV)}$$

$$\frac{dN}{dS} = k_R S^{-\gamma} \quad \text{RIXOS objects, S(0.5} - \text{2.0keV)}$$

There are two free parameters in this fit, the power law slope γ and the difference between the two normalisations (k_E/k_R); the actual normalisations are found by requiring that the number of objects predicted by the log N – log S for the sky coverage of RIXOS plus the sky coverage of the EMSS is equal to the total in RIXOS plus the total in the EMSS. The normalisation difference should be related simply to the empirical CF from *ROSAT* to *Einstein* fluxes by

$$\text{CF} = (k_E/k_R)^{1/(\gamma-1)}$$

We assumed upper flux limits of 2×10^{-11}erg s^{-1} cm^{-2} (0.3 to 3.5 keV) and 10^{-12}erg s^{-1} cm^{-2} (0.5 to 2.0 keV) for the EMSS and RIXOS respectively, to reflect the selection against very bright sources in these surveys. This has only a small effect on the results; changing the upper flux limits to any reasonable value (or removing them) changes the best fit by only a fraction of the 1 σ statistical errors quoted below. The best fit slope γ is found to be 2.56, consistent with the slopes found when the two samples are fit independently, 2.61 ± 0.06 for the EMSS and 2.45 ± 0.11 for RIXOS, where errors are 1 σ. Since the slope of the EMSS log N – log S curve is actually steeper than (although consistent with) that of RIXOS, there is no evidence from this comparison to support previous claims about incompleteness in the EMSS (e.g. Franceschini *et al.* 1994) in which incompleteness is thought to be a problem at low fluxes. The best fit CF is found to be 1.47 ± 0.11; again errors are 1 σ. The standard conversion factor of 1.8 is thus significantly different (rejected at $>99.0\%$) from that found by matching the log N - log S curves. There is, however, no evidence from the RIXOS and EMSS log N - log S that the CF should be as small as 1.0, a possibility considered in Boyle *et al.* (1994).

To assess the impact of the different conversion factors on AGN evolutionary models, values of 1.47 and 1.8 have both been used in the subsequent analysis and the results compared. Note that except where stated otherwise, all fluxes and luminosities quoted are 0.5 to 2.0 keV, i.e. the *Einstein* fluxes have been converted to the *ROSAT* flux band.

2.4 Evolution Testing and Fitting the Luminosity Function

2.4.1 $\langle V_e/V_a \rangle$

It is possible to test for evolution in a sample of AGN with the $\langle V_e/V_a \rangle$ variable described in Avni and Bahcall(1980). In this technique, each AGN is assigned a value V_e/V_a where V_e is the volume enclosed by the object (i.e. the total volume searched in the survey between here and the object) and V_a is the volume available to the object (i.e. the total volume of the survey in which the object could have been detected). V_e is a function of the object's redshift while V_a is a function of the object's intrinsic luminosity. $\langle V_e/V_a \rangle$, the mean of V_e/V_a is then determined from the whole sample. If the objects are uniformly distributed in space then $\langle V_e/V_a \rangle$ should be equal to 0.5 within its statistical uncertainty, and the individual values of V_e/V_a should be uniformly distributed between 0 and 1 (normally checked using a Kolmogorov Smirnov test, see Press *et al.* 1992). A $\langle V_e/V_a \rangle$ of greater than 0.5 indicates that that objects are found preferentially at greater than average distances, and hence that the density of objects is increasing with redshift. $\langle V_e/V_a \rangle$ less than

0.5 indicates that objects are found preferentially at smaller than average distances, hence that the either the space density of objects is decreasing with redshift, or that the completeness limits of the sample have been overestimated and objects which should have been included in the sample have been missed.

For testing pure density evolution (PDE) models, a related test, $\langle V_e'/V_a' \rangle$, uses weighted volumes V_e' and V_a'.

$$V'(z) = \int_0^z \rho(z) dV(z)$$

where ρ is the comoving density of observable objects determined from an evolutionary model. A model is acceptable if $\langle V_e'/V_a' \rangle = 0.5$ within its statistical uncertainty and the individual values of V_e'/V_a' are consistent with a uniform distribution between 0 and 1.

To test pure luminosity evolution (PLE) models, a modified version of the V_e/V_a test is used. The volume available to an object, V_a, is calculated under the assumption that it evolves according to the PLE model being tested. If the PLE model describes AGN luminosities increasing with redshift, then the volume available to each object V_a will be larger than in the no-evolution case. V_e is calculated as normal. As before, an evolution model is deemed acceptable if $\langle V_e/V_a \rangle = 0.5$ within its statistical uncertainty and the individual values of V_e/V_a are consistent with a uniform distribution between 0 and 1.

To investigate single parameter PLE models, without simultaneously modelling the $z = 0$ XLF, I use $\langle V_e/V_a \rangle$ tests in distinct redshift shells. In this case, V_a is adjusted so that the highest redshift at which an object could be detected is truncated if it exceeds the top of the redshift interval; the volume between the observer and the bottom of the redshift interval is subtracted from both V_e and V_a. The bins are chosen so that within each shell the evolution parameter has a 68% confidence region of about ±20% its value over the entire redshift range; this is a good compromise between resolution in redshift and constraint of the evolutionary properties of each bin. Use of $\langle V_e/V_a \rangle$ in redshift shells is discussed in detail in Della

Ceca *et al.* (1992).

We have also used the $\langle V_e/V_a \rangle$ test to examine evolution at high redshift in a model independent way. In this case the $\langle V_e/V_a \rangle$ test has been applied in the redshift interval $z_b < z < 3.5$, where z_b is the lower limit of the interval and is varied. Here, the test is used with no evolutionary model, and is capable of determining whether the data are consistent with the no evolution hypothesis between $z_b < z < 3.5$, and if not, whether the luminosity function is increasing with redshift ($\langle V_e/V_a \rangle \ > 0.5$), or decreasing with redshift ($\langle V_e/V_a \rangle \ < 0.5$). This use of the $\langle V_e/V_a \rangle$ test is described in more detail in Dunlop and Peacock (1990).

2.4.2 $1/V_a$

The $1/V_a$ statistic is widely used to construct a binned luminosity function. In this method, the space density of objects within a luminosity bin is determined by summing $1/V_a$ (where V_a is defined above) for all the objects within that bin. The space density in each luminosity bin is then divided by ΔL, the width of the luminosity bin, to convert from space density to the luminosity function. The 1σ uncertainty in each bin is computed as $\frac{1}{\Delta L}\sqrt{\sum_{i=1}^{N}\left(\frac{1}{V_a(i)}\right)^2}$.

Like $\langle V_e/V_a \rangle$ it is easy to use $1/V_a$ within redshift intervals, in which case V_a is adjusted as described above for $\langle V_e/V_a \rangle$. I use the $1/V_a$ statistic to produce a binned luminosity function in distinct redshift shells, which makes it possible to examine the evolution with the luminosity function without modelling either the luminosity function or the evolution. It is useful to compare model luminosity functions with the $1/V_a$ estimate to see how consistent they are at different luminosities and redshifts. For easy comparison with the binned luminosity function of Maccacaro *et al.* 1991, the same redshift intervals have been used, corresponding to intervals in look back time τ of 0.15.

2.4.3 Maximum Likelihood Fitting

The maximum likelihood method (Crawford, Jauncey and Murdoch 1970) has been used to obtain best fit evolution parameter(s) and $z = 0$ XLF for each evolution model, utilising the full RIXOS + EMSS sample of AGN. In this method, the probability density of observing the observed distribution of objects is maximised. The probability density P_i of observing an object with Luminosity L_i and redshift z_i is

$$P_i = \frac{\phi(L,z)}{\int dz \int \phi(L,z)\frac{dV}{dz}dL}$$

where the double integral is performed over all observable redshift luminosity space. The overall probability density P of the observed distribution of objects is therefore

$$P = \prod_{i=1}^{N} P_i$$

where N is the number of objects in the sample. This is equivalent to minimising S which is defined as

$$S = -ln(P) = \sum_{i=1}^{N} -P_i$$

Confidence regions can then be estimated by finding parameter values which give increased S, in the same way that $\Delta\chi^2$ is used in χ^2 fitting. This technique involves simultaneously fitting the evolution and the $z = 0$ XLF. There are four or five free parameters (three from the $z = 0$ XLF, γ_1, γ_2, and L_{break}, plus either one or two from the evolution model) in fitting the models considered in this chapter. The normalisation of the $z = 0$ XLF is set so that the total number of objects predicted by the model is equal to the number in the sample, and is not a free parameter in the fit.

Models have been fit, and subsequently tested, in the redshift and de-evolved luminosity plane over a range that includes all parameter values found in RIXOS and the EMSS, ($0 < z < 3.5, 10^{40} < L_0 < 10^{47}$) where L_0 is the de-evolved 0.5 - 2.0 keV luminosity in erg s^{-1}; note that L_0 is model dependent. Since there is no selection criterion based on observed X–ray luminosity, in this analysis, which would correspond to the $M_B < -23$ requirement often used optical QSO surveys, the test has not been performed over an interval in *observed* luminosity. Imposing a lower limit to observed luminosity in this way would introduce implicit density evolution to a PLE model (see Kassiola and Mathez 1990), and is hence undesirable.

2.4.4 The 2 Dimensional Kolmogorov Smirnov Test

To test the acceptability of evolutionary models, the two dimensional Kolmogorov-Smirnov (2D K.S.) test has been used. This test works on a similar principle to the ordinary 1 dimensional Kolmogorov Smirnov test which uses the largest difference D between the cumulative observed distribution and the cumulative model distribution to determine if the model is acceptable. In 2 dimensions, the model predicted number is compared to the observed number in each of the four quadrants $(x > X, y > Y)$, $(x > X, y < Y)$, $(x < X, y > Y)$, and $(x < X, y < Y)$, about the point (X, Y) on the x - y plane. Two alternatives have been used in the literature, the test described by Peacock (1983), and the test of Fasano & Franceschini (1987), which is also described in Press *et al.* (1992). The test of Peacock (1983) compares the model and predicted numbers around every combination of X_i and Y_j where source i has position (X_i, Y_i) and source j has position (X_j, Y_j), while that of Fasano & Franceschini (1987) only compares the model and observed numbers around each data point (X_i, Y_i). The test of Fasano & Franceschini (1987) requires less computing time: it requires of order N operations for a sample of N data points, while the test of Peacock (1983) requires N^2 operations. The result of either test is expressed as the chance probability of obtaining D, greater than that observed, if the data were drawn from the model distribution, and is referred to as P(>D). Low values of P(>D) indicate a poor model fit.

It is important to use the test most effective at rejecting poor models and accepting good models for the RIXOS and EMSS datasets, to ensure confidence in the results. To assess the most appropriate test to use, both were applied to simulated data as follows:

The two best fit XLFs and evolution models (see Section 2.1) from Maccacaro *et al.* (1991) were used to produce 200 simulated samples of AGN, 100 from each evolution model. Each sample was constructed using two completeness limits, appropriate to the RIXOS and EMSS samples respectively. The number of objects in each simulated sample was between 400 and 600, similar to the number of objects in the combined RIXOS + EMSS sample, and the tests were performed over exactly the same plane as those used on the real sample (see Section 2.4.3). In this way, the 2D K.S. tests were evaluated under very similar conditions to those under which they were actually to be applied. Each sample was tested once against its own parent XLF and evolutionary model, and once against the other, so that 200 tests were performed with correct models and 200 with incorrect models. The results of the two tests applied to the simulated data are shown in Figure 2.5.

The Peacock test rejected 100 incorrect models (50%) at the 95% level and 6 correct models, while the Fasano & Franceschini test rejected 84 incorrect models (42%) and 10 correct models. This indicates that the 2D K.S. test of Peacock is more efficient at distinguishing between good and bad models of our data. Because the EMSS and RIXOS contain a very large range of sky coverage at different completeness limits, the combined RIXOS + EMSS sample has a slightly lower redshift - de-evolved luminosity correlation coefficient (typically 0.43, but dependent on cosmological and evolutionary model) than the simulation models (typically 0.5 to 0.7). According to Fasano & Franceschini (1987), their test reaches maximum efficiency when compared to that of Peacock (1983) at *higher* correlation coefficients, and so it is reasonable to assume the results obtained from our simulations should hold for the actual data to be tested. The test of Peacock (1983) has therefore been used in this thesis.

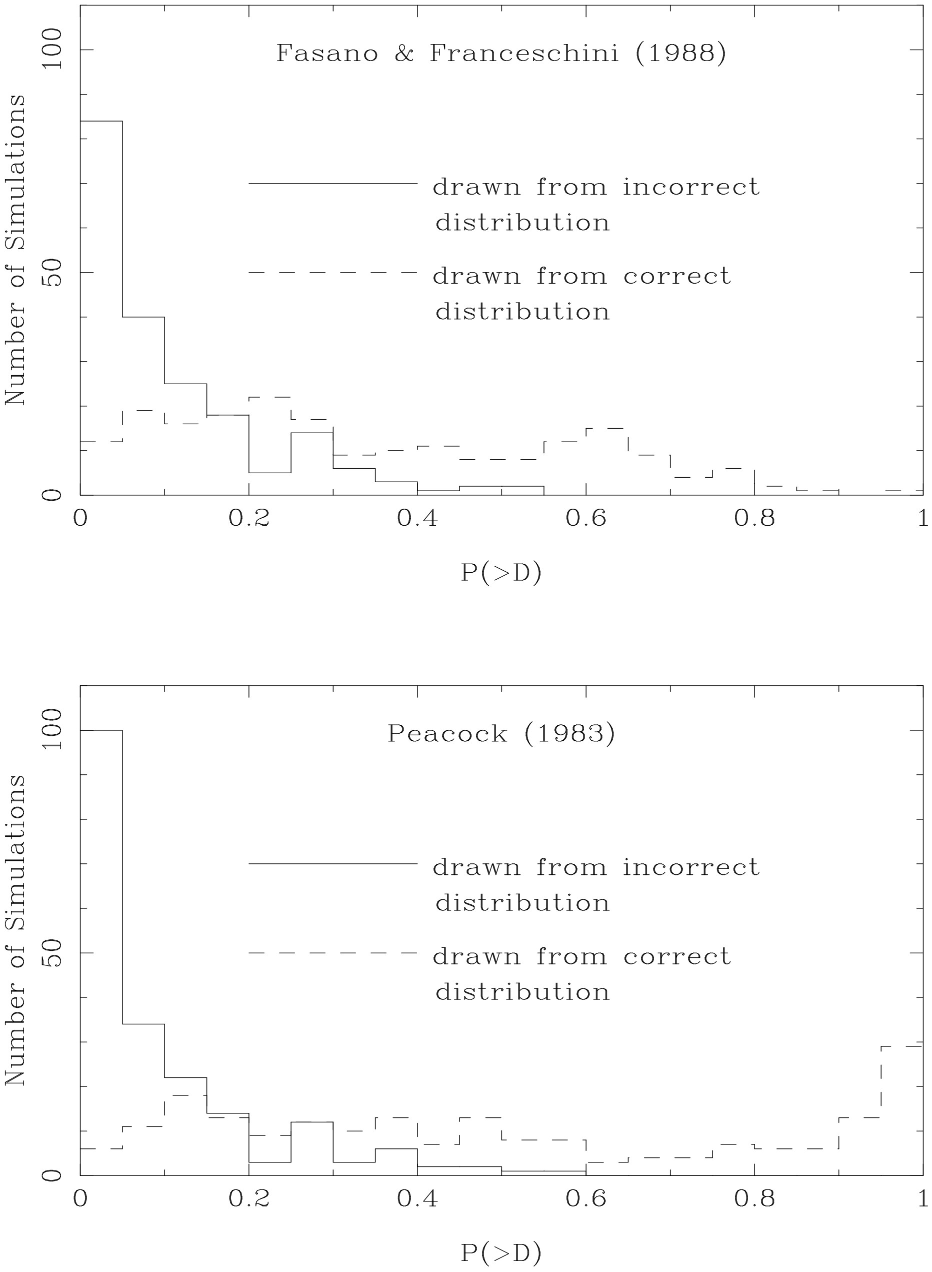

Figure 2.5: Results of applying the two different 2D K.S. tests to simulated data.

Table 2.2: Results of fitting evolution models

model	CF	q_0	z_{cut}	C	C_1	K_1[a]	γ_1	γ_2	log_{10} (L_{break})[c]	I_{XRB}[b]	P(>D) RIXOS +EMSS	P(>D) RIXOS	P(>D) EMSS
$(1+z)^C$	1.8	0.0	–	2.66	–	2.18	1.68	3.38	3.59	8.24	0.020	0.26	0.036
$e^{C\tau}$	1.8	0.0	–	4.74	–	1.59	1.64	3.23	3.29	7.31	0.033	0.047	0.033
$(1+z)^C$	1.8	0.0	1.82	2.91	–	1.83	1.65	3.30	3.49	6.88	0.27	0.62	0.096
$10^{Cz+C_1z^2}$	1.8	0.0	–	1.10	−0.230	1.56	1.62	3.27	3.52	6.47	0.36	0.45	0.17
$(1+z)^C$	1.8	0.5	–	2.35	–	1.75	1.62	3.38	3.57	4.56	0.015	0.62	0.017
$e^{C\tau}$	1.8	0.5	–	3.82	–	1.37	1.63	3.32	3.20	4.71	0.019	0.21	0.0048
$(1+z)^C$	1.8	0.5	1.42	2.94	–	1.22	1.57	3.30	3.38	4.18	0.69	0.24	0.25
$10^{Cz+C_1z^2}$	1.8	0.5	–	1.07	−0.238	1.48	1.60	3.33	3.46	4.20	0.58	0.58	0.21
$(1+z)^C$	1.47	0.0	–	2.46	–	2.00	1.64	3.23	3.64	8.28	0.055	0.55	0.042
$e^{C\tau}$	1.47	0.0	–	4.44	–	1.81	1.65	3.16	3.40	7.71	0.016	0.095	0.064
$(1+z)^C$	1.47	0.0	1.82	2.72	–	2.19	1.66	3.23	3.60	7.35	0.22	0.86	0.19
$10^{Cz+C_1z^2}$	1.47	0.0	–	1.04	−0.219	1.92	1.64	3.20	3.58	7.03	0.24	0.65	0.20
$(1+z)^C$	1.47	0.5	–	2.19	–	1.64	1.59	3.23	3.62	4.88	0.049	1.2	0.019
$e^{C\tau}$	1.47	0.5	–	3.47	–	1.52	1.61	3.19	3.31	4.86	0.026	0.24	0.045
$(1+z)^C$	1.47	0.5	1.41	2.73	–	1.39	1.57	3.19	3.48	4.57	0.22	0.38	0.14
$10^{Cz+C_1z^2}$	1.47	0.5	–	1.04	−0.238	1.54	1.58	3.22	3.51	4.69	0.38	0.80	0.18
±ERRORS													
$(1+z)^C$				0.08			0.08	0.08	0.10				
$e^{C\tau}$				0.20			0.07	0.08	0.05				
$(1+z)^C$			0.10	0.10			0.07	0.08	0.05				
$10^{Cz+C_1z^2}$				0.06	0.03		0.10	0.09	0.06				

---

[a] K_1 in units of $10^{-4}(10^{40}\text{ergs}^{-1})^{(\gamma_1-1)}$ Mpc^{-3}

[b] I_{XRB} in units of 10^{-9} erg s^{-1} cm^{-2}sr^{-1} (1 - 2 keV)

[c] L_{break} in units of 10^{40}erg s^{-1}

2.5 Results

The best fit evolution parameters and luminosity functions have been obtained from the combined RIXOS + EMSS sample. As a check for consistency between the two samples they have been tested for goodness of fit both individually and in combination. Table 2.2 shows the results for the maximum likelihood and 2D K.S. tests applied to the models that have been investigated. Errors quoted were obtained using the method of Lampton, Margon and Bowyer (1976), and correspond to $\Delta\chi^2 = 1$, i.e. 68% confidence intervals for one interesting parameter.

2.5.1 The Simplest Models

I have fit the evolution of the combined sample using the two simple PLE models used by Maccacaro *et al.* (1991), power law and exponential evolution, described by equations 2.1 and 2.2 respectively. The 2D K.S. test rejects both these simple models at the 95% level for the combined sample except the $q_0 = 0$, CF = 1.47 case where the power law model is just acceptable at the 95% level. Note that the case where the 2D K.S. probability $\mathrm{P}(> D)$ is 1.2 indicates that the difference between the expected and actual distributions is small, not that it is zero; it is possible for the test of Peacock (1983) to produce values for the $\mathrm{P}(> D)$ larger than 1, in which case it cannot be regarded as a probability, although the implication that a model is a good fit if $\mathrm{P}(> D)$ is high is certainly true.

Figures 2.6 and 2.7 show binned $1/V_a$ luminosity functions in redshift shells against the best fit power law and exponential evolution model luminosity functions. Figures 2.8 and 2.9 show evolution parameters acceptable at 68% for these two evolution models derived from the $\langle V_e/V_a \rangle$ test in redshift intervals. These figures suggest that the exponential model fails because it requires unacceptably rapid evolution at low redshift, (in Figure 2.9 the low redshift evolution parameter lies below any value which would be consistent with $z > 0.4$), while the power law model fails because it over predicts evolution at high redshift, (for $z > 1.5$ the model

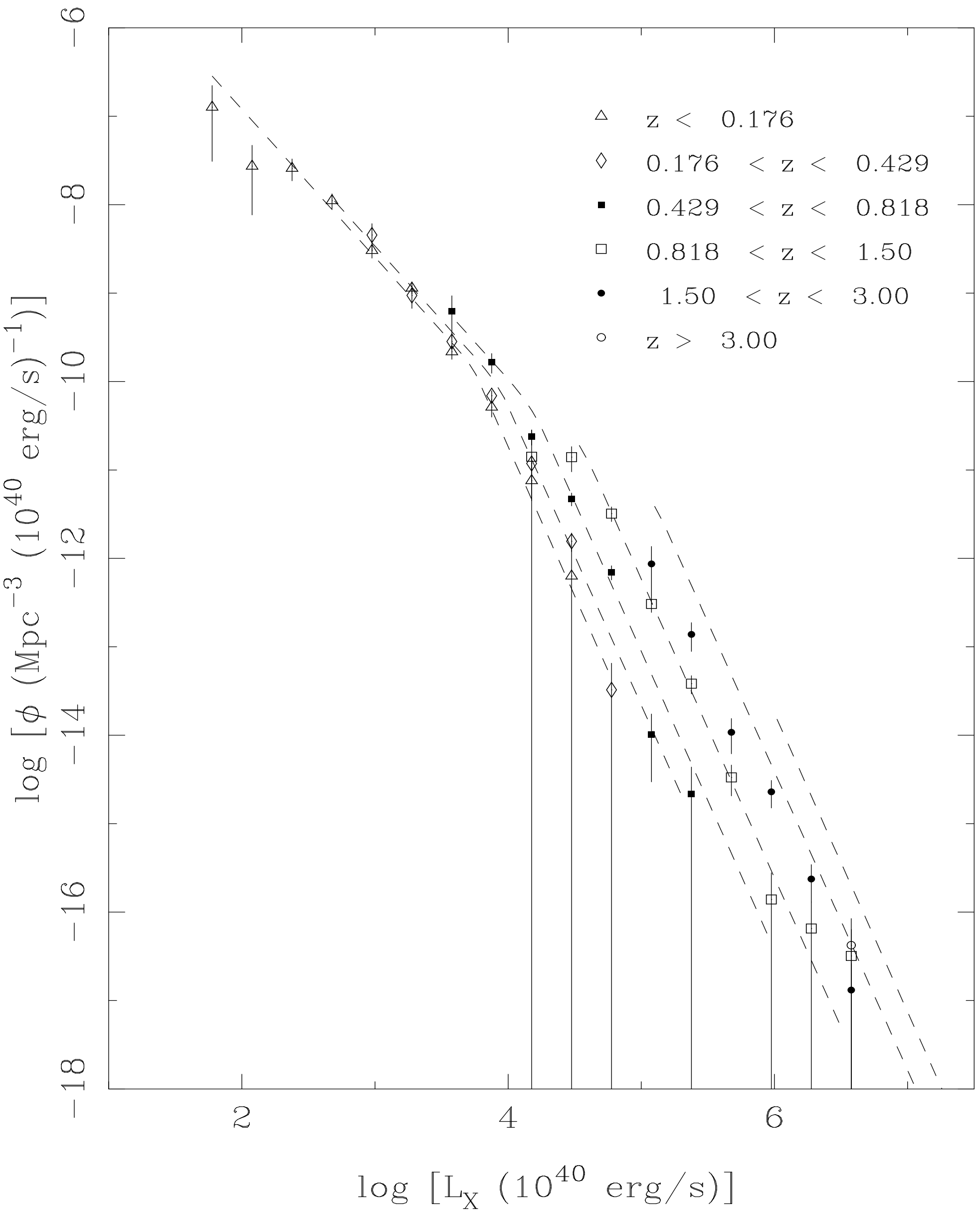

Figure 2.6: Binned $1/V_a$ XLF and best fit power law evolution model XLF (dashed lines) for $q_0 = 0$ and CF = 1.8.

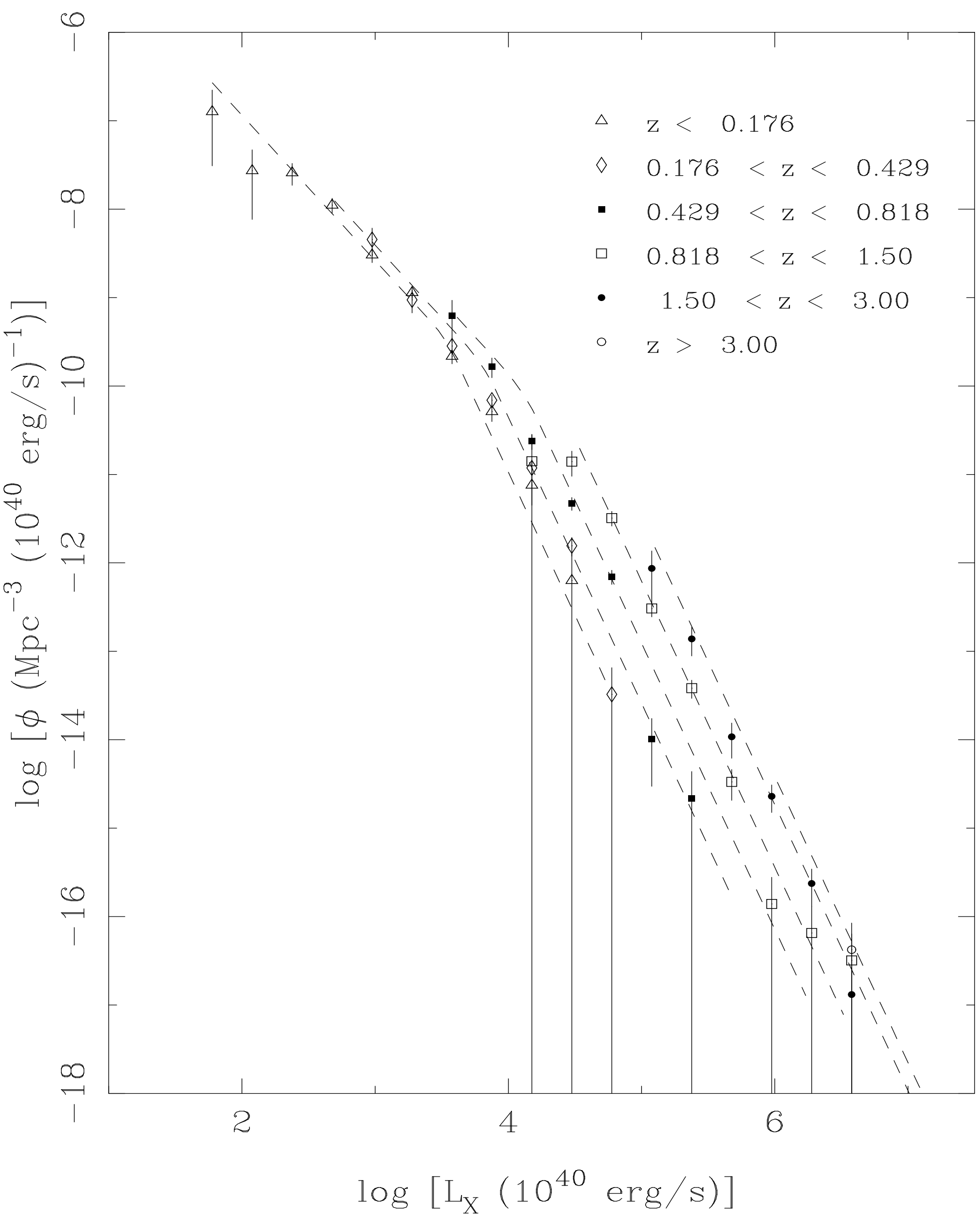

Figure 2.7: Binned $1/V_a$ XLF of the RIXOS + EMSS sample and best fit exponential evolution model XLF (dashed lines) for $q_0 = 0$ and CF = 1.8.

curves in Figure 2.6 lie well above the data). Evolution is slower at high redshift in the exponential model than in the power law model, and hence in Figure 2.7 the exponential model appears less discrepant at $z > 1.5$ than the power law model in Figure 2.6. Figures 2.6 to 2.9 have been constructed using $q_0 = 0$, CF $= 1.8$.

2.5.2 Two Parameter Evolution Models

As both single parameter models are rejected by the 2D K.S. test, more complex models have been investigated. From Figures 2.5 and 2.6 it appears there is little difference in the slope of the luminosity function in different redshift bins, so models in which the luminosity function changes slope with redshift have not been considered. A power law model with a redshift cutoff, z_{cut}, where

$$L = L_0 \times (1+z)^C \quad z < z_{cut}$$

$$L = L_0 \times (1+z_{cut})^C \quad z > z_{cut}$$

and alternatively, a polynomial evolution of the form

$$L = L_0 \times 10^{(Cz + C_1 z^2)}$$

both have two free parameters for the evolution (plus three for the luminosity function). Both of these models are accepted at the 95% level by the 2D K.S. test for the combined RIXOS + EMSS samples for both values of q_0 and CF; there is little justification, from the 2D K.S. probabilities obtained, to prefer one of the models. The similarity of the two models for $z < 1.5$ is illustrated by the predicted $N(z)$ relations plotted in Figure 2.2. The two evolution models are however radically different in shape beyond this redshift; in the polynomial evolution model, luminosities decline after $z \sim 2$, and at $z = 3.5$ the expected number of objects at 3×10^{-14}erg s^{-1} cm^{-2} differs by a factor of 5 for the two models. A larger sample of $z > 2$ objects are required to discriminate between them.

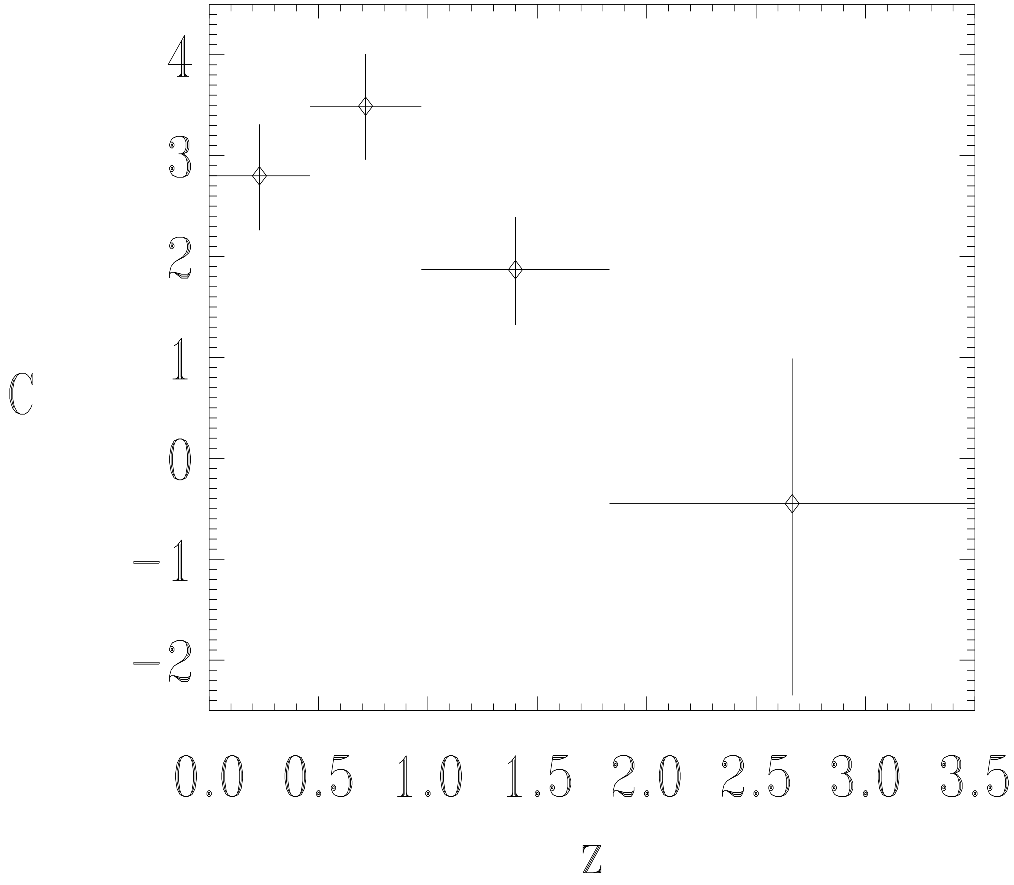

Figure 2.8: Power law evolution parameter C in redshift bins using the $\langle V_e/V_a \rangle$ test for $q_0 = 0$ and CF = 1.8.

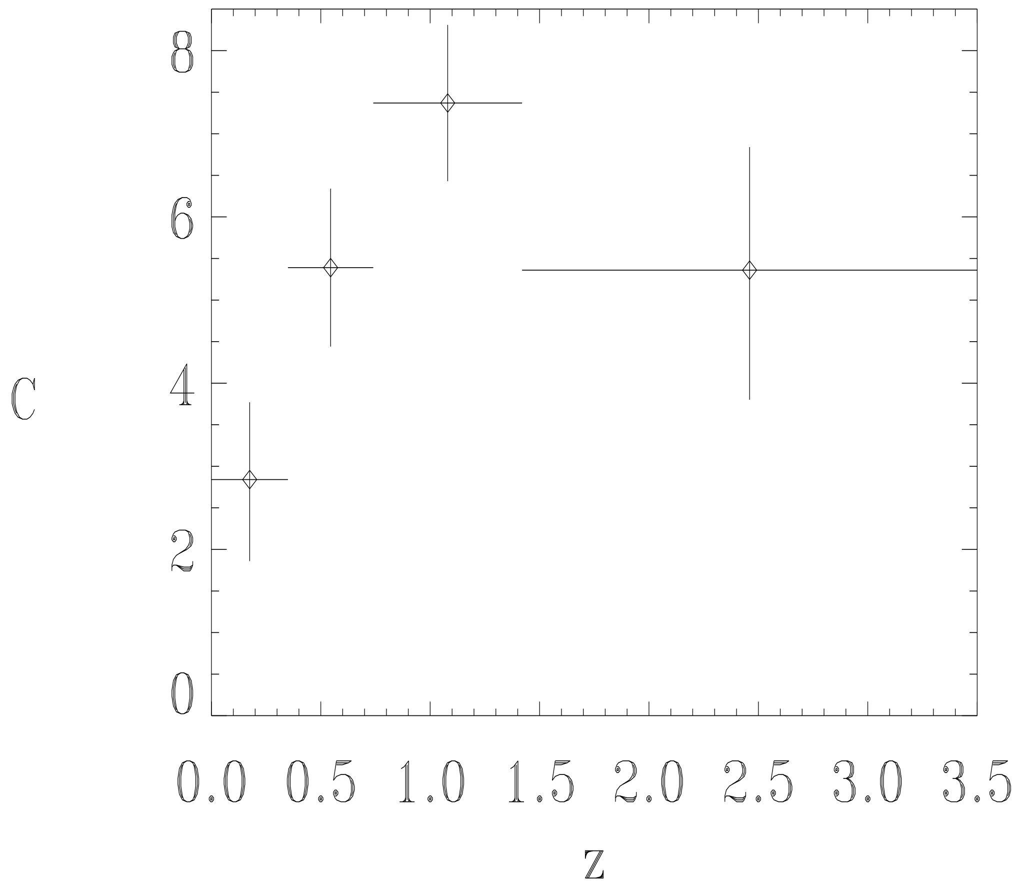

Figure 2.9: Exponential evolution parameter C in redshift bins using the $\langle V_e/V_a \rangle$ test for $q_0 = 0$ and CF = 1.8.

2.5.3 Evolution at High Redshift

It is seen in the previous section that PLE models in which evolution ceases or changes direction at high redshift are found more acceptable than models where evolution continues, for both values of q_0 and CF, indicating that evolution at $z > 2$ must be absent or slow compared to that at low redshift. As further evidence, the results of the $\langle V_e/V_a \rangle$ test from $z = z_b$ to $z = 3.5$ for the combined RIXOS + EMSS sample are shown in Figures 2.10 and 2.11. Both were constructed using a CF of 1.8; when 1.47 is used, $\langle V_e/V_a \rangle$ is a few percent lower; note that above $z_b = 2.4$ there are only 4 objects included in the test. From $z_b = 1.67$, with 30 AGN, the $\langle V_e/V_a \rangle$ test shows the data to be consistent at the 68% level with no evolution for both values of q_0 and CF. The $\langle V_e/V_a \rangle$ test used in this way is model independent, and this result is *not* restricted to PLE models.

2.6 Discussion

2.6.1 Effect of Changing the CF

Although changing the *ROSAT* to *Einstein* CF from 1.8 to 1.47 does not appear to affect the choice of model, (i.e. the power law with evolution cutoff and polynomial models are both significantly more acceptable than the simple power law and exponential models), it does have a significant effect on the best fit evolution parameter(s) and the $z = 0$ XLF. In all cases the best fit parameters for CF = 1.47 are outside the 90% confidence region of the parameters for CF = 1.8; evolution is slower, and the steep part of the XLF is less steep if the CF of 1.47 is used. The slope of the low luminosity region of the XLF is affected little by the choice of CF.

2.6.2 Comparison with Previous Results

The evolution parameter, C, for the exponential model is consistent at 68% with the EMSS value ($C = 4.18 \pm 0.35$ for $q_0 = 0$) only for CF = 1.47, and its low

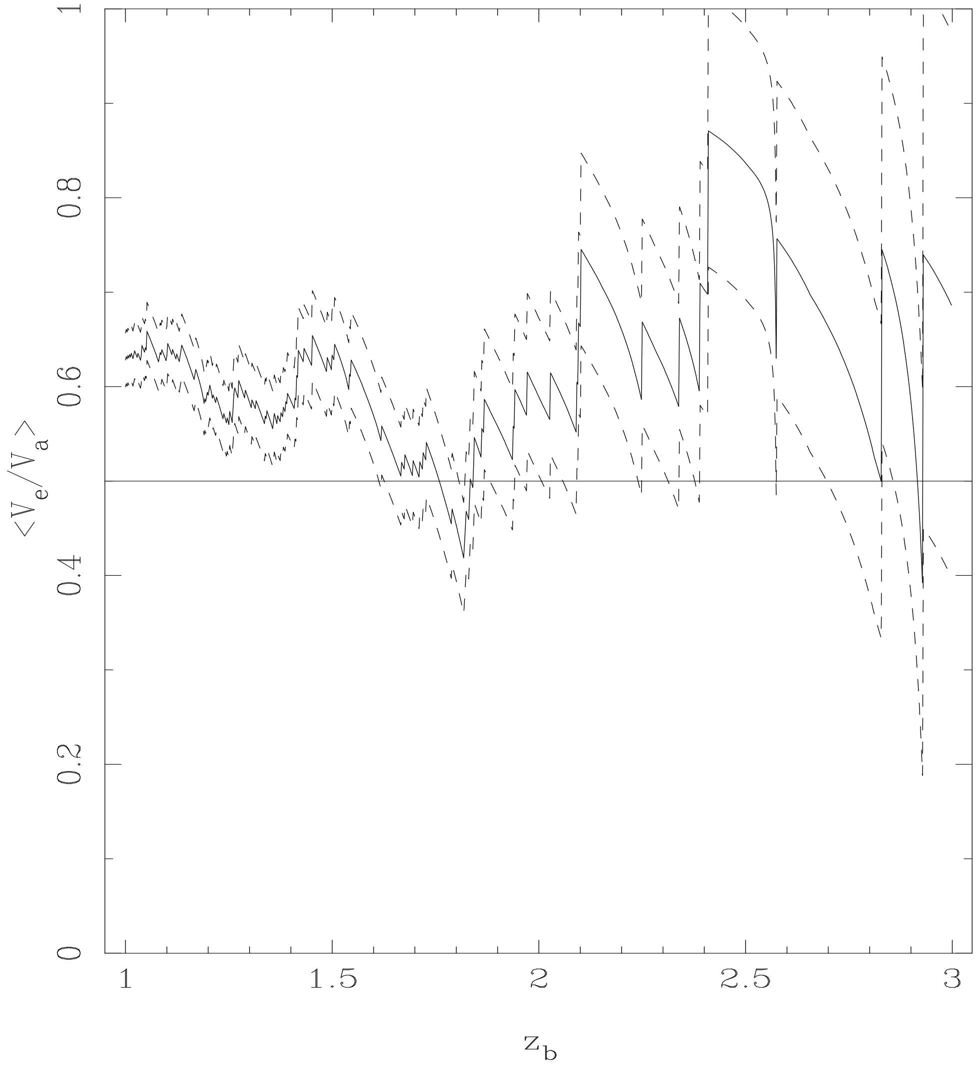

Figure 2.10: $\langle V_e/V_a \rangle$ test in the redshift interval $z = z_b$ to $z = 3.5$ using the RIXOS + EMSS sample for $q_0 = 0$.

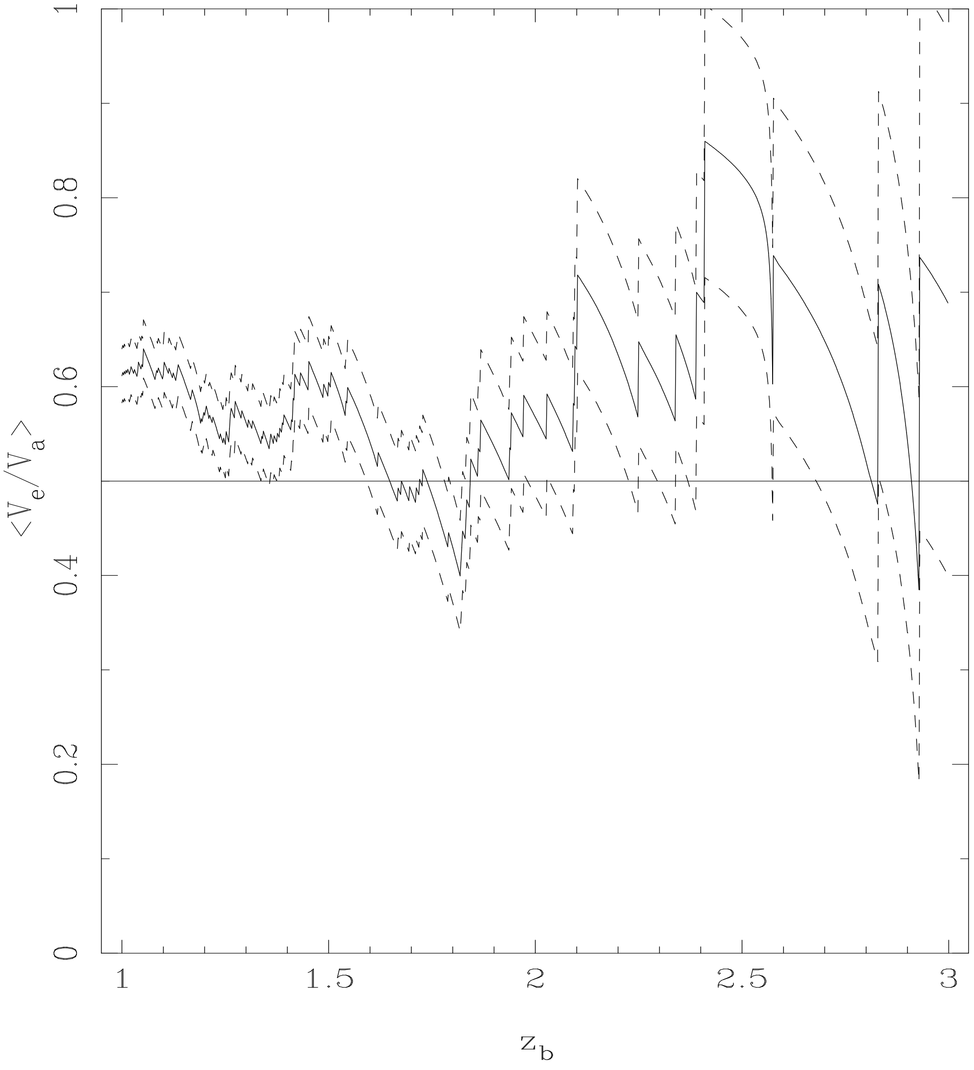

Figure 2.11: $\langle V_e/V_a \rangle$ test in the redshift interval $z = z_b$ to $z = 3.5$ using the RIXOS + EMSS sample for $q_0 = 0.5$.

K.S. probability confirms the result of Della Ceca *et al.* (1991) that this model is a poor description of AGN evolution. For the power law model, the value of C obtained here is consistent with that found by Maccacaro *et al.* (1990) (2.56 ± 0.17 for $q_0 = 0$) for both values of CF. The introduction of a cutoff in evolution at $z = 1.8$ significantly improves the 2D K.S. probability of the power law model for the RIXOS + EMSS sample; the last column of Table 2.2 shows that the EMSS data alone is also better fit with the evolution cutoff. Including an evolution cutoff at $z = 1.8$ in a $\langle V_e/V_a \rangle$ test to the EMSS data with a power law evolution model and $q_0 = 0$ gives $C = 2.74 \pm 0.20$, almost identical to the RIXOS+EMSS value for CF = 1.47 and still consistent for CF = 1.8.

Comparing the CF = 1.8, $q_0 = 0$ evolution parameters and $z = 0$ XLFs from the RIXOS+EMSS sample with those of Boyle *et al.* (1994), we find similar values for all but the exponential evolution model which evolves faster in Boyle *et al.* (1994). For $q_0 = 0.5$, there is less agreement, with the $z = 0$ XLFs of the exponential, power law, and polynomial evolution laws having significantly lower values for γ_1 (i.e. flatter slopes at low luminosity) in Boyle *et al.* (1994). The best fit $q_0 = 0.5$ power law with evolution cutoff model in Boyle *et al.* (1994), while having a similar $z = 0$ XLF and evolution rate C, has a much higher cutoff redshift ($z_{cut} = 1.7$), than the value found here, $z_{cut} = 1.4$ for $q_0 = 0.5$.

It is notable that almost all of the models considered in this paper are found more acceptable to the 2D K.S. test than in Boyle *et al.* (1994), in which almost all models are rejected at $> 99\%$. Boyle *et al.* used the test of Fasano & Franceschini (1987), while we have used that of Peacock (1983). However we have also tested our models against the RIXOS + EMSS dataset using the test of Fasano & Franceschini, and do not find them to be rejected at $> 99\%$. In Boyle *et al.* (1994), the inclusion of narrow line objects gave significantly increased 2D K.S. probabilities, (i.e. a better fit). However, narrow line objects which would be classified by Stocke *et al.* as AGN have been included throughout this analysis. If we exclude these objects, which are present in both the EMSS and RIXOS, we do find lower 2D K.S.

probabilities, although the polynomial and power law with evolution cutoff models are still acceptable at the 95% level while the simple power law and exponential evolution models are not. For the $z = 0$ XLF, typically γ_1 is reduced by about 0.1 and L_{break} is increased by 25% to 50% depending on the specific PLE model and choice of cosmology; the best fit values of γ_2 and z_{cut} change by no more than 0.02 and the evolution parameters remain within the errors quoted in Table 2.2. There are no broad line objects with $L_0 < 2 \times 10^{41}$erg s^{-1}.

The poor model fits of Boyle *et al.* (1994) may be attributable to the conversion between *ROSAT* and *Einstein* measured fluxes; the *ROSAT* sample of Boyle *et al.* (1994) combined with the EMSS AGN using a CF of 1.8 shows an evolution rate too high to be consistent with the EMSS sample alone. As we have discussed in Section 3, the effective CF from *ROSAT* to *Einstein* fluxes may be significantly lower than 1.8, and as seen in Table 2.2 a lower CF has the potential to reduce the evolution rate of combined *ROSAT* and *Einstein* data. A lower CF could improve the model fits and self consistency of the Boyle *et al.* (1994) results.

2.6.3 Fainter fluxes and the Soft X–ray Background

The log N - log S at faint fluxes derived from the CF = 1.8 models tested above, and extended to $z = 4$ are shown in Figure 2.12. None of the model curves exceed the total faint X–ray log N - log S obtained by fluctuation analysis in Hasinger *et al.* (1993), or Barcons *et al.* (1994). Notably, the log N - log S curves at faint fluxes for PLE are separated strongly by the value of q_0 used, while the specific choice of PLE model has a comparatively minor effect. In a $q_0 = 0.5$ universe, AGN undergoing PLE should represent between 30% and 45% of all sources with $S > 10^{-15}$erg s^{-1} cm^{-2}; in contrast, in a $q_0 = 0$ universe AGN evolving in this way would be expected to constitute between 55% and 100% of these sources. Above 3×10^{-14}erg s^{-1} cm^{-2} the log N - log S curves from the PLE models are all very similar and represent the data well.

The AGN contribution to the $1 - 2$ keV X–ray background has been calculated for $0 < z < 4$, $10^{40} < L_0 < 10^{47}$ (where L_0 is the de-evolved 0.5 - 2 keV luminosity in erg s^{-1}) for all the models tested in Section 5 and is shown in Table 2.2 (column entitled I_{XRB}). As expected from the log N - log S predictions, the contribution of AGN to the X–ray background from these models has a stronger dependence on the value of q_0 than the choice of PLE model. The values for the AGN X–ray background intensity given in Table 2.2 are in good agreement with those of Boyle *et al.* (1994). A recent measurement of the X–ray background (Chen, Fabian and Gendreau 1996) using both *ASCA* and *ROSAT* found an intensity of 1.46 $\times 10^{-8}$ergs^{-1}cm^{-2}sr^{-1} (1 - 2 keV). Using this value, our acceptable models (power law with evolution cutoff and polynomial) predict that AGN account for between 44% and 50% ($q_0 = 0$) or 29% and 32% ($q_0 = 0.5$) of the 1 - 2 keV X–ray background, where these ranges include the uncertainty in CF. Taking the value of 1.25 $\times 10^{-8}$ergs^{-1}cm^{-2}sr^{-1} for the 1 - 2 keV X–ray background (Hasinger 1992) used by Boyle *et al.* (1994), the contribution from AGN rises to between 52% and 60% ($q_0 = 0$) or 33% and 38% ($q_0 = 0.5$).

2.7 Conclusions

I have investigated the evolution of the XLF with redshift using a new sample of 198 X–ray selected AGN with a spectroscopic completeness of 93% at 3×10^{-14}erg s^{-1} cm^{-2} (0.5 to 2.0 keV). I find PLE models, consistent with our data, in which the XLF declines or ceases to evolve beyond $z \sim 1.8$, and I find no evidence for evolution beyond this redshift from the model independent $\langle V_e/V_a \rangle$ test. Narrow emission line galaxies at low redshift contaminating the AGN sample have little effect on the derived evolution properties. Furthermore, these conclusions are insensitive to the uncertainty in conversion of flux from the *Einstein* to *ROSAT* passbands, although this has a significant effect on the $z = 0$ XLF and evolution rate for $z < 1.8$.

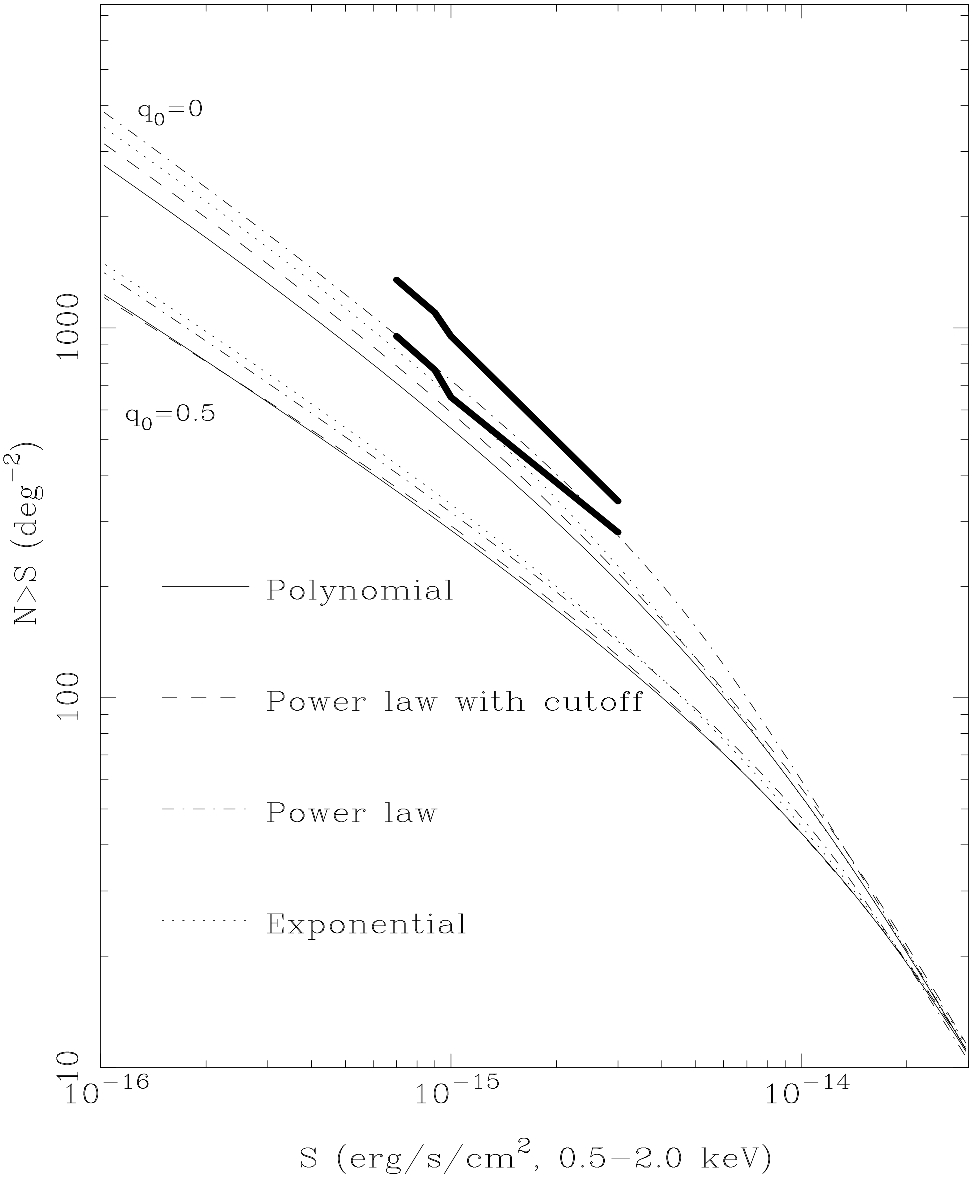

Figure 2.12: Log N - log S of the evolution models extrapolated to faint fluxes. The thick lines represent the 1σ confidence limits to the total log N - log S of all sources (i.e. not only AGN) at faint fluxes determined by fluctuation analysis of a deep *ROSAT* field by Barcons *et al.* (1994).

Chapter 3

Evolution of X–ray selected NELGs

3.1 Introduction

3.1.1 NELGs as a Component of X–ray Surveys

X–ray emission from NELGs was discovered in the 1970s during the optical identification of *Ariel* 5 , *SAS-3* and *HEAO-A3* sources (Ward *et al.* 1978, Schnopper *et al.* 1978, Griffiths *et al.* 1979). Subsequently, 31 X–ray sources in the EMSS were identified with galaxies which showed only narrow emission lines in their discovery spectra (Stocke *et al.* 1991). These are a mixture of starburst and Seyfert 2 galaxies (Boyle *et al.* 1995b), although it has been argued that the high X–ray luminosities of all these galaxies are due to active nuclei, i.e. are not stellar in origin (Halpern, Helfand and Moran 1995). It must be noted that *only* 31 of the 835 X–ray sources in the EMSS ($< 4\%$) were identified as possible NELGs, and until the launch of *ROSAT* it was not known that NELGs represented a large fraction of the sources at less than the *Einstein* sensitivity limit of $\sim 10^{-14}$erg s^{-1}cm^{-2} (0.3 – 3.5 keV).

3.1.2 Previous Determinations of the X–ray Evolution of NELGs

The importance of NELGs as contributors to the X–ray background and their possible relation to the rapidly evolving (optical) population of faint blue galaxies means that the X–ray evolution of NELGs is of great interest. Previous investigations of X–ray selected NELG evolution (Griffiths *et al.* 1996, Boyle *et al.* 1995a) have used combinations of the EMSS NELGs (found among the 'ambiguous' AGN of Stocke *et al.* 1991) and *ROSAT* discovered NELGs.

Boyle *et al.* (1995a) used 12 NELGs from the the Cambridge Cambridge *ROSAT* Serendipity Survey (CRSS, see Boyle *et al.* 1995a) and all 31 of the EMSS 'ambiguous' AGN. The CRSS has a flux limit of 2×10^{-14}erg s^{-1}cm^{-2} (0.5 – 2 keV) and covers ~ 4 deg^2. Approximately 90% of the 123 X–ray sources have been optically identified.

Although some of the 'ambiguous' EMSS AGN have only narrow lines (FWHM$<$ 1000km s^{-1}), around 30% turn out to have broad Hα which could not be detected in the EMSS optical spectra, in some cases because of poor signal-to-noise ratios, and in others because the spectra did not include redshifted Hα (many of the EMSS spectra were limited to $\lambda < 7000$Å). This is an important selection effect, because objects which would have been classed as as broad line AGN at lower redshifts were classed as EMSS 'ambiguous' AGN, and may have resulted in some spurious evolution of the Boyle *et al.* (1995a) NELG XLF. The possibility of a similar selection effect in the RIXOS and *ROSAT* UK Deep survey NELG samples is considered in Section 3.3.1

Griffiths *et al.* (1996) constructed their sample of 32 NELGs from the EMSS, CRSS and from the deep *ROSAT* survey of Boyle *et al.* (1994). Using improved optical spectroscopy, particularly of Hα , EMSS NELGs were separated from the other ‘ambiguous’ AGN which have Hα FWHM$>$ 1000km s^{-1}.

These studies have indicated that the NELG X–ray luminosity function is evolving rapidly with redshift, at a rate similar to the evolution rate of QSOs. Evolution analysis of the subclasses of NELGs, e.g. the Seyfert 2 and starburst galaxies is currently impossible because of the small sample sizes and the difficulty of assigning NELGs to the individual classes.

3.2 RIXOS and the UK Deep Survey

In this chapter I test the results of Boyle *et al.* (1995a) and Griffiths *et al.* (1996) using a sample of NELGs drawn exclusively from two *ROSAT* surveys, RIXOS, and the UK Deep survey. The sample of NELGs studied here is completely independent of those used by Boyle *et al.* (1995a) and Griffiths *et al.* (1996). The latter two samples have objects in common, and hence are not independent of each other. As in Chapter 2, I have assumed $H_0 = 50$ km s^{-1}Mpc^{-1}; results obtained using values of $q_0 = 0$ and $q_0 = 0.5$ are differentiated in the text.

RIXOS was described in Chapter 2; 17 X–ray sources were classified as NELGs, almost all of which were included in the AGN sample used in Chapter 2.

The *ROSAT* UK Deep survey covers a much smaller area of sky than RIXOS, 0.16 deg^2, but to a much lower flux limit, 2×10^{-15}erg s^{-1}cm^{-2} (0.5 – 2 keV), and contains 18 NELGs. Full details of both the X–ray and optical observations of the *ROSAT* UK Deep survey are given in McHardy *et al.* (1997). In total, 85% of the *ROSAT* UK Deep survey sources are identified.

High completeness is essential since NELGs represent only a small proportion of the total source population at high fluxes, and are among the most difficult sources to identify due to the paucity of unambiguous features in their optical spectra. The 7% of sources which are unidentified in RIXOS corresponds to 23 sources; this is a very significant number when compared to the 17 NELGs in RIXOS. It is therefore possible, although unlikely, that RIXOS is systematically underpopulated with NELGs. This is not as great a problem for the UK Deep survey, where only 11 sources remain unidentified compared to 18 NELGs. For the UK Deep survey, a source of systematic error may be chance association of the X–ray positions with faint galaxies. As explained in McHardy *et al.* (1997), the expected number of chance coincidences with NELGs at any redshift and R$<$ 21 mag is about 1.5. The NELG identifications in the UK Deep survey are very secure: only 2 of the 18 NELGs have R$>$ 22 mag, and both of these are at sufficiently large redshift ($z = 0.58$ and $z = 0.60$) that they are unlikely to be random coincidences between X–ray sources and optical galaxies. All but 1 of the RIXOS NELGs have R$<$ 20 mag; again the faint NELG has a relatively high redshift ($z = 0.43$). Sky areas, corrected for spectroscopic incompleteness, can be found in Chapter 2 for RIXOS, and Jones *et al.* (1996) for the *ROSAT* UK Deep survey.

The two surveys are complementary in providing a sample of X–ray selected NELGs covering a wide range of redshift – luminosity parameter space as shown in Figure 3.1. The X–ray spectra of the NELGs detected in RIXOS and the UK Deep survey have been fitted with power laws of the form $F_\nu \propto \nu^{-\alpha_X}$. The mean slope found for the UK Deep survey NELGs is $\alpha_X \sim 0.5$ (Romero Colmenero *et al.* 1996) while the mean slope found for the RIXOS NELGs is $\alpha_X \sim 1$ (Mittaz *et al.* 1997). The way in which the value of α_X affects the derived evolution will be examined in the following sections.

3.3 Detection of Evolution

3.3.1 $\langle V_e/V_a \rangle$ Testing

I have used the $\langle V_e/V_a \rangle$ test described by Avni and Bahcall (1980) to test for evolution in my NELG sample. When testing the RIXOS and UK Deep survey NELG samples separately, spectral slopes of $\alpha_X = 1$ and $\alpha_X = 0.5$ respectively have been used. The combined sample of RIXOS + UK Deep NELGs has been tested once

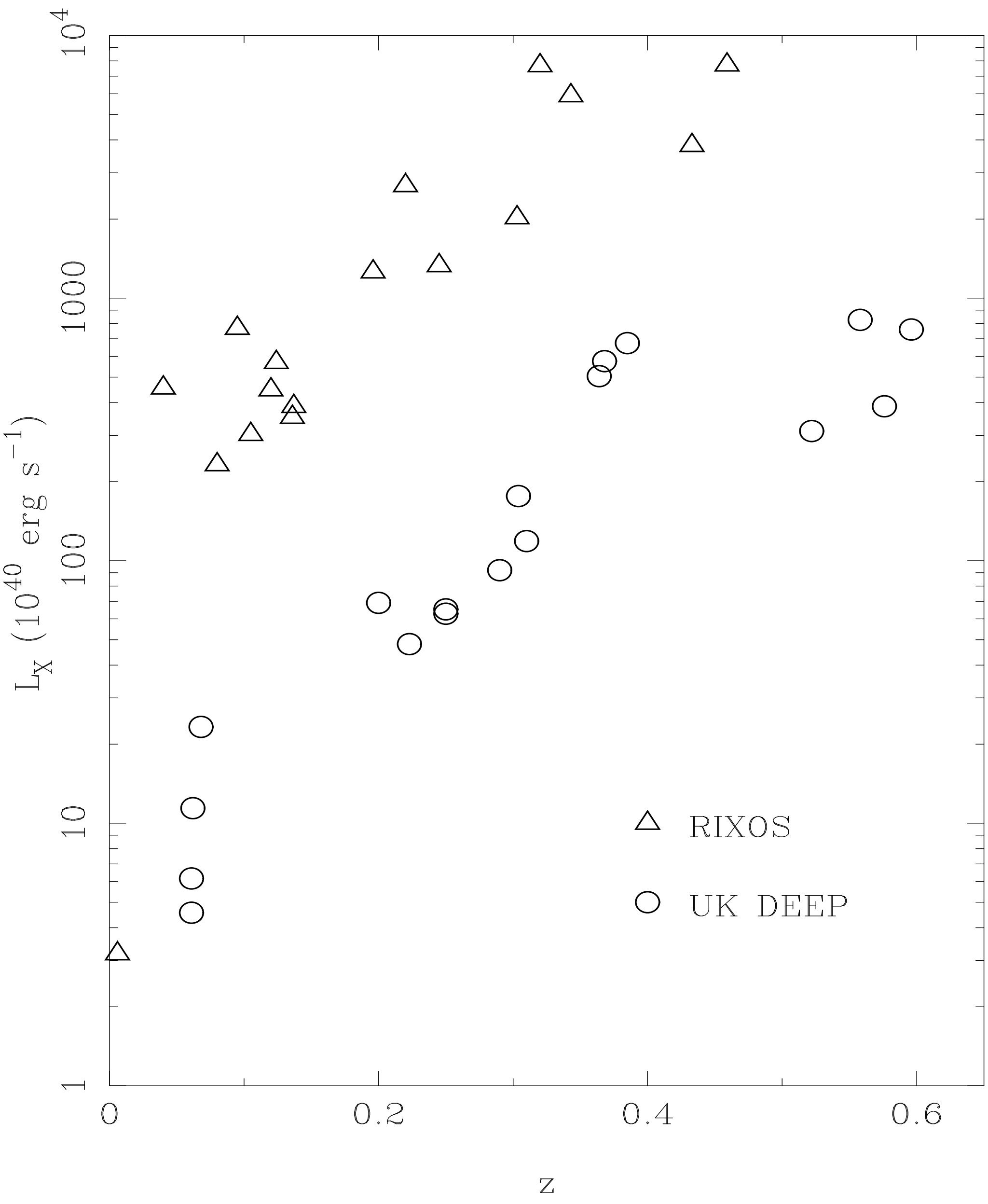

Figure 3.1: Redshift – luminosity distribution for RIXOS and UK Deep NELGs assuming $q_0 = 0$

Table 3.1: Results of $\langle V_e/V_a \rangle$ tests. Errors quoted are 68% (95%) confidence computed using the method of Avni and Bahcall (1980).

sample	number of NELGs	α_X	$\langle V_e/V_a \rangle$
RIXOS	17	1.0	0.45 ± 0.07 (± 0.13)
UK Deep	18	0.5	0.62 ± 0.07 (± 0.14)
UK Deep + RIXOS	35	1.0	0.66 ± 0.05 (± 0.10)
UK Deep + RIXOS	35	0.5	0.65 ± 0.05 (± 0.10)
UK Deep + RIXOS[a]	35	0.5/1.0	0.66 ± 0.05 (± 0.10)
UK Deep + RIXOS[b]	35	0.5	0.62 ± 0.05 (± 0.10)
UK Deep[c] + RIXOS	31	0.5	0.60 ± 0.05 (± 0.10)
UK Deep + RIXOS, $0 < z < 0.23$	17	0.5	0.58 ± 0.07 (± 0.14)
UK Deep + RIXOS, $0.23 < z < 0.6$	18	0.5	0.61 ± 0.07 (± 0.14)

[a] $\alpha_X = 1.0$ for RIXOS NELGs and $\alpha_X = 0.5$ for UK Deep NELGs

[b] RIXOS effective sky area at 3×10^{-14}ergs^{-1}cm^{-2} reduced by 30%

[c] 4 optically faintest NELG assumed to be chance associations

with each spectral index, and once with the mean spectral slopes of $\alpha_X = 1$ and $\alpha_X = 0.5$ assigned to the RIXOS and UK Deep NELGs respectively. A deceleration parameter of $q_0 = 0$ has been used; for $q_0 = 0.5$, $\langle V_e/V_a \rangle$ is different by no more than 0.01.

The results of the test are shown in Table 3.1; errors given are 68% without brackets, and 95% within brackets. Only the combined RIXOS + UK Deep sample has sufficient coverage of parameter space to detect evolution; $\langle V_e/V_a \rangle$ is greater than 0.5 with 99% confidence, hence evolution is detected at the 99% confidence level.

I have attempted to determine the effect that likely systematic errors may have on the test, as follows. If 10 of the 23 unidentified sources in RIXOS are NELGs, and assuming that they have similar redshifts and luminosities to the 17 which are identified, the RIXOS NELG sample is about 30% incomplete. I simulate this case by reducing the effective sky area of RIXOS by 30% at 3×10^{-14}ergs^{-1}cm^{-2}, the faintest flux limit in RIXOS, remembering that the unidentified fraction increases as the flux limit becomes fainter.

I quantify the importance of the expected chance NELG identifications in the UK Deep survey by removing the 4 optically faintest NELGs which, because of the rapidly increasing surface density of galaxies towards fainter magnitudes, are statistically the most likely to be chance associations.

I also consider a third possible systematic error, an optical selection effect caused by the spectroscopic wavelength range used to classify X–ray sources in both RIXOS and the UK Deep survey. At wavelengths longer than 8,000 Å, the identification spectra become increasingly noisy. AGN with a broad component to Hα but narrow Hβ, at $z < 0.2$ will be classified as AGN on the basis of the broad Hα. At $z > 0.2$ a broad base to Hα becomes difficult to distinguish from the noise, and so AGN with broad Hα but narrow Hβ may be classified as NELGs. At $z > 0.37$ Hα is redshifted completely out of the range of the identification spectra. It is therefore probable that the number of broad Hα AGN that are classified as NELGs increases with redshift at $z > 0.2$, imitating the evolution that I am trying to determine. I investigate this effect by splitting my sample of NELGS between those with $z < 0.23$ and those with $z > 0.23$; this splits the sample when the observed wavelength of Hα is just beyond 8,000 Å. There are approximately equal numbers of NELGs in the sample with $z < 0.23$ as $z > 0.23$, as seen in Figure 3.1, allowing a $\langle V_e/V_a \rangle$ test to be performed in both intervals.

It is seen in Table 3.1 that all of these systematic effects reduce the detection significance of evolution, but, except when the sample is split by redshift, the evolution is still significant at the 95% confidence level. When the sample is split by redshift, $\langle V_e/V_a \rangle$ is greater than 0.5 in *both* redshift ranges, proving that the apparent evolution cannot be (entirely) due to the spectroscopic selection effect discussed above. Hence it is unlikely that the evolution can be explained by selection effects in the RIXOS and UK Deep survey NELG samples.

3.3.2 The NELG X–ray Luminosity Function

In Figure 3.2 I show the X–ray luminosity function of the RIXOS + UK Deep NELG sample. It has been constructed in two redshift ranges, $0 < z < 0.23$ and $0.23 < z < 0.6$, using the $1/V_a$ method of Avni and Bahcall (1980), assuming $q_0 = 0$. As discussed earlier there are approximately equal numbers of NELGs with $z > 0.23$ and $z < 0.23$ in the sample. Evolution is apparent between the two redshift ranges: ϕ is larger in the higher redshift bin at all luminosities. In Figure 3.2, evolution of the luminosity of NELGs corresponds to a displacement of ϕ along a line with slope -1, while evolution of the space density of NELGs corresponds to a vertical displacement of ϕ. Either form of evolution could describe the change in ϕ between the two redshift ranges; the shape of the luminosity function is not well enough determined to distinguish between them.

3.4 Parameterising the Evolution

As discussed in the previous section, there are not sufficient NELGs in the sample to distinguish between luminosity evolution and density evolution. However, I parameterise the evolution as PLE to compare my results to those of previous researchers, and to compare the X–ray evolution of NELGs to that of broad line AGN. I consider a power law PLE model of the form:

$$L(z) = L_0 \times (1 + z)^C$$

which is used by Boyle *et al.* (1995a), Griffiths *et al.* (1996), and is widely used to model the evolution of broad line AGN.

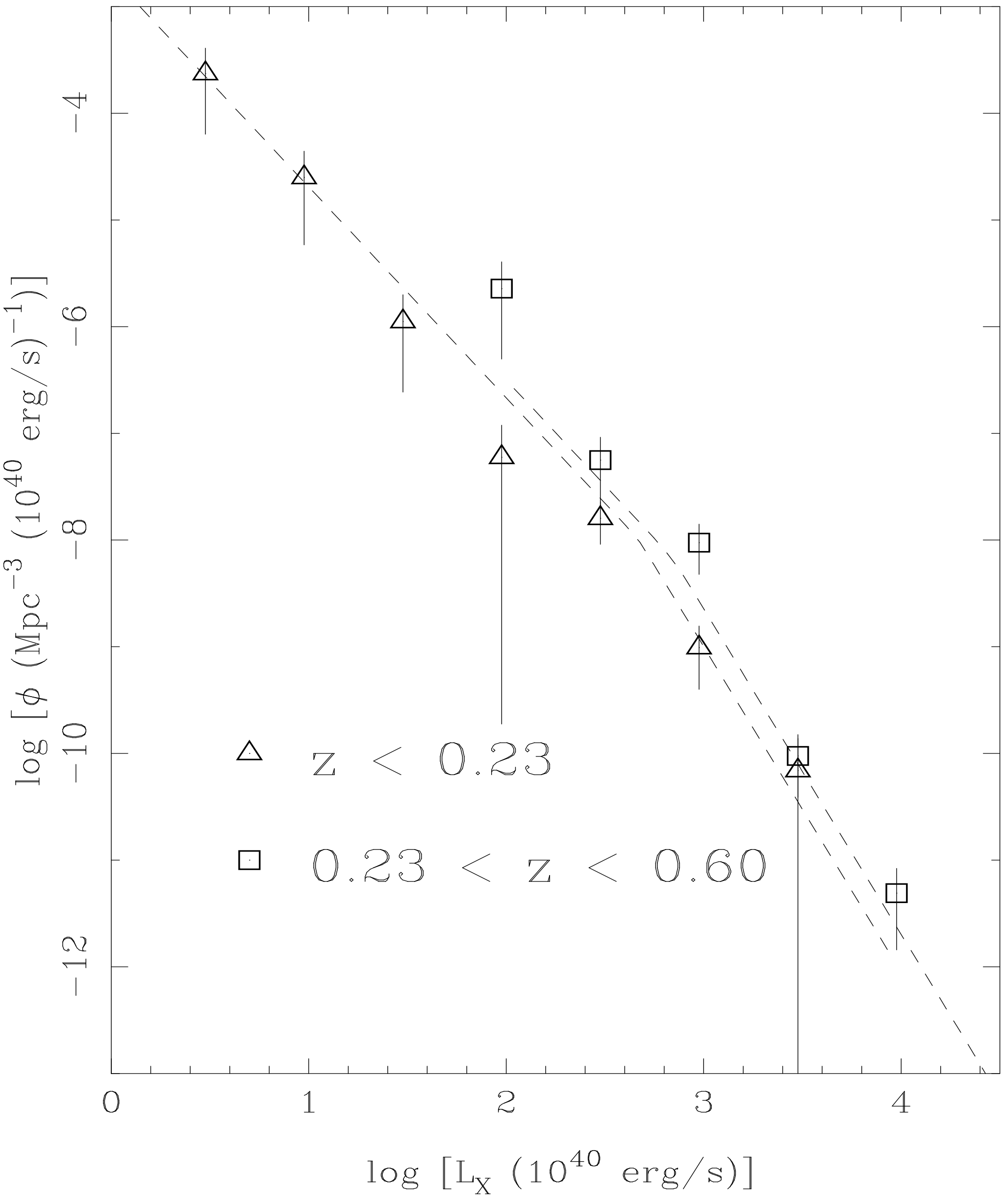

Figure 3.2: Binned $1/V_a$ NELG X–ray luminosity function in two redshift shells, assuming $q_0 = 0$ (symbols) and a model luminosity function in the same redshift shells (dashed line, see Section 3.4.2)

Table 3.2: Evolution rates and luminosity functions fitted to the RIXOS + UK Deep Survey NELG sample with maximum likelihood and $\langle V_e/V_a \rangle$ tests. A spectral index of $\alpha_X = 0.5$ has been assumed. Errors quoted are 68% (95%) for one interesting parameter.

Note	fitting	q_0	C	C	γ_1	γ_2	L_{break}[a]	K_1[b]	I_{XRB}[c]
	range		$\langle V_e/V_a \rangle$	max likelihood					
	0<z<1	0.5	$3.4^{+0.3}_{-0.7}(^{+0.4}_{-1.8})$	$1.9^{+0.9}_{-0.6}(^{+1.5}_{-1.0})$	$2.0^{+0.2}_{-0.2}(^{+0.3}_{-0.3})$	$3.0^{+0.3}_{-0.2}(^{+1.1}_{-0.5})$	$2.5^{+0.2}_{-0.2}(^{+0.7}_{-0.3})$	1.7	3.2
	0<z<3	0.5	$2.4^{+0.3}_{-0.4}(^{+0.7}_{-1.1})$	$0.8^{+0.6}_{-0.3}(^{+0.7}_{-0.4})$	$1.9^{+0.2}_{-0.2}(^{+0.3}_{-0.3})$	$3.1^{+0.3}_{-0.3}(^{+0.6}_{-0.5})$	$2.6^{+0.2}_{-0.1}(^{+0.6}_{-0.3})$	1.4	2.6
	0<z<1	0	$3.6^{+0.9}_{-1.1}(^{+2.0}_{-2.0})$	$1.8^{+0.8}_{-0.5}(^{+1.4}_{-0.9})$	$2.0^{+0.2}_{-0.2}(^{+0.3}_{-0.3})$	$3.1^{+0.3}_{-0.2}(^{+0.9}_{-0.4})$	$2.5^{+0.2}_{-0.2}(^{+0.6}_{-0.3})$	1.5	4.4
	0<z<3	0	$2.6^{+0.5}_{-0.6}(^{+0.9}_{-1.3})$	$1.0^{+0.6}_{-0.4}(^{+0.8}_{-0.5})$	$2.0^{+0.2}_{-0.2}(^{+0.3}_{-0.3})$	$3.2^{+0.2}_{-0.3}(^{+0.6}_{-0.5})$	$2.7^{+0.2}_{-0.2}(^{+0.4}_{-0.4})$	1.5	3.5
[d]	0<z<1	0	$2.7^{+1.0}_{-0.8}(^{+1.7}_{-1.8})$	$1.6^{+0.6}_{-0.6}(^{+1.2}_{-0.7})$	$2.0^{+0.2}_{-0.2}(^{+0.3}_{-0.3})$	$3.0^{+0.3}_{-0.3}(^{+1.0}_{-0.5})$	$2.6^{+0.2}_{-0.1}(^{+0.7}_{-0.4})$	1.9	5.0
[e]	0<z<1	0	$2.7^{+1.3}_{-1.0}(^{+2.6}_{-2.3})$	$1.5^{+0.6}_{-0.6}(^{+1.5}_{-0.7})$	$2.0^{+0.2}_{-0.2}(^{+0.3}_{-0.3})$	$3.1^{+0.2}_{-0.3}(^{+1.0}_{-0.5})$	$2.6^{+0.2}_{-0.2}(^{+0.7}_{-0.3})$	1.7	3.9

---

[a] L_{break} in units of 10^{40}erg s^{-1}

[b] K_1 in units of $10^{-3}(10^{40}\text{erg s}^{-1})^{(\gamma_1-1)}$ Mpc^{-3}

[c] I_{XRB} in units of 10^{-9} erg s^{-1} cm^{-2}sr^{-1} (1 - 2 keV)

[d] RIXOS effective sky area at 3×10^{-14}erg s^{-1}cm^{-2} reduced by 30%

[e] 4 optically faintest NELG assumed to be chance associations

3.4.1 $\langle V_e/V_a \rangle$

I have used the $\langle V_e/V_a \rangle$ test to find acceptable evolution parameters, as described by Maccacaro *et al.* (1983) and in Chapter 2 Section 2.4.1. This method has the advantage of requiring no assumptions about the shape of the luminosity function, and is the method used by Griffiths *et al.* (1996). Throughout I have assumed a spectral index of $\alpha_X = 0.5$; adopting $\alpha_X = 1.0$ as do Boyle *et al.* (1995a) and Griffiths *et al.* (1996) simply increases the evolution parameter C by 0.5. The value of C obtained from $\langle V_e/V_a \rangle$ testing, is listed in Table 3.2. The evolution is only constrained when the RIXOS + UK Deep sample is not split by survey or redshift. I have imposed two different upper limits to the redshift over which the test is carried out: performing the test over the very large redshift interval $0 < z < 3$ results in a reduced evolution rate compared to that obtained for $0 < z < 1$. I have only identified NELGs with $z < 0.6$, so imposing a limit of $z = 1$ is justified. It is seen from the Canada France Redshift Survey (Lilly *et al.* 1995) that identification of NELGs is possible to $z = 1$; at $z > 1$ the optical faintness of NELGs may make them particularly difficult to identify. However, obtaining evolution parameters using the larger redshift limit of $z = 3$ does illustrate that the results obtained for $z < 1$ cannot be reliably extrapolated to higher redshifts when calculating the contribution of NELGs to the X–ray background. The evolution rates obtained here for $0 < z < 3$ and $q_0 = 0$ are consistent with those found by Griffiths *et al.* (1996) using $\langle V_e/V_a \rangle$ over the same range (remembering that 0.5 must be subtracted from the values obtained by Griffiths *et al.* (1996) before comparison, because of the different values of α_X).

The errors quoted by Griffiths *et al.* (1996), for a sample of similar size to that used here, are extremely small. The sample of NELGs used by Griffiths *et al.* (1996) is drawn from three surveys (the EMSS, CRSS, and the deep survey described in Boyle *et al.* 1994) which in total contain a very large number of unidentified sources (>50) compared to their sample size of 32 NELGs. In addition, the evolution analysis of Griffiths *et al.* (1996) relies on a conversion from *Einstein* to *ROSAT* fluxes, which may not be well determined (see Chapter 2 Section 2.3), particularly given the lack of detailed knowledge of NELG X–ray spectra. It is also possible that the EMSS is systematically lacking bright, nearby NELGs, because they were observation targets and therefore excluded from the EMSS; 142 of the IPC images used for the EMSS were targeted on galaxies (Gioia *et al.* 1990). Thus the potential for systematic error is considerably larger in the sample of Griffiths *et al.* (1996), than in this work. We suggest that the realistic uncertainty on the evolution of NELGs is much larger than the uncertainty given by Griffiths *et al.* (1996).

3.4.2 Maximum Likelihood

I have also obtained values for the evolution parameter C, using a maximum likelihood test and assuming a two power law luminosity function of the form

$$\phi = K_1 L^{-\gamma_1} \quad L < L_{break}$$

$$\phi = K_2 L^{-\gamma_2} \quad L > L_{break}$$

where $K_2 = K_1 / L_{break}^{\gamma_1 - \gamma_2}$; this is the method used by Boyle *et al.* (1995a). I have used a de-evolved luminosity interval of $10^{40}\text{erg s}^{-1} < L_0 < 10^{45}\text{erg s}^{-1}$, and have used two redshift ranges, $0 < z < 1$ and $0 < z < 3$, which are those used earlier to determine C using the $\langle V_e/V_a \rangle$ test; again I have used $\alpha_X = 0.5$.

The results of the maximum likelihood analysis are given in Table 3.2. Errors quoted are 68% and 95% for one interesting parameter ($\Delta\chi^2 = 1$ and $\Delta\chi^2 = 4$ respectively) obtained using the method of Lampton , Margon and Bowyer (1976). The rate of PLE evolution obtained here from maximum likelihood testing is consistent with, although somewhat lower than, that obtained by Boyle *et al.* (1995a). The parameters are poorly constrained due to the small sample size; the errors on my maximum likelihood fit parameters are similar to those found by Boyle *et al.* (1995a) for a sample of similar size. Assuming that RIXOS has systematically missed some NELGs, or that some of the UK Deep survey NELGs are chance coincidences, leads to a lower evolution rate, but this difference is smaller than the statistical error on the evolution parameter C.

I have tested the fitted models in Table 3.2 for goodness of fit, using the two dimensional Kolmogorov Smirnov tests of Peacock (1983), and Fasano & Franceschini (1987); none of the models are rejected at 95%. My luminosity function parameters are consistent with those of Boyle *et al.* (1995a) given the large uncertainties due to the small sample sizes. Plotted in Figure 3.2. as dashed lines, are the luminosity functions for $0 < z < 0.23$ and $0.23 < z < 0.60$ obtained from the maximum likelihood fit in the interval $0 < z < 1$ for $q_0 = 0$. This model is an acceptable representation of the data when compared to the $1/V_a$ binned luminosity function (also shown in Figure 3.2), but the model evolution between $0 < z < 0.23$ and $0.23 < z < 0.60$ appears to be slightly underestimated. This is in keeping with the higher evolution rates obtained from $\langle V_e/V_a\rangle$ testing. The reason for this discrepancy is that no NELGs have been detected at $z > 0.6$ which has a significant effect when fitting the luminosity function, but comparatively little effect on the $\langle V_e/V_a\rangle$ test (and none at all on the $1/V_a$ binned luminosity function). The best fit evolution parameters obtained from $\langle V_e/V_a\rangle$ for $0 < z < 3$ are inconsistent with those found by maximum likelihood at the 95% level. This discrepancy is indicative that the evolution model is not representative of the data over the full redshift range.

3.5 Discussion

When considering what evolution models are reasonable for the NELG population over a wide range of redshift (i.e. $0 < z < 3$) and when comparing the NELG evolution to the X–ray evolution of QSOs, one must consider the sources which are not identified. In particular, the small number of unidentified sources (11) in the UK Deep survey, with its low limiting flux, provides the most realistic constraint to the number of high redshift NELGs which we could have failed to identify, but which reasonable evolution models predict should be present. Of course it is possible that some of the Deep Survey sources are misidentified and may in fact be high redshift NELGs. However, the approach taken by the Deep Survey team is conservative (see McHardy *et al.* 1997) in that any source is classified as unidentified unless the chance of the optical identification being correct is very high. To estimate the misidentification rate in detail, each class of X–ray source must be considered separately.

The QSOs make up the largest group (32) of Deep Survey X–ray sources. Assuming an average X–ray error circle of ~ 10 arc seconds radius (a pessimistic assumption, see McHardy *et al.* 1997) and the highest measured surface density of QSOs to date (230 $\deg^{-2}$ derived from the UK Deep survey itself, Jones *et al.* 1997) we would expect to have less than 0.5 chance coincidences between the X–ray sources and the QSOs, i.e. one can reasonably assume that all of the QSO identifications are correct. Only 3 objects are identified with Galactic stars; these all have optical to X–ray flux ratios typical of the active stars identified by Stocke *et al.* (1991); it is unlikely that any of these 3 sources are misidentified. 6 X–ray sources (of which two are extended) have been identified as clusters or groups of galaxies on the basis of an over density of close companion galaxies, while 18 X–ray sources have been identified as NELGs. All 4 clusters/groups which are not associated with extended X–ray emission contain at least one galaxy with $R < 21$ mag. These 4 clusters/groups are probably the least secure identifications, in that one of the individual galaxies may be the X–ray source. However, the measured redshift for the brightest galaxy is in all cases $z < 0.6$ and hence the clusters/groups are unlikely to be hiding any NELGs with $z > 0.6$ (but could plausibly be hiding $z < 0.6$ NELGs). The expected number of chance coincidences between the (non-QSO) X–ray sources and $R < 21$ galaxies of any spectral type and any redshift is ~ 3, and hence in total one might expect ~ 3 misidentifications caused by chance coincidence of X–ray and optical candidates.

However, at least 5 of the sources which are classed as unidentified have likely optical counterparts which are not $z > 0.6$ NELGs. I therefore take 11 as a reasonable upper limit to the number of $z > 0.6$ NELGs which are present, but unidentified, in the UK Deep survey. Note that the unidentified sources in the RIXOS survey are unlikely to be high redshift NELGs because of the high limiting flux of RIXOS; if RIXOS has systematically missed any NELGs they are likely to be of low redshift and hence lead to a lower evolution rate (see Section 3.4.2). This, and the larger number of unidentified sources in RIXOS than the UK Deep survey, mean that RIXOS does not provide a useful constraint on the number of high redshift NELGs (and has not been used as such).

The rapid rates of evolution found from $\langle V_e/V_a \rangle$ cannot reproduce the redshift distribution of the RIXOS and UK Deep samples, whether the fitting is performed for $0 < z < 3$ or $0 < z < 1$. If the pure luminosity evolution parameters are fixed at the rate obtained from the $\langle V_e/V_a \rangle$ test ($C \geq 2.7$ for $q_0 = 0$), and the luminosity function fitted in the interval $0 < z < 1$ using maximum likelihood, one would expect to have detected 4 NELGs with $0.6 < z < 1.0$ and 9 with $1.0 < z < 3.0$ in the UK Deep survey (see Figure 3.3). This already formally exceeds the total number of unidentified sources in the UK Deep survey, and hence optical incompleteness can only resolve this discrepancy if all the unidentified sources are NELGs with $z > 0.6$.

If the unidentified fraction of the UK Deep survey consists mostly of NELGs with $z > 0.6$, then there must be some *systematic* reason why they could not be identified. This may perhaps be explained by the observed wavelength of Hβ approaching 8000 Å at $z = 0.6$ and the optical faintness of galaxies at $z > 0.6$. This systematic selection effect must also affect RIXOS, the CRSS, and the deep *ROSAT* sample used by Griffiths *et al.* (1996), none of which contain *any* NELGs with $z > 0.6$. I have tested the data with the hypothesis that we are systematically unable to identify NELGs with $z > 0.6$ by imposing a limit of $z = 0.6$ on the $\langle V_e/V_a \rangle$ and maximum likelihood fitting. The resultant evolution rate from $\langle V_e/V_a \rangle$ is unreasonably high, with a 95% lower limit of $C = 3.6$ for $q_0 = 0$ and $C = 3.5$ for $q_0 = 0.5$, which would require at least 30 NELGs with $z > 0.6$ to have been present (but unidentified) in

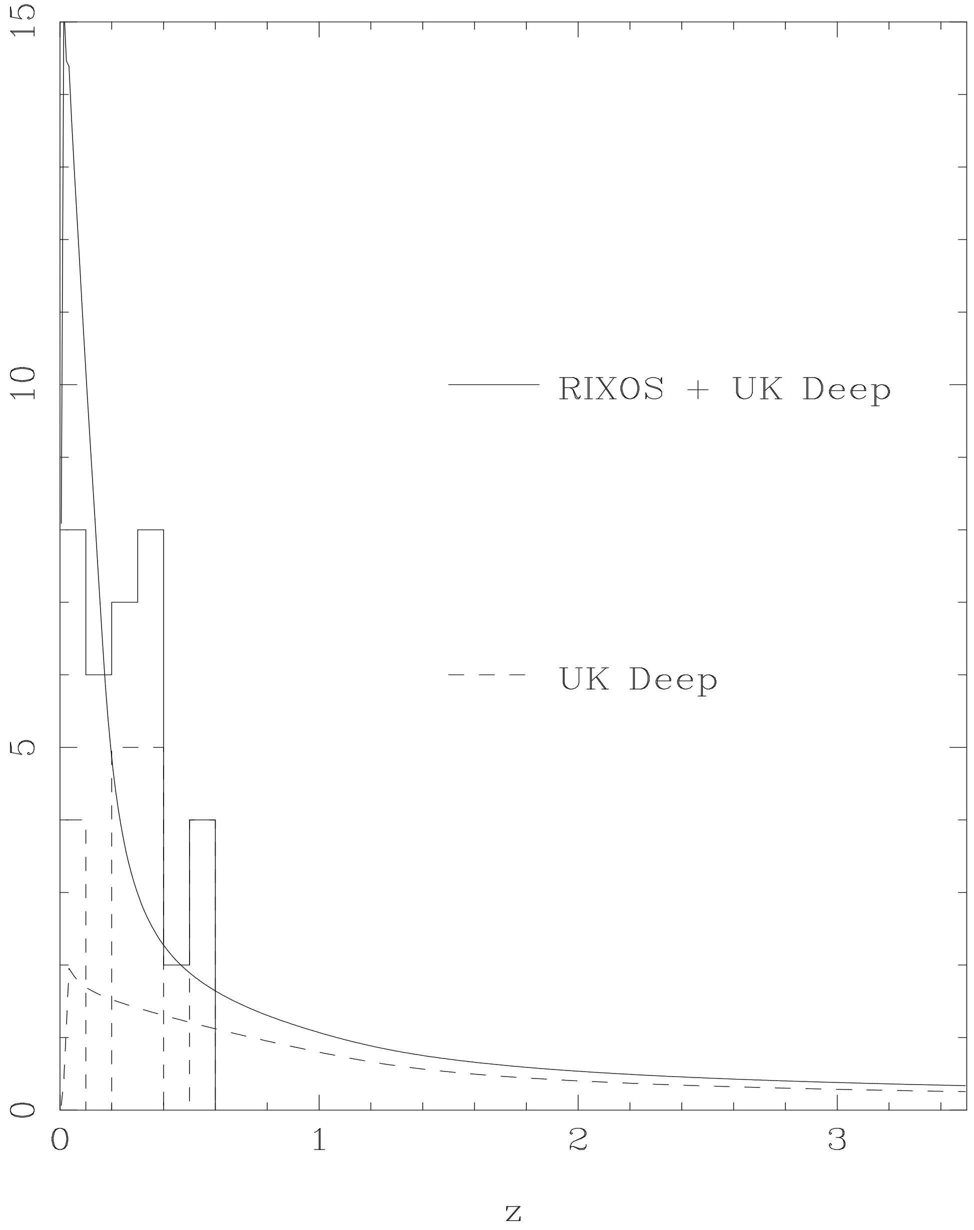

Figure 3.3: Observed redshift distribution of the full sample (solid histogram) and UK Deep sample (dashed histogram) compared to the predicted $q_0 = 0$ redshift distribution if NELGs are subject to PLE with an evolution parameter $C = 2.7$ (solid and dashed lines for the full sample and UK Deep sample respectively, see Section 3.5).

the UK Deep survey (impossible given that there are only 11 unidentified sources). Maximum likelihood gives a more modest 95% lower limit to the evolution rate of $C = 2.3$, which would be acceptable at $z > 0.6$ only if almost all the UK Deep survey unidentified sources are NELGs with $z > 0.6$. This means that under the extreme assumption that all the unidentified Deep survey sources are $z > 0.6$ NELGs which we were systematically unable to identify, only the lower limit to the pure luminosity evolution rate measured at $z < 0.6$ (C=0.3) provides a self consistent description of the data.

It is therefore clear that a high rate of evolution ($C > 2$) is not consistent with the dataset over the whole redshift range $0 < z < 3$. Either the evolution must be slower ($C \sim 1$), or the evolution must end at some fairly low redshift ($z < 1$). I propose that the latter is a better representation of the data given the very high $\langle V_e/V_a \rangle$ evolution rate determined at low redshift. The evolution observed in the NELG sample is therefore slower than and/or over a smaller redshift range than the evolution seen in X–ray selected broad line AGN, e.g. for $q_0 = 0$, $C \sim 3.0$ for $0 < z < 1.6$ (Jones *et al.* 1996), $C \sim 2.9$ for $0 < z < 1.8$ (Page *et al.* 1996), $C \sim 3.0$ for $0 < z < 1.9$ (Boyle *et al.* 1994).

The evolution rate I obtain from maximum likelihood fitting in the interval $0 < z < 1$ ($C = 1.9$) is similar to that seen in the optical luminosity function of I band selected blue galaxies by Lilly *et al.* (1995). Lilly *et al.* report that the change in the luminosity function of blue galaxies is equivalent to a brightening of galaxy luminosities by 1 magnitude between $0 < z < 0.5$ and $0.5 < z < 0.75$, which corresponds to an evolution parameter $C \sim 2$ in the pure luminosity evolution model fitted here. This is also consistent with the evolution rate $C = 2.5$ found by Boyle *et al.* (1995a), but is somewhat lower than the evolution rate ($C = 3.35$) found by Griffiths *et al.* (1996).

The evolution rate found for *IRAS* galaxies ($C = 3 \pm 1$, Saunders *et al.* 1990) is consistent with the evolution rate found here *and* those found by Griffiths *et al.* (1996) and Boyle *et al.* (1995a).

3.6 The NELG Contribution to the Soft X–ray Background

The NELG contribution to the 1–2 keV X–ray background has been calculated, for the luminosity function and maximum likelihood pure luminosity evolution parameters shown in Table 3.2, in the interval $0 < z < 3$ and $10^{40} < L_0 < 10^{45}$ where L_0 is the de-evolved 0.5 - 2 keV luminosity in erg s^{-1}. Where the fitting has been performed in the interval $0 < z < 1$, evolution has been assumed to stop at $z = 1$; where the fitting has been performed in the interval $0 < z < 3$ no limit has been applied to the evolution. A spectral index of $\alpha_X = 0.5$ has been assumed; the X–ray background intensity of each model is shown in Table 3.2 under the column entitled I_{XRB}. The NELG X–ray background intensities found here are in good agreement with those of Boyle *et al.* (1995a) and Griffiths *et al.* (1996). Assuming an X–ray background intensity of 1.46×10^{-8}erg $\mathrm{s}^{-1}\mathrm{cm}^{-2}\mathrm{sr}^{-1}$ between 1 and 2 keV (Chen, Fabian and Gendreau 1996), which is in good agreement with the X–ray background intensity determined from the UK Deep survey field itself, $1.4 \pm 0.1 \times 10^{-8}$erg $\mathrm{s}^{-1}\mathrm{cm}^{-2}\mathrm{sr}^{-1}$ (Branduardi-Raymont *et al.* 1994), my model luminosity functions predict that NELGs produce between 15% and 35% of the 1–2 keV X–ray background. I stress that the sample of NELGs is small, the assumption of pure luminosity evolution may not be correct, and I have not included the contribution of NELGs with $L < 10^{40}$erg s^{-1}, because none are detected in RIXOS or the *ROSAT* UK Deep survey. For these reasons, the real contribution of NELGs to the X–ray background may lie outside the range given above.

3.7 Conclusions

I detect evolution in a sample of NELGs obtained from RIXOS and the *ROSAT* UK Deep survey with 99% confidence. This sample is independent of the NELG samples for which evolution has been detected previously; selection effects can account for some, but not all, of the evolution. Currently, there are insufficient NELGs to determine what form the evolution takes; luminosity *or* density evolution can account for the change in the luminosity function with redshift. The evolution seen in the X–ray luminosity function of NELGs is of the same order as the evolution of the optical luminosity function of blue galaxies found by Lilly *et al.* (1995).

Using a power law pure luminosity evolution model commonly used to parameterise the evolution of broad line AGN, I find that the data are most consistent with evolution which is slower than that of broad line AGN ($C \sim 2$) and has stopped by $z = 1$. Maximum likelihood fitting of this evolution model does not reproduce the very high evolution rate found by Griffiths *et al.* (1996), but is broadly consistent with the evolution rate found by Boyle *et al.* (1995a). The lack of NELGs found at $z > 0.6$ indicates that their evolution is not as rapid as that seen in broad line AGN, unless it is confined to low redshifts ($z < 1$) only. This means that the evolution of the X–ray selected NELG luminosity function is probably *not* the same as that of broad line AGN.

My fits to the luminosity function and evolution of NELGs suggest that such objects with $L > 10^{40}$erg s^{-1} contribute between 15% and 35% of the 1–2 keV X–ray background.

Chapter 4

A Deeper look at the X–ray Evolution of QSOs

4.1 Introduction

In Chapter 2 I showed that PLE could describe the evolution of the RIXOS and EMSS AGN for both $q_0 = 0$ and $q_0 = 0.5$. I also showed that at $z > 1.8$ the data were consistent with no evolution. In this chapter I shall build on the results of Chapter 2, by increasing the AGN sample where RIXOS and the EMSS are deficient: at low luminosities and at high redshifts. This is achieved by including AGN from deeper *ROSAT* surveys.

Only broad line AGN (i.e. those with permitted line FWHM > 1000 km/s) are included in the sample; I will refer to these objects generically as QSOs throughout this chapter. In part this is to ensure compatibility in the selection criteria of all the surveys used in this chapter. It also serves to remove any possible contribution from NELGs, some of which may not have compact 'active' nuclei). This means that the

EMSS 'ambiguous' AGN, and all Seyfert 2 galaxies, have been excluded. NELGs are found only at low redshifts ($z < 0.6$) in the surveys from which my sample is drawn; the effect that inclusion of NELGs would have on the luminosity function is discussed in Section 4.6.

In this chapter, I consider the effect that the distribution of spectral slopes has on the derived evolution properties. This is introduced here, rather than in Chapter 2, for chronological reasons. The work in Chapter 2 was carried out before a thorough study of the dispersion of spectral indices for the AGN in RIXOS and some of the other *ROSAT* surveys had been made. The additional high redshift data used in this chapter also means that the dispersion in spectral indices has a more significant effect on the results in this chapter than those in Chapter 2. The effect that the dispersion of spectral slopes has on the evolution and XLF is explained in Section 4.3.1. The derivation of the expressions used is given in Appendix A.

4.2 The Sample of QSOs

4.2.1 X–ray Surveys From Which the Sample is Taken

The sample of QSOs used in this chapter is a combination of the largest, deepest and most complete soft X–ray selected AGN samples presently available. In addition to the EMSS and RIXOS samples, I have used three other, deeper surveys. These are detailed below:

The Cambridge - Cambridge *ROSAT* Serendipity Survey (CRSS, Boyle *et al.* 1995a) is slightly deeper than RIXOS with a limiting flux of 2×10^{-14}erg s^{-1} cm^{-2} but has a smaller sky coverage of 2 deg^2 at this limit, (4 deg^2 at 2×10^{-13}erg s^{-1} cm^{-2}) and is 90% optically identified. Details of the CRSS AGN are given in Ciliegi *et al.* (1996) and sky areas are taken from Boyle *et al.* (1995a)

The *ROSAT* UK Deep survey (McHardy *et al.* 1996) has a flux limit of 2×10^{-15}erg s^{-1} cm^{-2} which is an order of magnitude lower than that of either RIXOS or the CRSS. It covers only 0.16 $\deg^2$, but is 89% complete over this area. The properties of the UK Deep AGN are given in McHardy *et al.* (1996) and sky areas are given in Jones *et al.* (1996)

Finally, I have used the QSF1 and QSF3 fields from the deep survey of Boyle *et al.* (1994) (hereafter called the QSF sample) which has a flux limit of 4×10^{-15}erg s^{-1} cm^{-2} and covers 0.65 $\deg^2$. The QSF sample has the lowest identification percentage of 77%, but has been included because the 50 QSOs found in these fields occur in an otherwise sparse region of redshift - luminosity space (see Section 4.2.2). Details of the QSF AGN are given in Shanks *et al.* (1991) and Griffiths *et al.* (1995), which also contains the sky areas and flux limits of the two fields.

4.2.2 General Properties of the Sample

In total the sample contains 748 QSOs (182 from RIXOS, 32 from the UK Deep survey, 68 from the CRSS, 50 from the QSF fields and 416 from the EMSS, including the 'expected AGN' given in Maccacaro *et al.* 1991); their distribution in redshift – luminosity space is shown in Figure 4.1. The importance of both shallow, large area surveys, and deep, small area surveys is evident from their complementary coverage of parameter space.

The total cumulative sky area of the sample as a function of flux limit is shown in Figure 4.2.

I have assumed a power law X–ray spectrum of the form $f_\nu \propto \nu^{-\alpha_X}$. This was found to be an adequate model for AGN spectra in all five surveys from which this sample is drawn. Mean spectral indices of 1.03±0.05 (Maccacaro *et al.* 1988), 1.05±0.05 (Mittaz *et al.* 1997), 1.3±0.1 (Ciliegi *et al.* 1996), $1.2^{+0.05}_{-0.16}$ (Stewart *et al.* 1994) and 0.96±0.03 (Romero-Colmenero *et al.* 1996) were found for the AGN in the EMSS, RIXOS, the CRSS, the QSF fields and the UK Deep survey respectively. I have adopted a spectral index of $\alpha_X = 1$, which is representative of the above values and has been used by previous authors (e.g. Maccacaro *et al.* 1991, Boyle *et al.* 1994, Chapter 2 of this thesis). The assumption that a single spectral index could apply to all 748 AGN is unrealistic. Assuming a normal distribution of spectral indices, the dispersion σ_α has been measured by Maccacaro *et al.* (1988) for the EMSS AGN, Mittaz *et al.* (1997) for the RIXOS AGN and by Ciliegi *et al.* (1996) for the CRSS AGN, and values of 0.36, 0.55 and 0.33 respectively were obtained. Note that the values ($\sigma_\alpha = 0.36$ and $\sigma_\alpha = 0.33$) obtained by Maccacaro *et al.* (1988) and Ciliegi *et al.* (1996) are based on spectral slopes derived from hardness ratios, while the Mittaz (1997) value of $\sigma_\alpha = 0.55$ is based on spectral slopes found by a more reliable method: fitting three X–ray colours using the Cash statistic (Cash 1979). The effect of the dispersion in spectral indices on the luminosity function and its evolution has been investigated by using the value $\sigma_\alpha = 0.5$. For comparison I have also examined the evolution assuming no dispersion in the spectral indices (i.e. $\sigma_\alpha = 0$). Taking $\sigma_\alpha = 0.35$ (i.e. the dispersion found by Maccacaro *et al.* 1988 and Ciliegi *et al.* 1996) leads to about half as much spurious evolution as $\sigma_\alpha = 0.5$ (see Section 4.3.1) hence the evolution derived assuming $\sigma_\alpha = 0.35$ is approximately halfway between the evolution in the $\sigma_\alpha = 0$ and $\sigma_\alpha = 0.5$ cases.

4.2.3 Conversion from *Einstein* to *ROSAT* Fluxes

It has been noted before (Chapter 2, and Boyle *et al.* 1994) that the conversion factor 1.8, from *ROSAT* 0.5 to 2.0 keV fluxes to *Einstein* 0.3 to 3.5 keV fluxes, using the published response matrices for both satellites and a power law AGN spectrum of energy index $\alpha = 1$, produces discrepant AGN $\log N - \log S$ relations.

In Figure 4.3 I show the AGN $\log N - \log S$ relation obtained separately from all the surveys used here. Figure 4.3. has been constructed using a CF from of 1.8 from *Einstein* to *ROSAT* fluxes, and includes only the QSOs from each survey. The number of sources at each flux is larger for *all* of the *ROSAT* selected samples than the *Einstein* EMSS.

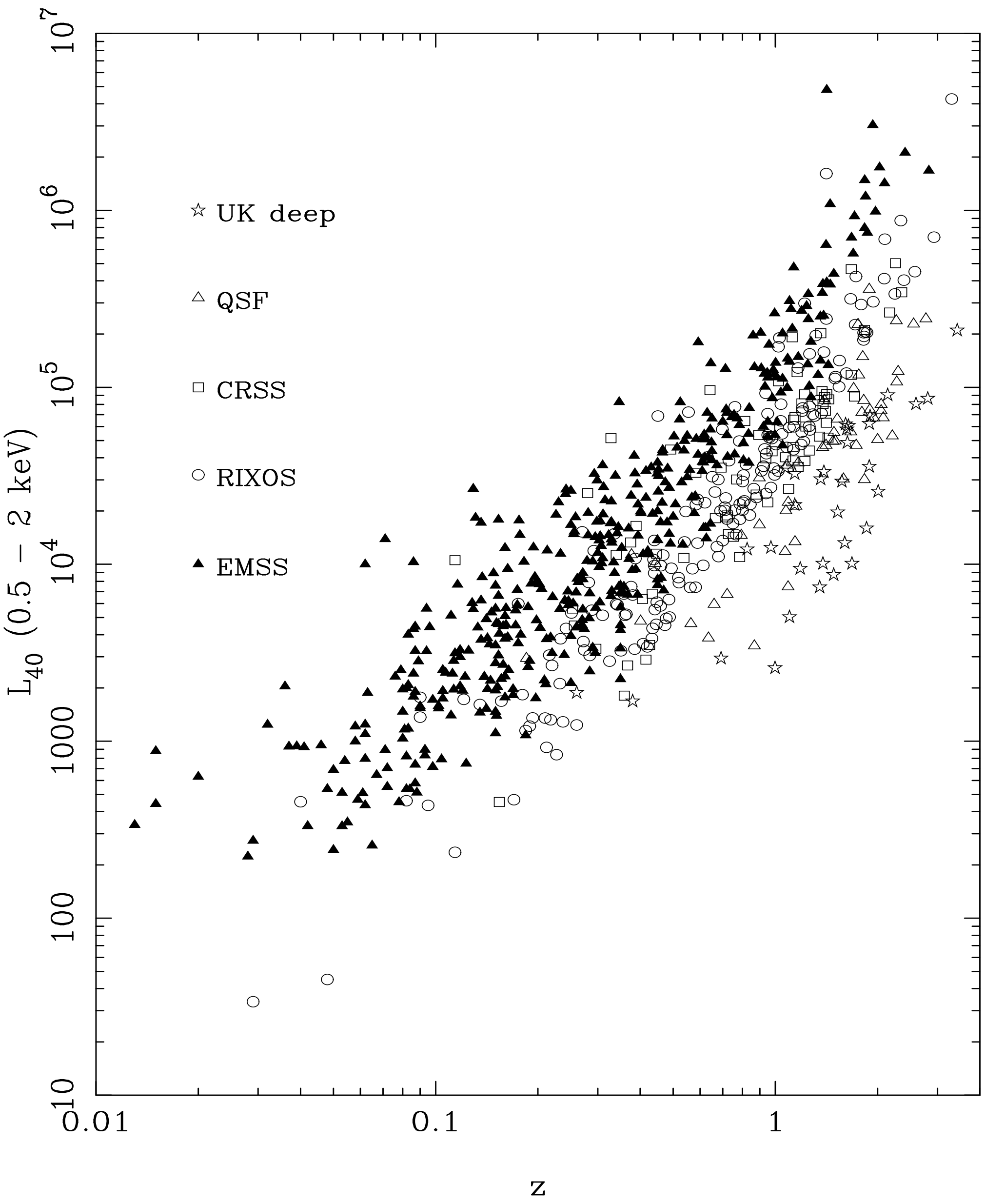

Figure 4.1: Luminosity and redshift of the AGN used in this analysis, calculated assuming $q_0 = 0$. *Einstein* 0.3 – 3.5 keV fluxes have been converted to 0.5 – 2 keV by dividing by a CF of 1.8 (see Section 4.2.3)

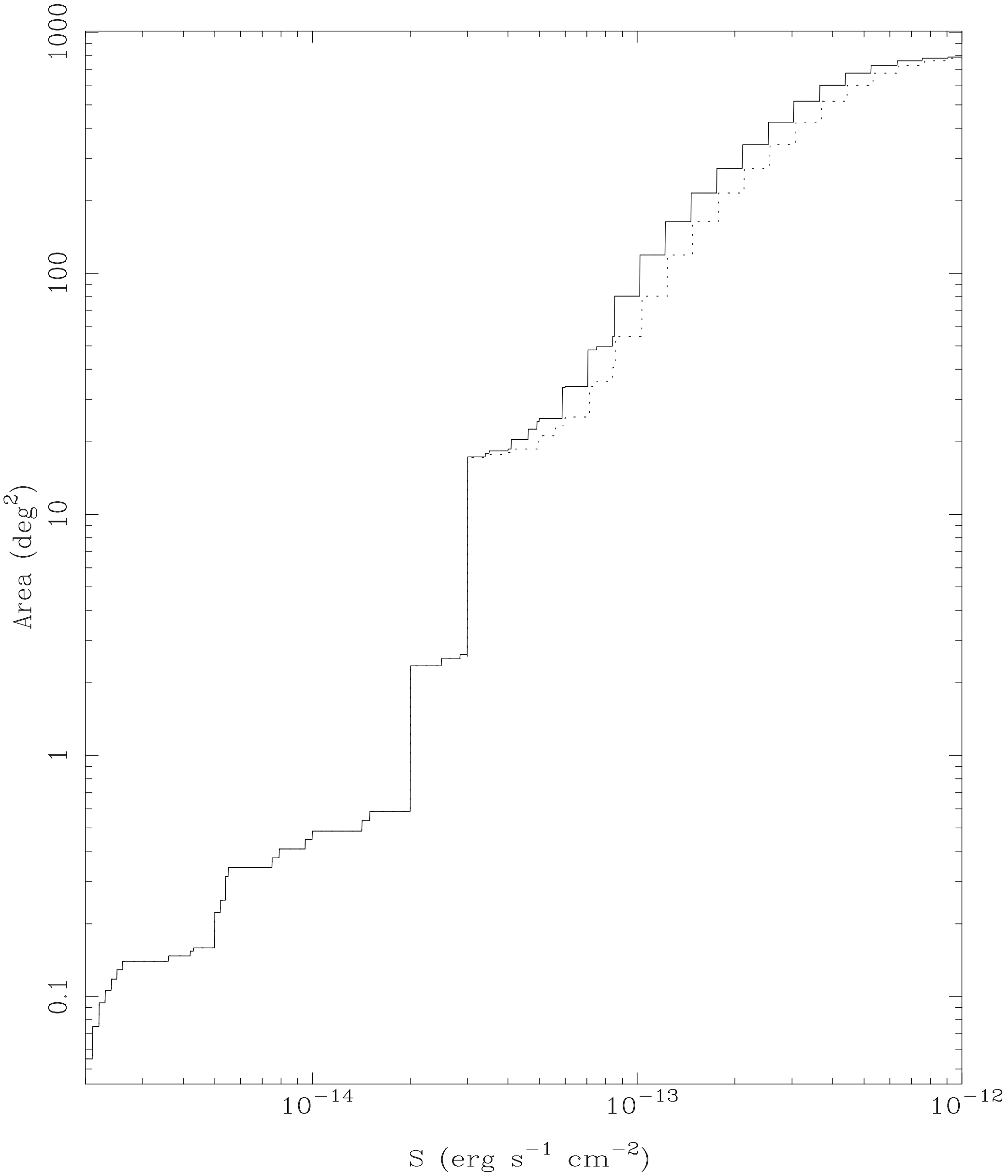

Figure 4.2: Sky area available to objects of flux $> S$ when *Einstein* 0.3 – 3.5 keV fluxes have been converted to 0.5 – 2 keV by dividing by a CF of 1.8 (solid line) and 1.47 (dotted line) as described in Section 4.2.3

It was proposed by Jones *et al.* (1996) that the discrepancy may be (partially) caused by the presence of oxygen edges in the spectrum of the AGN, which would affect the *ROSAT* passband more than that of *Einstein* . As explained in Jones *et al.* 1996, this would result in a K correction which is different for objects selected by the two satellites; at $z > 1$ the edges are redshifted out of the *ROSAT* passband, but remain in the *Einstein* passband until $z \sim 2.5$. I have constructed the AGN log $N -$ log S in the redshift ranges $z < 1$ and $1 < z < 2.5$ for the *Einstein* selected and *ROSAT* selected samples, to test this hypothesis. By fitting the log $N -$ log S relations using the maximum likelihood method outlined in Chapter 2, (excluding sources with 0.5 to 2 keV fluxes of less than 2×10^{-14}erg s^{-1} cm^{-2} which are beyond the break in the log $N -$ log S), I obtain values for the CF which are almost exactly the same for the two redshift ranges (1.50 ± 0.14 and 1.46 ± 0.19). This indicates that the cause of the discrepancy is probably not the presence of oxygen edges in the AGN spectra. Further evidence that this is not the cause of the difference between *ROSAT* and *Einstein* fluxes comes from the relative lack of very strong oxygen edges in the *ROSAT* spectra of the majority of the RIXOS AGN (Mittaz *et al.* 1997).

I have also found the best fit CF using each of the *ROSAT* samples separately (again excluding sources with 0.5 – 2 keV fluxes lower than 2×10^{-14}erg s^{-1} cm^{-2}). The maximum likelihood 1σ ($\Delta\chi^2 = 2.3$) confidence intervals on CF and the slope of the log $N -$ log S are shown in Figure 4.4 for RIXOS (solid line), the UK Deep survey (dashed line), the QSF fields (dotted line) and the CRSS (dot-dashed line). The different *ROSAT* samples have consistent log $N -$ log S slopes and give values of CF which are consistent with each other and with CF=1.47; only the UK Deep survey (which has few sources brighter than 2×10^{-14}erg s^{-1} cm^{-2}) is consistent with CF=1.8.

The origin of the normalisation difference between the EMSS and *ROSAT* log $N -$ log S is therefore still a mystery. Since I have shown that this normalisation is consistently different, independent of flux or redshift, I use the CF of 1.47 derived in Chapter 2, which brings the log $N -$ log S of the *ROSAT* surveys into consistency

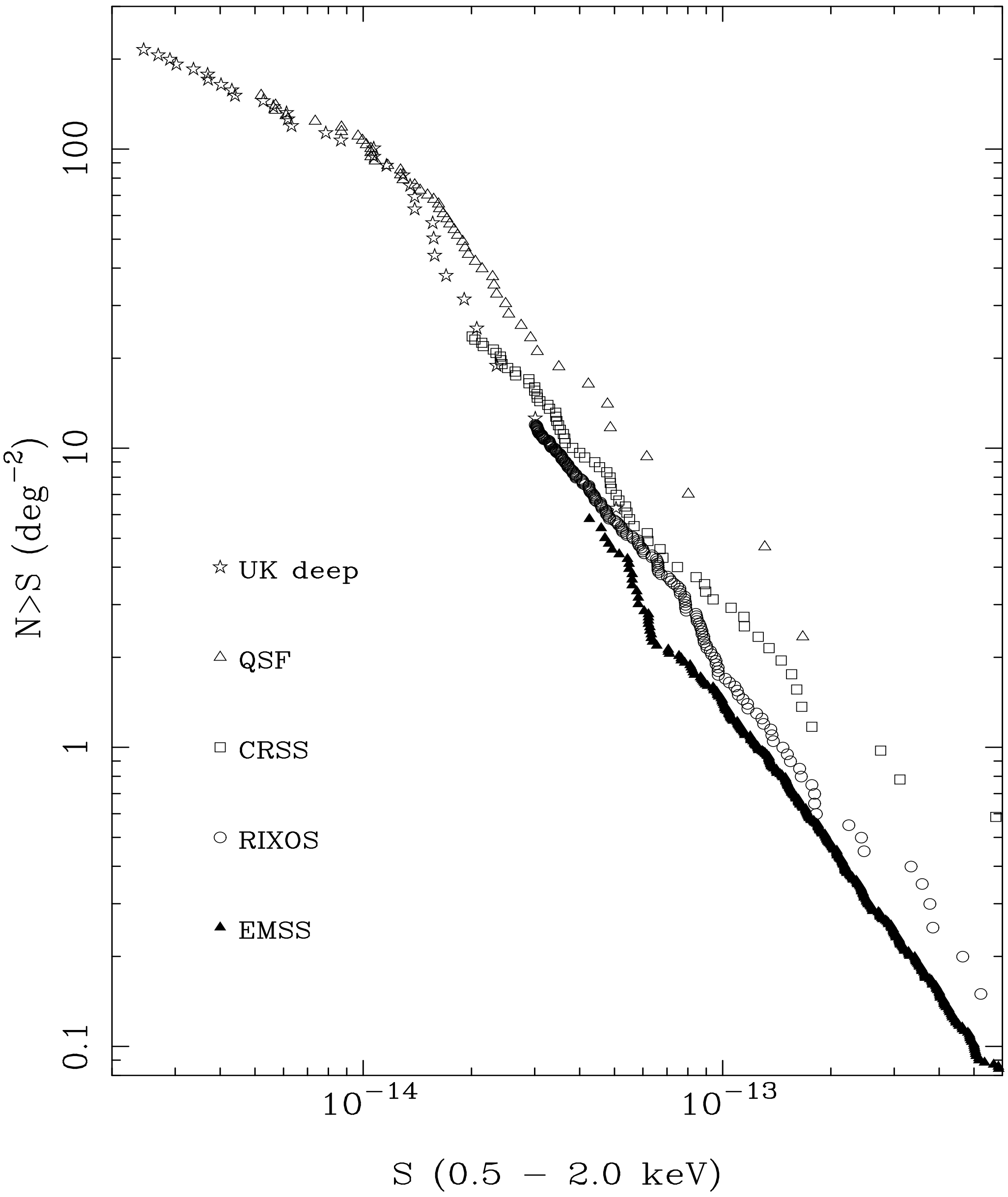

Figure 4.3: Integral log N – log S of *ROSAT* selected QSOs (open symbols) and *Einstein* selected QSOs (closed symbols).

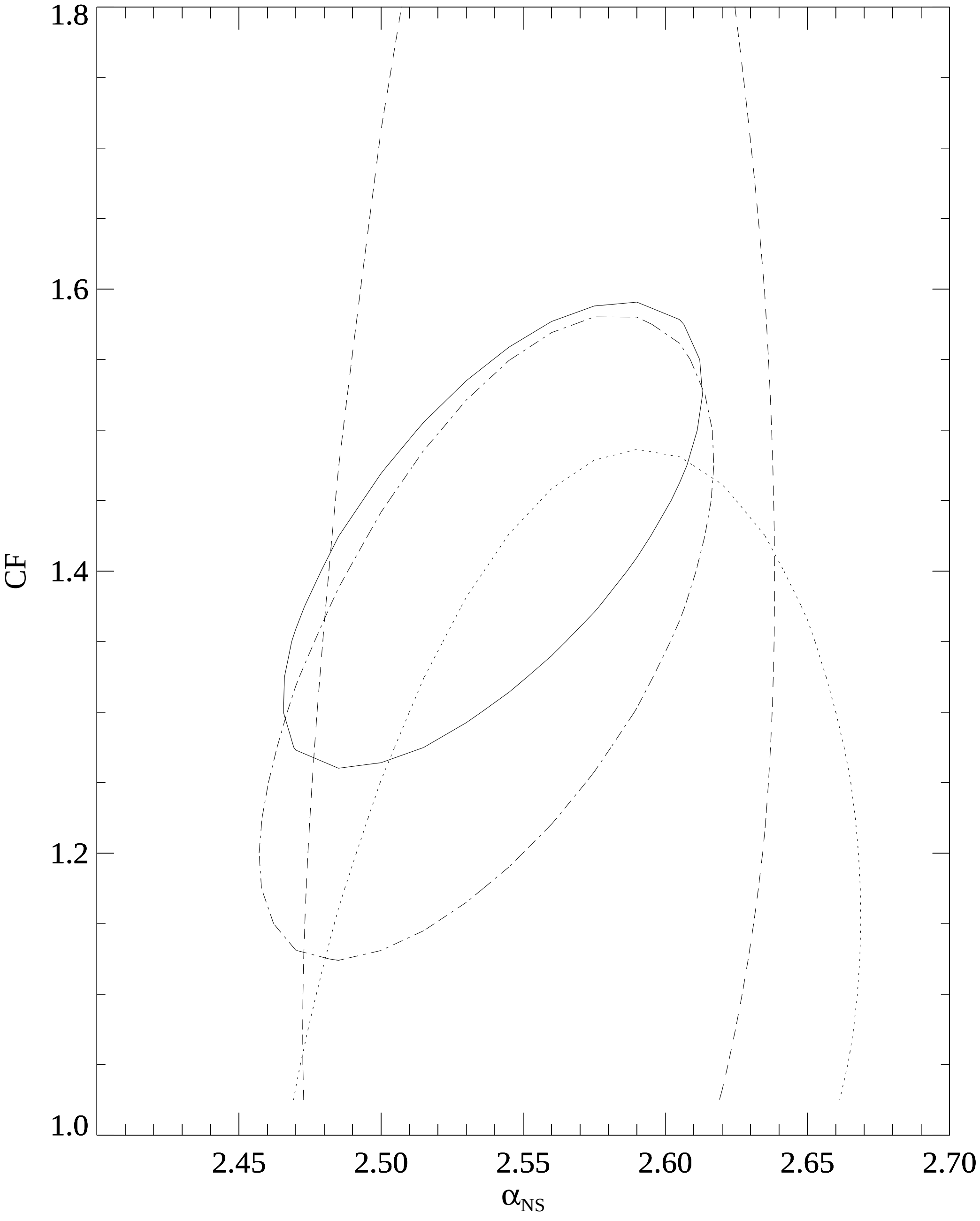

Figure 4.4: Confidence contours for the slope of the log $N -$ log S ($dN/dS \propto S^{-\alpha_{NS}}$) and CF (see Section 4.2.3) from the different *ROSAT* surveys. Contours are 1σ for two interesting parameters: RIXOS (solid line), UK Deep survey (dashed line), QSF survey (dotted line) and CRSS (dot-dashed line).

with that of the EMSS. I also use a CF of 1.8 which has been used in previous investigations of the XLF (e.g. Boyle *et al.* 1993, Boyle *et al.* 1994).

In the following sections all fluxes and luminosities are quoted in the 0.5 - 2 keV band, i.e. *Einstein* fluxes have been converted to *ROSAT* fluxes.

4.3 Luminosity Function and Evolution Models

I assume a two power law shape for the XLF, as in Chapter 2. I have used three PLE models to parameterise the evolution of the XLF:

a) power law evolution:

$$L = L_0 \times (1+z)^C$$

b) power law evolution with a redshift cutoff, z_{cut}:

$$L = L_0 \times (1+z)^C \quad z < z_{cut}$$

$$L = L_0 \times (1+z_{cut})^C \quad z > z_{cut}$$

and c) polynomial evolution:

$$L = L_0 \times 10^{(Cz + C_1 z^2)}$$

all of which were used in Chapter 2. I have not considered the exponential evolution model

$$L = L_0 \times e^{C\tau}$$

where C is the evolution parameter and τ is look back time, because in Chapter 2 I showed that it is not a good fit at low redshift, where the evolution is well constrained by EMSS and RIXOS data.

4.3.1 Dispersion in the Spectral Index α_X

It was shown by Francis (1993) that the observed evolution of the luminosity function has a dependence on the dispersion of spectral slopes around the mean. However, only the case in which the luminosity function is a single power law was considered. I expand on the results of Francis (1993) to obtain an approximation which is applicable to the case of a two power law luminosity function, which is commonly used for X–ray selected AGN (e.g. Maccacaro *et al.* 1991, Boyle *et al.* 1994). If the observed luminosity function at any redshift is $\phi_{obs}(L,z)$ and the actual luminosity function is $\phi(L,z)$, then

$$\phi_{obs}(L,z) = e^{(\sigma_\alpha log_e(1+z))^2(\gamma_1-1)(1-\gamma_2)/2} \times \frac{\phi(L/e^{(\sigma_\alpha log_e(1+z))^2(\gamma_1+\gamma_2-2)/2}, z)}{e^{(\sigma_\alpha log_e(1+z))^2(\gamma_1+\gamma_2-2)/2}}$$

the derivation of which is given in Appendix A.

The term $e^{(\sigma_\alpha log_e(1+z))^2(\gamma_1+\gamma_2-2)/2}$ is analogous to the evolution term $f(z)$ in Equation 1.5 for PLE, while the term $e^{(\sigma_\alpha log_e(1+z))^2(\gamma_1-1)(1-\gamma_2)/2}$ is analogous to the evolution term $g(z)$ in Equation 1.6 for PDE. Therefore, the spurious evolution of a two power law luminosity function, due to the dispersion in the spectral index, can be treated as a combination of PLE and PDE.

This is illustrated in Figure 4.5 which shows the spurious evolution of the XLF at $z = 2$ and $z = 4$ assuming $\sigma_\alpha = 0.5$. The solid line is an XLF without any evolution (i.e. $\sigma_\alpha \times z = 0$), the dotted line shows the same XLF with spurious evolution and the dashed line is the two power law approximation given above.

4.4 Construction of the XLF and Determination of its Evolution

Evolution models and model XLFs have been fitted to the data using the maximum likelihood method, and tested for goodness of fit using the 2D K.S. test of Peacock (1983) (see Chapter 2 for more details of these methods). Errors quoted are 68% and 95% for one interesting parameter corresponding to $\Delta\chi^2 = 1$ and $\Delta\chi^2 = 4$ respectively, and were calculated using the method of Lampton, Margon and Bowyer (1976).

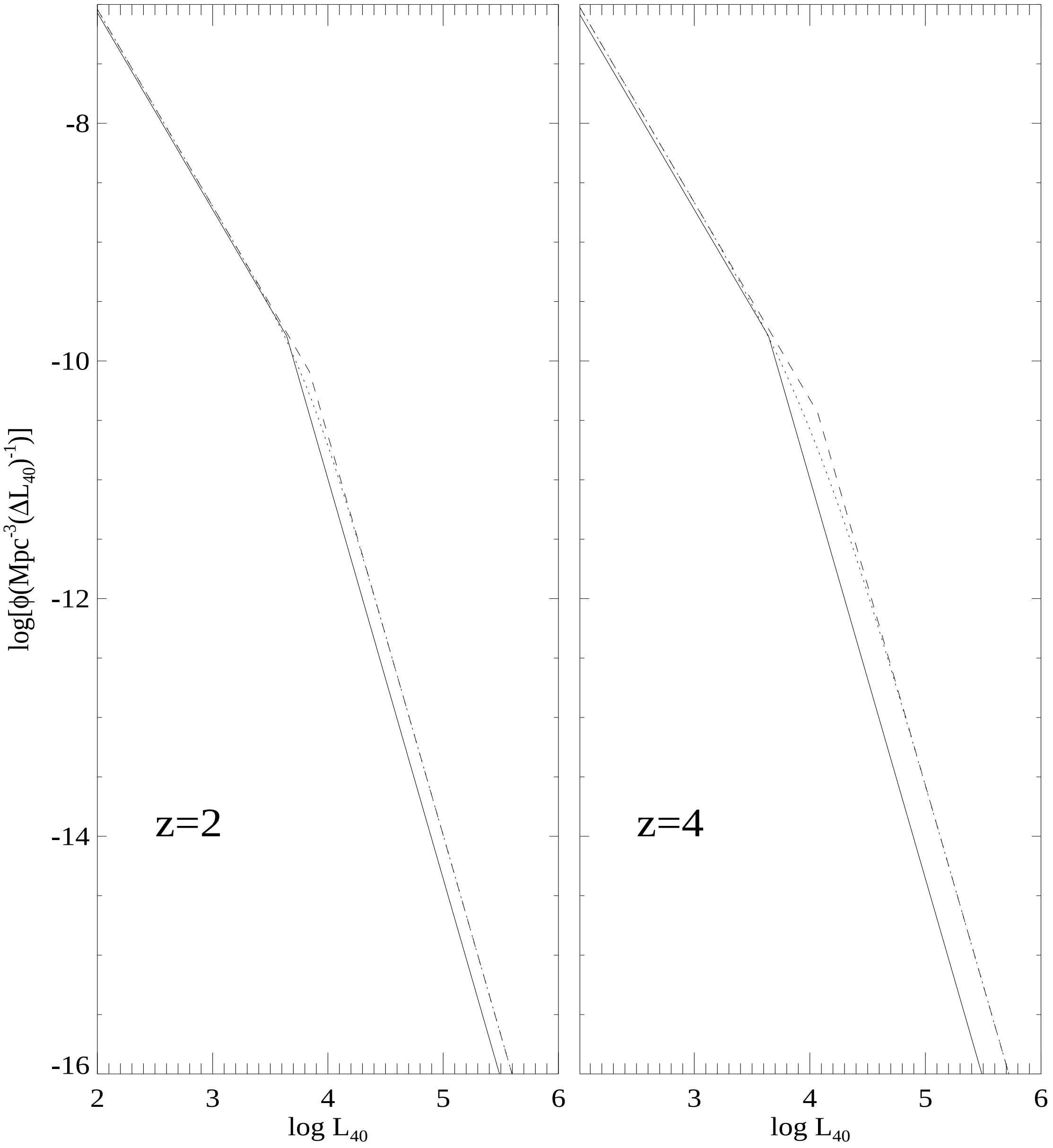

Figure 4.5: Spurious evolution due to a dispersion of spectral slopes $\sigma_\alpha = 0.5$ at $z = 2$ and $z = 4$. In both cases the initial ($z = 0$) XLF has $\gamma_1 = 1.66$ and $\gamma_1 = 3.36$ and is shown as a solid line. The dotted line is the same luminosity function after the spurious evolution, and the dashed line is the two power law approximation used in this work.

Both fitting and testing of models were performed in the region of redshift - de-evolved luminosity space $0 < z < 4$, 10^{40}erg s^{-1} cm^{-2} $< L_0 <$ 10^{48}erg s^{-1} cm^{-2}. I have tested to a higher redshift than in Chapter 2 (when I used $z = 3.5$ as my upper limit to redshift space) because many objects in RIXOS are sufficiently luminous that they could easily be detected out to $z = 4$ in the additional deeper fields used in this chapter.

For the $1/V_a$ binned XLF I have used a different definition of the luminosity function,

$$\phi(L, z) = \frac{d^2N}{dV d(logL)}$$

instead of Equation 1.1 in Section 1.5. This representation has the benefit that PLE is a shift of ϕ in the horizontal direction, while PDE is a shift of ϕ in the vertical direction. This is of considerable advantage in this chapter, where the increased coverage of parameter space means that PLE can really be tested. I have not corrected the $1/V_a$ binned estimates for the apparent evolution caused by the dispersion in spectral indices. Instead, the apparent evolution has been applied to model curves which are superimposed for comparison.

4.5 Results

Results of the maximum likelihood fitting and 2D KS testing are given in Table 4.1. Errors quoted are 68% and 95% for one interesting parameter, ($\Delta\chi^2 = 1$ and $\Delta\chi^2 = 4$ respectively). Power law evolution without a redshift cutoff is clearly rejected with P(>D)<1% for either value of q_0 and any combination of σ_α and CF.

For $q_0 = 0$, using CF=1.47, neither power law evolution with a redshift cutoff nor polynomial evolution are rejected strongly; with a CF of 1.8 the better fitting model depends on σ_α. The binned $1/V_a$ XLF for $q_0 = 0$ is shown in Figure 4.6 and was constructed using CF=1.47. The dashed curves are for power law evolution with a redshift cutoff fitted with $\sigma_\alpha = 0.5$ and are in the same redshift shells as the binned XLF. The spurious evolution due to the dispersion in spectral indices has

Table 4.1: Results of fitting evolution models

model	q_0	CF	σ_α	z_{cut}	C	C_1	${K_1}^a$	γ_1	γ_2	log_{10} $(L_{break})^c$	${I_{XRB}}^b$	P(>D)
$(1+z)^C$	0.0	1.8	0.0	–	2.58	–	0.581	1.52	3.47	3.67	6.0	6.4×10^{-4}
$(1+z)^C$	0.0	1.8	0.0	1.82	3.02	–	0.375	1.46	3.44	3.53	5.4	0.047
$10^{Cz+C_1z^2}$	0.0	1.8	0.0	–	1.18	-0.249	0.377	1.46	3.44	3.52	5.3	0.166
$(1+z)^C$	0.0	1.8	0.5	–	2.07	–	3.15	1.75	3.68	3.90	6.3	7.2×10^{-5}
$(1+z)^C$	0.0	1.8	0.5	1.42	3.00	–	1.74	1.67	3.49	3.54	5.5	0.10
$10^{Cz+C_1z^2}$	0.0	1.8	0.5	–	1.11	-0.253	1.55	1.65	3.51	3.58	5.9	0.046
$(1+z)^C$	0.0	1.47	0.0	–	2.39	–	0.589	1.51	3.34	3.75	6.1	2.64×10^{-3}
$(1+z)^C$	0.0	1.47	0.0	1.79	2.87	–	0.330	1.43	3.30	3.58	5.7	0.10
$10^{Cz+C_1z^2}$	0.0	1.47	0.0	–	1.11	-0.235	0.346	1.43	3.31	3.59	5.7	0.079
$(1+z)^C$	0.0	1.47	0.5	–	1.98	–	1.90	1.66	3.39	3.84	6.5	2.3×10^{-4}
$(1+z)^C$	0.0	1.47	0.5	1.42	2.76	–	1.76	1.66	3.36	3.64	5.7	0.15
$10^{Cz+C_1z^2}$	0.0	1.47	0.5	–	1.05	-0.244	1.41	1.62	3.33	3.63	6.1	0.084
$(1+z)^C$	0.5	1.8	0.0	–	2.34	–	0.274	1.37	3.41	3.53	3.8	3.9×10^{-6}
$(1+z)^C$	0.5	1.8	0.0	1.41	3.13	–	0.140	1.26	3.34	3.30	3.6	6.1×10^{-4}
$10^{Cz+C_1z^2}$	0.5	1.8	0.0	–	1.16	-0.264	0.168	1.29	3.36	3.36	3.6	3.8×10^{-3}
$(1+z)^C$	0.5	1.8	0.5	–	1.85	–	0.302	1.39	3.07	3.56	3.4	1.53×10^{-7}
$(1+z)^C$	0.5	1.8	0.5	1.39	2.74	–	0.288	1.38	3.13	3.37	3.2	0.034
$10^{Cz+C_1z^2}$	0.5	1.8	0.5	–	1.08	-0.268	0.242	1.35	3.13	3.38	3.3	0.035
$(1+z)^C$	0.5	1.47	0.0	–	2.20	–	0.242	1.34	3.28	3.59	4.1	4.5×10^{-5}
$(1+z)^C$	0.5	1.47	0.0	1.41	2.93	–	0.148	1.26	3.22	3.38	3.9	8.1×10^{-4}
$10^{Cz+C_1z^2}$	0.5	1.47	0.0	–	1.10	-0.253	0.160	1.27	3.23	3.42	3.9	8.26×10^{-3}
$(1+z)^C$	0.5	1.47	0.5	–	1.74	–	0.234	1.34	3.00	3.62	3.7	7.1×10^{-6}
$(1+z)^C$	0.5	1.47	0.5	1.37	2.63	–	0.234	1.34	3.07	3.44	3.5	0.018
$10^{Cz+C_1z^2}$	0.5	1.47	0.5	–	1.02	−0.255	0.242	1.34	3.04	3.45	3.7	0.065
±68%												
$(1+z)^C$					0.07			0.08	0.06	0.05		
$(1+z)^C$				0.06	0.10			0.08	0.06	0.04		
$10^{Cz+C_1z^2}$					0.05	0.02		0.09	0.06	0.04		
±95%												
$(1+z)^C$					0.14			0.23	0.13	0.14		
$(1+z)^C$				0.17	0.24			0.16	0.18	0.09		
$10^{Cz+C_1z^2}$					0.10	0.03		0.15	0.25	0.09		

---

[a] K_1 in units of $10^{-4}(10^{40}\mathrm{ergs}^{-1})^{(\gamma_1-1)}$ Mpc^{-3}

[b] I_{XRB} in units of 10^{-9} erg s^{-1} cm^{-2}sr^{-1} (1 - 2 keV)

[c] L_{break} in units of 10^{40}erg s^{-1}

been added to the model curves so that they can be compared with the binned data. The model curves are a good representation of the data at all redshifts.

For $q_0 = 0.5$, it is more difficult to find a PLE model that is a good fit to the data: the only model which is not rejected at the 95% level by the 2D KS test is the polynomial evolution model with CF=1.47 and $\sigma_\alpha = 0.5$. I have superimposed my best fit model on the binned $1/V_a$ XLF in Figure 4.7. The agreement between the model curves and the binned data is not impressive, particularly at $z > 1.4$ where there is a systematic excess of objects with $L < 5 \times 10^{44}$erg s^{-1} cm^{-2}. This excess is small enough ($\sim$ 15 objects) that the evolution model, over the whole redshift and luminosity range, is not rejected at 95% by the 2D KS test, but for $z > 1.4$ and $L < 5 \times 10^{44}$erg s^{-1} cm^{-2} (i.e. the region in Figure 4.7 where model and data appear to deviate) the number of observed AGN is larger than the model predicted number at $>$ 99% confidence. This discrepancy remains if a CF of 1.8 is used and/or the dispersion in spectral index is neglected. Changing the functional form of the PLE model cannot resolve this excess, because PLE corresponds to a horizontal shift in the XLF with redshift in Figure 4.7. Clearly, no horizontal shift can simultaneously align both the high and low luminosity portions of the high redshift ($z > 1.4$) XLF with those of the low redshift ($z < 0.4$) XLF. The spurious density evolution associated with the distribution in spectral indices is negative (i.e. downwards with increasing redshift in Figure 4.7) hence this *cannot* be the cause of the excess observed AGN, and arbitrarily increasing σ_α would only serve to make the difference between model and data larger in the problem area.

4.5.1 Evolution at High Redshift

Figure 4.8 shows the three PLE models considered in this chapter, using the bestfit parameters for $q_0 = 0$, CF=1.47 and $\sigma_\alpha = 0.5$. Model a is significantly rejected, but models b and c are both acceptable fits to the data according to the 2D KS test, and have different shapes beyond $z \sim 1$. For $q_0 = 0.5$ only model c is acceptable at 95%

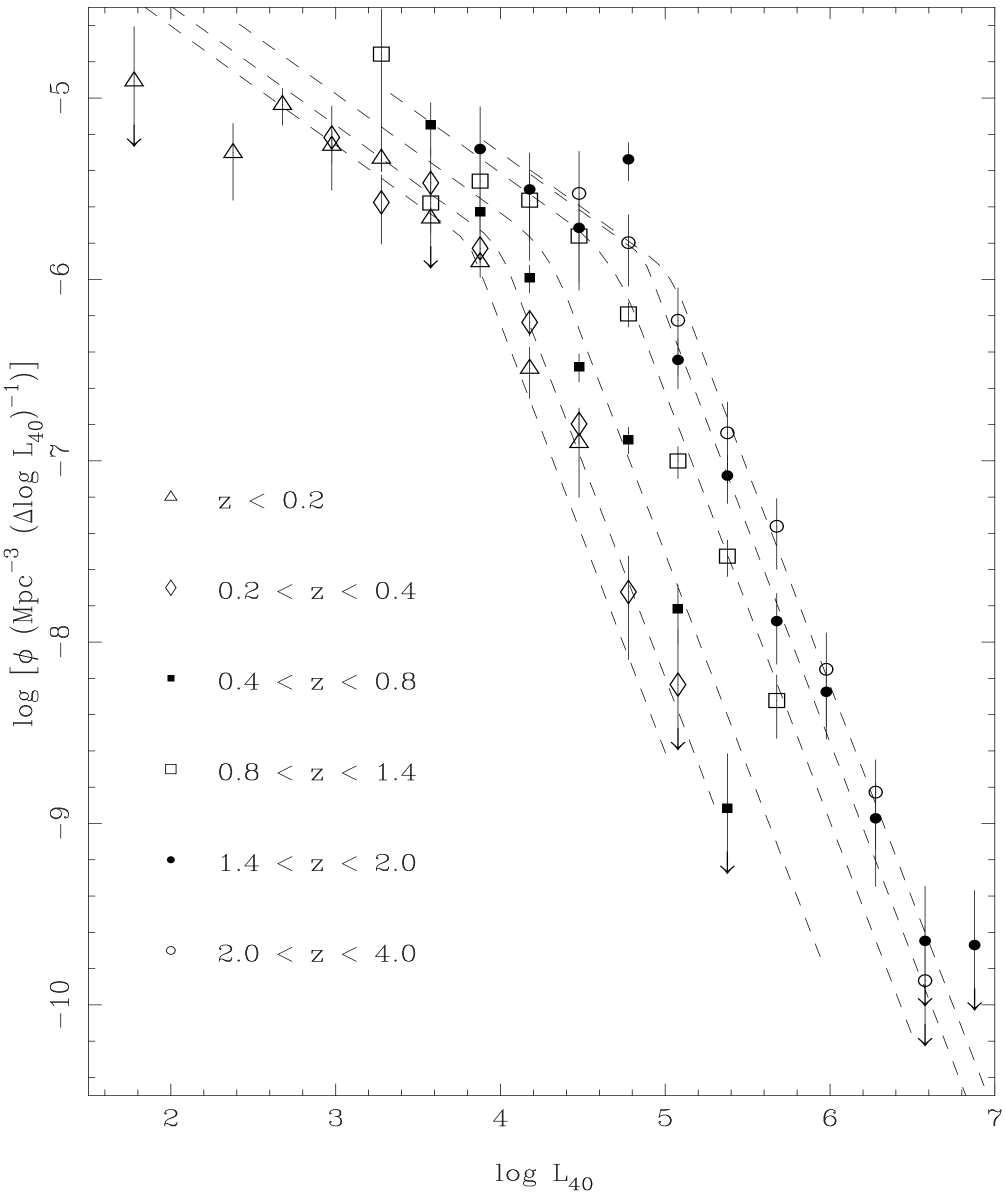

Figure 4.6: Binned $1/V_a$ estimates of ϕ in different redshift shells, for $q_0 = 0$, and CF=1.47. Model curves (dashed lines) are for power law evolution with a cutoff in evolution and $\sigma_\alpha = 0.5$, and are in the same redshift intervals as the data.

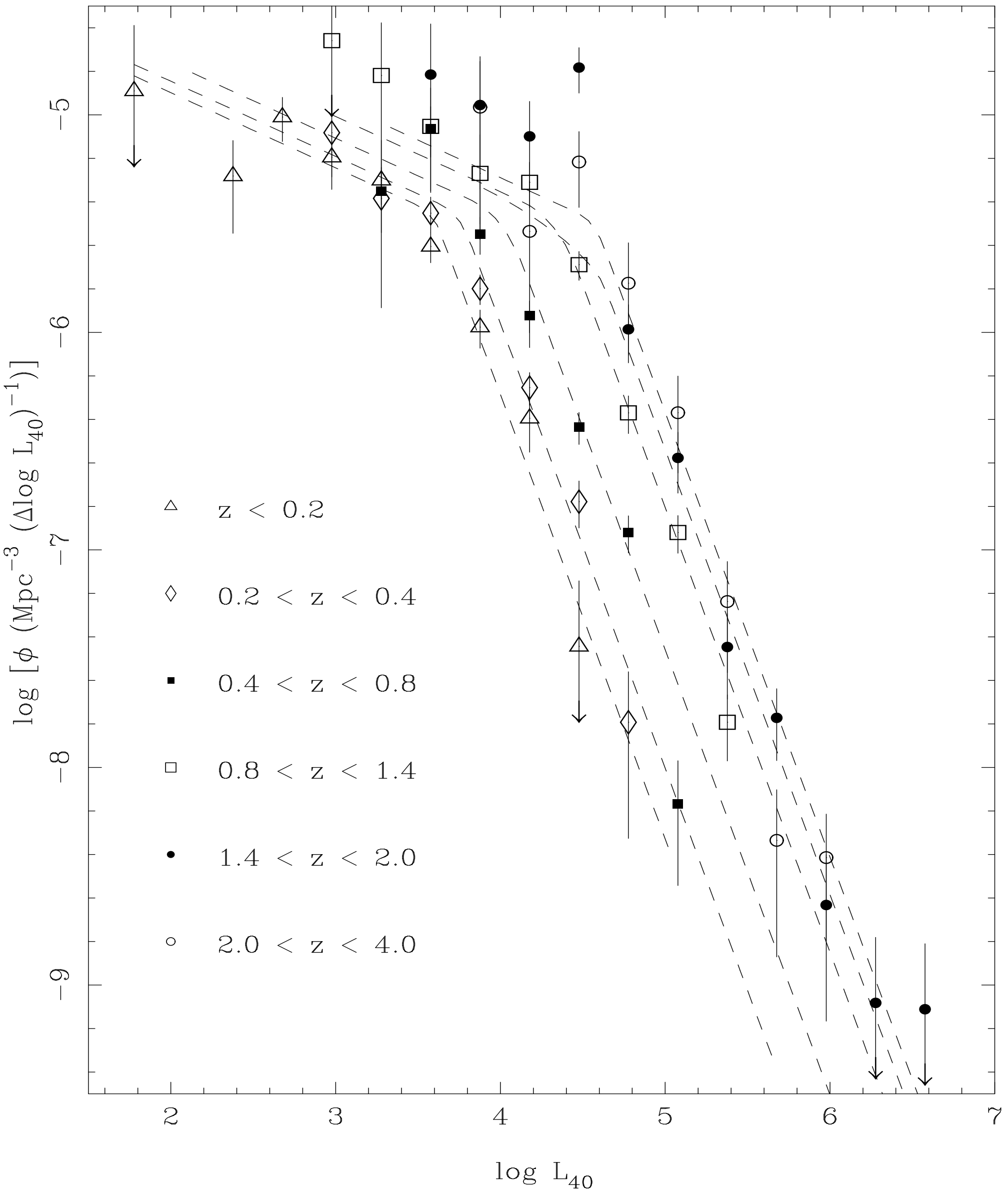

Figure 4.7: Binned $1/V_a$ estimates of ϕ in different redshift shells, for $q_0 = 0.5$, and CF=1.47. Model curves (dashed lines) are for polynomial evolution with $\sigma_\alpha = 0.5$, and are in the same redshift intervals as the data.

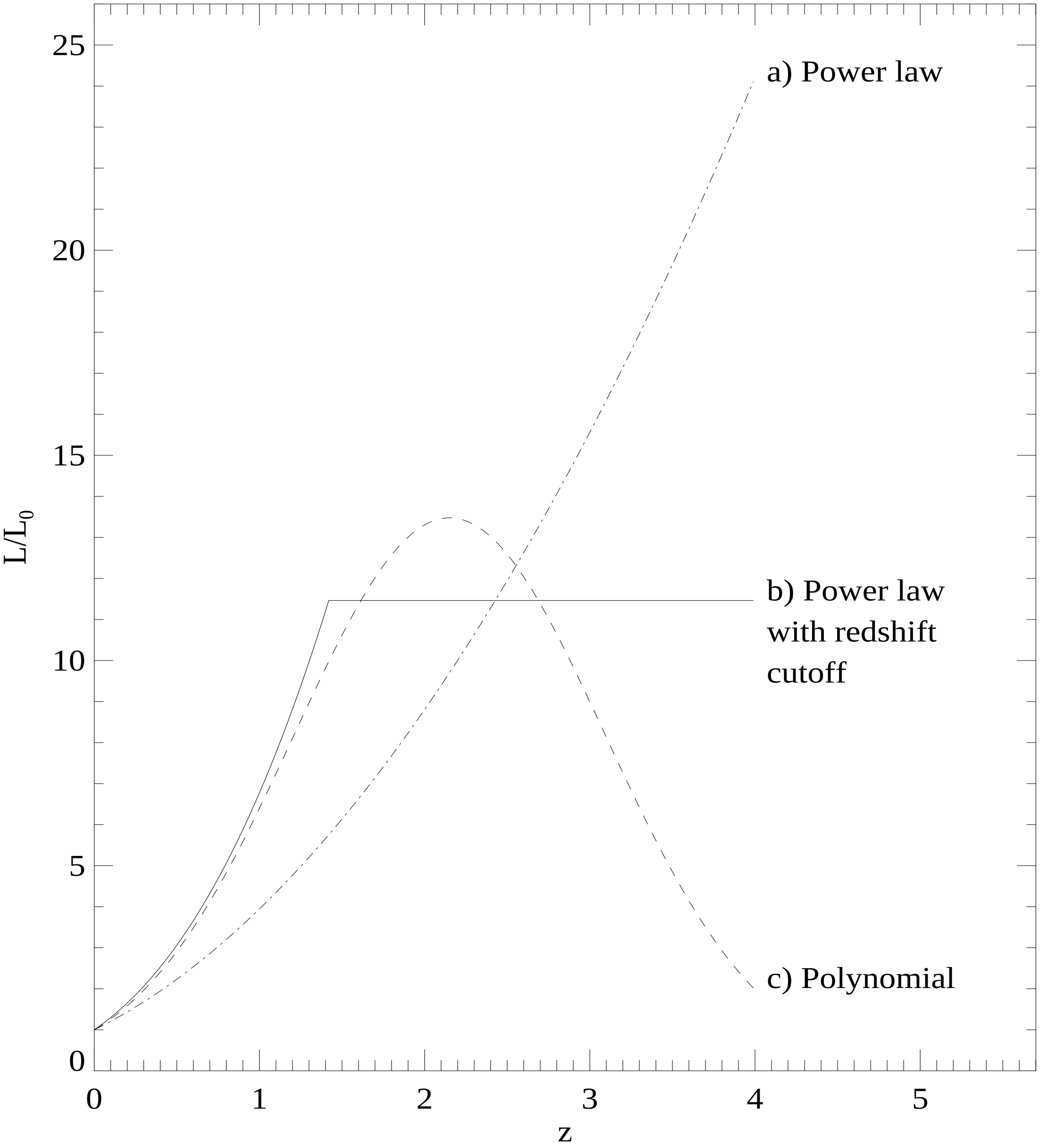

Figure 4.8: Comparison of the three PLE models. Parameters used are the bestfit for $q_0 = 0$, CF=1.47 and $\sigma_\alpha = 0.5$.

to the 2D K.S. test, but the assumption of PLE may not be appropriate for $q_0 = 0.5$ (see previous section) and hence an assessment of the high redshift evolution which does not depend on this assumption is desirable.

I investigate the evolution at high redshift in a model independent way by using the $\langle V_e/V_a \rangle$ test in a changing redshift interval, as in Chapter 2. The test has been applied in the redshift window $z_b < z < 4$ where the parameter z_b defines the bottom of the window. Where appropriate, V_e and V_a are weighted by the apparent density evolution, and V_a calculated assuming the apparent luminosity evolution, which result from the dispersion of AGN spectral slopes (see Section 4.3.1).

The results of this test are shown in Figures 4.9 and 4.10 for $q_0 = 0$ and $q_0 = 0.5$ respectively. In both cases CF=1.47 has been used; changing CF from 1.47 to 1.8 has almost no effect on $\langle V_e/V_a \rangle$ at these redshifts because most of the AGN are *ROSAT* selected. For the $q_0 = 0$ plot (Figure 4.9) the dispersion in spectral indices has been neglected, while for the $q_0 = 0.5$ plot I have used $\sigma_\alpha = 0.5$. $\langle V_e/V_a \rangle$ is smaller for $q_0 = 0.5$ and $\sigma_\alpha = 0.5$, hence Figures 4.9 and 4.10 correspond approximately to greatest and least evolution at high redshift for the adopted values of q_0 and σ_α.

In both cases, $\langle V_e/V_a \rangle$ becomes lower than 0.5 when $z_b \sim 1.8$. For $q_0 = 0$, this result is only significant at 1σ confidence if the dispersion in spectral slopes is neglected, but for the more realistic assumption that $\sigma_\alpha = 0.5$ it is significant at 2σ. For $q_0 = 0.5$, $\langle V_e/V_a \rangle$ is lower than 0.5 with 2σ confidence even if $\sigma_\alpha = 0$, and with 3σ confidence if the more realistic $\sigma_\alpha = 0.5$ is assumed.

This suggests that evolution at high redshift ($z > 1.8$) is probably in the negative sense, i.e. the space density and/or luminosities of QSOs are declining with redshift. However, I caution that this result is marginal for $q_0 = 0$ ($1\sigma - 2\sigma$) and for either value of q_0 is based on only 52 objects with $z > 1.8$.

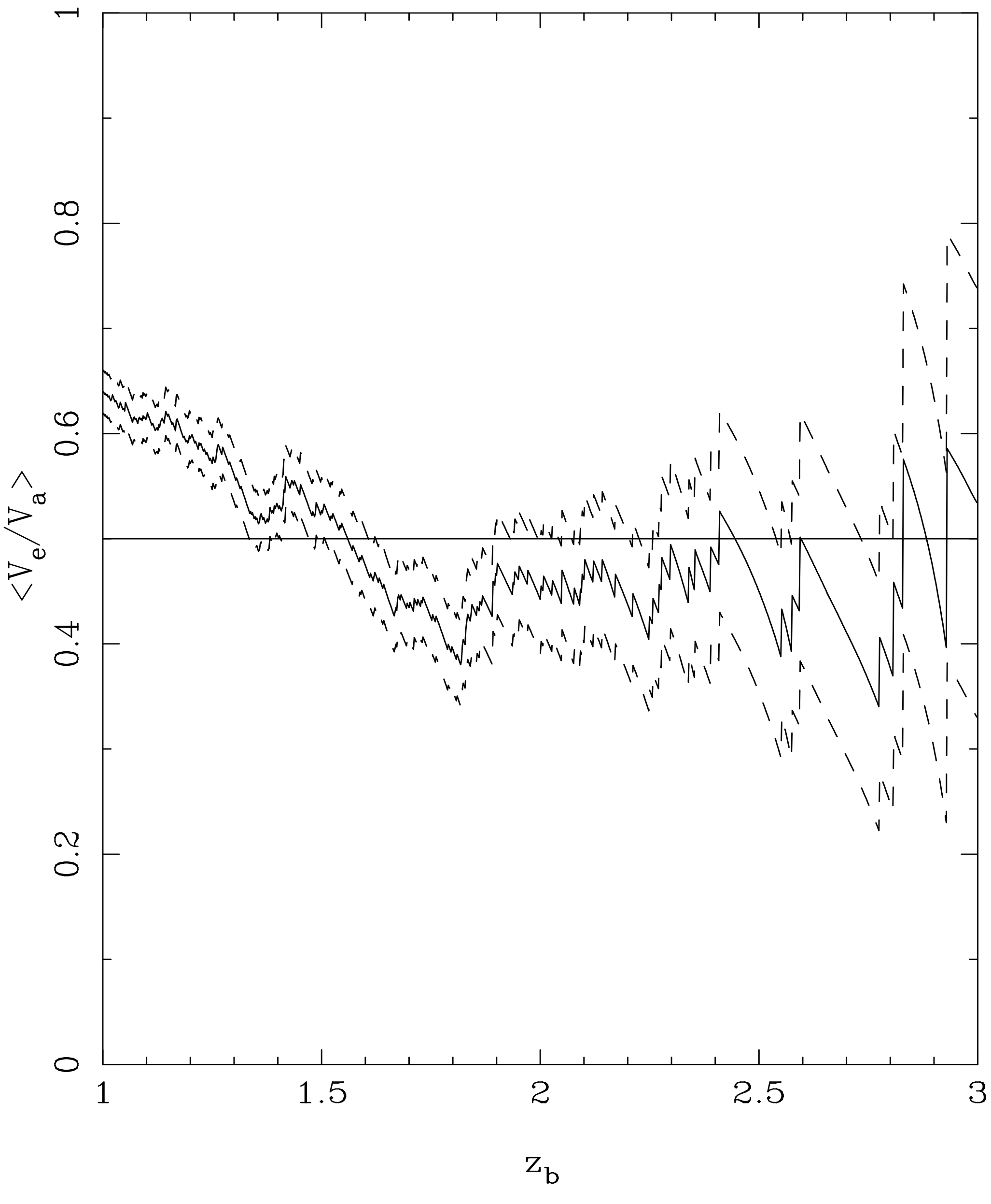

Figure 4.9: $\langle V_e/V_a\rangle$ test performed in the interval $z_b < z < 4$, where z_b is varied, for $q_0 = 0$, $\sigma_\alpha = 0$ and CF=1.47. $\langle V_e/V_a\rangle < 0.5$ indicates that the XLF declines as z increases, while $\langle V_e/V_a\rangle > 0.5$ indicates that the XLF increases with z. Dashed lines denote the 68% confidence region

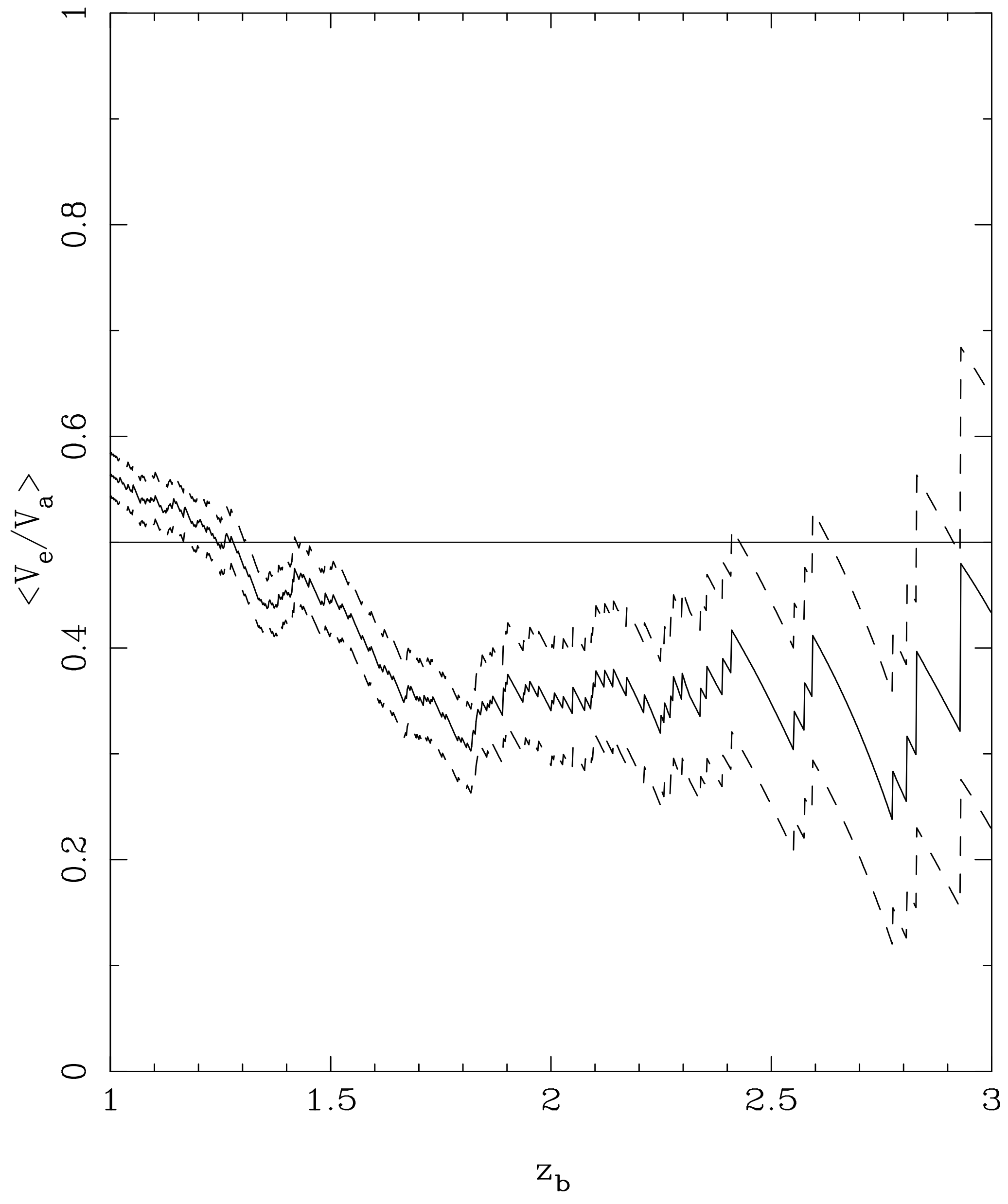

Figure 4.10: $\langle V_e/V_a \rangle$ test performed in the interval $z_b < z < 4$, where z_b is varied, for $q_0 = 0.5$, $\sigma_\alpha = 0.5$ and CF=1.47. $\langle V_e/V_a \rangle < 0.5$ indicates that the XLF declines as z increases, while $\langle V_e/V_a \rangle > 0.5$ indicates that the XLF increases with z. Dashed lines denote the 68% confidence region

4.6 Discussion

The excess of objects with $z > 1.4$ and $L < 5 \times 10^{44}$erg s^{-1} cm^{-2} for $q_0 = 0.5$, indicates that PLE is not a good model for $q_0 = 0.5$. The binned $1/V_a$ XLF in Figure 4.7 is consistent with a two power law shape which does not change with redshift, hence a combination of PLE and PDE (i.e. a combination of horizontal and vertical shifts between the XLF at different redshifts in Figure 4.7) could describe the evolution. Because the deviation from PLE corresponds to only a small number (~ 15) of AGN, I have not performed fits using luminosity and density evolution. It would not be possible to constrain the functional form of the density evolution with the present sample. More complex models, such as luminosity dependent luminosity evolution could equally describe the data.

If narrow emission line galaxies (NELGs) were included in the $q_0 = 0.5$ luminosity function, there would be a smaller excess of objects with $z > 1.4$ and $L < 5 \times 10^{44}$erg s^{-1} cm^{-2}. This is illustrated in Figure 4.11, where the XLF of a combination of broad line and narrow line AGN is shown for $z < 0.4$ and $1.4 < z < 2$. With the addition of the NELGs, deviations from PLE are smaller and are now restricted to a single luminosity bin. It is therefore possible that PLE can describe the X–ray evolution of AGN if the local NELG population is (at least in part) descended from QSOs. This scenario is also consistent with the evolution seen in NELGs. I showed in Chapter 3 that while NELGs may be undergoing PLE at low redshifts, there are too few high redshift ($z > 0.6$) NELGs for this evolution to continue beyond $z \sim 1$. If the NELGs become broad line AGN when they are at higher X–ray luminosities, this lack of high redshift NELGs is an obvious consequence, and the NELGs and QSOs could be modelled as a single population undergoing PLE. Indeed, it has already been noted that the addition of NELGs to a broad line AGN sample improves the 2D KS probabilities of PLE models (e.g. Boyle *et al.* 1994 and Chapter 2 of this thesis).

Comparing the behaviour of the XLF and that of the optical luminosity function

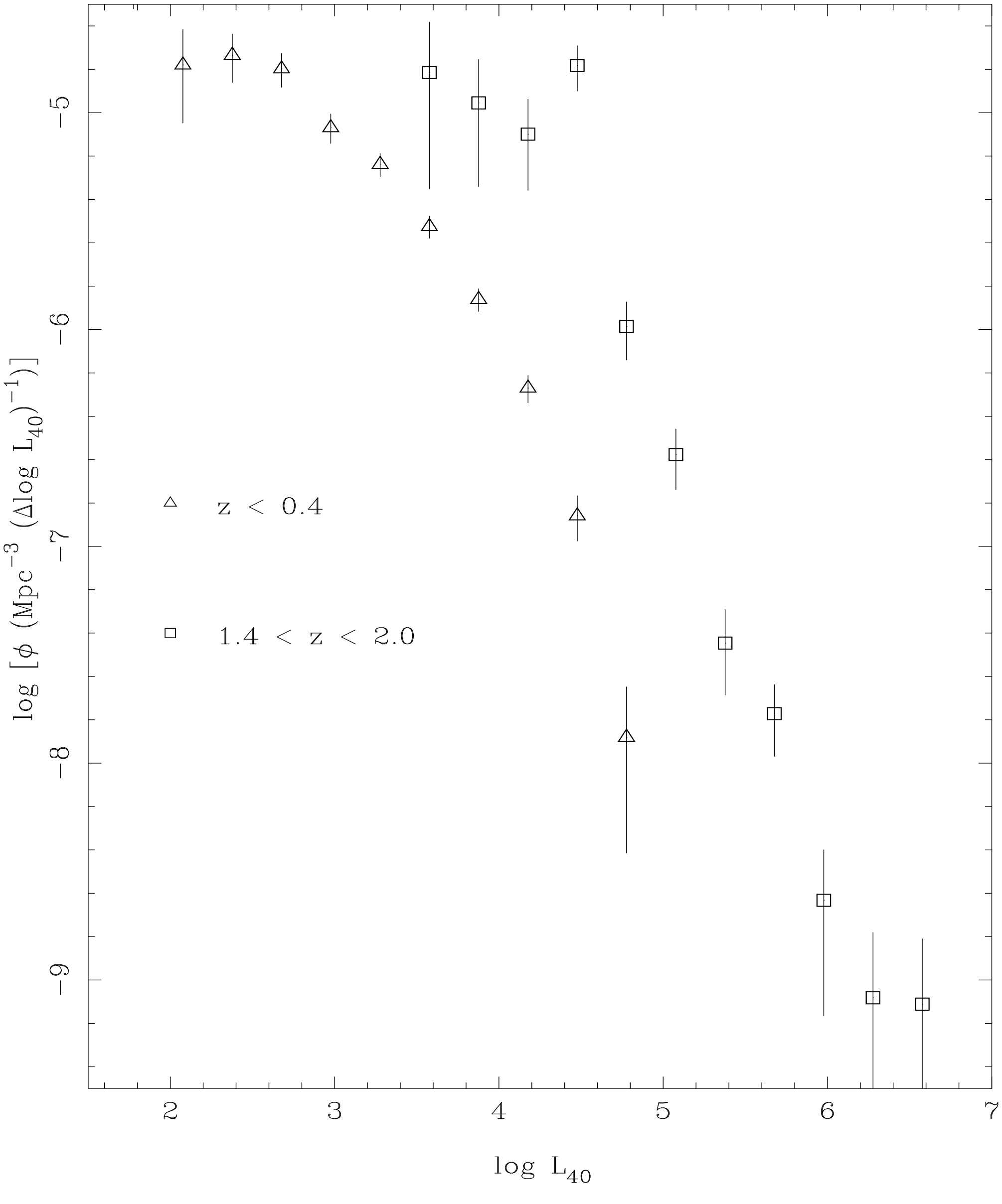

Figure 4.11: Binned $1/V_a$ estimates of ϕ in different redshift shells, for $q_0 = 0.5$, and CF=1.47, when X–ray selected NELGs are added to the QSO sample.

leads to an impressive agreement in many respects. The deviation from PLE for $q_0 = 0.5$ is very similar to that observed in the optical QSO luminosity function by Boyle, Shanks & Peterson (1988), who also suggested that a combination of luminosity evolution and density evolution could account for the evolution. Hewett, Foltz and Chaffee (1993) report a steepening of the Large Bright QSO survey optical luminosity function with redshift for $q_0 = 0.5$. This steepening, caused by an excess of low luminosity objects at high redshift, is also qualitatively similar to the behaviour of the XLF found here.

The data are well represented by PLE for $q_0 = 0$, and again this has been reported for the optical luminosity function by Boyle, Shanks & Peterson (1988). Hawkins & Veron (1995), and Hewett, Foltz and Chaffee (1993) report that the rapid evolution seen at low redshift drops off at $z = 1.5$, which is in good agreement with the XLF; Hewett, Foltz and Chaffee (1993) found that the optical luminosity function is slowly increasing for $2 < z < 3$ while Hawkins & Veron (1995) found a roughly constant optical luminosity function for the same redshift range. I find tentative evidence for negative evolution at $z > 2$ (which could be luminosity evolution, density evolution or both), but for $q_0 = 0$ the data can be successfully modelled with a XLF which is constant at $z > 2$ (model b). There is no correction for the dispersion in QSO optical spectral shapes in Hewett, Foltz and Chaffee (1993) or Hawkins & Veron (1995), which would reduce their high redshift evolution; hence the behaviour of the XLF is in reasonable agreement with that of the optical luminosity function.

It has been claimed that evolution is faster in the optical than at X–ray energies (e.g. Maccacaro *et al.* 1991) based on the different evolution parameters found in the two regimes, using power law or exponential PLE models. These models are not unique descriptions of the evolution in either the X–ray or optical wavebands; differences between the actual evolution and the analytic models would be expected to result in different evolution parameters for samples with different redshift distributions. Optical samples of QSOs (e.g. those of Boyle *et al.* 1988, Hewett, Foltz and Chaffee 1993 or Hawkins & Veron 1995) have few objects with $z < 0.3$ and a majority of objects with $z > 1$. Samples used to study the XLF typically include the EMSS AGN (e.g. Boyle *et al.* 1994, this thesis, Jones *et al.* 1996) and are dominated by objects with $z < 1$. The evolution parameters found in this work are slightly higher than those obtained in Chapter 2 which included fewer high redshift AGN, (e.g. $\Delta C \sim 0.1$ for $q_0 = 0$, power law evolution with a redshift cutoff). Similarly, when Boyle *et al.* (1994) used only their high redshift *ROSAT* sample (their models Q-T), they found higher evolution parameters than the when the EMSS AGN were added to the sample. More evidence for a redshift dependent bias in the evolution parameter is found in Chapter 2 Figure 2.7, which shows that a higher bestfit evolution rate is found for $0.5 < z < 1$ than $0 < z < 0.5$.

The possible redshift dependence of the evolution parameter determination, and the different redshift distributions of current X–ray and optical samples may be sufficient to account for the difference in the apparent evolution. The imperfect (and different) treatment of K correction, the dispersion of spectral slopes for the two wavebands, and the different systematics found in surveys in the optical (e.g. the UVX selection criteria) and X–ray domain (e.g. the uncertainty in CF in this work) can also account for some of the difference in the apparent rates of evolution.

4.7 The QSO Log N - Log S and the QSO Contribution to the Soft X–ray Background

The log N - log S of AGN at faint fluxes has been calculated for all the models in Table 4.1 which are not rejected at $> 99\%$ by the 2D KS test. The curves were computed over the redshift de-evolved luminosity interval $0 < z < 4$, 10^{40}erg s^{-1} cm^{-2} $< L_0 < 10^{48}$erg s^{-1} cm^{-2}, the same interval used for fitting and testing models. These model curves are shown in Figure 4.12, along with the actual cumulative log N - log S of the AGN sample used here (shown as crosses), and the 68% confidence limits to the log N - log S of *all* sources at faint fluxes determined from fluctuation analysis of the *ROSAT* UK Deep survey field by Barcons *et al.* (1994). Model curves for $q_0 = 0$ and $q_0 = 0.5$ are well separated. The excess AGN with $S < 2 \times 10^{-14}$erg s^{-1} cm^{-2} above the predictions of the $q_0 = 0.5$ PLE models correspond to the excess low luminosity objects at $z > 1.4$ above the PLE XLF seen in Figure 4.7. The difference between the log N - log S curves for polynomial evolution and power law evolution with a redshift cutoff, or between models fitted with different values of CF is smaller than that when the models are fitted with different values of σ_α. None of the models exceed the total log N - log S of all sources from Barcons *et al.* (1994).

The contribution of AGN to the 1 - 2 keV X–ray background is listed in Table 4.1, under the column entitled I_{XRB}, for each of the PLE models I have tested. Again, the region of parameter space $0 < z < 4$, 10^{40}erg s^{-1} cm^{-2} $< L_0 <$ 10^{48}erg s^{-1} cm^{-2} has been used.

A large difference is seen in the predicted QSO X–ray background contribution for the two different values of q_0; choice of evolution model, CF, and σ_α has a comparatively minor effect. The AGN X–ray background intensities obtained here are in excellent agreement with those of Jones *et al.* (1996) and Boyle *et al.* (1994) but are lower than those given in Chapter 2 in which NELGs are included in the AGN sample. I assume a 1 - 2 keV X–ray background intensity of 1.46×10^{-8}erg s^{-1} cm^{-2} sr^{-1} (Chen, Fabian & Gendreau 1996), which is consistent with the value 1.4 ± 0.1 found by Branduardi-Raymont *et al.* from the *ROSAT* UK Deep survey. Disregarding the models in Table 4.1 which are rejected at $> 99\%$, the AGN contribution to the X–ray background is between 37% and 42% for $q_0 = 0$ or 22% and 25% for $q_0 = 0.5$. As discussed above and in Section 4.6, the $q_0 = 0.5$ PLE models underpredict the number of faint AGN with $z > 1.4$, and hence the QSO contribution to the X–ray background is probably underestimated by using the $q_0 = 0.5$ PLE models.

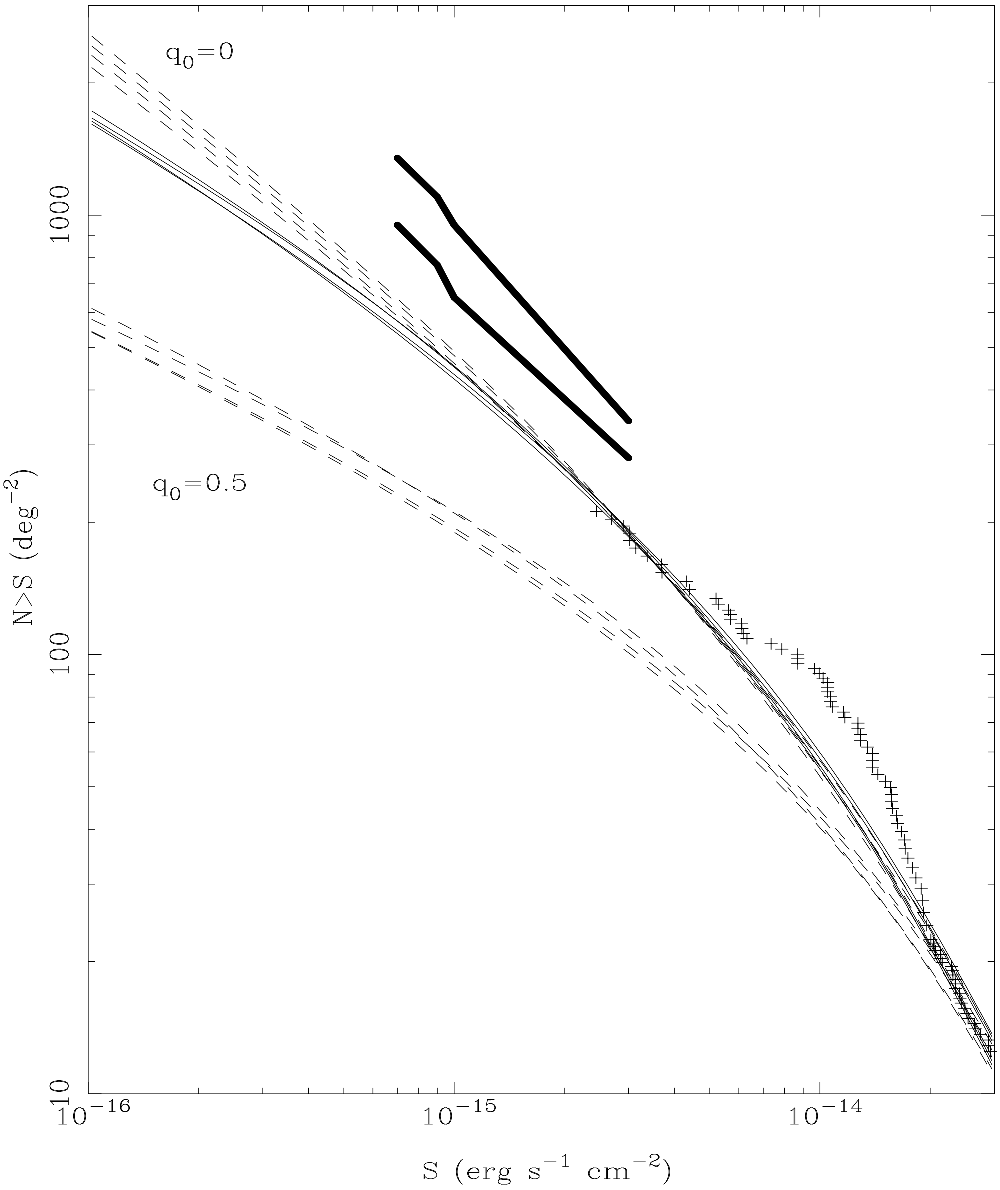

Figure 4.12: Log N - Log S curves for all models in Table 4.1 which are not rejected at $>$ 99%. Models fitted assuming a dispersion in spectral indices ($\sigma_\alpha = 0.5$) are shown as dashed lines and models fitted assuming no dispersion ($\sigma_\alpha = 0$) are shown as solid lines. The crosses are the observed Log N - Log S of the QSO sample, and the thick lines denote the 68% confidence limits of the total log N - log S of all sources (i.e. not only AGN) at faint fluxes from Barcons *et al.* (1994).

4.8 Conclusions

I have used 748 broad line AGN to investigate the evolution of the XLF with redshift. PLE models represent the data well for $q_0 = 0$, but for $q_0 = 0.5$ an excess of low luminosity AGN are seen at $z > 1.4$. This excess is not seen if NELGs are included in the AGN sample, indicating that PLE is an acceptable model for $q_0 = 0.5$ if QSOs become NELGs when they evolve to lower luminosities. Alternatively, the evolution could be modelled by a combination of PDE and PLE.

Power law PLE models in which the evolution does not stop at high redshift ($z > 1.8$) are rejected at high confidence for $q_0 = 0$ or $q_0 = 0.5$. PLE models in which the evolution stops or is negative at $z > 1.8$ are acceptable. Model independent $\langle V_e/V_a \rangle$ tests show that the evolution is probably negative at $z > 1.8$, for both values of q_0.

When taking into account the dispersion in AGN X–ray spectral slopes I find that the redshift at which evolution stops is lower, $z \sim 1.4$. PLE models are a better fit for $q_0 = 0.5$ when the dispersion in spectral slopes is taken into account, but the dispersion cannot account for the excess low luminosity AGN at high redshift.

Integrating my model XLF and evolution to $z = 4$ produces 1 - 2 keV X–ray background intensities of $5.7 \pm 0.4 \times 10^{-9}$erg s^{-1} cm^{-2} sr^{-1} ($\sim 37\% - 42\%$) for $q_0 = 0$ from QSOs.

For $q_0 = 0.5$ the predicted QSO contribution to the 1 - 2 keV X–ray background is $3.4 \pm 0.3 \times 10^{-9}$erg s^{-1} cm^{-2} sr^{-1}, but this and previous estimates for $q_0 = 0.5$ using PLE models are probably too small because some density evolution may be required.

Chapter 5

Epilogue

A long time ago in a galaxy far far away…

5.1 X–ray Astronomy in the Future

The X–ray observatories planned for launch in the next few years will revolutionise AGN research. In 1998 the American satellite *AXAF* is due for launch. It will offer unparalleled spatial resolution, and will have about twice the effective area of *ROSAT* at 1 keV. *AXAF* also has considerable spectroscopic capabilities with CCD detectors and an objective grating spectrometer. The European satellite *XMM* is scheduled for launch in late 1999. It will have an effective area $\sim$ 8 times that of *ROSAT* at 1 keV, and spatial resolution comparable to, or better than, that of the *ROSAT* PSPC. *XMM* will have unsurpassed spectral capabilities from its CCD detectors, and reflection grating spectrometer, and the broad spectral range (0.1 – 10.0 keV) will provide a much better understanding of the X–ray spectra of both bright *and* faint sources.

For the first time it will be possible to construct luminosity functions of AGN and NELGs, over a wide range of redshifts, in both the hard and soft bands, with the same instrument. The large collecting area and high spectral resolution of *XMM* mean that it will be possible to accurately K correct each individual source with flux greater than $\sim 10^{-14}$erg s^{-1} cm^{-2} (0.5 – 2 keV). It will therefore not be necessary to correct for the dispersion in spectral indices for bright luminosity functions. X–ray spectral emission lines may provide redshifts without the need for optical spectroscopy.

In this chapter I will use the *ROSAT* results presented earlier in this thesis to estimate the content of future surveys. In particular I attempt to determine the optimum X–ray survey for the study of AGN at $z > 2$.

5.2 Source Populations at Faint Fluxes

The integral log N - log S of sources in the 0.5 - 2 keV band is plotted in Figure 5.1. The stepped line is the log N - log S of all sources in the *ROSAT* UK Deep and Medium surveys (Branduardi-Raymont *et al.* 1994), each increment corresponding to one source. The two bold continuous lines are the 68% confidence limits to the faint source log N - log S from fluctuation analysis of the UK Deep survey field (Barcons *et al.* 1994). The log N - log S of QSOs, marked as triangles, comes from the sample used in Chapter 4 while the log N - log S of stars, NELGs and clusters/groups come from a combination of RIXOS and the UK Deep survey. All fluxes are calculated assuming a power law spectral form, and have been corrected for absorption by Galactic $N_{\rm H}$. Although this does not give realistic flux estimates for the stars, which do not have power law spectra and are mostly subject to much smaller absorbing columns, it is appropriate for assessing their contaminating effect on any survey which is intended to study the extragalactic population.

It is clear from Figure 5.1 that broad line AGN are the most important population at fluxes $> 2 \times 10^{-15}$erg s^{-1} cm^{-2} in the 0.5 - 2 keV band. At the faintest limit of the UK Deep Survey (2×10^{-15}erg s^{-1} cm^{-2}) the log N -log S of NELGs is steeper than that of QSOs and the sky density of NELGs may exceed that of QSOs by

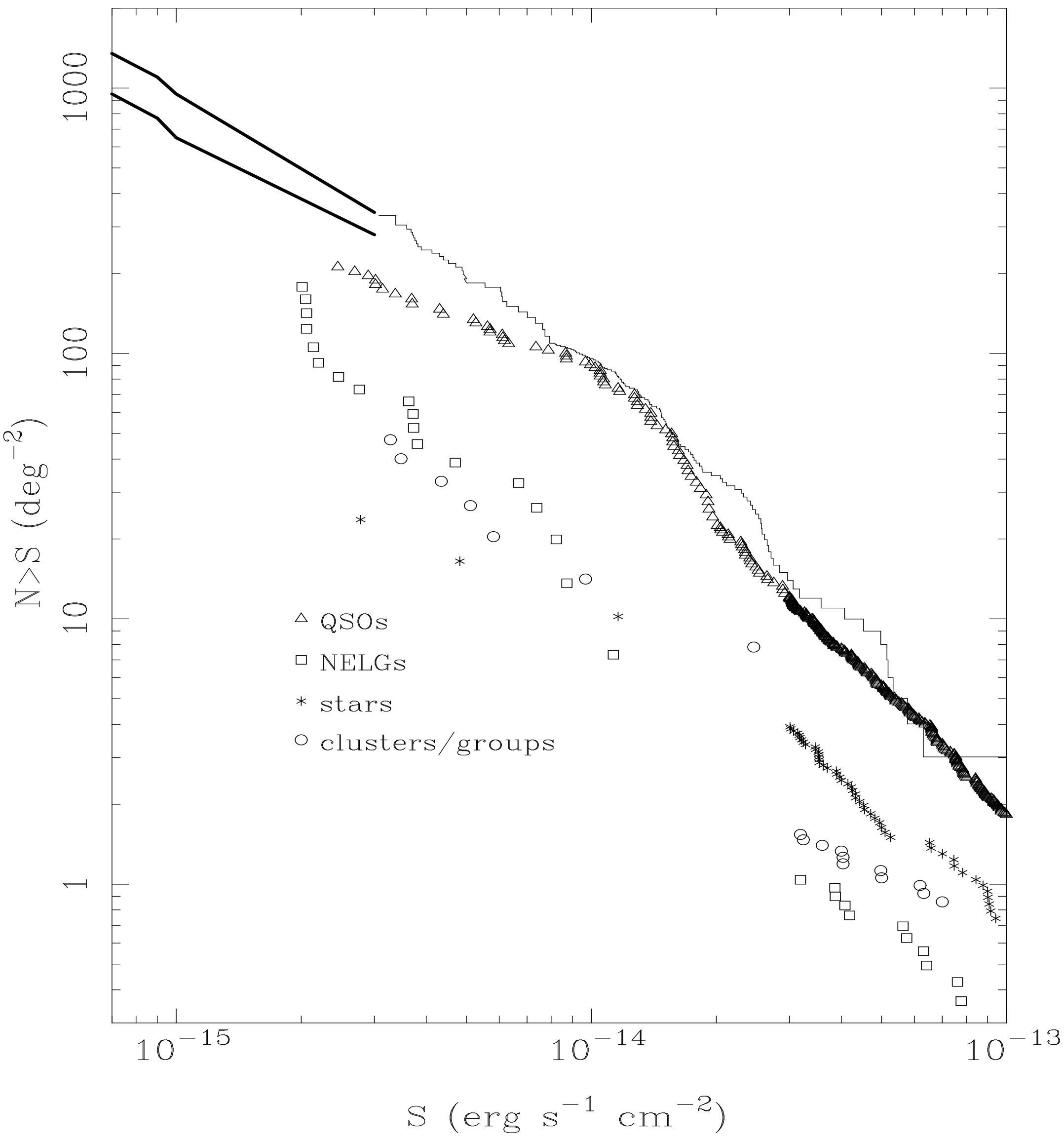

Figure 5.1: Log N - log S of different classes of sources from 0.5 - 2 keV. The stepped line is the log N - log S of all sources detected in the UK Deep and Medium surveys, and the two solid lines represent 68% confidence limits to the faint source population from fluctuation analysis of the UK Deep survey by Barcons *et al.* (1994)

$\sim 10^{-15}$erg s^{-1} cm^{-2}. Stars appear to be relatively unimportant to the faint X–ray population, and are the least significant class of object at the UK Deep survey flux limit. Clusters and groups also have a smaller sky density than NELGs or QSOs at a few $\times 10^{-15}$erg s^{-1} cm^{-2}, and few are detected in the UK Deep survey, but their log N -log S may be steeper than that of QSOs at these flux levels, and hence clusters/groups may become relatively more important at $< 10^{-15}$erg s^{-1} cm^{-2}. The rapidly increasing population of NELGs indicates that as the flux limits decrease below $\sim 10^{-14}$erg s^{-1} cm^{-2} a smaller proportion of the sources will be QSOs.

5.3 Energy Range for Selection

XMM and *AXAF* will have a much larger spectral range than *ROSAT* , for *XMM* the useful range of the EPIC detectors is expected to be 0.1 - 10 keV. *ROSAT* is sensitive to photons from 0.1 - 2.5 keV, but the 0.5 - 2 keV band was used to select sources in RIXOS and the UK Deep Survey. At softer energies a large proportion of the sources are Galactic in origin; white dwarfs and some cataclysmic variables are intrinsically soft sources, and extragalactic sources are strongly absorbed at < 0.5 keV by intervening material in our Galaxy.

However, of all the classes of sources detected in RIXOS, QSOs appear to have the softest spectra (see Mittaz *et al.* 1996). In the *ROSAT* UK Deep survey, the NELGs, which are becoming so numerous at faint fluxes, have harder spectra, $\alpha_X \sim 0.5$, than the QSOs which have $\alpha_X \sim 1.0$ (Romero - Colmenero *et al.* 1996). Assuming $\alpha_X = 1.0$ for QSOs, the log N - log S from 0.5 - 2 keV is identical to the log N - log S from 2 - 8 keV, because the logarithmic width of the band is identical. Assuming $\alpha_X = 0.5$ for the NELGs, the flux of each NELG in the 2 - 8 keV band will be a factor 2 larger than in the 0.5 - 2 keV band. This corresponds to a shift of the NELG log N - log S to the right by $\Delta\log S = 0.3$; shifting the NELG log N - log S in Figure 5.1 by this amount makes them more numerous than QSOs at 4×10^{-15}erg s^{-1} cm^{-2}. It is thus more efficient to select QSOs at 0.5 - 2 keV than at higher energies.

Selecting QSOs from 0.5 - 2 keV would also allow accurate K correction of each QSO directly from its own spectrum up to $z = 4$ (i.e. when the intrinsic 0.5 - 2 keV spectrum is observed at 0.1 - 0.4 keV). It would also be possible to directly measure the K correction which would be appropriate for the low redshift objects, were they to be viewed at higher redshift, again up to $z = 4$ with *XMM* which is sensitive up to 10 keV. This would allow a much better determination of the maximum redshift to which our objects could have been included in the sample, with consequent improvements in fitting the luminosity function and an accurate determination of V_a for $\langle V_e/V_a \rangle$ testing.

Another advantage of the 0.5 - 2 keV range is the relative ease with which future surveys could be compared to and/or combined with the surveys already conducted in this band by *ROSAT* .

For these reasons I propose that the optimum survey of $z > 2$ AGN should be carried out in the 0.5 - 2 keV energy range. Fluxes and luminosities quoted for the remainder of this chapter are in the 0.5 – 2 keV range unless otherwise stated.

5.4 Limitations of Deep Surveys

Future deep surveys will be limited by two factors: source confusion and sensitivity. *ROSAT* has already probed flux levels at which source confusion is important (e.g. the UK Deep Survey). *XMM* has a much larger effective area than *ROSAT* , but will probably have only a small improvement in spatial resolution compared to the PSPC. Confusion of sources will almost certainly limit the depth that *XMM* surveys will be capable of reaching, and will probably be a major problem by $\sim 10^{-15}$erg s^{-1} cm^{-2}. The much better spatial resolution of *AXAF* mean that it will be able to resolve essentially all the sources at and below this limit. According to the *AXAF* Science Instrument Notebook (available on line from the *AXAF* Science Centre), the sensitivity of *AXAF* will probably limit detection of sources to those brighter than $\sim 7 \times 10^{-16}$erg s^{-1} cm^{-2} if exposure times of 100 ksec or less are employed.

5.5 Requirements for a Study of the $z > 2$ AGN Luminosity Function

The luminosity function of AGN with $z > 2$ is of particular interest. From the surveys performed so far with *ROSAT* there is strong evidence that the luminosity function of AGN declines with redshift at $z > 2$, and there is already some evidence that PLE is not a good model for $q_0 = 0.5$ at high redshift (see Chapter 4). To make an effective study of the AGN luminosity function at $z > 2$ it will be necessary to obtain a sample of AGN which are found at a range of redshifts and luminosities. In particular, to test PLE or to formulate some more realistic evolution model, the AGN sample must contain objects found on either side of the break in the luminosity function, over the full redshift range of interest. A sample with around 100 high luminosity objects and 100 low luminosity objects would offer a huge improvement to our knowledge of evolution at $z > 2$.

5.6 The Optimum Survey of $2 < z < 3$ QSOs

In practice, the optical identification of X–ray sources becomes easier as the flux limit of the survey is increased. Brighter X–ray sources are statistically more likely to have bright optical counterparts; in particular, AGN have an approximately linear relation between X–ray and optical luminosity (see La Franca *et al.* 1994, Franceschini *et al.* 1994). Positions for bright X–ray sources can be calculated more accurately than for faint ones. Source confusion will be a far greater problem for surveys with low flux limits than for those with high flux limits. Furthermore, the steep log N - log S of NELGs means that QSO surveys become less efficient as the flux limit decreases below $\sim 10^{-14}$erg s^{-1} cm^{-2}. Therefore, the most effective method for investigating the $2 < z < 3$ AGN luminosity function will be to apply the *largest* flux limit with which the necessary sample can be obtained. Because we require, as a bare minimum, objects brighter than, *and* objects fainter than, the break in the luminosity function, the most effective survey would have two flux limits. I have based the following predictions on the $q_0 = 0$ luminosity function, undergoing power law PLE with a cutoff at $z = 1.8$, with CF=1.47 and no correction for dispersion of spectral index, which was obtained in Chapter 4. This is a good fit to the data (P>D=0.1). This model is not evolving in the redshift range that we are interested in ($z > 2$), hence its application in this regime is simple. Comparing data to the predictions of this model should therefore indicate whether the space density of AGN is increasing or decreasing with z at $z > 2$. The case for $q_0 = 0.5$ is more complex, most PLE models are a poor fit; only the polynomial model with a dispersion in spectral indices is not rejected by the 2D KS test, and visual inspection of the luminosity function suggests that PLE may not be the best model. Because the $q_0 = 0$ PLE model reproduces all the current data well, it is the natural choice for prediction of the $z > 2$ luminosity function.

5.7 High Luminosity AGN at $2 < z < 3$

The break in the luminosity function at $z > 2$ is at a luminosity of $\sim 7 \times 10^{44}$ergs^{-1}. I have taken a lower limit of twice this luminosity to ensure AGN, which are on the steep high luminosity portion of the luminosity function are selected. The model predicted log N - log S for the high luminosity AGN at $2 < z < 3$ is shown in the top panel of Figure (5.2) while the bottom panel shows the redshift distribution as a function of limiting flux. The colour scale is linear, normalised to the total number of objects at each flux limit; dark areas denote a lack of objects while light areas denote a concentration of sources.

It is seen from the log N - log S that the total sky density of high luminosity AGN with $2 < z < 3$ is only ~ 3.5 deg^{-2}, and decreasing the flux limit below

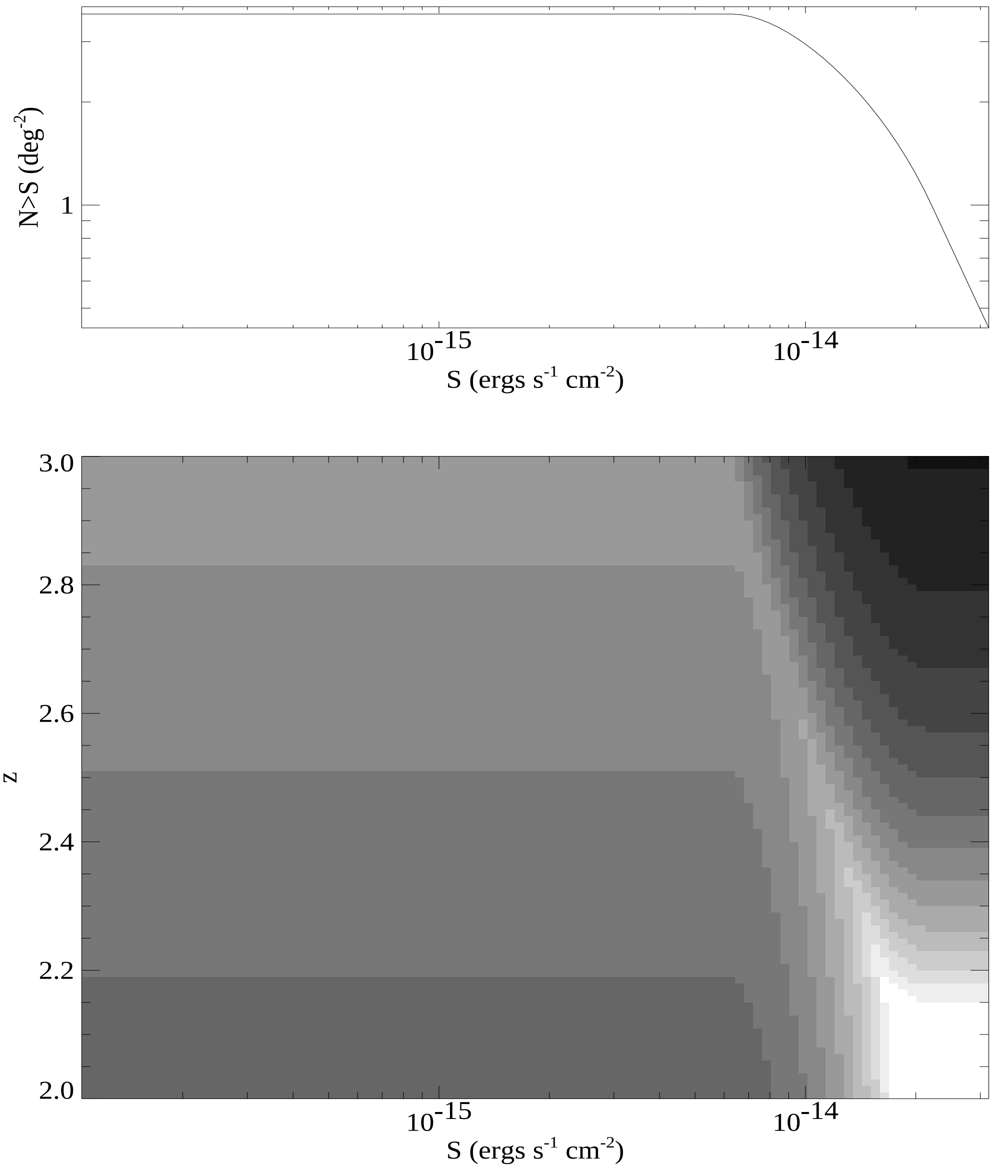

Figure 5.2: Log N - log S of high luminosity ($> 1.4 \times 10^{45}$ergs^{-1}) $2 < z < 3$ AGN (top panel) and the relative redshift distribution as a function of flux limit (bottom panel). Dark colours indicate a lack of sources

6×10^{-15}erg s^{-1} cm^{-2} does not result in any increase in the number detected. The redshift distribution changes very rapidly between 1 and 2×10^{-14}erg s^{-1} cm^{-2}: at 2×10^{-14}erg s^{-1} cm^{-2} almost all the high luminosity AGN are at z close to 2, while at 10^{-14}erg s^{-1} cm^{-2} they are distributed fairly evenly over the whole redshift range. About 10^{-14}erg s^{-1} cm^{-2} is the most efficient flux limit for selecting these objects; at this flux limit there are about 3 deg^{-2} while the total sources population is ~ 90 deg^{-2} (see Figure 5.1). Only 1 in 30 sources are high luminosity $2 < z < 3$ AGN, hence to obtain a sample of 100 objects it would be necessary to survey 33 square degrees, containing a total of 3000 sources with $S > 10^{-14}$erg s^{-1} cm^{-2}. This would be a very large project!

5.8 Low Luminosity AGN at $2 < z < 3$

I have used an upper limit to luminosity of 3.5×10^{44} erg s^{-1}, which is half the luminosity of the break in the $z > 2$ luminosity function, to define the AGN which lie on the less steep, low luminosity portion, of the luminosity function. The upper and lower panels of Figure 5.3 show the log N - log S of the low luminosity AGN and their redshift distribution, again the colour scale of the redshift distribution is linear and darker areas contain (relatively) fewer sources. A much lower flux limit is required for the low luminosity sources: to detect any sources at all the flux limit must be below 5×10^{-15}erg s^{-1} cm^{-2}. The lower panel clearly shows that to get a reasonable distribution in redshift the flux limit must be as low as 10^{-15}erg s^{-1} cm^{-2}; at any higher flux limit the sample is dominated by objects with redshift close to 2. With a flux limit of 10^{-15}erg s^{-1} cm^{-2} X–ray source confusion is likely to be a problem for *XMM* , but this flux limit is still viable (it is only a factor 2 deeper than the *ROSAT* UK deep survey). The total source population is between 600 deg^{-2} and 1000 deg^{-2} (see Figure 5.1) while the number of low luminosity $2 < z < 3$ AGN is ~ 80 deg^{-2}, i.e. about 10% efficient. To obtain a sample of 100 of these objects would require ~ 1.2 deg^2 which would be expected to contain ~ 1000 sources with

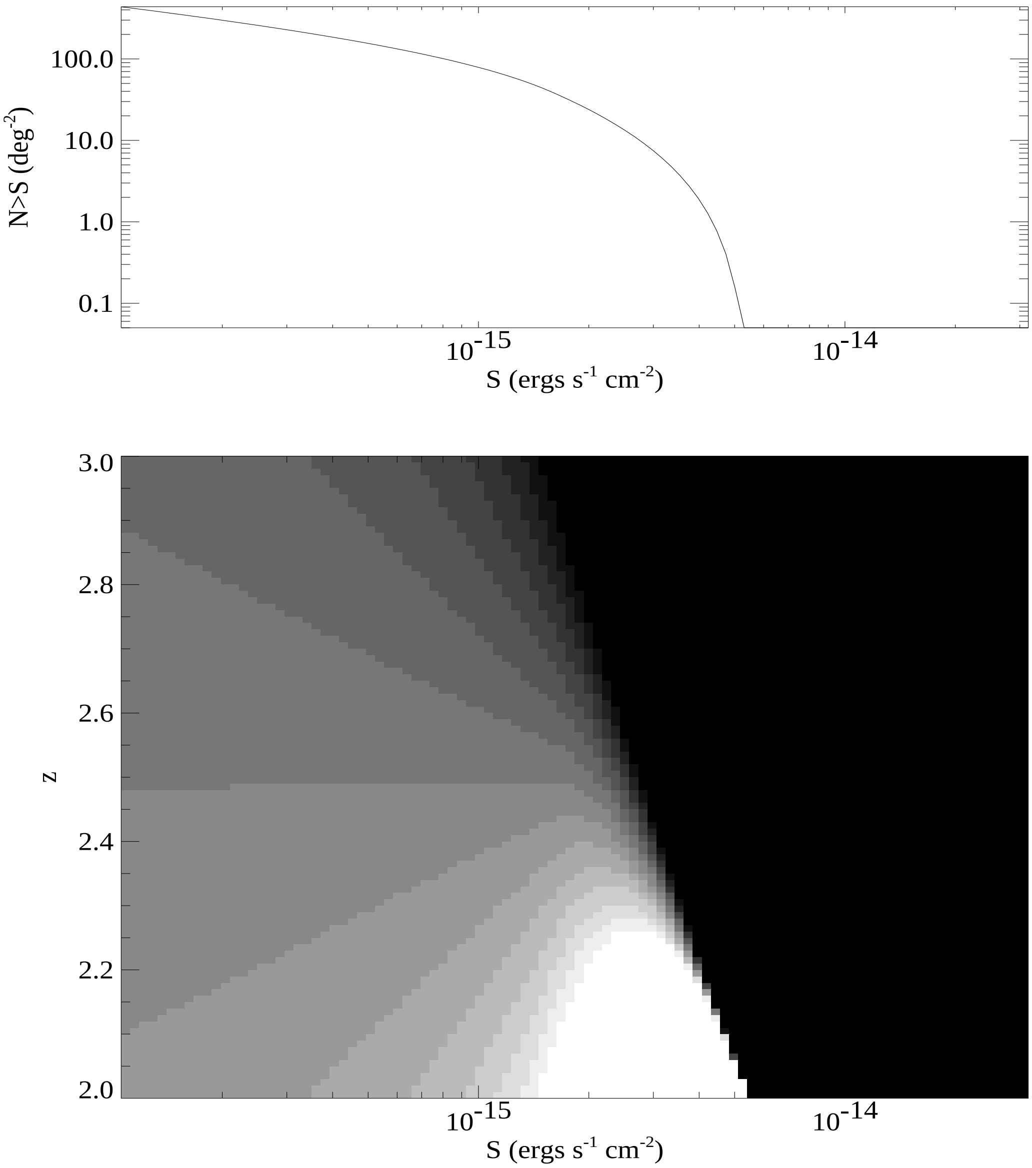

Figure 5.3: Log N - log S of low luminosity ($< 3.5 \times 10^{44}$ergs^{-1}) $2 < z < 3$ AGN (top panel) and the relative redshift distribution as a function of flux limit (bottom panel). Dark colours indicate a lack of sources

$S > 10^{-15}$erg s^{-1} cm^{-2}.

5.9 AGN at $z > 3$

We can not be as selective for AGN with $z > 3$ as for $z < 3$. To detect the very low luminosity objects over a wide redshift range would require a flux limit lower than we can expect to achieve. Although radio and optically selected AGN, with $z > 3$, have been detected at X–ray energies (e.g. Bechtold *et al.* 1994), the number of X–ray selected AGN with $z > 3$ is currently very small (< 10). This means that our knowledge of the XLF and its evolution at $z > 3$ is extremely poor, and identifying even a few objects in future X–ray surveys would be a major improvement. Therefore, I do not split AGN with $z > 3$ into two luminosity groups and instead examine the population as a whole.

Figures 5.4 and 5.5 show the log N - log S and predicted redshift distributions of AGN with $3 < z < 4$ and $4 < z < 5$ respectively.

At 10^{-14}erg s^{-1} cm^{-2}, our model predicts that we will detect 0.6 AGN deg^{-2} with $3 < z < 4$ and 0.1 deg^{-2} with $4 < z < 5$. This is not a practical flux limit to obtain a sample of $z > 3$ AGN, since there are $\sim$ 90 sources deg^{-2} in total at this flux limit. The predicted log N - log S of $3 < z < 4$ AGN flattens at $\sim 10^{-15}$erg s^{-1} cm^{-2}, while the redshift distribution broadens at $< 2\times10^{-15}$erg s^{-1} cm^{-2}. At 10^{-15}erg s^{-1} cm^{-2} the model predicts that there are 70 AGN deg^{-2} with $3 < z < 4$ and 20 AGN deg^{-2} with $4 < z < 5$. These numbers drop to 25 deg^{-2} and 4 deg^{-2} respectively at 2×10^{-15}erg s^{-1} cm^{-2}. The highest flux limit at which the XLF and evolution of $z >$ 3 AGN could be constrained is therefore $\sim 10^{-15}$erg s^{-1} cm^{-2}. Long observations with *AXAF* will probably detect sources fainter than this, and this is probably our only hope of finding objects on the low luminosity part of the XLF at $z > 4$.

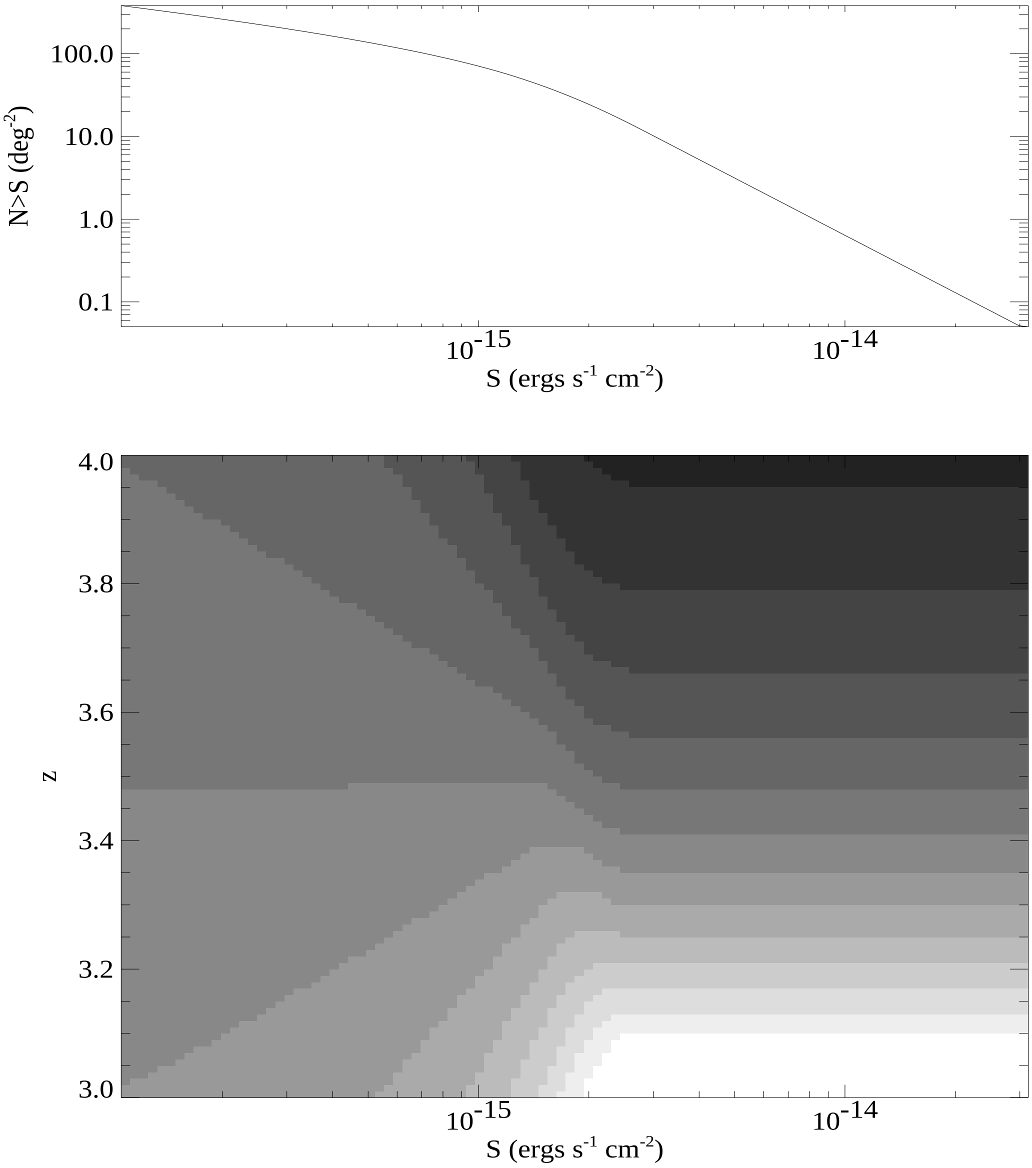

Figure 5.4: Log N - log S of $3 < z < 4$ AGN (top panel) and the relative redshift distribution as a function of flux limit (bottom panel). Dark colours indicate a lack of sources

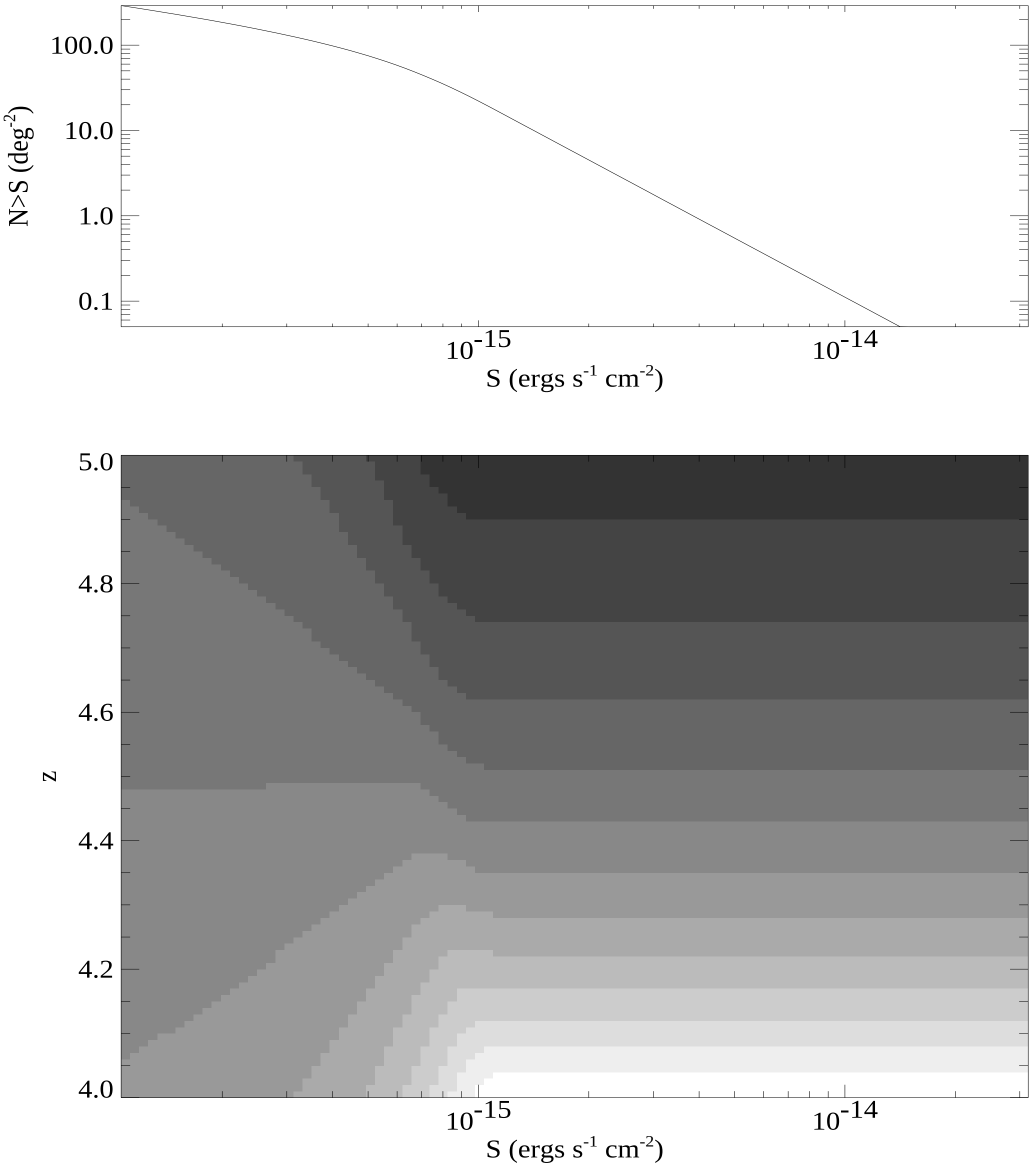

Figure 5.5: Log N - log S of $z > 4$ AGN (top panel) and the relative redshift distribution as a function of flux limit (bottom panel). Dark colours indicate a lack of sources

Chapter 6

The Variable Soft X–ray Spectrum of the Narrow Line Seyfert 1 Galaxy Markarian 766

6.1 Introduction

Studying the X–ray emission from active galactic nuclei allows us to probe deep into their central regions, a few light minutes to a few light days from the central engine. Timing and spectroscopy of the X–ray emission therefore allow us to examine the conditions and environment in which matter accretes onto a massive black hole.

Of particular importance is the soft X–ray band (0.1 – 2 keV) which has been made easily accessible by *ROSAT* . Two principle emission components are found in AGN spectra in this band, a power law which extends to much higher energies (> 40 keV) and an excess at low energies (typically < 0.5 keV). This soft excess may be the high energy tail of the big blue bump, which dominates the bolometric luminosity of most radio quiet AGN (e.g. Walter & Fink 1993, Turner & Pounds 1989). Understanding the mechanism by which the soft excess is produced is therefore essential for the construction of a realistic model of the central regions of AGN.

6.1.1 Models of the X–ray Power Law and Soft Excess

In radio loud AGN, the mechanism responsible for the hard power law is probably synchrotron or synchrotron self Compton radiation from relativistic jets (Shastri *et al.* 1993). This may not be the case for the power law component seen in the X–ray spectra of radio quiet AGN, which are in general softer than those from radio loud objects (Lawson *et al.* 1992). At >5 keV, radio quiet AGN show spectral features (Fe line emission and a hardening of the spectrum above 10 keV, Pounds *et al.* 1990) which suggest that some of the X–rays are reflected from material near the black hole; in MCG 6-30-15, for which high signal to noise *ASCA* data are available, the Fe line is relativistically broadened (Tanaka *et al.* 1995). The X–ray power law component may originate in a hot corona above a relativistic accretion disk so that $\sim 50\%$ of the X–rays generated in the corona shine down on the accretion disk, and are reflected from its surface. In this model the X–ray power law may be due to photons which are originally emitted from the accretion disk itself, and then Compton upscattered either by electrons in a hot plasma (Walter & Courvoisier 1992), or by a non-thermal distribution of relativistic electrons injected into a compact region, in which the radiation density may be so high that photon - photon collisions result in production of electron - positron pairs (Zdziarsky *et al.* 1990).

A number of models have been put forward to explain the soft excess emission of AGN. One obvious model is that the soft excess (and the whole of the big blue bump) is thermal emission from an accretion disk surrounding a supermassive black hole (e.g. Ross, Fabian and Mineshige 1992). Alternatively, the soft excess may be due to reprocessing of the power law component by optically thin clouds that surround the central regions (e.g. Guilbert & Rees 1988), or the surface of an accretion disk (e.g. Ross & Fabian 1993). Reprocessing of the radiation by electron - positron pairs can also produce a soft excess (Zdziarski *et al.* 1990). In the reprocessing models, the soft excess responds to changes in the power law flux, with a time delay related to the distance between the power law emitter and the reprocessing material. If the power law component is caused by Compton upscattering of accretion disk photons, and the soft excess is thermal emission from a hot accretion disk, then the delay between the power law and soft excess components is expected to be in the opposite sense, i.e. the soft excess changes before the power law component. If the soft excess is due to reprocessing of X–rays by electron - positron pairs, time delays between the power law component and soft excess depend on the compactness of the emission region (Done & Fabian 1989).

6.1.2 The Narrow Line Seyfert 1 Galaxy Markarian 766

Narrow line Seyfert 1 galaxies (NLS1s hereafter) are known to have strong soft excesses, (Puchnarewicz *et al.* 1992, Boller, Brandt & Fink 1996) and are therefore obvious candidates for investigating the interrelation between the power law and soft excess components. However, detailed studies of individual objects have tended to concentrate on those with extreme properties, of either abnormally steep soft X–ray spectra and/or unusually large variability, e.g. RE J1034+393 (Puchnarewicz *et al.* 1995), IRAS 13224-3809 (Otani *et al.* 1996), RE J1237+264 (Brandt, Pounds & Fink 1995).

In this chapter I present a study of the X–ray emission of the nearby (z=0.013), radio quiet, NLS1 galaxy Markarian 766. Markarian 766 fell within the field of view of the *ROSAT* PSPC during no less than 9 different observations, was observed at least once in each of the years 1991 to 1994 inclusive, and is a bright PSPC source (1 – 6 counts s^{-1}). The long sampling time scale provides a rare opportunity to study *both* the long and short term behaviour of the source.

Markarian 766 has a significant but not *extreme* soft excess (Boller, Brandt & Fink 1996), and is known to vary in a few hours (Molendi, Maccacaro & Schaeidt 1992); these are essential properties if time delays between the soft excess and power law components are to be investigated within the time scales of individual *ROSAT* observations. It is a strong Fe II emitter (González Delgado & Peŕez 1996) and has significant optical polarization of $> 2\%$ perpendicular to its radio axis (Goodrich 1989).

Results from some *ROSAT* observations of Markarian 766 have already been published. Molendi, Maccacaro & Schaeidt (1993) showed that Markarian 766 varied by a factor of ~ 3 in the two days of observation during the *ROSAT* all sky survey. Molendi & Maccacaro (1992) and Netzer, Turner & George (1994) used pointed *ROSAT* observations and concluded that the variable X–ray spectrum is not the result of a variable warm absorber.

Markarian 766 has recently been observed with *ASCA* (Leighly *et al.* 1996), and was shown to have a variable power law component and a warm absorber (evidenced by absorption edges at $\sim 0.7 - 0.8$ keV). Although a soft excess was detected, it is poorly constrained because *ASCA* is not sensitive to photons with energies < 0.4 keV.

6.2 Observations

Details of the 9 *ROSAT* datasets used in this analysis are given in Table 6.1. I will refer to them as P1, P2, etc.. All data were obtained using PSPC-B, and all data reduction has been carried out using the Starlink ASTERIX package. All observations have been filtered using the same event rate and master-veto rate criteria, and all times with poor aspect solution have been excluded.

Markarian 766 was at the centre of the PSPC field of view during 4 of the observations, and in the remaining 5 it was at different off axis angles, ranging between 13.5 and 43.9 arc minutes (see Table 6.1).

Table 6.1: The 9 *ROSAT* observation datasets used in this analysis

Name	ROR number	start date	start MJD	observation length (seconds)	exposure time (seconds)	offaxis angle (arcmin)	countrate counts/s
P1	RP700221	15 June 1991	48422.0	86246	8313	19.4 *	1.1
P2	RP701203	16 June 1992	48789.2	426470	6563	0.0	3.8
P3	RP701056	18 June 1992	48791.1	419862	7178	43.9 *	2.2
P4	RP701091n00	8 Dec. 1992	48964.6	138240	5871	0.0	3.5
P5	RP701203m01	9 Dec. 1992	48965.1	8640	2597	39.6	3.8
P6	RP700970	21 Dec. 1992	48977.7	149472	14613	13.5	3.3
P7	RP701413	16 Dec. 1993	49337.5	25920	3093	39.0	3.1
P8	RP701353	17 Dec. 1993	49338.9	17280	3044	0.0	2.3
P9	RP701091a01	5 June 1994	49508.8	7600	2703	0.0	6.3

* In these observations Markarian 766 is close to the PSPC ribs

6.2.1 Use of Off axis Observations

The point spread function (PSF) of the *ROSAT* PSPC changes dramatically with off axis angle, hence for the six different detector locations, different regions have been used for collecting source and background counts. Source and background regions were chosen to be at similar off axis angles; they do not overlap with the region obscured by the PSPC rib support structure, and contain no contaminating bright sources. The use of observations with different off axis angles is justified because the dependence of the *ROSAT* PSF with off axis angle is well known except for the very low energy response (Hasinger *et al.* 1994). In observations in which Markarian 766 is far off axis (P3, P5 and P7), large circles (6 arc min radius) have been used as source and background regions to ensure that the majority of the source counts are included.

In two observations (P1 and P3), Markarian 766 was occulted by the ribs of the PSPC. To avoid any systematic errors in the X–ray flux as a function of time, data from all times when the source extraction region entered the ribs have been excluded; in general this means that only a portion of the spacecraft wobble period has been included (*ROSAT* wobbles once every 400 seconds to prevent the detector window wire grid from systematically occulting sources). Note that because I use the *same* part of each spacecraft wobble, this procedure is not expected to introduce significant spurious variability. The effectiveness of this technique was verified using time filtered images and lightcurves folded on the 400 second wobble period of *ROSAT* .

Because of the proximity of Markarian 766 to the ribs in P1 it was necessary to use a small circle of only 0.9 arc min radius to collect source counts, and hence the correction for counts falling outside this circle is much larger for P1 than that for the other observations (see Section 6.3.1). P1 also differs from the other observations in that it took place before the October 1991 change of the gain (and hence spectral response) of the *ROSAT* PSPC-B detector. P1 contains the most time intensive monitoring of Markarian 766, and during P1 Markarian 766 was particularly faint; for these reasons it is a particularly interesting observation and is retained despite the technical difficulties.

6.2.2 Use of the Data

The data are examined in two ways: using data from three broad X–ray bands and spectral fitting at full resolution. Together they allow me to extract the maximum information about the spectral variability of Markarian 766.

I first construct X–ray lightcurves in three energy bands (Section 6.4). Using the lightcurves as a guide, I construct X–ray spectra at six different flux levels (Section 6.5), allowing me to examine the spectral shape of Markarian 766 as it changes in brightness, and determine the contributions of the different emission components to the three X–ray bands. Variations in the three colour lightcurves and hardness ratios are then used to study variability of the emission components (Section 6.6). Finally, I cross correlate the flux in the three different bands to look for temporal relations between the emission components (Section 6.7). This is particularly important as it can test models for the origin of the soft excess and hard power law emission.

6.3 The Three X–ray Bands

The primary purpose for constructing a light curve in three different X–ray bands is to examine how the overall spectrum changes with time. The three bands are therefore required to have energy responses which are as independent as possible to prevent the smearing out of spectral changes when photons of the same energy contribute to the flux in more than one band. With a proportional counter such as the *ROSAT* PSPC, it is impossible to find three energy bands which are *completely* independent. I have chosen the bands R1L, R4, and R7 (channels 11-19, 52-69 and 132-201 respectively) from Snowden *et al.* (1994). They are centred at approximately 0.2, 0.7 and 1.7 keV respectively, and their energy responses overlap with effective areas $< 10\%$ of their peak. Note that with bands this narrow, a large number of PSPC channels (and hence a considerable number of source counts) are excluded; this is acceptable because Markarian 766 is a bright source.

6.3.1 Correction for the PSPC PSF

It was explained in Section 6.2.1 that the *ROSAT* PSPC PSF changes with off axis angle; some fraction of the PSF lies outside the circular region used to collect source counts. It is therefore necessary to renormalise the count rates to the full PSF before data from observations with different off axis angles can be compared. The PSF of the *ROSAT* PSPC depends on energy as well as position. At the energies corresponding to the R4 and R7 bands, the dependence of the PSF with off axis angle is well understood, and is described by the analytic expressions given in Hasinger *et al.* (1994); R4 and R7 count rates have therefore been renormalised using these expressions.

Hasinger *et al.* (1994) do not provide a good description of the PSF at low energies (i.e. the R1L band) because of a problem known as ghost imaging, in which the positions of low pulse height events can be incorrectly determined by the PSPC (see Snowden *et al.* 1994). The counts in R1L have been corrected using a Gaussian fit to the observed R1L PSF in each observation. The 90% statistical error on this Gaussian fit translates to a 5% uncertainty in the corrected R1L flux of observation P1, which has the largest uncertainty because only a small circle is used to collect source counts (see Section 6.2.1). In the other observations the renormalisation of R1 amounts to a change of less than 10%, and hence the uncertainty on the R1L flux from the PSF correction is not likely to be more than a few percent.

6.3.2 Hardness Ratio Definitions

Two hardness ratios have been used to examine spectral changes:

$$HR_{\mathrm{soft}} = \frac{R4 - R1L}{R4 + R1L}$$

$$HR_{\mathrm{hard}} = \frac{R7 - R4}{R7 + R4}$$

Both HR_{soft} and HR_{hard} increase as the spectrum becomes harder.

6.4 The X–ray Lightcurves

To obtain good signal to noise (typically >30), counts in each band have been binned to 5760 seconds (i.e. 1 *ROSAT* orbit).

The X–ray lightcurves in the three X–ray bands for the four years of observation are shown in the top three panels of Figure 6.1; note that the x-axis is not continuous. Markarian 766 exhibits substantial variability (> factor 2 in the R4 and R7 bands) during every observation, excepting observations P5 and P9, which lasted only a single *ROSAT* orbit each. Hardness ratios, computed from the three light curves are shown in the bottom two panels of Figure 6.1. Hardness ratio changes, and therefore changes in the spectral shape, are seen during all the periods of observation (again except P5 and P9 which are too short for the variability to be addressed).

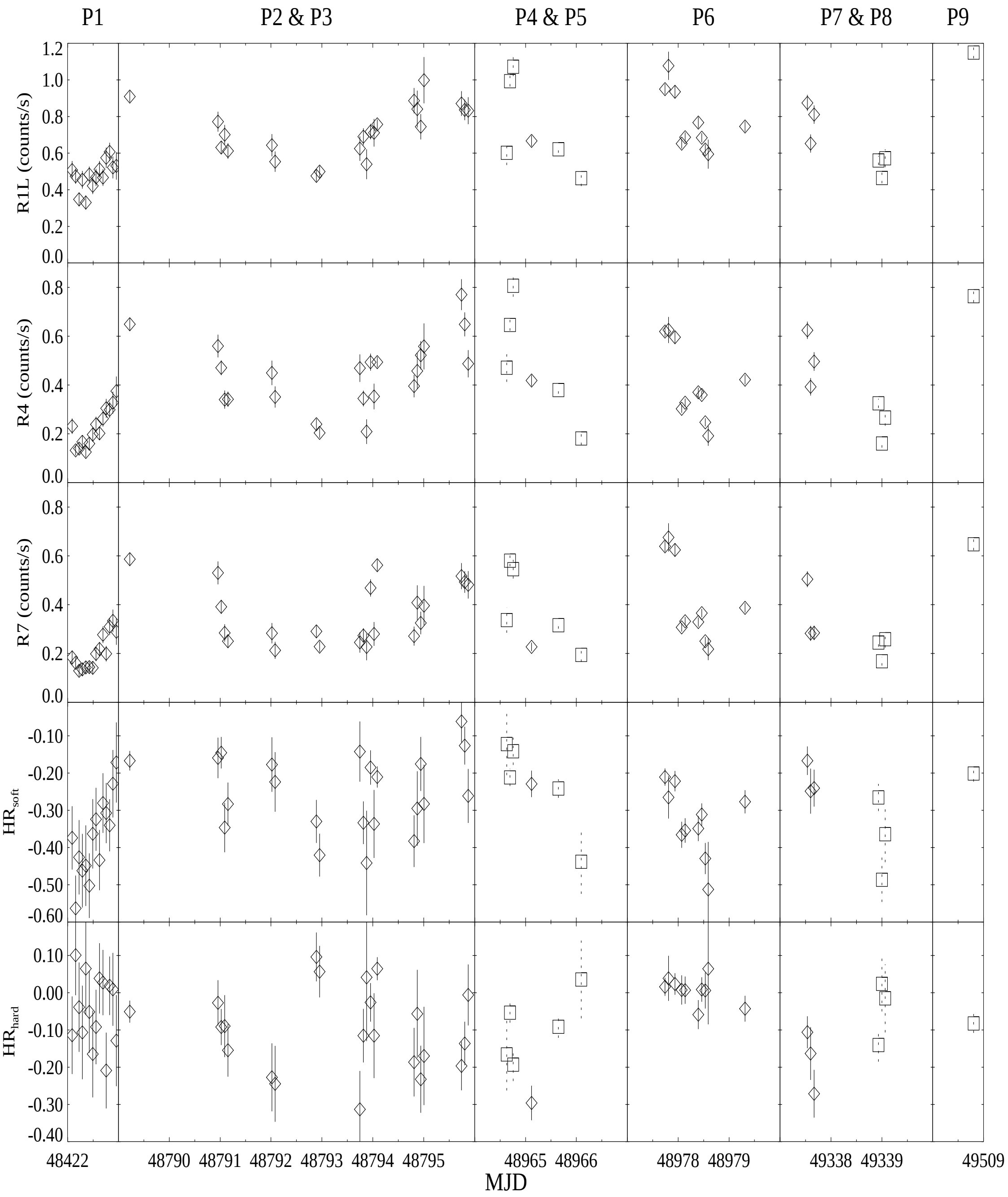

Figure 6.1: Variations in the 3 colour count rates and hardness ratios of Markarian 766 binned in *ROSAT* orbits (5760s). The three observations with low fitted N_{H} are shown as squares with dotted error bars, (see Section 6.5.3) while the rest are shown as diamonds with solid error bars. The vertical divisions indicate breaks between observations; the X–axis has the same scale for all observations.

6.5 Spectral Modelling

6.5.1 Splitting the observations

Before relating the lightcurves and hardness ratio changes to changes in specific components of the X–ray spectrum of Markarian 766, it is necessary to examine the spectrum itself, and obtain a good spectral model.

The variable hardness ratios shown in Figure 6.1 show that the spectrum is changing within the observations. I have extracted several spectra from each observation, that correspond to different levels of brightness of Markarian 766, to explore the full dynamic range of spectral shapes.

Traditionally, the overall *ROSAT* count rate would be used to define the intensity of the source (e.g. Molendi and Maccacaro 1993). This is not practical for the current dataset which includes observations at different off axis angles, because the broadband *ROSAT* count rate is sensitive to the position of the source on the PSPC and it must be convolved with a model spectrum to correct for the proportion of the PSF outside the source extraction circle, because the PSF is energy dependent. To extract spectra as a function of overall *ROSAT* count rate, consistently for each observation, would therefore require a prior knowledge of the spectra to be extracted!

This problem has been avoided by using the R4 count rate to define the intensity of Markarian 766, instead of the broadband count rate. R4 covers a narrow enough energy range that it is easy to correct for the PSF in a consistent way for all observations without a detailed prior knowledge of the spectrum. R7 could equally have been used; R4 has been preferred because it is more central to the *ROSAT* bandpass.

Six different levels of intensity have been defined according to the R4 count rate, and observations have been split up by their R4 count rates averaged in 5760 second bins, as shown in Table 6.2. For each observation, all counts collected during a given range of R4 count rate were combined to make a single spectrum. Up to six spectra were therefore constructed from each observation; as seen in Table 6.2 a total of 31

Table 6.2: Exposure times of spectra taken for different R4 count rates and observations.

Data	time $R4 < 0.2$ (seconds)	time $0.2 < R4 < 0.3$ (seconds)	time $0.3 < R4 < 0.4$ (seconds)	time $0.4 < R4 < 0.5$ (seconds)	time $0.5 < R4 < 0.6$ (seconds)	time $0.6 < R4$ (seconds)
P1	4132	2803	1378	–	–	–
P2	–	1303	543	2856	575	1286
P3	–	216	2466	2874	571	1051
P4	870	–	343	189	–	4469
P5	–	–	–	2597	–	–
P6	165	1315	6683	2585	1502	2363
P7	–	–	1233	896	–	964
P8	1186	1047	811	–	–	–
P9	–	–	–	–	–	2703

spectra were constructed.

I have not combined spectra from different observations because of their different off axis angles and hence effective areas. Having the spectra split by observation also allows some comparison of the long and short term spectral changes. The effective area (as a function of energy) for each spectrum has been normalised to the source count collecting region using the analytical expressions of Hasinger *et al.* (1994).

Spectra were binned in energy with a minimum of 30 counts per bin, and analysed using the spectral fitting program XSPEC ; bad channels (1-7 and > 200 for P1, 1-11 and > 200 for the other observations, as defined in Snowden *et al.* 1994) were ignored and an additional systematic error of 2% assumed for each channel to reflect the uncertainty in the PSPC energy response. As stated above, observation P1 was made before the PSPC gain reduction in October 1991 and hence the spectra from this observation have been fitted using the high gain response matrix; the other observations have been fitted using the low gain response matrix.

6.5.2 Model Fitting

As a starting point for spectral modelling, I use a simple power law model with neutral absorption fixed at the Galactic column of 1.76×10^{20} cm^{-2} (Stark *et al.* 1992). The power law slope and normalisation are fit individually for all 31 spectra. The fitted photon indices α range between 1.1 and 1.7 but the overall fit is very poor ($\chi^2/\nu = 1.8$ for 2342 degrees of freedom), and the residuals show evidence for both a soft excess and additional neutral absorption (see Figure 6.2).

Allowing the absorbing column to vary in each spectral fit results in a significant improvement in the fit ($\chi^2/\nu = 1.3$ for 2313 degrees of freedom) and results in a column which is larger than the Galactic value. The redshift of Markarian 766 is so low ($z = 0.013$), that using a redshifted absorber to represent the additional column instead of $z = 0$ column makes no difference to the goodness of fit or the fitted column; I have verified this using XSPEC .

Addition of a blackbody component to represent the soft excess also results in a significantly better, although still poor, fit ($\chi^2/\nu = 1.2$ for 2280 degrees of freedom) with fixed $N_{\rm H}$. Adding a blackbody component *and* allowing the column to vary results in a good fit, with $\chi^2/\nu = 1.0$ for 2249 degrees of freedom.

A warm (partially ionised) absorber can often mimic the effect of a soft excess in *ROSAT* spectra. Its principal signature in the *ROSAT* band is the presence of absorption edges at 0.74 keV and 0.87 keV (rest energies) from O VII and O VIII respectively. These edges can not be resolved from each other with the *ROSAT* PSPC, and can be approximated as a single edge. It is known that Markarian 766 has a warm absorber from *ASCA* data. Approximating the warm absorber as a single edge in the *ASCA* data resulted in an observed edge energy at 0.75 keV, and to keep the number of fitted parameters to a minimum I have used an edge with a fixed observed energy of 0.75 keV to represent a warm absorber. Substituting the blackbody soft excess with an edge at 0.75 keV, again leaving the neutral column free, results in $\chi^2/\nu = 1.1$ for 2280 degrees of freedom. This is better than the

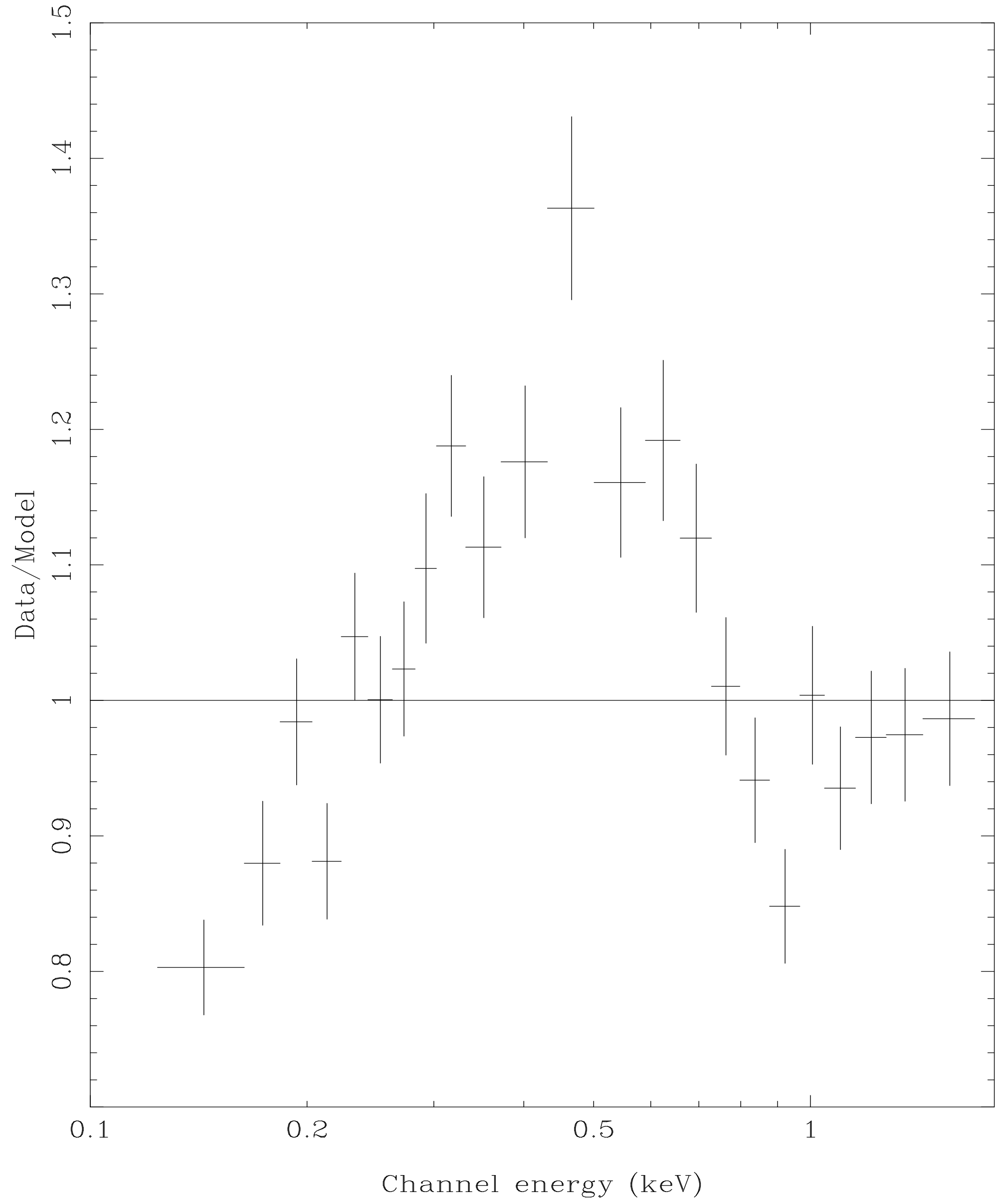

Figure 6.2: Residuals from a power law model (best fit $\alpha = 1.2$) with fixed Galactic $N_{\rm H}$, to the 0.4<R4<0.5 P2 spectrum. Note the residuals at the very lowest energies which are indicative of intrinsic neutral absorption and the bump from 0.3 to 0.7 keV which suggests a soft excess.

fit without the edge, but is much poorer than the fit with a soft excess (the edge model can be statistically rejected with 95% confidence). Including both an edge and a blackbody soft excess results in only a very slightly better χ^2/ν than using just the blackbody soft excess; an F-test shows that the improvement in the fit is not significant.

A good fit to the *ROSAT* spectrum of Markarian 766 therefore requires three components: a power law, a soft excess and some intrinsic neutral absorption.

6.5.3 Absorption

In the previous section I allowed the neutral absorbing column to vary freely between spectra. Neutral material is not expected close to the central regions of an AGN, hence rapid variability of the absorbing material intrinsic to Markarian 766 is not expected. I have therefore fitted the 31 spectra with only a single value of $N_{\rm H}$ for each observation (i.e. 9 values of $N_{\rm H}$), once using a blackbody, once using two black bodies with fixed temperatures of 50 eV and 80 eV (see Section 6.5.5), and once using a bremsstrahlung to represent the soft excess. χ^2 and fitted values of $N_{\rm H}$ are shown in Table 6.3; in each case I find a small reduction in χ^2/ν, compared to that when the column is fitted individually for each spectrum. The F-test shows that for any of these soft excess shapes, allowing $N_{\rm H}$ to vary within each observation does not lead to a significantly better fit than using a single value of $N_{\rm H}$ for each observation, and when the column is allowed a different value for each spectrum within an observation, the values are consistent within the observation. **This shows that there is no detectable change in the neutral absorbing column within any of our observations, regardless of which model is used for the soft excess.**

However, the fitted values of $N_{\rm H}$ in different observations are not consistent with each other.

With a blackbody soft excess, the fitted column for observations P4, P8 and P9

Table 6.3: Fitting of spectra grouped by observation. For each model, χ^2/ν is given by observation and in total. In cases where spectra have been fitted using only a single value of one or more parameter per observation, the parameters are listed in parentheses beneath the model and values are given for each observation. Errors are 68% for one interesting parameter.

Model	P1	P2	P3	P4	P5	P6	P7	P8	P9	Total
Data points	179	412	308	223	87	614	200	158	152	2333
BB	149/164	360/387	324/283	225/203	93/82	593/584	171/185	128/143	138/147	2182/2249
BB	151/166	361/391	326/287	230/206	93/82	595/589	171/187	130/145	138/147	2196/2271
(N_{H})	2.8±0.3	3.0±0.3	3.4±0.3	1.8±0.2	2.9±0.5	3.6±0.2	4.3±0.6	1.8±0.3	2.0±0.2	
BB	155/168	380/395	335/291	249/209	93/82	607/594	172/189	134/147	138/147	2263/2293
(BB_T)	60±5	70±5	69±5	95±5	81±7	63±3	65±6	88±5	100±5	
(BB_L)	3.4±1.5	3.5±1.1	6.2±2.0	2.0±0.4	5.2±1.7	5.9±1.5	10.7±5.5	2.0±0.5	3.3±1.4	
BR	151/166	361/391	331/287	240/206	89/82	592/589	171/187	131/145	149/147	2213/2271
(N_{H})	3.4±0.4	3.4±0.2	4.2±0.4	2.5±0.2	3.5±0.4	4.2±0.2	5.1±0.6	2.6±0.3	2.4±0.2	
2BB	149/166	366/391	335/287	230/206	90/82	590/589	170/187	128/145	139/147	2197/2271
(N_{H})	3.2±0.3	3.3±0.2	4.0±0.3	1.9±0.2	3.4±0.6	4.0±0.2	4.7±0.5	2.0±0.4	2.2±0.2	

BB model spectrum has a power law, a blackbody soft excess and absorption by neutral material
2BB model spectrum has a power law, two black bodies at temperatures of 50 eV and 80 eV
to represent the soft excess, and absorption by neutral material
BR model spectrum has a power law, a bremsstrahlung soft excess and absorption by neutral material
BB_T is the blackbody temperature in eV
BB_L is the blackbody normalisation in units of $10^{37}\mathrm{ergs}^{-1}/D^2$ where D is distance to source in kpc
N_{H} is the neutral absorbing column in units of $10^{20}\mathrm{cm}^{-2}$

are all $N_{\rm H} \leq 2\times 10^{20}{\rm cm}^{-2}$ while the other observations have $N_{\rm H} \geq 2.8\times 10^{20}{\rm cm}^{-2}$. A similar difference in fitted column (between P4, P8, P9 and the other observations) is found when the soft excess is modelled as a bremsstrahlung or as two black bodies (see Table 6.3).

The data from the low column observations (P4, P8, and P9) are shown as squares with dashed error bars while data from the other observations are shown as diamonds with solid error bars on Figure 6.1. In two cases, there is very little time (less than the length of some observations) between observations which apparently have high and low columns: P7 and P8 are separated by only one day, and observation P5 was made during a break in P4. This would appear to contradict the findings above, that there is no detectable short term variability of $N_{\rm H}$.

Other spectral differences are seen between Markarian 766 in the low and high fitted column observations. For example, if the soft excess is modelled as a single blackbody, Markarian 766 has systematically higher fitted blackbody temperatures, but lower blackbody normalisations, in observations P4, P8 and P9, than the other observations (see Figure 6.3). The difference in spectral shapes can be illustrated by comparing the residuals of a power law fit with neutral absorption fixed at the Galactic value for observations P9 (Figure 6.4) and P2 (Figure 6.2), as in both cases the best fit power law has a slope of $\alpha = 1.2$. The residuals seen in observation P9 have a different shape to those of observation P2. There is no physical reason why the neutral column to Markarian 766 should be related to the temperature of the soft excess.

I have tested that the difference in fitted columns is not caused by ghost imaging and consequently inadequate PSF correction at low energy, by refitting all the spectra and excluding all PSPC channels below 20. Although the best fit column values change slightly, and the uncertainty on the fitted column increases, the observations are still divided between high and low column as before. Furthermore, the PSF is the same in the low column observations P4, P8 and P9 as the PSF in P2 which has a high fitted column (all four observations had Markarian 766 at the centre of the

PSPC). It would therefore seem very unlikely that the difference in fitted column is related to inadequate correction for the energy dependent PSF.

Therefore, since there is no other satisfactory solution, **the change in fitted column is interpreted as a calibration problem with the *ROSAT* PSPC**.

6.5.4 PSPC Calibration Uncertainties

There are known PSPC calibration problems. Before I began the work presented in this chapter, it was known that the gain of the *ROSAT* PSPC has drifted over the course of the mission (Turner 1993). While this work was underway, Snowden *et al.* (1995) found that the drift of the PSPC gain is position dependent, i.e. the gain has changed differently at different positions on the PSPC. The largest gain change is found at the centre of the detector. Software is now available (at the time of writing) in the FTOOLS package which is intended to correct PSPC data for spatial/temporal gain changes by interpolating between calibration Al Kα detector maps which have been produced for a number of epochs during the *ROSAT* mission. However, much *ROSAT* data (including some of the Markarian 766 datasets) has yet to be released in FTOOLS compatible format, and a new response matrix (not yet available) is required for the corrected PSPC data.

I have fitted the spectra of two other bright objects which are in the same *ROSAT* field as Markarian 766 during observations P2, P4, P8 and P9, to investigate the change in fitted column caused by temporal/spatial gain changes. They are located 20 and 44 arc minutes from the centre of the PSPC. I have used a power law plus blackbody and neutral absorber model to fit the spectra which were binned to a minimum of 30 counts per bin (exactly the same as for Markarian 766). The fits were acceptable ($\chi^2/\nu = 149/147$ and $494/435$), but in contrast to the fitting results for Markarian 766, the best fit column densities found for the two objects during observations P4, P8 and P9 were no lower than during observation P2. However, a large change in the response near the centre of the PSPC is seen when comparing two

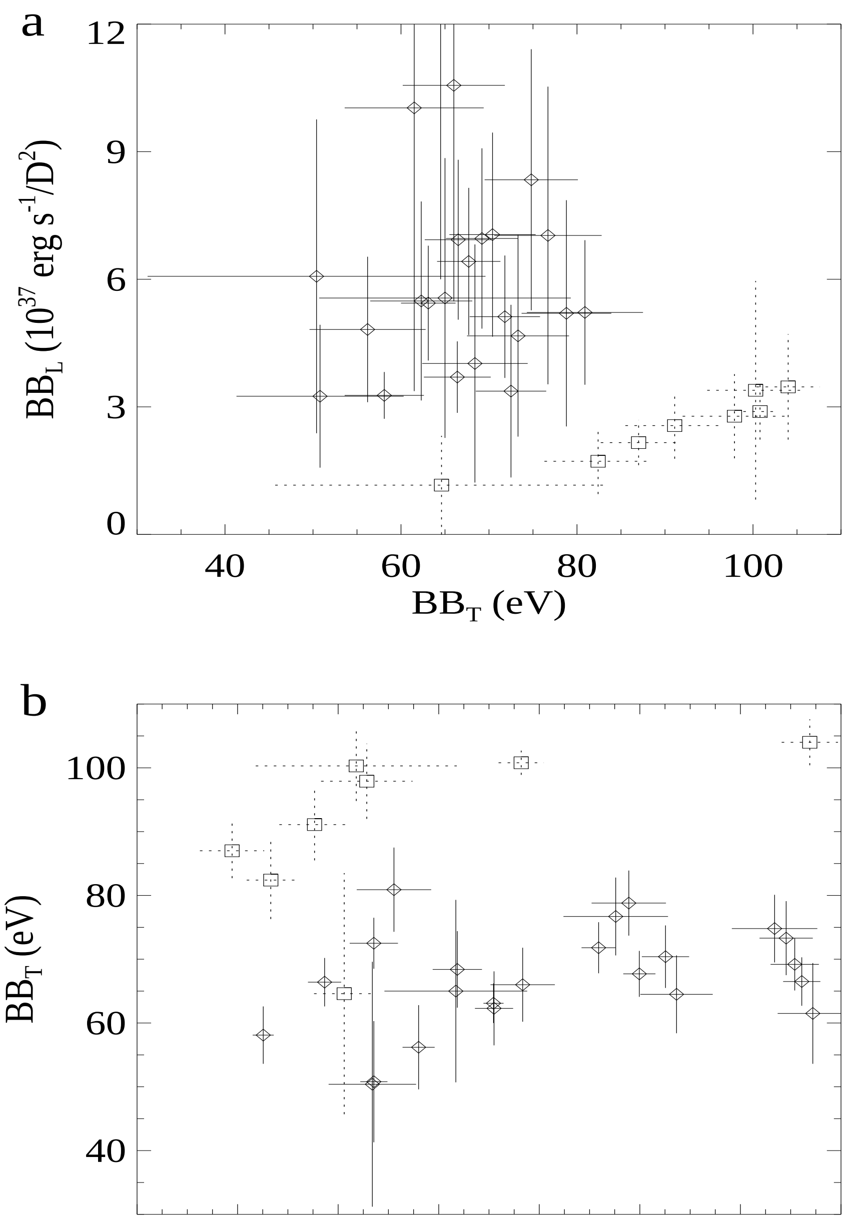

Figure 6.3: Best fit parameters for a blackbody soft excess. All spectra from a single observation have been fit simultaneously with a single value for the neutral absorbing column (see Table 6.3). Errors shown are 68% for one interesting parameter.

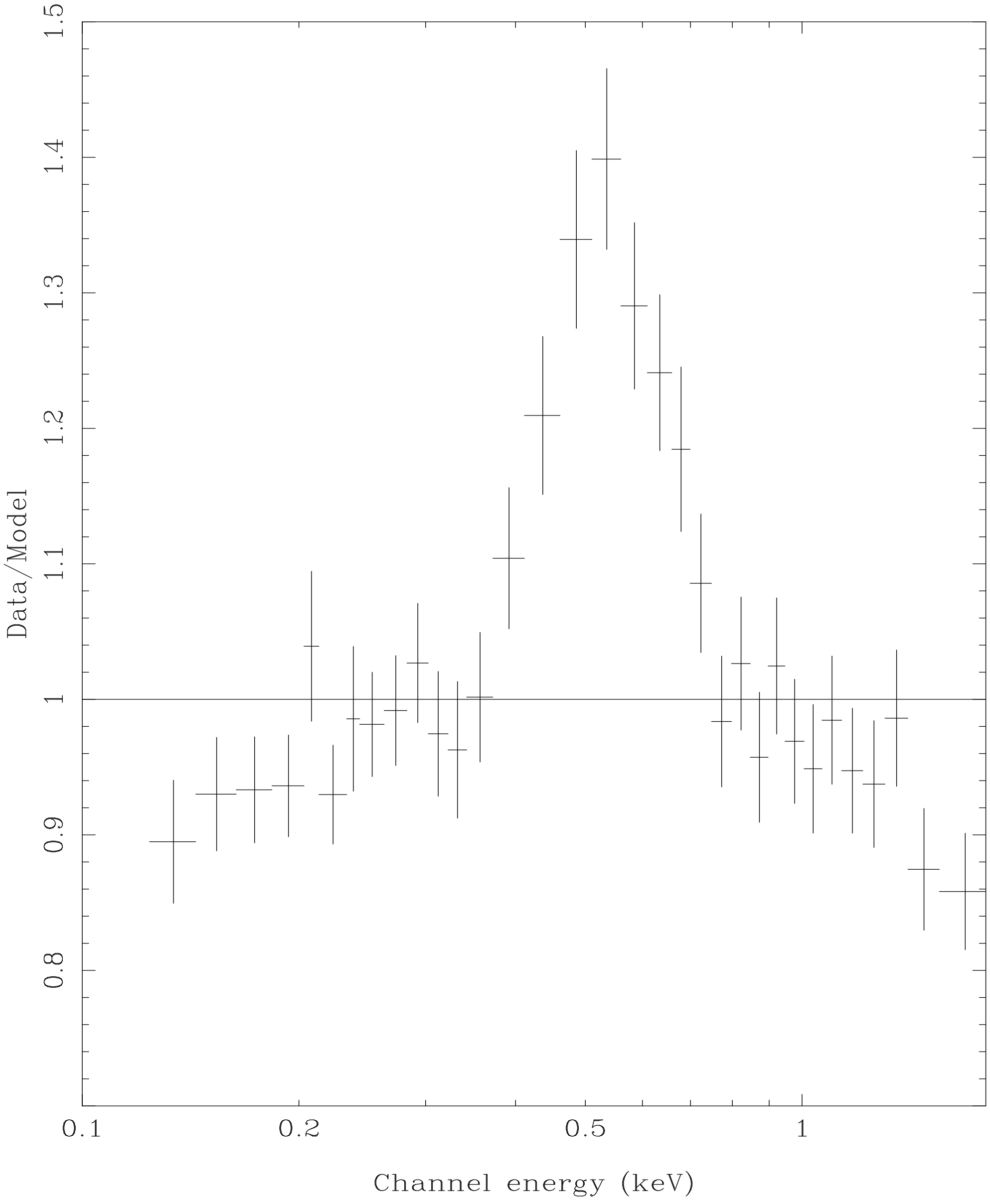

Figure 6.4: Residuals from a power law model (best fit $\alpha = 1.2$) with fixed Galactic N_{H}, to the P9 spectrum. Note that the residuals are found at higher energies than for the P2 spectrum shown in Figure 6.2.

observations of the galaxy cluster (a constant source) A2199 (J.P.D.Mittaz, private communication). A model was fitted to the first spectrum; the ratio of the data from both observations to this model is shown in Figure 6.5. The observed response change (an increase of very low energy counts, and a lack of counts around 0.4 keV) in the later observation is compatible with the different shape of the residuals shown in Figures 6.2 and 6.4 for Markarian 766, supporting the hypothesis that the apparent change in Markarian 766's column is caused by the spatial/temporal gain change of the PSPC.

These results are consistent with the long term gain change being relatively unimportant except at the centre of the PSPC. I will assume that the published response matrices are not appropriate for observations P4, P8, and P9; spectral fitting of these observations will consequently not be used to examine the shape of the soft excess.

6.5.5 The Shape of the Soft Excess

Several models were tried for the soft excess component, and the lowest χ^2 was found for a single blackbody. A bremsstrahlung model for the soft excess has only a slightly higher χ^2 than the blackbody model but is poorly constrained for the low count rate observations with a best fit temperature < 100 eV. Two blackbodies with fixed temperatures at 50 eV and 80 eV, approximately the lowest and highest temperatures found for the single blackbody (see Figure 6.3), were fitted to represent a broader shape than a single blackbody. Again the χ^2 is slightly poorer for this model than for a single blackbody. These models are all acceptable fits to the data, with $\chi^2/\nu = 1.0$; it is not possible to distinguish between them using goodness of fit.

However, it is possible to discriminate between them by examining the behaviour of the power law component when the soft excess is described by different models. The power law parameters for bremsstrahlung and blackbody soft excess models

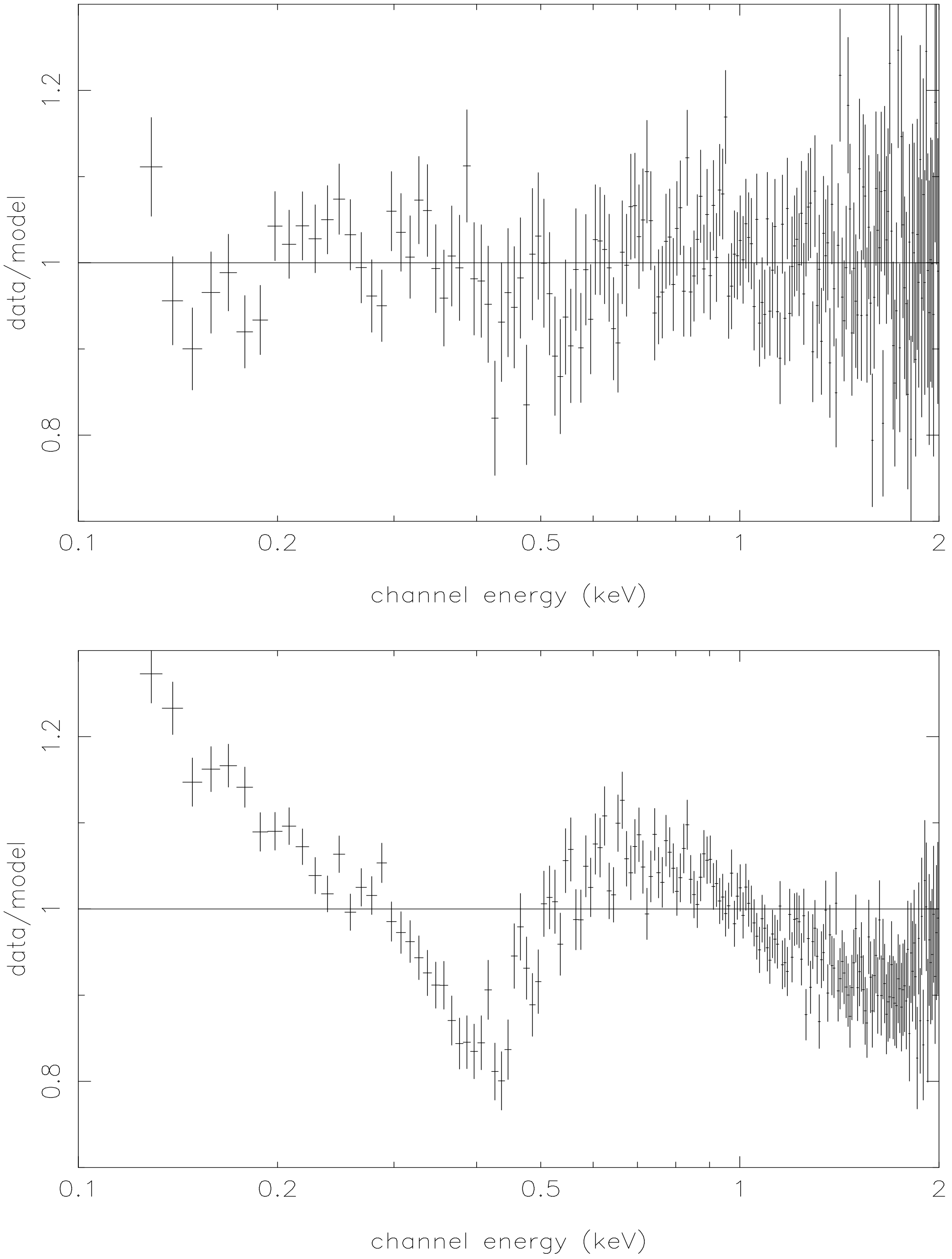

Figure 6.5: Model/Data for two *ROSAT* PSPC spectra of the galaxy cluster A2199. The model was fitted to the early (1991) PSPC spectrum and the residuals are shown in the top panel. The bottom panel compares the same model with data from a late (1993) PSPC observation. *ROSAT* was centred on A2199 in both observations and in both cases data were taken from the same region at the centre of the PSPC. Courtesy of J.P.D. Mittaz.

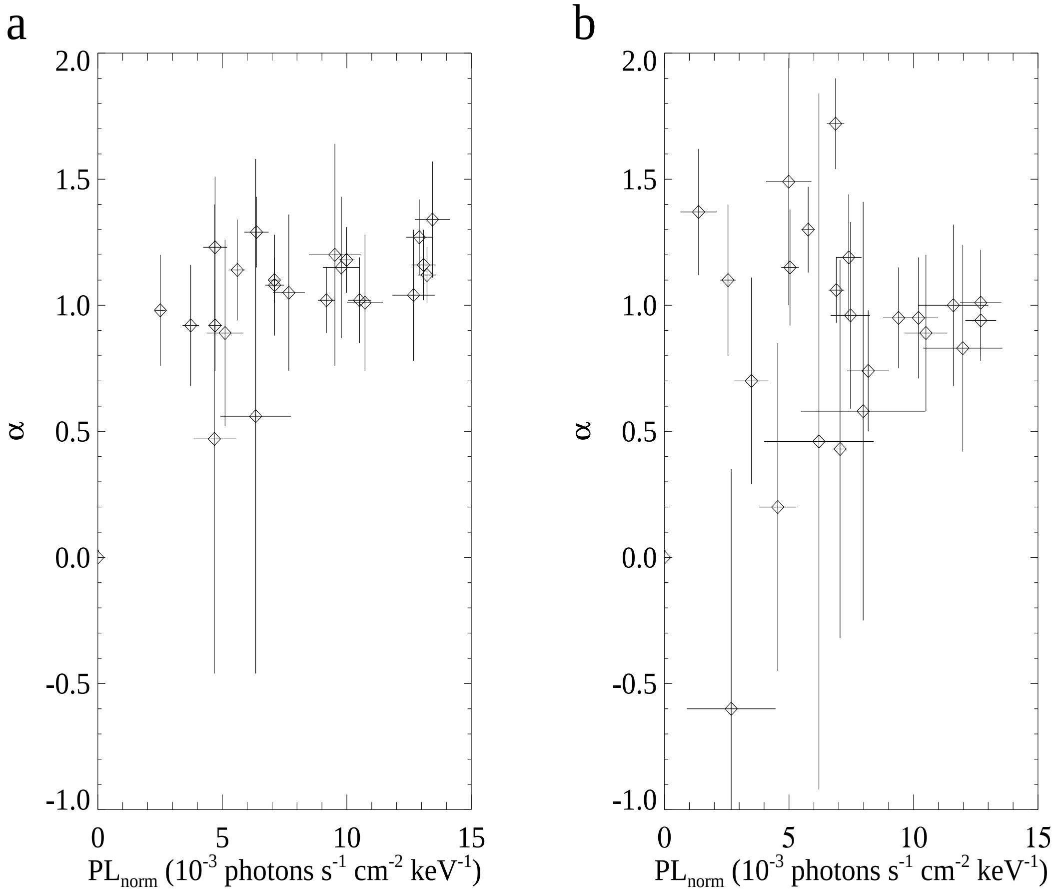

Figure 6.6: Behaviour of the power law component when the soft excess is modelled with (a) a blackbody shape and (b) a bremsstrahlung shape.

are compared in Figure 6.6. If the soft excess is modelled as a bremsstrahlung, the power law spectral index shows a very large dispersion, from very soft ($\alpha = 1.7$) to very hard ($\alpha < 0$). The dispersion in spectral indices is much smaller when the soft excess is modelled as a blackbody, and is consistent with $1.4 < \alpha < 0.8$. When the soft excess is modelled as two black bodies, the behaviour of the power law component is qualitatively the same as for a single blackbody (Figure 6.6a) but with a slightly harder power law slope (α is reduced by ~ 0.2 on average). The observations of Markarian 766 using the ME experiment on *EXOSAT* (Molendi, Maccacaro and Schaeidt 1993), show values of spectral index range from $\alpha = 0.5$ to $\alpha = 1.2$, and the *ASCA* observation of Markarian 766 (Leighly *et al.* 1996) shows spectral indices of $\alpha = 1.0$ and $\alpha = 0.6$. Both *ASCA* and *EXOSAT* ME observations are affected little by the soft excess (which barely enters their energy passband), so provide power law slopes which do not depend on the shape of the soft excess. The large dispersion of spectral slopes when the soft excess is modelled as a bremsstrahlung is not found in higher energy data, indicating that a narrower shape for the soft excess is more likely. Modelling the soft excess as a blackbody results in power law slopes which are a little softer (by $\Delta\alpha \sim 0.2$) than those seen in *ASCA* and *EXOSAT* data, but with a similar dispersion of slopes. Using two black bodies to represent the soft excess also results in a good agreement between the range of power law slopes found with *ROSAT* and the range of power law slopes found in *ASCA* and *EXOSAT* observations.

6.5.6 The Spectral Model Translated to the Three X–ray Bands

The three X–ray bands R1L, R4 and R7 will be used in the next section to interpret the spectral variability of Markarian 766 in terms of variability of the soft excess and the power law components. The spectral modelling described above allows separate estimates of the count rates in all three bands to be determined for both the two components.

When the soft excess is modelled as a blackbody, its temperature never exceeds 90 eV. A blackbody component at 90 eV or less has an R7 count rate which is over 100 times smaller than the R1L and R4 count rates, even when attenuated by a neutral absorbing column of $3 \times 10^{20}\mathrm{cm}^{-2}$. Similarly, when the soft excess is modelled as two black bodies, the contribution to R7 is negligible. Even when the soft excess is modelled using the much broader bremsstrahlung shape, the highest fitted bremsstrahlung temperature (0.22 keV) leads to an R7 count rate which is 15 times smaller than the R1L or R4 count rates. An important result from the spectral modelling is therefore that the soft excess in Markarian 766 produces a negligible contribution to the R7 count rate.

In the following section I assume a blackbody shape for the soft excess, and a neutral column of $3\times10^{20}\mathrm{cm}^{-2}$. The detailed shape of the soft excess does not matter for the variability study because the soft excess is only observed in the two bands R1L and R4: changing the black body temperature changes the contribution of the soft excess to R4 relative to R1L. The mean fitted blackbody temperature is $\sim$ 70 eV when observations P4, P8 and P9 are excluded (see Figure 6.3). A blackbody of this temperature, absorbed by $3 \times 10^{20}\mathrm{cm}^{-2}$ of neutral, material produces an R1L/R4 ratio of 4/1.

Therefore, spectral modelling indicates that the soft excess will provide the majority of its contribution in the R1L band. The power law component must dominate the R7 band, and probably dominates the R4 band as well.

6.6 Three Colour and Hardness Ratio Variability

I now return to the lightcurve and hardness ratios shown in Section 6.4. In light of the spectral modelling results presented in the previous section, the variability in the three X–ray bands R1L, R4 and R7 is examined and related to variability of the power law and soft excess components. Each observation will be examined separately to ensure that the results are robust against the different positions that Markarian 766 has on the PSPC in different observations, and to ensure that the temporal/spatial uncertainty in the PSPC gain has a minimal effect. Variability in observations P5 and P9 can not be examined in detail because they were only a single *ROSAT* orbit (5760 seconds) in duration.

The count rates in the three X–ray bands are strongly correlated with each other, both between and within the observations, as shown in Figure 6.7. When data from all the observations are combined, the probability that any of the pairs of bands are not correlated is $< 10^{-18}$; the dashed lines in Figure 6.7 are the best fitting straight lines to the (R4,R1L), (R7,R1L), and (R7,R4) relations, and comparison with data from individual observations reveals that the source always varies in a similar fashion. Treating the dashed lines as crude estimates of the (R4,R1L), (R7,R1L), and (R7,R4) relations, it is seen that when R7=0 (i.e. the power law component has disappeared) there is still considerable flux ($\sim$ 0.2 counts/s) in the R1L band. The same is true when R4=0, but the dashed line for (R7,R4) passes closer to (0,0). **This 'residual' flux in R1L betrays the presence of the soft excess, and confirms that it peaks in the R1L band.**

6.6.1 Changes in the Spectrum

The simplest model to explain the variability of the three colour fluxes described in the previous section is that the power law is variable and the soft excess is constant. The variability can be examined in more detail by comparing hardness ratios with count rates in the three bands, and allows questions to be asked such as whether

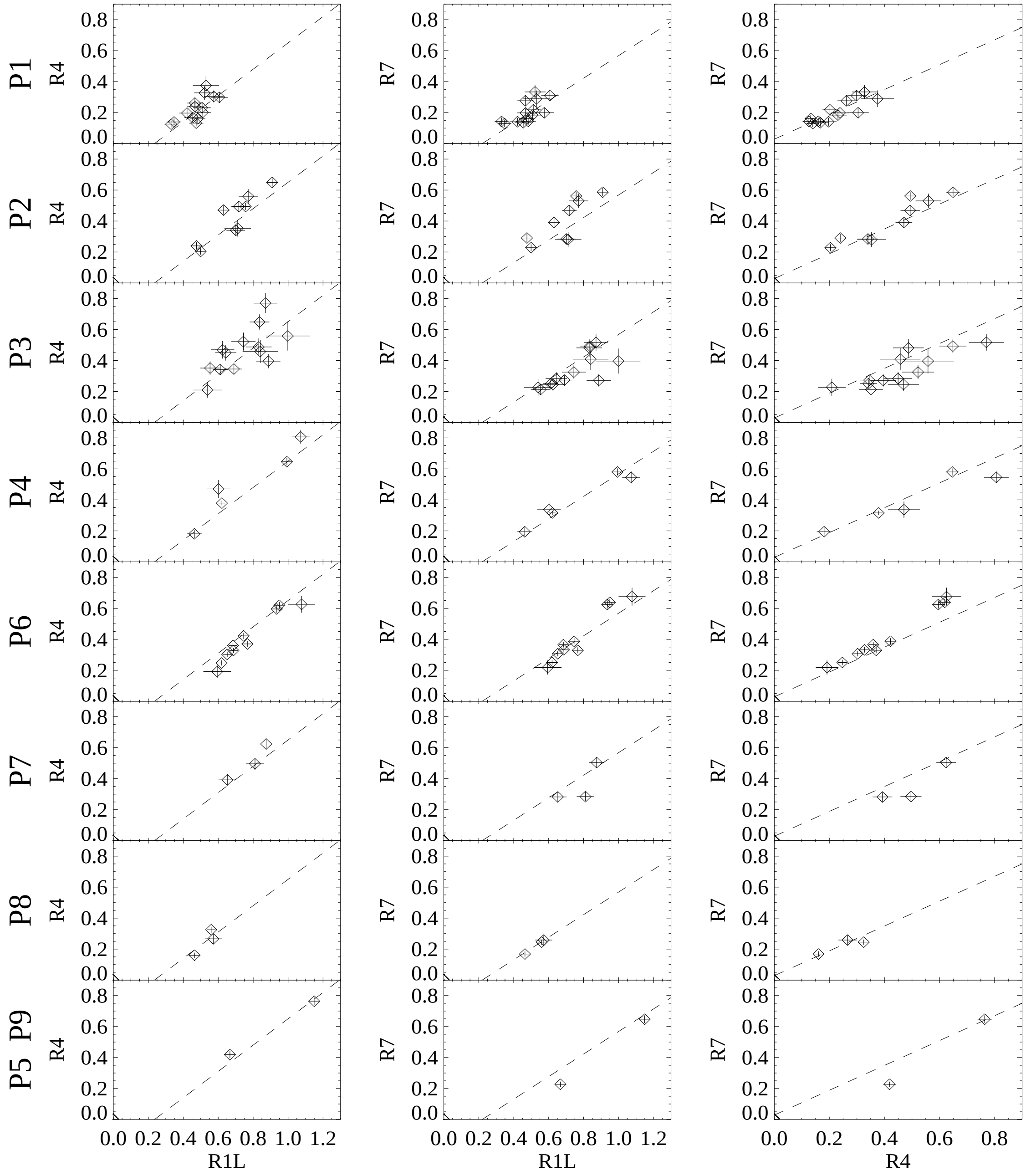

Figure 6.7: Comparison of the countrates for Markarian 766 in the 3 X–ray bands R1L, R4 and R7. Each observation is shown separately, except P5 and P9 which are shown together. The same dashed lines are plotted for each observation, and represent linear fits to the combined 3 colour data from all the observations.

the change in power law flux is accompanied by a change in power law slope, and whether variability of the soft excess, as well as variability of the power law, is required by the data. The most robust comparisons are between HR_{hard} and R1L, and between HR_{soft} and R7. R1L is not used in the calculation of HR_{hard}, hence the errors on the two quantities are independent; similarly for R7 and HR_{soft}. I will examine changes in hardness ratios within the five longest observations: P1, P2, P3, P4 and P6; the other observations have too few data points to examine properly hardness ratio changes.

From the spectral modelling performed in Section 6.5, one can estimate the extent of parameter space which requires investigation. Figure 6.3 shows that when the soft excess is described as a blackbody, the data are consistent with a temperature BB_T between 60 eV and 80 eV, and a normalisation BB_L between 3 and 9 ($\times 10^{37}$erg s$^{-1}/D^2$ where D is the distance to Markarian 766 in kpc). Figure 6.6a shows that my spectral modelling is consistent with power law slopes α between 0.7 and 1.3.

The hardness ratios are plotted in Figure 6.8 and repeated in Figures 6.9 and 6.10. Each solid curve is the expected locus of hardness ratios for pure flux variability (i.e. no change in slope) of the power law component, with a constant blackbody soft excess; curves are provided for a range of soft excess temperatures in Figure 6.8, soft excess normalisations in Figure 6.9 and power law slopes in Figure 6.10. Note that I have made no attempt to 'fit' the data in this section.

The relation between HR_{soft} and the R7 count rate can be reproduced well by pure flux variability of the power law. For any combination of soft excess parameters and power law slopes, power law flux variability predicts that HR_{soft} should increase with R7, which is the observed behaviour.

However, pure flux variability of the power law predicts that HR_{hard} is a monotonically increasing function of R1L count rate. This does not match the observed behaviour of HR_{hard}, which *does not* increase with R1L for R1L < 0.8 as seen in Figures 6.8 to 6.10. The relation between HR_{hard} and R1L can be reproduced by a

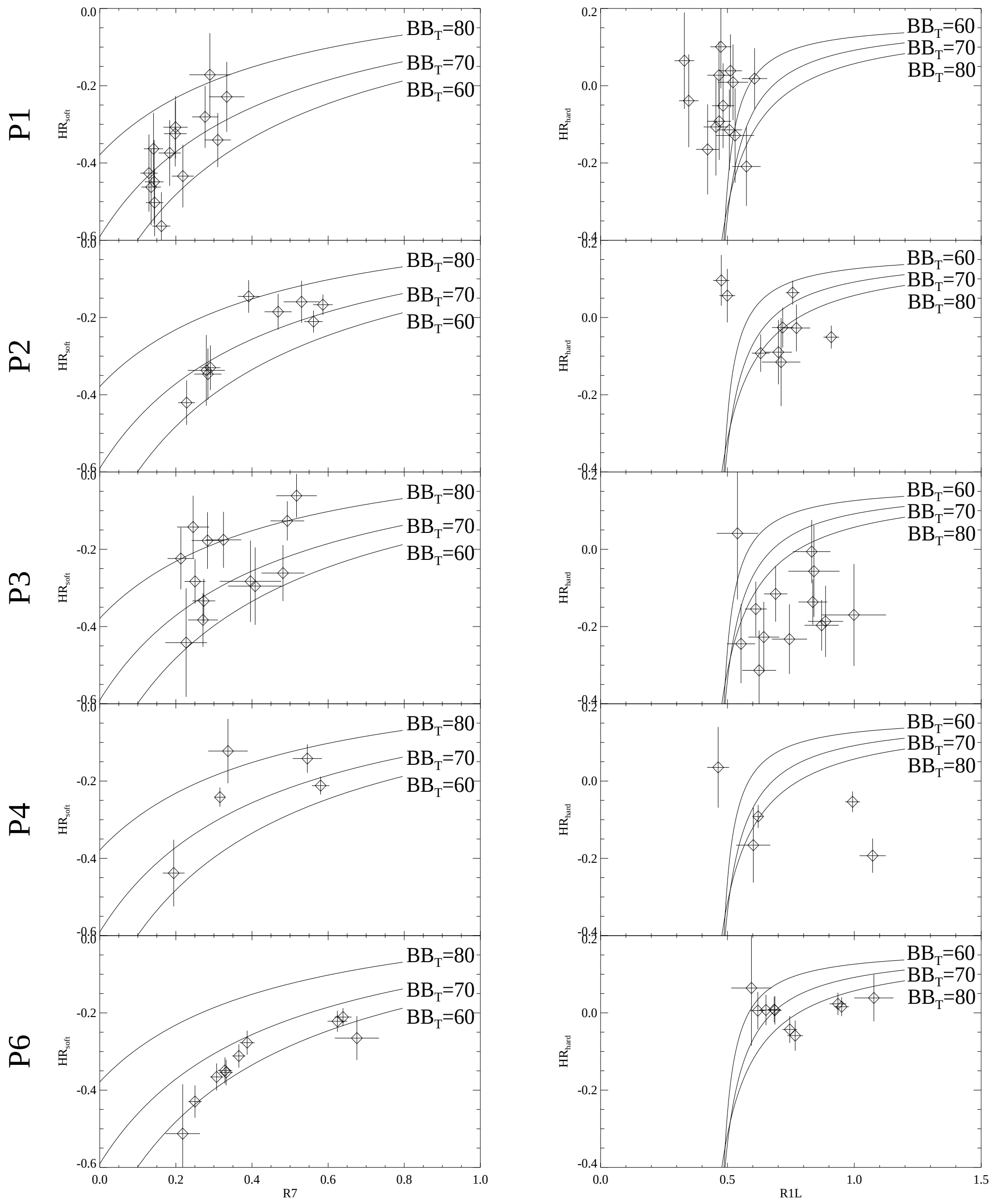

Figure 6.8: HR_{soft} as a function of (hard) R7 countrate and HR_{hard} as a function of (soft) R1L countrate. The model curves are for flux variability of a $\alpha = 1$ power law; the soft excess has normalisation $BB_L = 6 \times 10^{37}$ergs$^{-1}/D^2$ (where D is the distance in kpc), and temperature BB_T in eV as indicated on the curves.

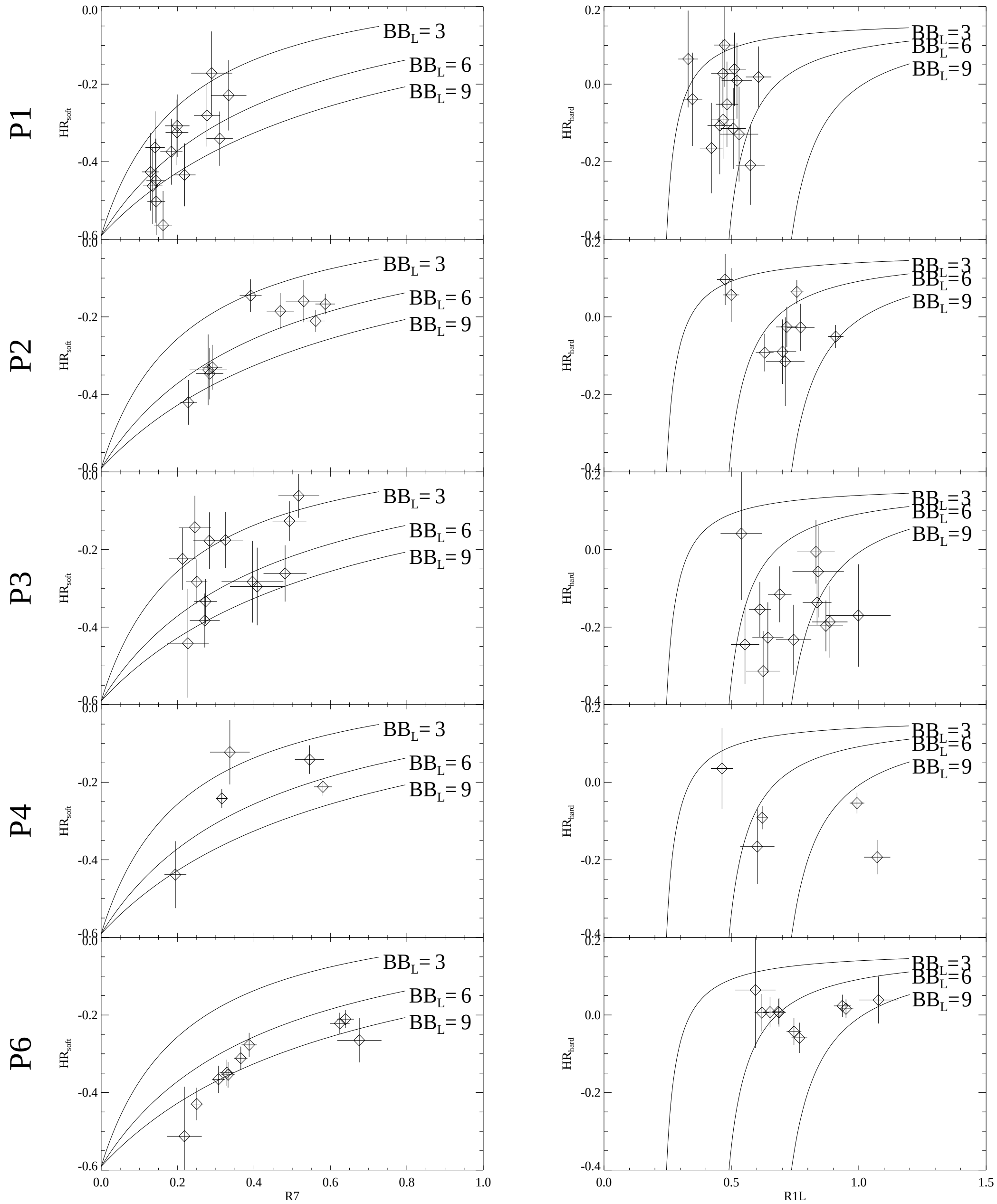

Figure 6.9: HR_{soft} as a function of (hard) R7 countrate and HR_{hard} as a function of (soft) R1L countrate. The model curves are for flux variability of a $\alpha = 1$ power law; the soft excess has a temperature of 70 eV and normalisation BB_L (in units of $10^{37} ergs^{-1}/D^2$ where D is the distance in kpc), as indicated on the curves.

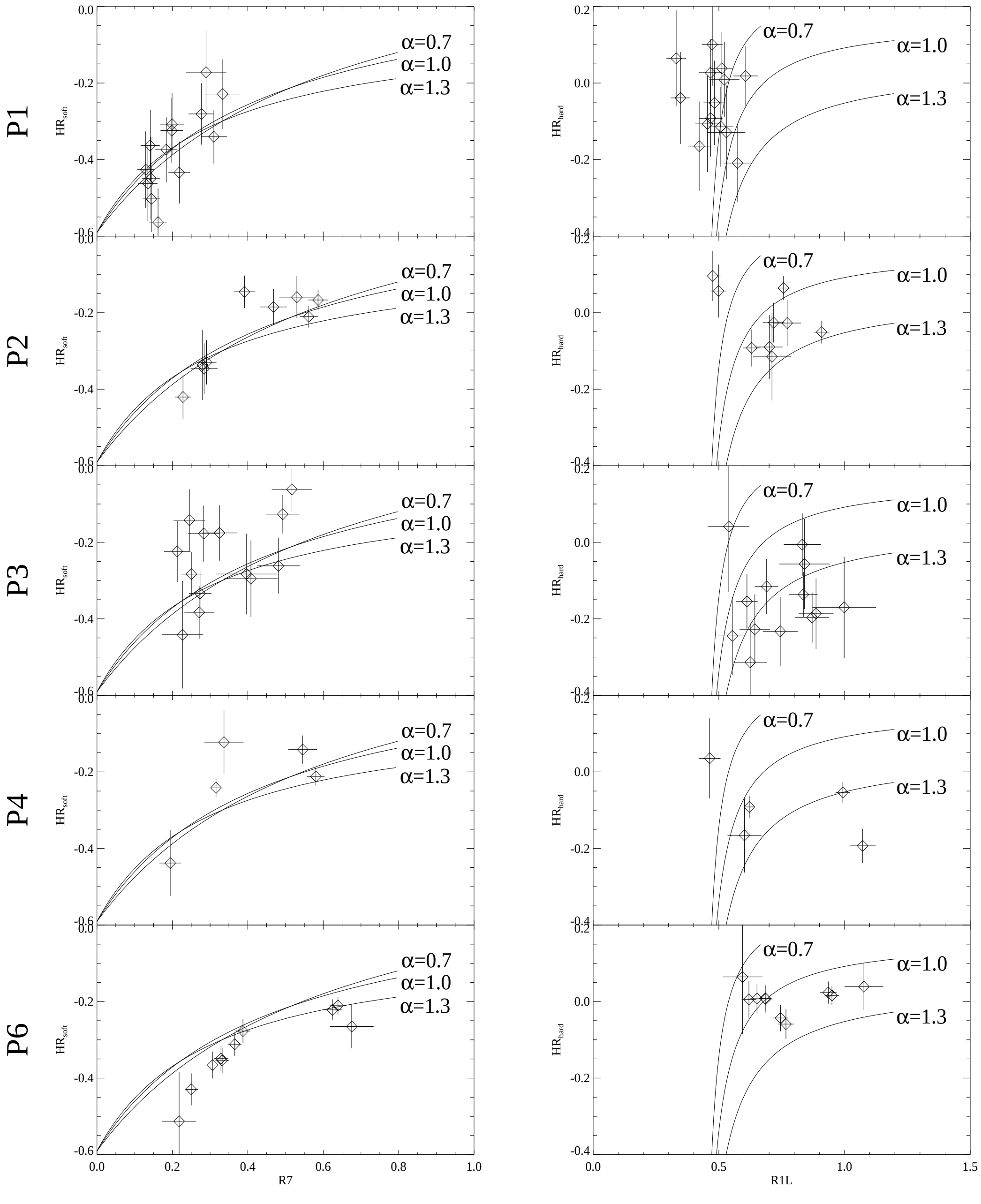

Figure 6.10: HR_{soft} as a function of (hard) R7 countrate and HR_{hard} as a function of (soft) R1L countrate. The model curves are for flux variability of power laws with slopes $\alpha = 0.7$, $\alpha = 1.0$ and $\alpha = 1.3$. The soft excess has temperature $BB_T = 70$ eV and normalisation $BB_L = 6 \times 10^{37} ergs^{-1}/D^2$ (where D is the distance in kpc).

Table 6.4: Normalised variability amplitude in the three X–ray bands for each of the observations.

ROSAT pointing	number of points	R1L variability amplitude (%)	R4 variability amplitude (%)	R7 variability amplitude (%)
P1	14	12	32	31
P2	9	19	34	33
P3	13	17	29	29
P4	5	35	48	41
P6	10	20	38	40
P7	3	13	22	35
P8	3	9	32	19

steepening of the power law with increasing power law flux (see Figure 6.10) and/or an increase in the blackbody normalisation (see Figure 6.9) with increasing power law flux.

6.6.2 Variability Amplitude

A simple means of examining the variability of the different spectral components is to compare the variability amplitude in the three X-ray bands. For this I have used the normalised variability amplitude, which is defined as the standard deviation σ_{int} divided by the mean count rate. This is corrected for measurement errors by assuming that

$$\sigma_{int}^2 = \sigma_{obs}^2 - \sigma_{err}^2 \tag{6.1}$$

where σ_{int} is the true standard deviation, σ_{obs} is the observed standard deviation, and σ_{err} is the measurement error (see Edelson 1992).

The variability amplitude in the three bands is shown in Table 6.4. In *every* observation the variability is smaller in the R1L band than in either R4 or R7. This shows that the more variable component is the power law, which dominates the flux in R4 and R7 bands; the reduced variability amplitude in R1L is due to the relatively invariant soft excess diluting the overall (power law + soft excess) R1L variability. **This means that to explain the hardness ratio variability in Section 6.6.1, the power law slope must vary.** The soft excess does not undergo substantial (e.g. factor 2) variability over the time scale of an observation ($\leq$ 1 week), but smaller amplitude variability of the soft excess can not be ruled out.

6.7 Cross Correlation Analysis

If the soft excess and power law components are emitted from physically distinct regions near the centre of Markarian 766, then some time delay is expected between changes in the two components, and can be used to distinguish between different models for their production (see Section 6.1.1).

The time dependence of changes in the soft excess and power law components has been studied by cross correlating the count rates in the three bands using the discrete correlation function (DCF hereafter, see Edelson and Krolik 1988).

The DCF for the R1L and R4 lightcurves is defined as

$$\mathrm{DCF}(\tau) = \frac{1}{M}\sum\frac{(R1L(t) - < R1L >)(R4(t+\tau) - < R4 >)}{\sigma_{R1L} \quad \sigma_{R4}}$$

where the sum is made over all M values of t for which there is a measurement of R1L at time t and a measurement of R4 at time t+τ. $< R1L >$ and $< R4 >$ are the mean R1L and R4 count rates respectively; σ_{R1L} and σ_{R4} are the standard deviations of the R1L and R4 count rates respectively and have been corrected for measurement error using equation 6.1 in Section 6.6.2. The standard error on the DCF is defined as

$$\sigma_{DCF}(\tau) = \frac{1}{M-1}\sqrt{\sum\left[\frac{(R1L(t) - < R1L >)(R4(t+\tau) - < R4 >)}{\sigma_{R1L} \quad \sigma_{R4}} - DCF(\tau)\right]^2} \tag{6.2}$$

The DCF is similarly defined for any combination of R1L, R4 and R7. This method is appropriate to our *ROSAT* data since it requires no interpolation, and provides simple error estimates.

ROSAT wobbles with a period of 400s, preventing the wire grid of the PSPC window from permanently masking sources; 400s is the smallest time binning which does not introduce spurious variability associated with the spacecraft wobble. Hence lightcurves with 400s time bins have been cross correlated. Due to the orbital interruptions in *ROSAT* observations the number of pairs available for cross correlation is very small for time differences greater than 1200 seconds. Only the five longest observations have been used: the others are too short to provide a useful number of pairs for cross correlation.

The results of the cross correlation analysis are shown in Figure 6.11 The error bars are 68% as given by equation 6.2 above. The cross correlation was intended to reveal whether changes in the soft excess component preceded changes in the hard power law or vice-versa. The time bins are the same for all three bands, so there is no asymmetry in the DCF originating from the temporal sampling. Since the points of the DCF are not independent, we require some simple means of testing the significance of the observed DCF against the null hypothesis that neither component leads the other. I have used a bootstrap error method: for each time lag, pairs of points were chosen at random from all the original pairs with corresponding positive *or* negative time lag and the DCF constructed with the same number of pairs as the real DCF; this was repeated 1000 times and the solid line in Figure 6.11 corresponds to the region bounding 68% of the symmetrical bootstrap simulations. It is seen in Figure 6.11 that the only significant deviation from the symmetrical bootstrap simulations is in observation P1 where there is a marked asymmetry in the DCF of R1L and R4. To improve the signal to noise further, the DCF has been computed using a single bin for positive time lags and a single bin for negative time lags. Applying our bootstrap error method we find that the observed asymmetry of the DCF of R1L and R4 is significant at the 95% level, and that of R1L and R7 is significant at 85% for observation P1. The DCF is within the 68% confidence limits for R7 and R4 in observation P1 and for all combinations of R1L, R4 and R7 for the other observations.

Thus, in P1, when Markarian 766 is at its faintest, and consequently the power law component is smallest relative to the soft excess, changes in the soft excess component appear to precede changes in the power law component. When Markarian 766 is brighter, this appears not to be true, although in this case the power law component dominates even in R1L, and hence any temporal relation between the power law and soft excess components may be swamped.

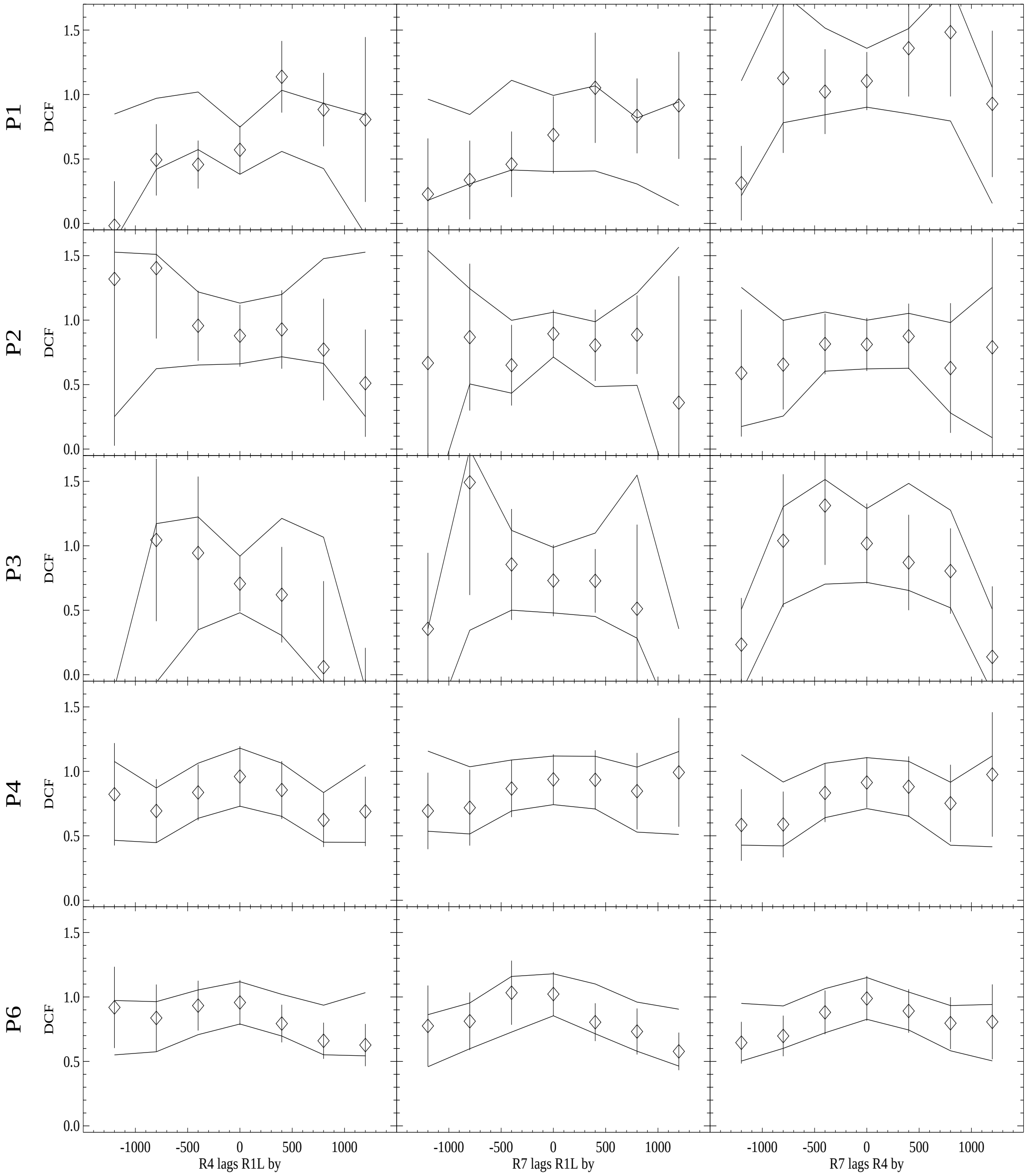

Figure 6.11: Discrete correlation function (DCF) of R1L, R4, and R7 for the five long observations. The solid lines are the bootstrap 68% confidence limits to the DCF if it is symmetric.

Chapter 7

The Properties of Markarian 766 and other NLS1s

In this chapter I discuss the possible mechanisms for the X–ray emission in Markarian 766 in light of the results presented in Chapter 6. I also consider the results in the context of X–ray and multiwavelength emission from other NLS1s.

7.1 Long and Short Term Variability Properties of Markarian 766

There is no apparent long term variability trend present in the *ROSAT* observations of Markarian 766. On a time scale of hours, Markarian 766 varies continuously in every observation period. The spectral variability takes the same form in every observation, which can be explained by variability of the power law slope and normalisation.

Given that the behaviour is the same throughout the PSPC pointed observations from 1991 to 1994, the same spectral variability would be expected in the *ASCA* observation of Markarian 766 in 1993. Leighly *et al.* (1996) report that the major change in the *ASCA* band was that the power law slope became steeper as the power law flux in the *ASCA* band increased. This behaviour is entirely consistent with the spectral variability seen in the *ROSAT* observations.

7.2 The Origin of the Power Law

There are two popular models for the power law X–ray component of radio quiet AGN; both are based on Compton upscattering of UV or soft X–ray photons from an accretion disk or optically thin plasma. In the first model, the observed power law emission is simply that from upscattering of the soft photons in a hot (kT $\sim$ 500 keV) plasma, or by a non - thermal distribution of relativistic electrons (Walter & Courvoisier 1992). In the second model, the emission originates in a region in which the radiation density is large enough that the region is opaque to photon - photon collisions (γ–ray - γ–ray or γ–ray - X–ray) which give rise to electron - positron pairs. These pairs down scatter the γ–ray radiation and produce the observed X–ray spectrum, including the soft X–ray excess (Zdziarski *et al.* 1990). *Both* these models predict that in the variability of a single source the power law slope is softer when the power law flux is higher (Done & Fabian 1989, G. Torricelli-Ciamponi & Courvoisier 1995) as observed in Markarian 766.

Leighly *et al.* (1996) show that Markarian 766 has sufficient radiation density in the emission region that pair production may be important. The compactness parameter is defined as

$$l = L\sigma_T/Rm_ec^3$$

where L is the luminosity, R is the size of the source, σ_T is the Thompson scattering cross section, m_e is the mass of the electron and c is the speed of light; pair production may be important if $l > 10$ (Svensson 1987). Using the shortest factor 2 variability time from the *ASCA* lightcurve ($\Delta t \sim 1000s$) to define the size of the source, assuming $R < c\Delta t$, Leigly *et al.* found $l \sim 12$. Leighly *et al.* (1996) propose that the variability observed during the *ASCA* observation is best explained by pair reprocessing, because the major spectral variability was confined to a single rapid increase in the flux of Markarian 766 (after which it remained relatively constant), and because the soft excess is not required to fit the high count rate spectrum. This would be expected if the energies of the relativistic electrons were to increase suddenly: the first order pair reprocessed spectrum (seen as the soft excess) is replaced by a non-linear pair cascade, which produces the $\alpha \sim 1$ power law spectrum.

However, from the *ROSAT* observations it is clear that the soft excess *does not* disappear when the power law increases in flux and slope, as this would lead to exactly the opposite behaviour of HR_{hard} from that seen in Figures 6.8 to 6.10.

If the spectral changes in a source of compactness $l \sim 12$ are determined by pair reprocessing, the hard X–rays would be expected to vary $\sim$ half a light crossing time before the soft X–rays (Done & Fabian 1989). Assuming 1000s as the light crossing time for Markarian 766 this delay is $\sim$ 500s. This should lead to a significant asymmetry in the cross correlations in Figure 6.11, such that changes in the R7 band (and to a lesser extent R4 band) lead the changes in the R1L band. No such asymmetry is seen (the DCF from observation P1 is asymmetric in the opposite sense).

If the power law component is produced by relativistic particles scattering soft photons and pairs are not important, then changes in the power law component may be simultaneous at all energies. At first sight the asymmetry in the cross correlation of observation P1 (changes in the soft flux leading changes in the hard flux) would appear to support this type of model, in that the soft excess changes before the power law, which is scattered soft excess photons. However, in current models (e.g. Torricelli-Ciamponi & Courvoisier 1995), the change in spectral index with power law flux is brought about by a change in the relativistic electron energy spectrum, not a change in the number of soft photons, and hence there is no expectation that the soft flux should change first.

7.3 The Origin of the Soft Excess

The low variability amplitude in the R1L band compared to the harder R4 and R7 bands (see Table 6.4) would suggest that the soft excess is relatively invariant on short time scales compared to the power law component. This suggests that the soft excess and power law are different components, and hence a pair reprocessing origin for the soft excess is not likely.

The relative invariance of the soft excess also rules out models whereby the soft excess is power law emission reflected or reprocessed close to the central regions. However, if the soft excess were power law emission reprocessed at regions some distance (light days or more) from the central regions, then the soft excess variability would be smeared out by the long response; such a model is therefore compatible with the *ROSAT* data.

The lack of short term soft excess variability is consistent with it being part of the big blue bump, which is known to have a longer variability time scale than the power law X–ray emission in radio quiet AGN (e.g. NGC4051, Done *et al.* 1990). The soft excess spectrum is well fit by one or two black bodies, and hence is consistent with the shape expected from the high energy tail of a hot accretion disk (e.g. Ross, Fabian & Mineshige 1992.)

I can not determine if the soft excess of Markarian 766 varies over a longer time scale than 1 week. Different values for the blackbody parameters are obtained from different observations, but the difference in off axis angles between the observations, and uncalibrated gain drift of the *ROSAT* PSPC, mean that it is not possible to assess long term variability with any certainty.

I note that the results presented here, i.e. that short term variability in the soft excess component is not detected, are in marked contrast with the findings of Molendi & Maccacaro (1994). Their study of Markarian 766 is based on observation P2, in which they find that the soft excess varies with the power law component by approximately the same amplitude, and hence that the two components are related to the same physical process or are causally connected. However, they determine the blackbody and power law parameters by fitting models to spectra in four states defined by overall count rate. They do not quote uncertainties on the power law and blackbody normalisations; the apparent correlation between blackbody and power law normalisation may be caused by the coupled nature of the blackbody temperature and power law slope when fitting low resolution *ROSAT* spectra. The three colour data (see Figure 6.7), and lower variability amplitude in R1L than the R4 and R7 (Table 6.4), for all the *ROSAT* observations, including P2, show that the blackbody flux *can not* vary as much as the power law flux. Consequently, the model presented by Molendi & Maccacaro whereby changes in the accretion rate of an accretion disk determine the variability time scales in the *ROSAT* band is not valid, because the soft excess, assumed to be the high energy tail of an accretion disk, probably does not vary with the time scales found in the *ROSAT* lightcurve.

7.4 X–ray Emission from Markarian 766 and Other NLS1 Galaxies

Markarian 766 has one of the hardest *ROSAT* spectra of the NLS1s in the sample of Boller, Brandt and Fink (1995). Indeed, some NLS1 galaxies have X–ray spectra so soft that they are quite unlike that of Markarian 766 (e.g. WPVS 007, Grupe *et al.* 1995, RE J1034+396, Puchnarewicz *et al.* 1995). It is therefore important to question whether the X–ray emission observed in the ultrasoft NLS1s could come from the same physical processes as that observed in the very much harder NLS1s like Markarian 766. Variability and spectral properties are important diagnostics; similar physical processes can be expected to produce similar spectral shapes and similar variability characteristics. The results presented here show that the X–ray spectrum of Markarian 766 has two important X–ray emission components (the power law and soft excess) which have different spectral shapes and different variability properties:

a power law component which varies rapidly (thousands of seconds) and is softer when it is brighter, and a soft excess which does not exhibit any measurable rapid variability.

NLS1 galaxies which do not have extremely soft *ROSAT* spectra might be expected to be most similar to Markarian 766. The best studied of these at X–ray wavelengths are NGC4051 and MCG-6-30-15. In both these AGN the power law component shows rapid (hundreds of seconds) variability, and becomes softer as it increases in flux. This variability is found in *EXOSAT* and *GINGA* observations (Papadakis & Lawrence 1995, Matsuoka *et al.* 1990, Kunieda *et al.* 1992, Pounds, Turner & Warwick 1986), i.e. has continued for a number of years. This is exactly the behaviour found in Markarian 766.

The ultra-soft NLS1 galaxies show a more varied picture; some like RE J1034+396 show no significant rapid variability in either power law or soft excess components (Pounds, Done & Osborne 1995), while at least one ultrasoft NLS1, IRAS 13224-3809, does vary significantly (factor 2 in 800s). An *ASCA* observations of IRAS 13224-3809 is consistent with the variability originating in the power law component, which steepens as it brightens as in Markarian 766 (Otani *et al.* 1996), and a *ROSAT* observation is also consistent with this hypothesis (the spectrum hardens as the source brightens, which indicates that the power law is varying rather than the soft excess). Some ultra-soft objects have shown extreme variations in their soft excess, which can not be attributed to variations in the power law components. However, these variations are over a relatively long time scale (e.g. the *ROSAT* count rate of RE J1237+264 varied by a factor of ~ 70 between two observations separated by one year with no measurable spectral change, and the *ROSAT* count rate of WPVS 007 varied by a factor of ~ 400 in one year). There are no observations of NLS1s to date where rapid X–ray variability can unambiguously be attributed to the soft excess.

It is therefore plausible that the rapid variability observed in NLS1s may be related to the power law component, even in those with strong soft excesses. This has important consequences, because the rapid soft X–ray variability has often been assumed to come from the soft excess in these objects (a natural assumption given that NLS1s as a class are unusual in showing both large soft excesses and rapid soft X–ray variability). This has important consequences for the sizes of the emission regions; if the rapid variability is confined to the power law component, then the maximum size of the soft excess emission region is not given by the minimum *ROSAT* count rate doubling time scale. In this case, the *ROSAT* count rate doubling time scale *does* give an upper limit to the size of the power law emission region.

7.5 Analogy with Galactic Black Hole Candidates

Galactic black hole candidates (GBHCs) have X–ray spectra that are qualitatively similar (power law component with a soft excess, an Fe line and reflection hump), to those of Seyfert 1 galaxies. Both types of objects are thought to be powered by accretion onto a black hole, and it is possible that the physical processes which produce X–ray emission are the same in both types of objects. GBHCs have two states: in the 'low' state they have hard ($0.3 < \alpha < 0.8$) power law spectra with low energy (< 2 keV) soft excesses and in the 'high' state they have steep power law components ($1.3 < \alpha < 1.8$) and powerful soft excesses which dominate the spectra below ~ 8 keV (Ebisawa *et al.* 1996). In the low state, GBHCs exhibit very rapid (millisecond) variability of the power law component, but vary less rapidly when they are in the high state.

The connection between GBHCs and Seyfert 1 galaxies has been strengthened by the discovery that RE J1034+396 has an extremely steep power law component and an extremely powerful soft excess, and does not vary rapidly, i.e. it is like a GBHC in a high state (Pounds, Done & Osborne 1995). In this analogy, Markarian 766 is equivalent to a low state GBHC in that it shows continuous variability of the power law component, the spectral index of which is similar to those found in low state GBHCs. The variability time scales of GBHCs are much smaller than those of Seyfert galaxies like Markarian 766, but this is not surprising given the large difference in the central black hole masses and hence overall dimensions inferred for Seyfert nuclei and GBHCs. It is believed that the soft excess in the GBHC Cygnus X-1 comes from a region of larger spatial extent (and hence varies on a longer time scale) than that producing the power law emission (Done *et al.* 1992); the results presented here show that the same is probably true for Markarian 766. Furthermore, changes in the soft X-ray flux in Cygnus X-1 lead changes in the hard X–ray flux (Miyamoto & Kitamoto 1989), which appears to be true also for Markarian 766 in observation P1 (see Section 6.7).

Note that while Seyfert 1s with lines much broader than the NLS1s are not found with ultrasoft spectra, i.e. are only analogous to GBHCs in the low state, *both* GBHC states are represented among the NLS1s.

7.6 The Multiwavelength Spectrum of Markarian 766 and Other Narrow Line Seyfert 1s

The multiwavelength spectrum of Markarian 766 is shown in Figure 7.1. The largest and smallest blackbody and power law model components from the *ROSAT* spectral fitting are shown as solid lines. Also shown, as dotted lines, are the power law components from the two spectral states identified in *ASCA* data by Leighly *et al.* (1996). The optical spectrum is taken from González-Delgado & Pérez (1996). Note that the data in this plot are not simultaneous, the optical and ultraviolet spectra have not been dereddened, and the model X–ray spectrum has not been adjusted for absorption by neutral material. Markarian 766 has a large *IRAS* bump: it emits more power from 10 - 100 microns than in the *ROSAT* energy range.

The spectrum is unusual among Seyfert 1 galaxies in that it shows no evidence for the big blue bump in the ultraviolet. This has been noticed before by Walter & Fink (1993) in that Markarian 766 has an unusually low ratio of ultraviolet to soft

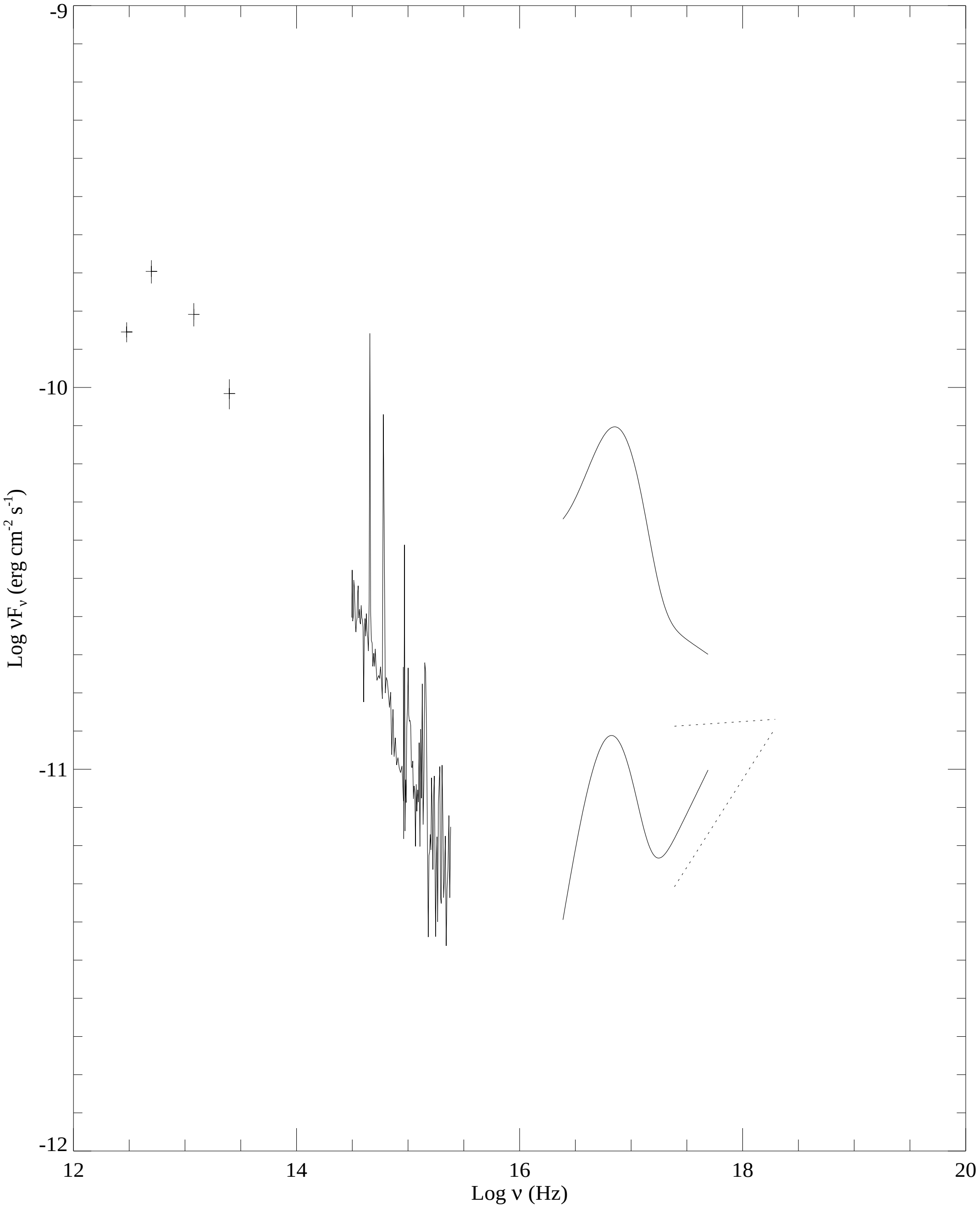

Figure 7.1: The multiwavelength spectrum of Markarian 766

Table 7.1: Data sources for Figure 7.2

Object	νF_ν shift	IR	Optical	X–ray
Markarian 766	0	*IRAS* *	González-Delgado & Pérez 1996	this work
IRAS 13349+2438	+2	Beichman *et al.* 1986	Wills *et al.* 1992	Brandt *et al.* 1996
MCG 6-30-15	-2	*IRAS* *	Morris & Ward 1988	Walter & Fink 1993
Akn 564	-7	-	Cruz-González *et al.* 1994	Brandt *et al.* 1994
NGC4051	-5	*IRAS* *	Ho, Filippenko & Sargent 1995	McHardy *et al.* 1995

* *IRAS* fluxes were obtained via the NASA extragalactic database (NED).

All ultraviolet data obtained from the Rutherford Appleton IUE archive.

X–ray flux given its soft X–ray slope. Most of the Walter & Fink (1993) sample of *ROSAT* all sky survey selected Seyfert 1 galaxies fit a strong correlation between soft X–ray slope and the ratio of ultraviolet (1375 Å) to soft X–ray flux, suggesting that they have big blue bumps which rise in the UV, peak in the EUV and extend to soft X–ray energies. Besides Markarian 766, five other outliers were found by Walter & Fink (see their figure 8), which have a low ultraviolet to soft X–ray flux ratio given their soft X–ray spectral slopes. Of these five, one is the broad line Seyfert 1 galaxy IC4329A, in which the lack of ultraviolet flux is probably caused by attenuation by dust in the edge on host galaxy. The remaining four Seyferts, Akn 564, NGC 4051, IRAS 13349+2438, and MCG-6-30-15 could all be classified as NLS1s by the criteria of Goodrich (1989). The multiwavelength spectra of these objects are plotted in Figure 7.2, and sources for these data are given in Table 7.1. All are particularly similar to that of Markarian 766; they have very large infrared bumps and falling optical – ultraviolet spectral shapes. The lack of ultraviolet flux in these objects may be a result of their having very high temperature soft excesses, or (as suggested by Walter & Fink 1993) it may be due to reddening by dust.

These objects are also very similar to Markarian 766 in their X–ray spectral and variability properties. NGC 4051 has a highly variable power law component which softens as it increases in flux (Papadakis & Lawrence 1995) and a soft excess blackbody component with kT $\sim$ 100 eV (Mihara *et al.* 1994, Pounds *et al.* 1994).

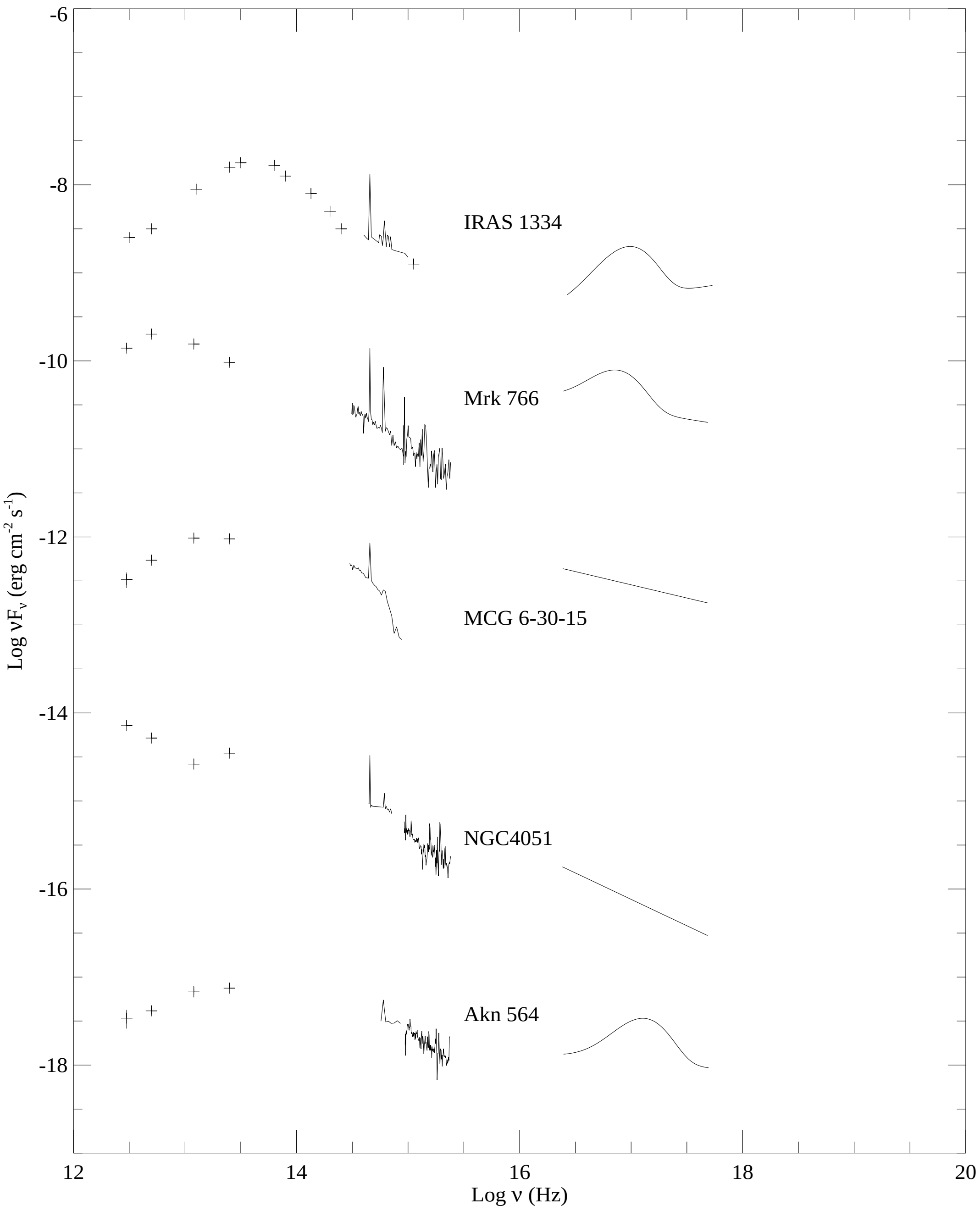

Figure 7.2: The multiwavelength spectra of the outlying NLS1s of Walter & Fink (1993). Note that the spectra have been vertically shifted for clarity.

Papadakis & Lawrence's cross correlation between the soft (0.1 - 2 keV) and hard (2 - 8 keV) flux is highly asymmetric such that the soft flux tends to lead the hard flux, and the power spectrum of the soft flux is steeper than that of the hard flux (i.e. the soft flux has more change over longer time scales) which would be consistent with a slowly varying soft excess and a rapidly varying power law component. Akn 564 shows variability by around 20% over 1500s during the *ROSAT* observations of Brandt *et al.* (1994), and when the soft excess is modelled as a blackbody the power law component has a similar slope ($\alpha \sim 1.1$ and the blackbody a similar temperature (kT $\sim$ 130 eV) to Markarian 766. IRAS 13349+2438 is also variable, although as yet no rapid variability has been seen, and when the *ROSAT* spectrum is modelled as a power law and blackbody soft excess has a similar power law index ($\alpha \sim 0.8$) and soft excess temperature (kT $\sim$ 90 eV) to Markarian 766, (Brandt *et al.* 1995). MCG-6-30-15 also varies rapidly (Reynolds *et al.* 1995), and has a hard power law component which softens as it increases in flux, although no soft excess has as yet been detected.

Brandt *et al.* (1994 and 1995) found no evidence for any intrinsic neutral column in *ROSAT* spectra of Akn 564 or IRAS 13349+2438, and preferred spectral models without a soft excess component because the presence of a soft excess would require a neutral column which is smaller than the measured Galactic column; their spectral fitting was based on *ROSAT* observations performed in December 1992 (IRAS 13349+2438) and November 1993 (Akn 564), with both targets at the centre of the PSPC. As shown in Section 6.5.3, the observations made around these times with Markarian 766 at the centre of the PSPC are miscalibrated, with the result that the fitted absorbing column is probably underestimated. Even with an edge to represent absorption from O VII and O VIII, the underlying spectra in these two objects are unusually steep ($\alpha > 1.5$), suggesting that they *do* have soft excesses.

The very similar multiwavelength spectra and X–ray properties in these objects probably mean that they lack ultraviolet flux for a common reason.

Attributing the lack of ultraviolet flux to reddening by dust in the line of sight is an attractive solution. Optical polarization of Markarian 766, of $\sim 2\%$ increasing to the blue, indicates scattering from dust grains. These dust grains are probably located within the narrow line region, because the broad lines show more polarization than the narrow lines (Goodrich 1989). For Markarian 766, the required amount of reddening to make the ultraviolet flux match the Walter & Fink (1993) ultraviolet – soft X–ray relation is consistent with its high Balmer decrement ($H_\alpha/H_\beta = 5.1$) seen in the optical spectrum. This amount of reddening is about twenty times that expected for a Galactic gas to dust ratio and the measured cold absorbing column of $\sim 3 \times 10^{20}\mathrm{cm}^{-2}$ (Walter & Fink 1993). This is reasonable if the dust is located in the narrow line region where hydrogen and helium will be predominantly ionized. The cross section for photoelectric absorption by metals in dust grains can be much smaller than for metals in the gas phase because of self blanketing (e.g. Fireman 1974 states that the 0.3 keV photoelectric cross section for 0.6 μ radius dust grains is only $\sim 20\%$ its value for gaseous metals.) Similar conclusions can be drawn from polarization properties and Balmer decrements of IRAS 13349+2438 and MCG 6-30-15 (Wills *et al.* 1992, Thomson & Martin 1988).

Thermal emission from dust is also probably the best explanation of the large *IRAS* bumps in these objects. A large excess of 10 - 100 micron emission appears to be a common property in many NLS1 galaxies, including those which are ultrasoft such as RE J1034 +396 (Puchnarewicz *et al.* 1995), which has a similar infrared to ultraviolet spectral energy distribution to the objects discussed above. Detailed submillimetre observations of the NLS1 1Zw1 indicate that the IRAS bump is well fitted by thermal emission from dust, but is poorly fitted by synchrotron models (Hughes, *et al.* 1993). The evidence for dust in these objects is extremely strong, *even if the deficit of ultraviolet flux is related to unusually high big blue bump temperatures.*

It is therefore likely that dusty Seyfert 1 galaxies are preferentially those which have narrow lines. This is supported by the fact that the only five Seyfert 1s of the Walter & Fink (1993) sample to show evidence for dust reddening have narrow lines. It is further supported by the large ratio of narrow to broad line Seyfert 1s found in *IRAS* surveys ($> 20\%$ in the *IRAS* samples of Spinoglio & Malkan 1989 and Osterbrock & DeRobertis 1985) and small ratio ($\sim 10\%$) of narrow to broad line Seyfert 1s found in optical surveys (Stephens 1989).

Finally, in the unified model for AGN, Seyfert 2 galaxies are Seyfert 1 galaxies viewed side-on, such that the broad line regions are obscured from us (see Figure 1.1 in the Introduction to this thesis). The hidden broad line regions (and Seyfert 1 type optical continua) of Seyfert 2 galaxies can be seen in polarized light. This is scattered into our line of sight by free electrons, which scatter optical light more or less independently of wavelength, or dust, which scatters blue light much more than red light (Antonucci 1993). If more dust is found beyond the broad line region in NLS1s than in broad line Seyfert 1s, we would expect those Seyfert 2s which have the largest red-blue polarization gradient to have hidden broad line profiles like those of NLS1s. The numbers and qualities of spectropolarimetric observations of Seyfert 2 galaxies are not sufficient to address this issue quantatively, but this hypothesis is qualitatively supported: of the Miller & Goodrich (1990) sample of eight highly polarized Seyfert 2 galaxies, one (NGC7674) has NLS1 width polarised broad Hα and Hβ components, and this object also has the highest red-blue polarisation gradient.

7.7 Conclusions

I have examined the variable soft X–ray emission of Markarian 766 using hardness ratios and spectral analysis of 9 *ROSAT* datasets. The spectrum is well described by a power law and a blackbody (kT $\sim$ 70 eV) soft excess. Hardness ratios and the variability amplitudes in three energy bands show that the power law component varies continuously on a time scale of $\sim$ 5000s but the soft excess component probably does not vary significantly within the observations. The power law component is always steeper when it is brighter. This variability can be explained if the power law is produced by thermal or non-thermal Comptonisation of soft photons. While pair reprocessing could produce the correlation between power law spectral index and flux, delays expected between changes in the hard and soft flux are not seen.

The behaviour of Markarian 766 is highly analogous to that of Galactic black hole candidates in the low state, which have rapidly variable power law components and less variable (extended) soft excesses.

I show that X–ray variability properties of other NLS1s are consistent with the picture suggested for Markarian 766 (i.e. that the rapid variability occurs in the power law component and that the soft excess varies over long time scales only). The time scale for variation in the *ROSAT* band probably provides an upper limit for the size of the region in which the power law (but not necessarily the soft excess) is produced. This means that the physical size of the soft excess region may be much larger than the X–ray power law producing region, and hence is consistent with the soft excess having the same variability time scales as the ultraviolet part of the big blue bump.

Markarian 766 is known to have a deficit of ultraviolet flux relative to its X–ray emission. I show that the four other objects in the Walter & Fink (1993) sample of *ROSAT* all sky survey selected Seyfert 1 galaxies, which show a lack of ultraviolet emission (excluding IC4329a which is probably strongly absorbed by its edge-on host galaxy) have very similar infrared to X–ray flux distributions to Markarian 766. These galaxies could all be classed as NLS1s, and are seen to have very similar X–ray spectral and variability properties to Markarian 766 (calibration uncertainties in the *ROSAT* PSPC mean that two of these objects, IRAS 13349+2438 and Ark 564, may be more like Markarian 766 than was previously thought). I argue that the multiwavelength flux distributions of these objects support the Walter & Fink suggestion that the ultraviolet flux deficit is related to dust extinction, and show that other independent data are consistent with a picture in which NLS1s have more dust in their narrow line regions than broad line Seyfert 1s.

Chapter 8

Conclusions

8.1 The Big Picture

In this final chapter I will put my results into a wider context. In Chapters 2 and 4 I studied how the AGN population has changed with cosmic epoch. In Chapter 3 I examined the NELG population while in Chapters 6 and 7 I have studied a single NLS1 galaxy and the physical processes which give rise to its (and other NLS1's) X–ray emission. These seemingly disparate threads are drawn together in the wider picture of AGN evolution: what has actually happened to the centre of galaxies since the big bang to the present day? Were all the QSOs formed at $z > 2$ and have they slowly dimmed ever since, or do QSOs live brief, bright lives to be replaced by fresh QSOs which are, on average, slightly less luminous? Do dim QSOs flare up again when fresh fuel is available, perhaps after interactions with other galaxies? Have many of the once mighty QSOs ended up as somewhat more humble NELGs, or are the NELGs a completely different population? And where do the NLS1s fit in, are they remnants of ancient QSOs or are they young objects at the peak of their activity? Where does the remainder of the X–ray background come from? Answers to these and similar questions are the ultimate goal of much of the research I have described.

8.2 Some Current Theories

Cavaliere & Padovani (1988) break the range of possibilities for QSO evolution into 3 groups:

1) QSOs are long lived, slowly dimming since their formation at $z > 2$, so that only a small fraction of galaxies (a few percent) will ever have hosted QSOs.

2) QSO activity is a single, short lived episode in the history of (virtually) every galaxy. If this were the case, (virtually) every galaxy at the present day must harbour a QSO remnant - a massive, but in most cases 'inactive', black hole.

3) A form of evolution which is intermediate between these two possibilities, such that a subset of all galaxies contain QSOs which undergo short lived but recurrent activity.

The important thing to note about these possibilities it that they each specify different time scales of activity and different fractions of galaxies which have contained active nuclei. The length of time a QSO spends 'active', and hence with an appreciable accretion rate, determines the present day mass of the central black hole. It follows that if QSOs are long lived, their central black holes must be extremely massive in the present day. It is simple to calculate the mass of present day long lived QSOs assuming a power law PLE model for the evolution. The mass gain rate of a massive black hole is given by (Frank, King & Raine 1992):

$$L = \eta c^2 \frac{dM}{dt} \tag{8.1}$$

where L is the luminosity, c is the speed of light, M is the mass of the black hole, t is time, and η is the efficiency of the accretion process. L at redshift z (and the corresponding time) is related to present epoch luminosity L_0 by the PLE model

$L(z) = f(z)L_0$, and dt is related to dz by equations 1.2 and 1.3 in Chapter 1. It follows that

$$M_0 = M_1 + \frac{L_0}{\eta c^2} \int_0^{z_1} f(z) \frac{-dt}{dz} dz \tag{8.2}$$

where the subscript 0 refers to the present epoch and the subscript 1 refers to some previous epoch. Under the assumption $f(z) = (1+z)^{2.9}$ (see Chapters 2 and 4) and $\eta = 0.1$, AGN have gained $\sim 10^7 M_\odot$ since redshift $z_1 = 2$ for every 10^{40} erg s^{-1} of present bolometric luminosity. A present day bolometric luminosity range for Seyfert 1 nuclei between 10^{43} and 10^{45} erg s^{-1} thus corresponds to a range of black hole masses of at least $10^{10} M_\odot$ to $10^{12} M_\odot$ in the present epoch. A similar mass range has been calculated by Cavaliere & Padovani (1988) for exponential PLE of the luminosity function. The situation is more complicated if objects have only been active for a short period or are recurrent, because the remnants are distributed between currently active *and inactive* galaxies. The mass range then depends on what fraction of galaxies have ever been active and hence on the length of time of activity. Cavaliere & Padovani (1988) estimate that the mass range could be at least 2 orders of magnitude smaller if AGN are short lived.

It is hence possible to constrain the history of AGN evolution by examining AGN (and ordinary galaxies which may contain the remnants of previous activity) in the present epoch ($z \sim 0$) and determining, from dynamical arguments, the mass of the central regions. From this perspective, Cavaliere & Padovani (1989) propose that AGN activity is probably short lived and recurrent but acknowledge that astronomers limited understanding of the central regions of AGN lead to some considerable uncertainty in calculating the mass.

Haehnelt and Rees (1993) propose that in a hierarchical cosmogony such as cold dark matter (see White *et al.* 1995 and references therein), a short lived active nucleus to every galaxy is expected: a new AGN forms at the same time as a galaxy-scale structure forms. The evolution of the luminosity function is explained by the evolution of structure in the universe, the peak of AGN activity occurring naturally at the expected peak of galaxy formation, $2 < z < 3$.

More recently, Yi (1996) has proposed that the evolution of the QSO luminosity function, and in particular the strong evolution for $z < 2$, can be explained well by changes in the accretion mode (from high to low efficiency) of long lived AGN which were born at $3 < z < 4$. As yet, there is no clear answer to the problem of AGN evolution.

8.3 What Light Does This Thesis Shed on These Issues?

8.3.1 The AGN Luminosity Function

In Chapters 2 and 4 I showed that the evolution of the luminosity function can be described by PLE for $q_0 = 0$. If NELGs are included with the broad line AGN, this is also true of $q_0 = 0.5$, and even if the NELGs are not included *most* of the evolution is luminosity (rather than density) evolution. This behaviour of the luminosity function is reproduced very naturally by a slowly dimming population of long-lived QSOs.

Models of QSO activity which are short lived or recurrent can reproduce PLE type behaviour of the luminosity function, but require some external (environmental) factor to reduce the luminosity of each successive flare up or generation of AGN. In a scenario where AGN are produced at the formation of a galactic scale structure it could be envisaged that later AGN are less luminous, but it would be difficult for this scenario to reproduce the PLE behaviour of the X–ray luminosity function, because it is essentially a form of density evolution. If AGN are recurrent, then we require that the successive outbursts be of decreasing luminosity, leading to PLE behaviour of the luminosity function. If the periods of activity are caused by interactions with other nearby galaxies, the required decrease in the luminosity of the outbursts may be explained by the nature of the encounters changing as scale and structure in the universe evolve (e.g. encounters may on average occur at a greater distance in the present epoch). Alternatively, the available fuel may be depleted during the outbursts or by some other mechanism (e.g. stripping of gas and dust by an intracluster medium). However, if encounters with other galaxies lead to outbursts, the majority of QSOs would be expected to inhabit regions where the space density of galaxies is enhanced, i.e. clusters of galaxies; this is not thought to be the case (e.g. Boyle & Couch 1993).

8.3.2 NELGs

The X–ray selected NELGs are probably a mixed bag of objects, and some may be powered by star formation and not related to AGN activity at all. However, NELGs do appear to be undergoing evolution which (at least at low redshift) is similar to the evolution of QSOs (although this could also be related to star formation as evidenced by the evolution of the optical NELG population). On average, they also have harder X–ray spectra than QSOs (Romero-Colmenero *et al.* 1996), and NELGs typically have X–ray luminosities which are orders of magnitude lower than QSOs. The hard spectrum may be the signature of an evolved, very low accretion rate QSO. By analogy, the Galactic black hole candidates are believed to be in a low accretion mode when they show a hard spectrum. Additionally or alternatively, their spectra could be hard because of intrinsic absorption; this is certainly believed to be the case for Seyfert 2 nuclei. These properties make NELGs good candidates for the low-state QSOs or remnants of QSOs and it is thus worth considering what implications this would have for QSO evolution.

The properties of the X–ray selected NELG population support the hypothesis that they are the remnants of long-lived, slowly dimming QSOs, rather than the remnants of short-lived or recurrent QSOs, for two reasons:

1) They are currently found in optically luminous galaxies (McHardy *et al.* 1997, in preparation) which represent only a small fraction of galaxies (remembering that if QSOs are long lived they are probably found in no more than a few percent of all

galaxies).

2) Whilst the exact form of NELG evolution cannot yet be determined, NELGs are evolving in the sense that they are now less numerous and/or less luminous than at higher redshift (at least up to $z = 0.6$). This behaviour is expected if the NELGs are the slowly dimming remnants of slowly dimming QSOs. If QSOs are brief, bright, once-only events, one would expect the number of remnants to be increasing with time, so if X–ray NELGs are the remnants, their evolution should be in the opposite sense to that observed. Alternatively, if NELGs are the remnants *and* the precursors of single event QSOs they need not evolve at all, but again this is contrary to the observed evolution of NELGs. Therefore if QSOs are recurrent events and NELGs are the remnants, then there is no explanation as to why the X–ray NELGs should be dimming or becoming less numerous. If the NELGs are low-state recurrent AGN, their observed evolution requires that their luminosities are declining in both the flare-up and quiescent states, which is really a combination of the recurrent model and long lived, slowly dimming model. There would be a requirement for a long lived declining component in support of the idea that the evolution is driven by the slow dimming of long lived AGN.

8.3.3 NLS1s

If the hard X–ray spectra of NELGs makes them good candidates for the massive evolved remnants of QSOs, the typically very soft X–ray spectra of NLS1's would appear to make them very poor candidates. In the case of Markarian 766, I find that the soft excess could well be the high energy tail of the primary emission from an accretion disk. Current models suggest that only high accretion rate, low mass $(< 10^7)\mathrm{M}_\odot$ AGN have accretion disks that radiate appreciably in the soft X–ray band (Ross, Fabian & Mineshige 1992). High accretion rate has been suggested by other authors (e.g. Boller, Brandt & Fink 1996) to explain the overall properties of NLS1s. If NLS1s really are low mass, high accretion rate objects, then they do not fit with the scenario in which QSOs are long lived and have been gradually dimming since $z > 2$, but would certainly be expected if QSOs are short lived or recurrent. Of course these simple models for QSO evolution can only be expected to describe the typical/average behaviour of AGN. The very existence of NLS1s is not sufficient reason to disregard the slowly dimming QSO model, even if they are low mass high accretion rate objects: a few QSOs may have formed late or flared up because of recent interactions but the majority could still be slowly dimming since $z = 2$. How much a threat NLS1s could present to the model in which AGN are slowly dimming depends on how numerous the NLS1s are relative to other AGN. This would be difficult to determine because NLS1s have a different multiwavelength spectrum to other AGN (the strong infrared bump, strong soft X–ray excess and relatively red optical continuum). Hence samples of AGN are biased towards or against the detection of NLS1s relative to other AGN depending on the selection wavelength.

8.3.4 The X–ray Background

There is one further piece of observational evidence to consider. The X–ray background has a harder spectrum from 1 - 10 keV than most AGN. At present, NELGs look like the best candidates to supply the majority of this radiation. If NELGs are the burnt out remnants of old, long lived QSOs, or of brief bright QSO phases, then one would not expect to find them in large numbers at $z > 2$ when QSOs are at their prime. However, in the recurrent QSO model there is no reason why the number of inactive AGN should be small at high redshift and hence the discovery of a large population of X–ray NELGs at $z > 2$ would be evidence in *favour* of the recurrent QSO model. Therefore, identifying the redshift of origin of the bulk of the X–ray background at >1 keV, and constraining the evolution of NELGs at $z > 1$ are therefore crucial tests. From the work presented in Chapter 3, it would appear that NELGs do not continue to evolve rapidly at $z > 1$, but could still supply a considerable fraction of the X–ray background.

8.4 Multiwavelength Evolution

Perhaps the best way to examine the physical evolution of AGN will be to study the multiwavelength spectral evolution of AGN, such as a comparison of the evolution rates at infrared, optical, and X–ray wavelengths. The multiwavelength spectral evolution can then be compared with that predicted by physical models of AGN. For example, current models of accretion disks (e.g. Ross, Fabian & Mineshige 1992) predict that for the same luminosity, a higher mass black hole will have a lower temperature accretion disk spectrum and hence a smaller soft X–ray/optical ratio. Therefore, for long lived QSOs the accretion disk should dim faster at soft X–ray than at optical wavelengths, and hence the soft X–ray evolution should be faster than the optical evolution. Unfortunately, primary emission from an accretion disk is not the only emission component found in the soft X–ray or optical spectra of AGN, and indeed it is not proven that the big blue bump is emission from an accretion disk at all.

At present, the selection effects in different bands are not sufficiently well understood, the samples are still too small, and our understanding of the physical origin of AGN emission at different wavelengths is not adequate to determine the large scale history of QSOs from multiwavelength spectral evolution. With the next generation of space and ground based observatories, these problems may be solved.

8.5 In Summary

The results presented in this thesis are essentially consistent with a scenario in which on average, AGN are long lived and slowly dimming since $z = 2$: the evolution and X–ray luminosity functions of QSOs and NELGs are hard to explain if QSOs lead brief, bright lives or experience recurrent flares. However, a sizable population of narrow line Seyfert 1s would be hard for the long lived model to accommodate.

Acknowledgements

Constructing a Ph.D. thesis is a task of sufficient intensity that it has, at times, taken a substantial toll from my sanity and from those poor souls who have had to put up with me. Of these, I should like to thank first and foremost my wife Amanda who has tolerated my weird and obsessive behaviour, my strange and sometimes long working hours, and our total lack of cash for more than three years. I am very grateful to my Mum and Dad who have been a fortress of support through *all* my days as a student, my brother who kindly donated the computer on which I am now writing, and my Nan and Grandad who gave me a place to live for a whole year (I've never eaten so well before or since!) I would never have reached this point were it not for the support and encouragement of all these people.

This thesis itself would have been vastly inferior were it not for the observations, suggestions, discussions, and arguments with the many powerful minds at MSSL. In particular Francisco Carrera played a most important role in directing my efforts at the beginning of the Ph.D. and has been a gold mine of ideas ever since. Much of my basic grasp of astrophysical method and statistics has come from Jon Mittaz and Dave Wonnacott, who must have had incredible patience to put up with me. I benefited greatly from my time sharing the student office with Stephen Potter, Encarni Romero-Colmenero, Lee Sproats, Vito Graffagnino, Kerry Nicholson and Kate Harrop-Allin, who put up with my perpetual eating and foot tapping. Phil Smith deserves thanks for his continuous help with all things computer related. I would like to thank my supervisor Keith Mason for his solid advice and the considerable time spent reading and commenting on the thesis, despite being the busiest person ever. Chapters 6 and 7 are much improved after valuable discussion with Liz Puchnarewicz and Graziella Branduardi-Raymont.

The work contained in this thesis would not have been possible were it not for the studentship support of the Science and Engineering Research Council (and subsequently PPARC). Nor would it have been possible without the efforts of many people working on RIXOS and the UK Deep survey, to whom I owe thanks.

Finally, I would like to thank the people who have contributed by keeping me sane and happy the last three years, particularly my in-laws Ann and Allan and my good friends from Chelmsford, without whom I would be a fish eating hermit in a seaside cave by now.

Bibliography

Antonucci R., 1993, Annu. Rev. Astron. Astrophys., 31, 473

Avni Y., and Bahcall J.N., 1980, ApJ, 235, 694

Barcons X., Branduardi-Raymont G., Warwick R.S., Fabian A.C., Mason K.O., McHardy I.M., Rowan-Robinson M. 1994, MNRAS, 268, 833

Bechtold J., Elvis M., Fiore F., Kuhn O., Cutri R.M., McDowell J.C., Rieke M., Siemiginowska A., Wilkes B.J., 1994, AJ, 108, 759

Beichman C.A., Soifer B.T., Helou G., Chester T.J., Neugebauer G., Gillett F.C., Low F.J., 1986, ApJ, 308, L1

Boller Th., Brandt W.N., Fink H., 1996, A&A, 305, 53

Boyle B.J., Shanks T., Peterson B.A., 1988, MNRAS, 235, 935

Boyle B.J., Griffiths R.E., Shanks T., Stewart G.C., Georgantopoulos I., 1993, MNRAS, 260, 49

Boyle B.J. & Couch W.J., 1993, MNRAS, 264, 604

Boyle B.J., Shanks T., Georgantopoulos I., Stewart G.C., Griffiths R.E., 1994, MNRAS, 271, 639

Boyle B.J., McMahon R.G., Wilkes B.J., Elvis M., 1995a, MNRAS, 272, 462

Boyle B.J., McMahon R.G., Wilkes B.J., Elvis M., 1995b, MNRAS, 276, 315

Branduardi-Raymont G., Mason K.O., Warwick R.S., Carrera F.J., Graffagnino V.G., Mittaz J.P.D., Puchnarewicz E.M., Smith P.J., Barber C.R., Pounds K.A., Stewart G.C., McHardy I.M., Jones L.R., Merrifield M.R., Fabian A.C., McMahon R., Ward M.J., George I.M., Jones M.H., Lawrence A., Rowan-Robinson M., 1994, MNRAS, 270, 947

Brandt W.N., Fabian A.C., Nandra K., Reynolds C.S., Brinkmann W., 1994, MNRAS, 271, 958

Brandt W.N., Pounds K.A., Fink H., 1995, MNRAS, 273, L47

Brandt W.N., Fabian A.C. and Pounds K.A., 1996, MNRAS, 278, 326

Burns J.O., White R.A., Hough D.H., 1981, AJ, 96, 1

Cash J., 1979, ApJ, 228, 939

Cavaliere A., & Padovani P., 1988, ApJ, 333, L33

Cavaliere A., & Padovani P., 1989, ApJ, 340, L5

Chen L.-W., Fabian A.C., Gendreau K.C., submitted to MNRAS

Ciliegi P., Elvis M., Wilkes B.J., Boyle B.J., McMahon R.G., Maccacaro T., 1995, MNRAS, 277, 1463

Ciliegi P., Elvis M., Wilkes B.J., Boyle B.J., McMahon R.G., 1997, MNRAS, 1997, 284, 401

Clements D.L., Sutherland W.J., Saunders W., Efstathiou G.P., McMahon R.G., Lawrence A., Rowan-Robinson M., 1996, MNRAS, 279, 459

Crawford D.E., Jauncey D.L., Murdoch H.S., 1970, ApJ, 162, 405

Cruz-González I., Carrasco L., Serrano A., Guichard J., Dultzin-Hacyan D., Bisiacchi G. F., 1994, ApJs, 94, 47

Della Ceca R., Maccacaro T., Gioia I.M., Wolter A., Stocke T.J., 1992, ApJ, 389, 491

Done C., Fabian A.C., 1989, MNRAS, 240, 81

Done C., Fabian A.C., Ward M.J. Kunieda H., Tsuruta S., 1990, MNRAS, 243, 713

Done C., Mulchaey J.S., Mushotzky R.F., Arnaud K.A., 1992, ApJ, 395, 275

Dunlop J.S. & Peacock J.A., 1990, MNRAS, 247,19

Ebisawa K., Titarchuk L., Chakrabarti S.K., 1996, PASJ, 48, 59

Edelson R.A. and Krolik J.H., 1988, ApJ, 333, 646

Ellis R.S., Colless M., Broadhurst T., Heyl J., Glazebrook K., 1996, MNRAS, 280, 235

Fabian A.C., & Barcons X., 1992, Annu. Rev. Astron. Astrophys., 30, 429

Fasano G. and Franceschini A., 1987, MNRAS, 225, 155

Fireman E.L., 1974, ApJ, 187, 57

Franceschini A., La Franca F., Cristiani S. and Martin-Mirones J.M., 1994, MNRAS, 269, 683

Francis P.J., 1993, ApJ, 407, 519

Frank J., King A.R., Raine D.J., 1992, 'Accretion power in astrophysics', Cambridge University Press

Giacconi R., Gursky H., Paolini F., Rossi B., 1962, Phys. Rev. Lett., 9, 439

Gioia I.M., Maccacaro T., Schild R.E., Wolter A., Stocke J.T., Morris S.L., Henry J.P., 1990, ApJS, 72, 567

González-Delgado R.M., 1995, PASP, 107, 1130

González-Delgado R.M. & Pérez E., 1996, MNRAS, 278, 737

Goodrich R.W., 1989, ApJ, 342, 224

Griffiths R.E., Doxsey R.E., Johnston M.D., Schwartz D.A., Schwartz J., Blades J.C., 1979, ApJ, 230, L21

Griffiths R.E., Georgantopoulos I., Boyle B.J., Stewart G.C., Shanks T., Della Ceca R., 1995, MNRAS, 275, 77

Griffiths R.E., Della Ceca, R., Georgantopoulos I., Boyle B.J., Stewart G.C., Shanks T., Fruscione A., 1996, MNRAS, 281, 71

de Grijp M.H.K., Keel W.C., Miley G.K., Goudfrooij P., Lub J., 1992, A&AS, 96, 389

Grupe D., Beuerman K., Mannheim K., Thomas H.-C., Fink H.H., de Martino D., 1995, A&A, 300, L21

Guilbert P.W. and Rees M.J., 1988, MNRAS, 233, 475

Haehnelt M.G., & Rees M.J., 1993, MNRAS, 263, 168

Halpern J.P., Helfand D.J., Moran E.C., 1995, ApJ, 453, 611

Hasinger G., 1992, in: Barcons X., Fabian A.C. (eds.), The X–ray Background, Cambridge University Press, p.229

Hasinger G., Burg R., Giacconi R., Hartner G., Schmidt M., Trumper J., Zamorani G., 1993, A&A, 275, 1

Hasinger G., Boese G., Predehl P., Turner T.J., Yusaf R., George I.M., Rohrbach G., 1994, MPE/OGIP Calibration Memo CAL/ROS/93-015

Hawkins M.R.S., Veron P., 1995, MNRAS, 275, 1102

Hawkins M.R.S., Veron P., 1996, MNRAS, 281, 348

Hewett P.C., Foltz C.B., Chaffee F.H., 1993, ApJ, 406, L43

Ho L.C., Filippenko A.V. & Sargent W.L., 1995, ApJS, 98, 477

Hughes D.H., Robson E.I., Dunlop J.S., Gear W.K., 1993, MNRAS, 263, 607

Jones C., Forman W., 1984, ApJ, 276, 38

Jones L.R., McHardy I.M., Merrifield M.R., Mason K.O., Smith P.J., Abraham R.G., Branduardi-Raymont G., Newsam A.M., Romero-Colmenero E., 1995, Röntgenstrahlung from the Universe, Zimmermann H.U., Trümper J.E., Yorke H., (eds), MPE report 263

Jones L.R., McHardy I.M., Merrifield M.R., Mason K.O., Smith P.J., Abraham R.G., Branduardi-Raymont G., Newsam A.M., Dalton G., Rowan-Robinson M., Luppino G., 1997, submitted to MNRAS

Kassiola A., and Mathez G., 1990, A&A, 230, 255

Keel W.C., de Grijp M.H.K., Miley G.K., 1988, A&A, 203, 250

Kunieda H., Hayakawa S., Tawara Y., Koyama K., Tsusaka Y., Leighly K., 1992, ApJ, 384, 482

La Franca F., Franceschini A., Cristiani S., Vio R., 1995, A&A, 299, 19

Lampton M., Margon B., Bowyer S., 1976, ApJ, 208, 177

Lawson A.J., Turner M.J.L., Williams O.R., Stewart G.C., Saxton R.D., 1992, MNRAS, 259, 743

Leighly K.M., Mushotzky R.F., Yaqoob T., Kunieda H., Edelson R., 1996, ApJ, in press

Lilly S.J., Tresse L., Hammer F., Crampton D., Le Fèvre O., 1995, ApJ, 455, 108

Maccacaro T., Avni Y., Gioia I.M., Giommi P., Griffiths R.E., Liebert J., Stocke J., Danziger J., 1983, ApJ, 266, L73

Maccacaro T., Gioia I.M., Wolter A., Zamorani G., Stocke J.T., 1988, ApJ, 326, 680

Maccacaro T., Della Ceca R., Gioia I.M., Morris S.L., Stocke J.T., Wolter A., 1991, ApJ, 374, 117

Marshall F.E. *et al.* , 1980, ApJ, 235, 4

Marshall H.L., Avni Y., Braccesi A., Huchra J., Tananbaum H., Zamorani G., Zitelli V., 1984, ApJ, 283, 50

Marshall N., Warwick R.S., Pounds K., 1981, MNRAS, 194, 987

Mason *et al.* 1995, in preparation

Mather J.C., Cheng E.S., Eplee R.E., Isaacman R.B., Meyer S.S., 1990, ApJ, 354, L37

Matsuoka M., Piro M., Yamauchi M., Murakami T., 1990, ApJ, 361, 440

McCammon D.& Saunders W.T., 1990, Annu. Rev. Astron. Astrophys., 28, 657

McHardy I.M., Green A.R., Done C., Puchnarewicz E.M., Mason K.O., Branduardi-Raymont G., Jones M.H., 1995, MNRAS, 273, 549

Mchardy I.M., Jones L.R., Merrifield M.R., Mason K.O., Abraham R.G., Newsam A.M., Dalton G.B., Carrera F.J., Smith P.J., Rowan-Robinson M., Wegner G.A., Lehto H.J., Branduardi-Raymont G., Luppino G.A., Efstathiou G., Ponman T.J., Allan D.J., Quenby J.J., 1997, submitted to MNRAS

Mihara T., Matsuoka M., Mushotzky R.F., Kunieda H., Otani C., Miyamoto S., Yamauchi M., 1994, PASJ, 46, 137

Miller J.S. & Goodrich R., 1990, ApJ, 355, 456

Mittaz J.P.D., Carrera F.J., Romero-Colmenero E., Mason K.O., Hasinger G., McMahon R.G., Andernach H., Burgos-Martin J., González-Serrano I., Wonnacott D., 1997, MNRAS, submitted

Miyamoto S. & Kitamoto S., 1989, Nature, 342, 773

Molendi S., Maccacaro T. and Schaeidt S., 1993, A&A, 271, 18

Molendi S. and Maccacaro T., 1994, A&A, 291, 420

Morris S.L. & Ward M.J., 1988, MNRAS, 230, 639

Mushotzky R.F., Done C., Pounds K.A., 1993, Annu. Rev. Astron. Astrophys., 31, 717

Netzer H., Turner T.J. and George I.M., 1994, ApJ, 435, 106

Osterbrock D.E. & DeRobertis M.M., 1985, PASP, 97, 902

Osterbrock D.E. & Pogge R.W., 1985, ApJ, 297, 166

Osterbrock D.E., 1993, ApJ, 404, 551

Otani C., Tsuneo K., Kayoko M., 1996, MPE Report 263, 'Röntgenstrahlung from the Universe', Zimmermann U., Trumper J.E., Yorke H. (eds)

Papadakis I.E., & Lawrence A., 1995, MNRAS, 272, 161

Peacock J.A., 1983, MNRAS, 202, 615

Peacock J.A., 1985, MNRAS, 217, 601

Piccinotti G., Mushotzky R.F., Boldt E.A., Holt S.S., Marshall F.E., Serlemitsos P.J., Schafer R.A., 1982, ApJ, 253, 485

Pounds K.A., Turner T.J., Warwick R.S., 1986, MNRAS, 221, 7P

Pounds K.A., Nandra K., Stewart G.C., George I.M., Fabian A.C., 1990, Nature, 344, 132

Pounds K.A., Nandra K., Fink H.H. and Makino F., 1994, MNRAS, 267, 193

Pounds K.A., Done C., Osborne J.P., 1995, MNRAS, 277, 5P

Press W.H., Teukolsky S.A., Vetterling W.T., Flannery B.P., 1992, Numerical Recipes in Fortran, Cambridge University Press, p.640

Primini F.A., Murray S.S., Huchra J., Schild R., Burgh R., Giacconi R., 1991, ApJ, 374, 440

Puchnarewicz E.M., Mason K.O., Cordova F.A., Kartje J., Branduardi-Raymont G., Mittaz J.P.D., Murdin P.G., Allington-Smith J., 1992, MNRAS, 256, 589

Puchnarewicz E.M., Mason K.O., Siemiginowska A., Pounds K.A., 1995, MNRAS, 276, 1281

Pye J.P. & Warwick R.S., 1979, MNRAS, 187, 905

Rees M.J., 1984, Annu. Rev. Astron. Astrophys., 22, 471

Reynolds C.S., Fabian A.C., Nandra K., Inoue H., Kunieda H., Iwasawa K., 1995, MNRAS, 277, 901

Romero Colmenero E., Branduardi-Raymont G., Carrera F.J., Jones L.R., Mason K.O., McHardy I.M., Mittaz J.P.D., 1996, MNRAS, 282, 94

Ross R.R., Fabian A.C. and Mineshige S., 1992, MNRAS, 258, 189

Ross R.R. and Fabian A.C., 1993, MNRAS, 261, 74

Rowan-Robinson M., C.R. Benn, Lawrence A., McMahon R.G., Broadhurst T.J., 1993, MNRAS, 263, 123

Saunders W., Rowan-Robinson M., Lawrence A., Efstathiou G., Kaiser N., 1990, MNRAS, 242, 318

Schmidt M., 1968, ApJ, 151, 394

Schmidt M. & Green R.F., 1983, ApJ, 269, 352

Schmidt M., Schneider D.P., Gunn J.E., 1995, AJ, 110, 68

Schnopper H.W., Davis M., Delvaille P., Geller M.J., Huchra J.P., 1978, Nature, 275, 719

Shanks T., Georgantopoulos I., Stewart G.C., Pounds K.A., Boyle B.J., Griffiths R.E., 1991, Nature, 353, 315

Shastri P., Wilkes B.J., Elvis M., McDowell J., 1993, ApJ, 410, 29

Snowden S.L., McCammon D., Burrows D.N. and Mendenhall J.A., 1994, ApJ, 424, 714

Snowden S.L., Turner T.J., George I.M., Yusaf R., Predehl P., Prieto A., 1995, OGIP Calibration Memo CAL/ROS/95-003

Spinoglio L. & Malkan M.A., 1989, ApJ, 342, 83

Stark, A.A., Gammie, C.F., Wilson R.W., Bally J., Linke R., Heiles C., Hurwitz M., 1992, APJS, 79, 77

Stephens S.A., 1989, AJ, 97, 10

Stocke J.T., Morris S.L., Gioia I.M., Maccacaro T., Schild R., Wolter A., Fleming T.A., Henry J.P., 1991, ApJS, 76, 813

Stewart G.C., Georgantopoulos, I., Boyle B.J., Shanks T., Griffiths R.E., 1994, in Makino, F. & Ohashi T. ed, Universal Academy Press, Tokyo, (New Horizon in X–ray Astronomy: First results from ASCA), p331

Tanaka Y., Nandra K., Fabian A.C., Inoue H., Otani C., Dotani T., Hayashida K., Iwasawa K., Kii T., Kunieda H., Makino F., Matsuoka M., 1995, Nature, 375, 659

Terlevich R., Tenorio-Tagle G., Franco J., Melnick J., 1992, MNRAS, 255, 713

Terlevich R., Tenorio-Tagle G., Rozyczka M., Franco J., Melnick J., 1995, MNRAS, 272, 198

Thompson I.B., Martin P.G., 1988, ApJ, 330, 121

Torricelli-Ciamponi G. & Courvoisier T.J.-L., 1995, A&A, 296, 651

Tresse L., Rola C., Hammer F., Stasińska G., Le Fèvre O., Lilly S.J., Crampton D., 1996, MNRAS, in press

Turner T.J., Pounds K.A., 1989, MNRAS, 240, 833

Turner T.J., 1993, OGIP Calibration Memo CAL/ROS/93-007

Tyson J.A., 1988, AJ, 96, 1

Walter R., & Courvoisier T.J.-L., 1992, A&A, 266, 65

Walter R. & Fink H.H., 1993, A&A, 274, 105

Ward M.J., Wilson A.S., Penston M.V., Elvis M., Maccacaro T., Tritton K.P., 1978, ApJ, 223, 788

Weedman D., 1986, Quasar astronomy, Cambridge Univ. Press, Cambridge

White M., Scott D., Silk J., Davis M., 1995, MNRAS, 276, L69

Wills B.J., Wills D., Evans N.J., Natta A., Thompson K.L., Breger M., Sitko M.L., 1992, ApJ, 400, 96

Yi I., 1996, ApJ, 473, 645

Zdiarzki A.A., Ghisellini G., George I.M., Svensson R., Fabian A.C., Done C., 1990, ApJ, 363, L1

Appendix A

Distribution of spectral slopes and the luminosity function

A.1 Introduction

The concept of the K correction, which is used to correct luminosities and luminosity functions to a constant emitted bandpass, was introduced in chapter 1. With the poor spectral resolution of *ROSAT* , and limited exposure time, it is not possible to determine an accurate K correction for each source individually. Normally, the mean spectrum is used for K correction, but this leads to a redshift dependent overestimation of the luminosity function. This was shown by Francis (1992) for the case of a single power law luminosity function and a gaussian distribution of AGN spectral slopes. I expand his results to suit the more realistic case of a two power law luminosity function, which is used in this thesis.

The purpose of this treatment is to relate quantitatively the observed luminosity function $\phi_{obs}(L, z)$ to the intrinsic luminosity function $\phi(L, z)$.

I assume that AGN have a normal distribution of spectral slopes with standard deviation σ_α about the mean slope α_0, both of which are defined at the present epoch $z = 0$. I also assume that AGN spectral slopes are not intrinsically related to luminosity (i.e. AGN at different luminosities have the same distribution of spectral slopes) and that the intrinsic spectral slopes of AGN do not evolve with redshift. The number of objects per unit comoving volume per unit luminosity interval per unit interval in spectral slope at the present epoch ($z = 0$) can be defined as

$$\frac{d^3N}{dVdL_0d\alpha}(L_0, \alpha) = \phi_0(L_0) \times \psi(\alpha)$$

where

$$\psi(\alpha) = \frac{e^{-(\alpha-\alpha_0)^2/2\sigma_\alpha^2}}{\sigma_\alpha\sqrt{2\pi}}$$

is the normalised gaussian distribution of spectral slopes.

First I consider the simple case of a single unbounded power law luminosity function which has no intrinsic evolution with redshift, which is the case treated by Francis (1992).

A.2 Single Unbounded Power Law Luminosity Function

$$\phi_0(L_0) = kL_0^{-\gamma}$$

and hence,

$$\frac{d^3N}{dVdL_0\,d\alpha}(L_0, z, \alpha) = kLo^{-\gamma}\,\frac{e^{-(\alpha-\alpha_0)^2/2\sigma_\alpha^2}}{\sigma_\alpha\sqrt{2\pi}} \qquad \text{(A.1)}$$

The luminosity function and distribution of spectral slopes do not evolve with redshift, but for $z \neq 0$ the observed bandpass will be different to the emitted bandpass. Using the expression for K correction of a power law spectrum given in chapter 1, section 1.2, one obtains

$$L_{obs} = L_0 \times (1+z)^{1-\alpha} \qquad \text{(A.2)}$$

where L_{obs} is the luminosity in the observers bandpass and L_0 is the luminosity in the emitted bandpass. Substituting in equation A.1 gives

$$\frac{d^3N}{dV\,dL_{obs}\,d\alpha}(L_{obs}, z, \alpha) = kL_{obs}^{-\gamma}(1+z)^{(1-\alpha)(\gamma-1)}\,\frac{e^{-(\alpha-\alpha_0)^2/2\sigma_\alpha^2}}{\sigma_\alpha\sqrt{2\pi}} \tag{A.3}$$

Rearranging,

$$\frac{d^3N}{dV\,dL_{obs}\,d\alpha}(L_{obs}, z, \alpha) = kL_{obs}^{-\gamma}(1+z)^{(1-\alpha_0)(\gamma-1)}e^{[\sigma_\alpha(\gamma-1)log_e(1+z)]^2/2}$$

$$\times\frac{e^{-[\alpha-(\alpha_0-(\gamma-1)log_e(1+z)\sigma_\alpha^2)]^2/2\sigma_\alpha^2}}{\sigma_\alpha\sqrt{2\pi}}$$

It is convenient to K correct using the average spectral slope α_0. This amounts to changing the from the variable L_{obs} to

$$L = L_{obs} \times (1+z)^{\alpha_0-1}$$

giving

$$\frac{d^3N}{dV\,dL\,d\alpha}(L, z, \alpha) = kL^{-\gamma}e^{[\sigma_\alpha(\gamma-1)log_e(1+z)]^2/2} \tag{A.4}$$

$$\times\frac{e^{-[\alpha-(\alpha_0-(\gamma-1)log_e(1+z)\sigma_\alpha^2)]^2/2\sigma_\alpha^2}}{\sigma_\alpha\sqrt{2\pi}}$$

Integrating over all values of α gives

$$\frac{d^2N}{dV\,dL}(L, z) = \phi_{obs}(L, z) = kL^{-\gamma}e^{(\sigma_\alpha(\gamma-1)log_e(1+z))^2/2} \tag{A.5}$$

Hence the observed luminosity function of objects K corrected using the mean spectrum, $\phi_{obs}(L, z)$, is $e^{(\sigma_\alpha(\gamma-1)log_e(1+z))^2/2}$ times larger than the actual luminosity function, $\phi(L, z)$. This is the result given by Francis (1992).

A.3 Real evolution

At this stage, I introduce real evolution of the luminosity function (because in reality the luminosity function is evolving), and I will assume that the luminosity function retains its shape at all redshifts, i.e. the evolution is some combination of PLE and PDE. Hence

$$\phi(L,z) = g(z)\frac{\phi_0(L/f(z))}{f(z)}$$

and $L = f(z)L_0$ so that g(z) and f(z) represent density and luminosity evolution respectively (see chapter 1, sections 1.5.2 and 1.5.1 for more details). Equation A.2 is replaced by

$$L_{obs} = L_0 \times f(z) \times (1+z)^{1-\alpha}$$

and equation A.3 is replaced by

$$\frac{d^3N}{dVdL_{obs}\,d\alpha}(L_{obs},z,\alpha) = g(z)\frac{k(L_{obs}/f(z))^{-\gamma}}{f(z)}(1+z)^{(1-\alpha)(\gamma-1)}\frac{e^{-(\alpha-\alpha_0)^2/2\sigma_\alpha^2}}{\sigma_\alpha\sqrt{2\pi}} \tag{A.6}$$

K correcting with the average spectral slope and rearranging,

$$\frac{d^3N}{dVdL\,d\alpha}(L,z,\alpha) = g(z)\frac{k(L/f(z))^{-\gamma}}{f(z)}e^{[\sigma_\alpha(\gamma-1)log_e(1+z)]^2/2} \tag{A.7}$$

$$\times\frac{e^{-[\alpha-(\alpha_0-(\gamma-1)log_e(1+z)\sigma_\alpha^2)]^2/2\sigma_\alpha^2}}{\sigma_\alpha\sqrt{2\pi}}$$

Integrating over all values of α,

$$\phi_{obs}(L,z) = g(z)\frac{k(L/f(z))^{-\gamma}}{f(z)}e^{[\sigma_\alpha(\gamma-1)log_e(1+z)]^2/2} \tag{A.8}$$

A.4 Bounded Power Law Luminosity Function

The luminosity function of AGN is *not* an unbounded power law, hence the above treatment is not appropriate. It is useful to consider the extreme example where the $z=0$ luminosity function is a power law within limits, and is zero otherwise:

$$\phi_0(L_0) = L_0^{-\gamma} \qquad L_1 < L_0 < L_2$$

$$\phi_0(L_0) = 0 \qquad L_0 < L_1, \quad L_0 > L_2$$

ϕ_{obs} is obtained by integrating expression A.7 for $\frac{d^3N}{dVdL\,d\alpha}(L,z,\alpha)$ with respect to α between the limits

$$\alpha = \alpha_0 - \frac{log_e(\frac{L}{L_1 f(z)})}{log_e(1+z)}$$

and

$$\alpha = \alpha_0 - \frac{log_e(\frac{L}{L_2 f(z)})}{log_e(1+z)}$$

This is an integration over the gaussian distribution of α, hence the difference between the bounded and unbounded case will be small ($< 5\%$) when

$$L_1 f(z)(1+z)^{[(\gamma-1)log_e(1+z)\sigma_\alpha^2+2\sigma_\alpha]} < L < L_2 f(z)(1+z)^{[(\gamma-1)log_e(1+z)\sigma_\alpha^2-2\sigma_\alpha]}$$

Using reasonable values found for X–ray selected AGN, $1.5 < \gamma < 3.5$, $z < 5$, and $\sigma_\alpha < 0.6$ the difference between the bounded and unbounded case is always small for values of L between, but more than 1 decade from, the 'end points' of ϕ_{obs}.

A.5 Two Power Law Luminosity Function

The $z = 0$ X–ray luminosity function is commonly parametrised as two power laws:

$$\phi_0(L_0) = K_1 L_0^{-\gamma_1} \qquad L_0 < L_{break}$$

$$\phi_0(L_0) = K_2 L_0^{-\gamma_2} \qquad L_{break} < L_0$$

and the luminosity function is required to be continuous so that

$$K_2 = K_1 L_{break}^{(\gamma_2-\gamma_1)} \tag{A.9}$$

When all AGN are assumed to have the same slope, and are subject to PLE, PDE, or any combination of the two, the observed luminosity function has this form at all redshifts. When we take into account the distribution of AGN slopes, this is no longer true. The exact form of ϕ_{obs} is obtained by summing the observed luminosity functions from two power law luminosity functions which are bounded at $L_{break} f(z)$ (see the previous section). As redshift increases, the sharp knee in the luminosity function will become increasingly rounded off, but away from the knee the slopes of the luminosity function do not change.

For practical reasons, it is preferable to approximate ϕ_{obs} as a broken power law, which retains its shape at all redshifts. I will compare this approximation with the exact treatment at the end of this section. Away from the break, the luminosity function behaves as if it were two unbounded power laws, but as $\gamma_1 \neq \gamma_2$, both sides of ϕ_{obs} evolve at a different rate, so that they no longer meet at $L_{break}f(z)$. The new intercept is calculated by treating the two parts of the luminosity function as if they are unbounded power laws, i.e. by applying equation A.8 to each half seperately.

$$\phi_{obs}(L,z) = g(z)\frac{K_1(Lf(z))^{-\gamma_1}}{f(z)}e^{[\sigma_\alpha(\gamma_1-1)log_e(1+z)]^2/2} \quad L < L_{obs_{break}}$$

$$\phi_{obs}(z,L) = g(z)\frac{K_2(Lf(z))^{-\gamma_2}}{f(z)}e^{[\sigma_\alpha(\gamma_2-1)log_e(1+z)]^2/2} \quad L > L_{obs_{break}}$$

Equating and substituting for K_2 using equation A.9 one obtains:

$$L_{obs_{break}} = L_{break}f(z)e^{[\sigma_\alpha log_e(1+z)]^2(\gamma_2+\gamma_1-2)/2}$$

If one defines

$$f^*(z) = e^{[\sigma_\alpha log_e(1+z)]^2(\gamma_2+\gamma_1-2)/2}$$

$$g^*(z) = e^{[\sigma_\alpha log_e(1+z)]^2(\gamma_1-1)(1-\gamma_2)/2}$$

then

$$\phi_{obs}(L,z) = g(z)g^*(z)\frac{\phi_0[L/(f(z)f^*(z))]}{f(z)f^*(z)}$$

Hence the spurious evolution is now parameterised as a combination of spurious luminosity evolution $f^*(z)$ and spurious density evolution $g^*(z)$.

A comparison between this approximation for ϕ_{obs} and the actual shape is given in chapter 4, figure 4.5. As expected, the approximation is extremely good except for a small region around the knee in the luminosity function.

Appendix B

RIXOS data used in this thesis

The information is presented in two tables: one contains data on the RIXOS fields (i.e. the *ROSAT* pointings used for RIXOS) while the other contains data on the RIXOS sources.

Table B.1: RIXOS fields used in this thesis

Field	Name	$N_{\rm H}^a$	R.A. (2000)	Dec. (2000)	Expos^b	Flux^c limit	Field	Name	$N_{\rm H}^a$	R.A. (2000)	Dec. (2000)	Expos^b	Flux^c limit
110	P200329	1.07	217.1799	33.1793	18250	3.0	115	NOWER1	2.50	152.7500	28.2500	38910	3.0
116	NOWER2	1.22	181.0000	56.1700	30590	3.0	122	MEATYP2	4.12	247.3500	78.0800	38450	3.0
123	P700228	1.22	169.7700	21.3100	24950	3.0	124	P700232	1.64	181.1700	27.9000	17400	8.4
125	P200322	5.04	351.3300	23.4100	26300	3.0	126	P700223	1.95	185.3900	28.2300	10400	3.0
127	P700221	1.71	184.4800	30.1100	22400	8.4	133	P300137	1.19	164.2300	49.7000	9400	3.0
205	P100578	4.31	348.0900	10.7800	10313	3.0	206	P200453	3.65	126.7196	26.6300	15927	3.0
208	P700264	0.73	152.5696	53.7500	17331	3.0	211	P700210	3.95	110.4696	71.3400	21043	3.0
212	P700255	1.19	247.5800	37.3200	8933	3.0	213	P700258	4.35	121.1300	65.0000	8354	3.0
215	P150046	1.18	214.9400	54.3900	11516	3.0	216	P700211	3.54	140.4000	62.2600	19495	3.0
217	P700248	1.13	213.4500	44.0000	25319	3.0	218	P400059	3.01	148.2900	7.9300	9038	3.0
219	P700208	1.29	194.0600	56.8700	24340	3.0	220	P701200	3.94	261.5500	74.5200	10578	3.0
221	P700546	2.90	132.0800	37.6700	12391	3.0	222	P701202	2.43	180.3096	-3.6800	13563	8.4
223	P200721	1.84	248.6000	57.1500	47467	3.0	224	HZ43N	1.01	199.1000	29.1000	34943	3.0
225	P200076	2.19	154.9096	19.8700	26522	3.0	226	P700073	1.19	194.2396	47.3400	48051	3.0
227	P200091	1.77	174.1396	29.8000	33886	3.0	228	P400020	3.66	129.6996	36.5200	10978	3.0
229	P700263	0.79	152.5596	52.7500	14616	8.4	230	P700265	0.79	152.5596	51.7500	23995	8.4
231	P900213	0.73	152.5696	54.7500	16813	8.4	232	P900214	0.84	152.5500	50.7500	15911	3.0
234	P700112	4.05	115.6696	65.1800	19844	3.0	236	P700123	2.55	255.3496	51.8200	8196	3.0
237	P700230	2.95	243.4896	65.7200	8442	8.4	238	P700246	4.08	248.6196	70.5300	9357	3.0
240	P700055	1.22	179.4840	55.4539	58534	3.0	245	P700099	8.81	52.1106	2.7999	25727	3.0
246	P300003	6.19	31.7196	15.3000	25174	8.4	248	P700329	1.50	137.3896	42.9000	23561	3.0
250	P700436	3.52	134.6696	14.1500	21565	8.4	252	P700319	0.78	150.4896	55.6800	19006	3.0
253	P700387	1.59	145.2696	38.9000	17193	3.0	254	P700391	1.05	206.1796	55.8900	17116	3.0
255	P700315	5.07	119.6196	37.7900	15992	3.0	257	P700326	2.18	136.3796	34.1300	14511	3.0
258	P700358	3.36	169.5696	7.7700	14425	3.0	259	P700010	1.96	170.0696	13.5900	14061	3.0
260	P300158	0.93	161.8096	54.3100	14008	3.0	261	P201103	3.31	233.6696	26.7200	13937	3.0
262	P701048	3.37	21.1396	3.8000	13894	3.0	265	P700216	1.10	197.6196	32.3500	13034	3.0
266	P700435	2.05	188.0096	20.1600	12299	8.4	268	P700392	2.08	209.0096	18.3700	11553	3.0
270	P700271	3.57	61.3896	-13.1400	10879	8.4	271	P700510	2.07	171.1800	38.7600	10676	3.0
272	P700489	4.67	271.7100	69.8200	10461	3.0	273	P700384	2.81	160.6896	12.0600	10209	3.0
274	P700227	2.16	211.5900	22.4000	10141	3.0	277	P700473	1.74	204.5696	48.2800	9918	8.4
278	P701034	1.94	203.1000	11.1100	9611	3.0	279	P700531	4.28	58.4500	-10.4200	9547	8.4
281	P701092	5.76	2.6196	10.9700	9117	3.0	283	P701055	10.46	64.2196	1.0900	9043	3.0
285	P400141	3.43	145.9300	16.5200	8957	3.0	286	P700774	2.33	151.0800	5.2200	8868	3.0
287	P700499	1.06	171.4000	54.3800	8827	3.0	288	P700506	1.43	187.1000	31.4800	8820	8.4
289	P700496	4.50	178.3000	80.9700	8575	8.4	290	P700389	1.46	144.9696	35.9000	8158	3.0
291	P200127	2.02	165.8496	36.0400	16670	3.0	292	P200468	3.48	25.8396	4.3300	8663	8.4
293	P200473	4.59	124.9496	37.5200	8954	3.0	294	P200474	4.25	349.6896	12.6000	9488	3.0
299	P700262	1.56	141.3000	52.2900	10298	8.4	302	P700540	1.23	156.1396	47.1500	19359	3.0
303	P700872	3.55	166.6958	72.5700	13081	8.4	304	P700887	3.56	133.2896	13.8800	18552	8.4
305	P701214	2.25	147.4396	73.2400	12532	3.0							

a Galactic column (10^{20} cm^{-2})

b Exposure time (seconds)

c 0.5-2 keV flux limit (10^{-14} erg s^{-1} cm^{-2})

Table B.2: RIXOS sources used in this thesis

Field	Source	Flux[a]	Type	z	Field	Source	Flux[a]	Type	z	Field	Source	Flux[a]	Type	z
110	1	6.54	AGN	0.364	110	8	3.07	AGN	0.938	110	34	3.07	AGN	0.42
110	35	3.05	AGN	0.582	110	50	3.91	AGN	1.34	115	53	33.43	AGN	0.555
116	14	35.89	AGN	0.090	116	28	3.04	AGN	0.766	122	1	4.40	AGN	1.134
122	13	8.85	AGN	0.358	122	14	7.61	AGN	0.380	122	16	20.42	NELG	0.006
122	21	8.70	AGN	0.376	123	1	17.71	AGN	0.282	123	27	4.42	AGN	0.351
123	28	3.90	AGN	0.212	123	41	3.57	AGN	1.818	123	42	3.29	AGN	0.477
123	46	3.65	AGN	1.288	123	66	5.81	AGN	0.494	123	85	9.71	AGN	0.652
124	36	8.48	NELG	0.343	125	14	3.83	AGN	1.84	125	17	7.19	AGN	0.44
126	1	9.04	AGN	0.029	126	27	12.86	AGN	3.305	133	17	3.40	AGN	2.390
133	22	5.94	AGN	1.788	133	24	4.15	AGN	0.360	205	1	5.06	AGN	0.71
205	22	10.98	AGN	0.44	205	23	7.83	AGN	0.62	205	25	6.31	NELG	0.196
205	34	3.71	AGN	0.75	206	6	5.40	AGN	0.690	206	9	5.81	AGN	0.805
206	507	6.00	AGN	0.484	206	522	9.00	AGN	0.73	208	2	11.72	AGN	0.387
208	18	7.12	AGN	0.46	208	55	5.14	AGN	1.718	211	30	6.61	AGN	1.39
211	35	4.24	AGN	0.459	211	42	7.32	AGN	0.232	212	6	4.84	AGN	1.004
212	16	3.52	AGN	0.843	212	25	5.41	AGN	0.801	212	32a	4.57	AGN	0.923
212	32b	4.57	AGN	0.923	213	7	6.60	AGN	0.54	213	11	3.15	AGN	1.54
213	17	8.66	AGN	0.438	213	19	7.88	AGN	0.467	213	20	7.60	AGN	0.664
215	1	3.43	AGN	2.248	215	19	8.86	AGN	0.584	215	32	3.57	AGN	0.613
216	7	4.09	AGN	0.804	216	30	5.11	AGN	0.941	216	33	3.46	AGN	0.786
217	3	3.71	AGN	0.99	217	5	4.19	NELG	0.137	217	21	3.31	AGN	0.562
217	34	4.62	AGN	1.200	217	35	3.60	AGN	0.435	217	59	5.24	AGN	0.590
217	560	18.00	NELG	0.095	218	1	9.59	AGN	0.545	218	9	4.26	AGN	0.52
218	13	3.93	AGN	1.450	218	14	10.44	NELG	0.22	218	21	4.27	AGN	0.76
218	27	13.61	AGN	0.631	219	15	3.06	AGN	1.190	219	26	7.62	NELG	0.124
219	45	8.49	AGN	1.261	219	48	3.12	AGN	1.367	220	13	3.04	AGN	0.970
220	18	4.42	AGN	0.442	220	23	7.02	AGN	0.193	220	25	5.83	AGN	0.210
221	7	24.75	AGN	0.292	221	16	6.61	AGN	0.184	221	35	52.26	AGN	0.451
223	17	11.76	AGN	0.288	223	97	4.93	AGN	0.059	224	26	8.99	AGN	0.277
224	201	4.39	AGN	1.544	225	1	3.17	AGN	0.488	226	41	9.58	AGN	1.315
226	74	3.86	NELG	0.303	226	114	3.74	AGN	0.8	227	19	3.67	AGN	1.861
227	37	9.72	AGN	1.413	227	301	3.77	AGN	0.114	227	513	6.00	AGN	0.959
228	1	9.49	AGN	1.726	229	301	38.43	AGN	0.175	231	301	9.71	AGN	0.783
231	503	13.00	AGN	0.233	232	16	3.05	AGN	0.227	232	301	3.65	AGN	0.385

Table B.2 continued

Field	Source	Flux[a]	Type	z	Field	Source	Flux[a]	Type	z	Field	Source	Flux[a]	Type	z
234	1	7.87	AGN	1.666	234	33	3.30	AGN	1.019	236	5	3.07	AGN	0.473
236	21	3.29	AGN	1.13	236	22	4.33	AGN	0.048	238	11	4.61	AGN	0.325
240	15	3.14	AGN	1.263	240	60	4.08	NELG	0.245	240	82	4.59	AGN	0.518
245	4	3.54	AGN	0.7	245	543	63.46	NELG	0.04	248	2	7.84	AGN	0.274
248	51	13.70	AGN	0.242	252	1	5.25	AGN	0.218	252	9	3.61	AGN	0.673
252	31	64.45	AGN	1.413	252	34	3.09	AGN	0.680	252	36	6.05	AGN	1.037
252	38	12.43	AGN	0.216	252	46	5.22	AGN	2.091	253	5	3.03	AGN	1.211
253	32	4.25	AGN	0.237	254	6	5.63	NELG	0.459	254	10	11.38	AGN	0.936
254	11	8.76	AGN	1.166	254	41	4.02	AGN	0.486	255	7	3.32	AGN	0.260
255	13	4.08	AGN	0.57	255	19	4.06	AGN	0.864	255	23	4.36	AGN	0.72
257	1	16.55	AGN	1.021	257	14	4.75	AGN	1.099	257	20	3.44	AGN	1.304
257	38	4.29	AGN	1.260	258	1	15.13	AGN	0.698	258	5	4.09	AGN	0.81
258	30	3.09	AGN	0.84	258	32	3.26	AGN	1.618	258	101	3.87	NELG	0.136
259	5	5.64	AGN	0.977	259	7	3.42	AGN	0.408	259	11	3.34	AGN	0.995
259	30	4.84	AGN	1.94	260	8	3.71	AGN	1.823	260	28	5.75	NELG	0.105
260	44	3.84	AGN	1.504	262	1	3.45	AGN	0.88	262	2	4.79	AGN	1.202
262	10	22.43	AGN	0.336	262	12	5.61	AGN	0.93	262	34	9.32	AGN	0.31
265	1	7.88	AGN	2.34	265	17	4.72	AGN	0.448	266	527	18.01	AGN	0.135
268	11	3.55	AGN	1.196	268	24	15.43	AGN	0.251	270	14	24.31	AGN	0.121
271	2	3.57	AGN	0.446	271	7	7.48	AGN	1.039	272	8	3.91	AGN	1.82
272	10	12.93	NELG	0.32	272	18	9.24	AGN	0.59	272	23	10.17	NELG	0.095
272	28	7.92	AGN	0.44	273	4	4.99	AGN	1.046	273	6	37.71	AGN	0.270
273	18	6.58	AGN	0.361	273	22	3.84	AGN	1.080	273	23	3.19	AGN	0.433
274	8	13.83	AGN	0.156	278	9	8.42	AGN	0.949	278	10	46.51	AGN	0.090
278	15	7.78	NELG	0.080	279	6	11.06	AGN	0.18	281	11	3.14	AGN	2.93
281	21	8.76	AGN	0.34	283	6	18.01	AGN	1.219	283	11	8.89	AGN	0.272
283	14	6.74	AGN	0.284	283	21	5.86	AGN	0.714	286	2	3.79	AGN	1.498
290	21	3.01	AGN	2.575	293	1	6.36	AGN	0.82	293	6	14.70	AGN	0.082
293	10	16.36	AGN	0.760	293	12	4.46	AGN	0.91	293	13	6.60	AGN	0.189
294	1	5.27	AGN	0.71	294	6	6.42	NELG	0.12	302	14	3.48	AGN	0.786
302	18	6.36	AGN	0.95	303	105	8.46	AGN	0.679	303	107	8.60	AGN	2.100
304	10	11.03	AGN	0.19	305	11	10.81	AGN	0.252	305	18	6.64	AGN	0.386

[a] 0.5-2 keV flux (10^{-14} erg s^{-1} cm^{-2}) after correction for Galactic N_{H}